Cocontinuous Polymer Blends: Controlling Morphology via Interfacial Modification and Rheology

A DISSERTATION
SUBMITTED TO THE FACULTY OF
UNIVERSITY OF MINNESOTA
BY

Aaron Thomas Hedegaard

IN PARTIAL FULFILLMENT OF THE REQUIREMENTS
FOR THE DEGREE OF
DOCTOR OF PHILOSOPHY

Christopher W. Macosko, Adviser

March 2014

Acknowledgements

I would like to thank my advisor, Chris Macosko. When I first joined his research group, it is safe to say that I did not know the first thing about rheology. Now, a little over 5 years later, the fact that this thesis exists is a testament to his ability as a leader and mentor. He has been a role model and inspiration both in and out of the lab, and his support is dearly appreciated.

I would also like to thank all the people who helped by contributing their time and knowledge to this project to make this research possible. Thanks to Carlos Lopez-Barron, who introduced me to the project, and played an integral part in developing the 3D imaging techniques used here. Thanks to Milana Trifkovic and Liangliang Gu for the direct collaboration at various stages of the project. I would like to thank my industrial collaborators: Gibson Batch with 3M for helping with the continuous processing of the blends, Adam Pawloski with Interfacial Solutions for providing the PLA materials, and Matt Hansen from Dow for providing silica-free PEO to investigate the effect of these nanoparticles on the material rheology. I would like to thank all the undergraduate researchers for all their hard work in the lab over the years: Feida Chen, Huikang Fu, Anasmita Ghosh, Sijia Huang, Kyle Huston, Yalin Liu, Zach Oberholtzer, Lia Palmore, and Renxuan Xie. Thanks to Kumar Varoon for the assistance with to the diffusion cell. Thanks to Yuanyan Gu for providing the ionic liquid materials for the design of the gas separation membranes. Thanks to David Giles for all the guidance with the rheometers. And thanks to all the Macosko group members who provided valuable discussions, questions, and support.

This research was possible thanks to the various facilities available at the University of Minnesota: the Characterization Facility, the Biomedical Image Processing Laboratory, and the Minnesota Supercomputing Institute. Also, thanks to Lambton College in Sarnia, Ontario, Canada, for allowing the use of their twin screw extruder. This project was generously funded by University of Minnesota Materials Research Science and Engineering Center (UMN-MRSEC), through the National Science Foundation.

Most of all, I would like to thank my friends and family, who were always supportive of my academic life and never lost faith in my ability to persevere and get the job done. A special thanks to my brothers, Brock and Jared. You guys are the best brothers and friends a guy could ever ask for. Also, I would like to extend big thanks to my parents, for being a constant encouragement from day one.

Dedication

To Mom, Dad, Brock, and Jared

Abstract

Cocontinuous polymer blends are formed by melt blending two or more immiscible polymers to form multiple continuous interpenetrated networks. These are non-equilibrium structures where the morphology is determined by a combination of processing conditions, interfacial properties, and rheology. Thermodynamic instability causes the morphology to coarsen during annealing. Furthermore, a thorough understanding of the conditions and mechanism of cocontinuity formation has not been developed, and predictive models are empirical and frequently contradictory. This thesis seeks to advance the field of immiscible polymer blends by providing insight to two critical questions. First, can a better understanding of the role of interfacial stabilization on cocontinuity be developed? Second, can morphological predictions based on rheology be improved?

Concerning interfacial stabilization, this thesis approaches the problem via reactive blending and interfacially localized clay nanoparticles. The effectiveness of reactive blending was found to be heavily dependent on the molecular weight of the reactive polymers. Also, the formation of a copolymer brush at the interface was able to prevent coarsening due to a compression of that brush when interfacial area decreased. Nanoclays, when interfacially localized, were found to also prevent coarsening by jamming at the interface, and the combined compatibilization mechanism of reaction and clay was found to achieve the smallest phase sizes. As an application, these compatibilized blends were also tested as gas separation membranes.

Concerning the predictions of cocontinuity, various models from the literature were tested against experimental data to determine the center of the compositions that resulted in cocontinuity. It was found that models based on droplet packing worked best, though they gave no information concerning the range of cocontinuous compositions. Various mechanisms and rules of thumb were developed from the present work to provide much-needed insight for predicting the relative size of these ranges. This study also investigated the role of extensional

viscosity on cocontinuity by blending with long-chain branched polymers, where it was found that strain hardening branched polymers significantly broadened the range of cocontinuity. This demonstrated a shortcoming in the existing predictive models, which have only considered shear rheology when predicting cocontinuity.

Table of Contents

List of Tables

List of Figures

Chapter 1: Introduction

1.1 Motivation

Melt processing of immiscible polymers provides a relatively simple and inexpensive route to the development of new materials with superior properties compared to a single polymer. These immiscible blends can attain a variety of different morphologies, including dispersed droplets, fibers, lamellae, and cocontinuous morphologies.[1-4] Of these morphologies, cocontinuous blends are unique in that they possess two continuously percolated and interpenetrated phases.[3-8] A three-dimensional reconstruction of a cocontinuous blend, imaged by laser scanning confocal microscopy, is shown in Figure 1.1.

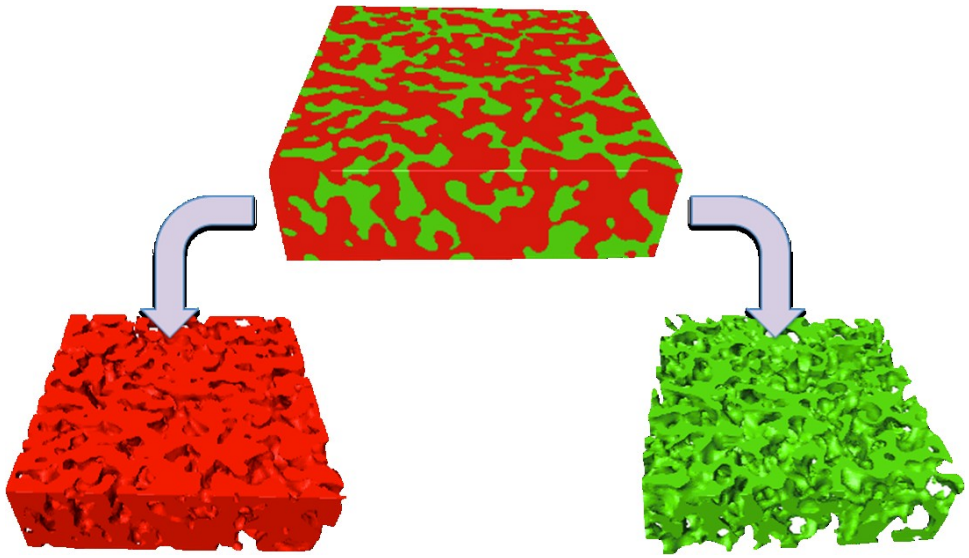

Figure 1.1. 3D reconstruction of a cocontinuous LDPE/PEO blend, as imaged by laser scanning confocal microscopy and shown also separated into each continuous phase.

Due to the continuity of multiple phases within the structure, cocontinuous blends can be used in applications requiring continuity of two materials with disparate properties. One such application includes razor blade lubricating strips, where a continuous phase of lubricating polymer such as polyethylene oxide is combined with a continuous mechanical support such as

polyethylene or polystyrene.[9] A cross-section of a lubricating strip is shown in Figure 1.2. Another application is conductive polymer blends,[10,11] where a conductive polymer with poor material properties can be supported by a mechanically robust polymer while retaining the continuity of the conductive phase. Various studies have also explored porous polymers from cocontinuous blends by solvent extraction or etching of a single continuous phase.[4,8,12-15] A melt processing method for producing such a porous film is shown in Figure 1.3.

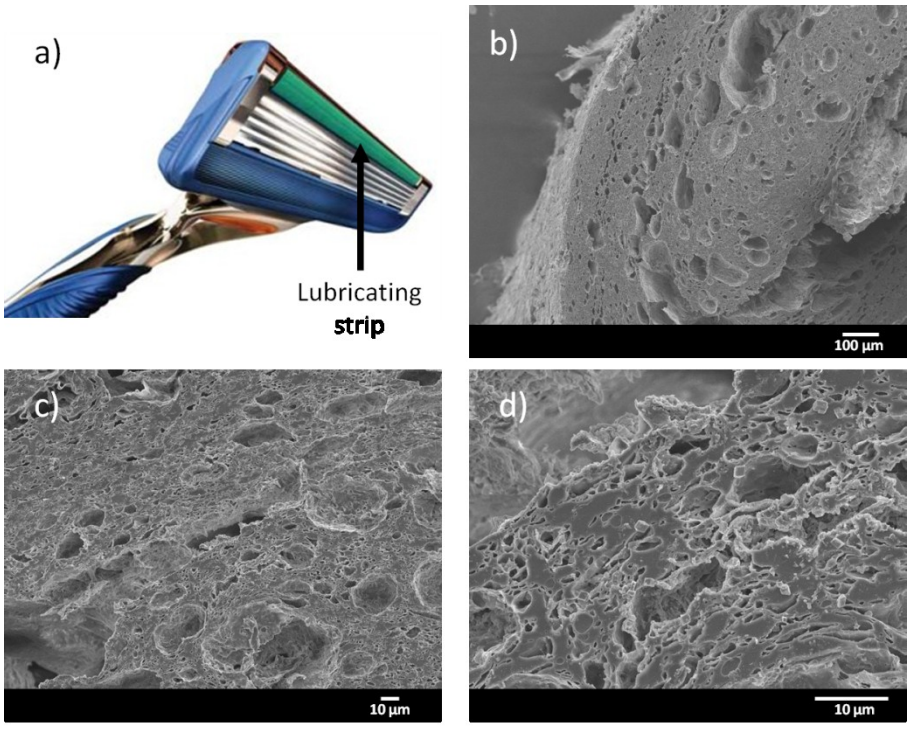

Figure 1.2. SEM micrographs of a cross section of a razor blade lubricating strip. Razor image in a) from Proctor and Gamble.

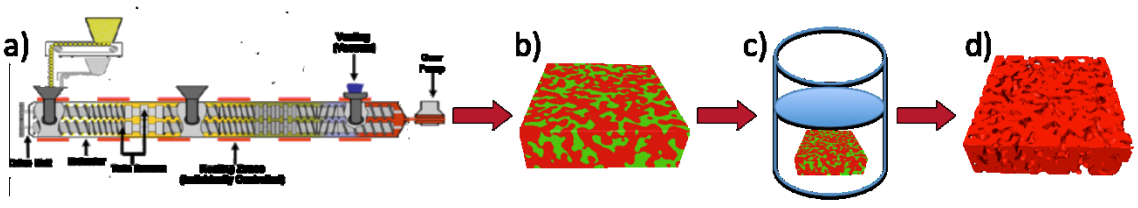

Figure 1.3. Process of producing porous materials from cocontinuous polymer blends. a) Materials are melt blended together via twin-screw extrusion or a batch microcompounder. b) Cocontinuous extrudate is collected. c) Blend is immersed in a selected solvent for one of the phases. d) Sample is collected and dried, yielding self-supporting porous materials.

At first glance, cocontinuous polymer blends appear similar to other cocontinuous polymer morphologies such as bicontinuous microemulsions,[16,17] and bicontinuous "gyroid" structures for AB block copolymers.[18] However, in contrast to these other structures, cocontinuous blends are thermodynamically unstable and are formed by kinetically trapping the morphology in a non-equilibrium structure.[12,19,20] As such, the resulting morphology of an immiscible blend is dictated by rheology, interfacial tension, composition, and melt processing conditions, and not exclusively by thermodynamics.[1-4,21-23]

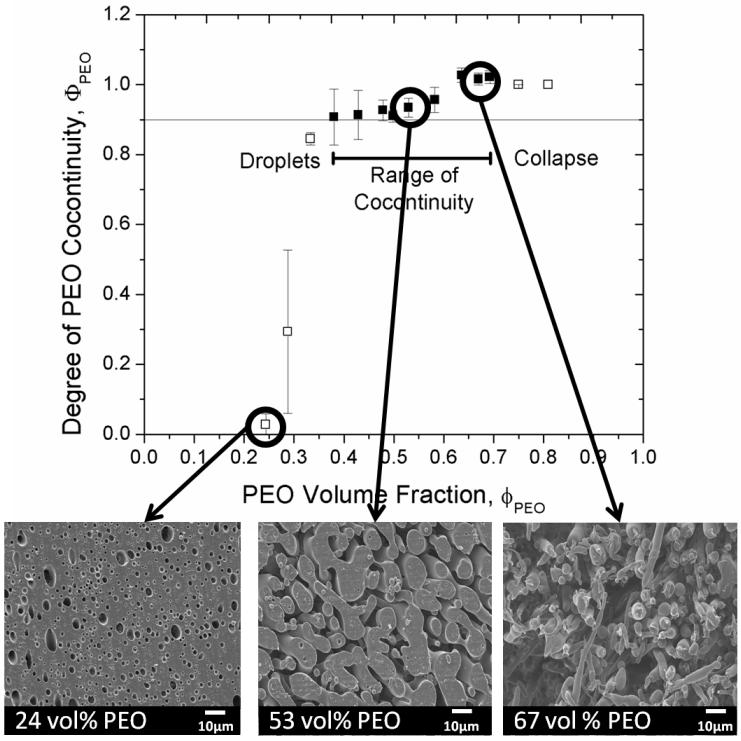

Figure 1.4. Degree of PEO phase continuity of LDPE/40K PEO blends. The filled in points represent the range of compositions which exhibited a cocontinuous morphology. SEM micrographs represent the morphological transitions between dispersed droplets and cocontinuity.

The thermodynamic instability of cocontinuous blends presents a number of both fundamental and practical challenges to the understanding and the application of these structures. The first challenge is that since the morphology is determined by a combination of kinetic effects (rheology, processing conditions) and thermodynamic effects (interfacial tension between the two

phases), no traditional "phase diagram" exists for predicting the resulting morphology of a blending process. Numerous morphological predictions for cocontinuity have been proposed, primarily revolving around the concept of phase inversion: the composition at which an immiscible blend is expect to invert the major continuous phase and the minor dispersed phase.[20,24-32] Cocontinuity typically occurs over a range of compositions, as shown by the example in Figure 1.4, which plots the degree of continuity (which can be thought of as the fraction of a phase that exists within continuously connected features) versus blend composition. It is expected that the phase inversion composition predicts the center of the range of cocontinuity. However, these empirical predictions traditionally fall short of predicting general blend behavior, and also provide no information concerning the range of compositions that result in cocontinuity. Therefore, predicting when an immiscible blend will result in cocontinuity is a difficult and poorly understood problem.

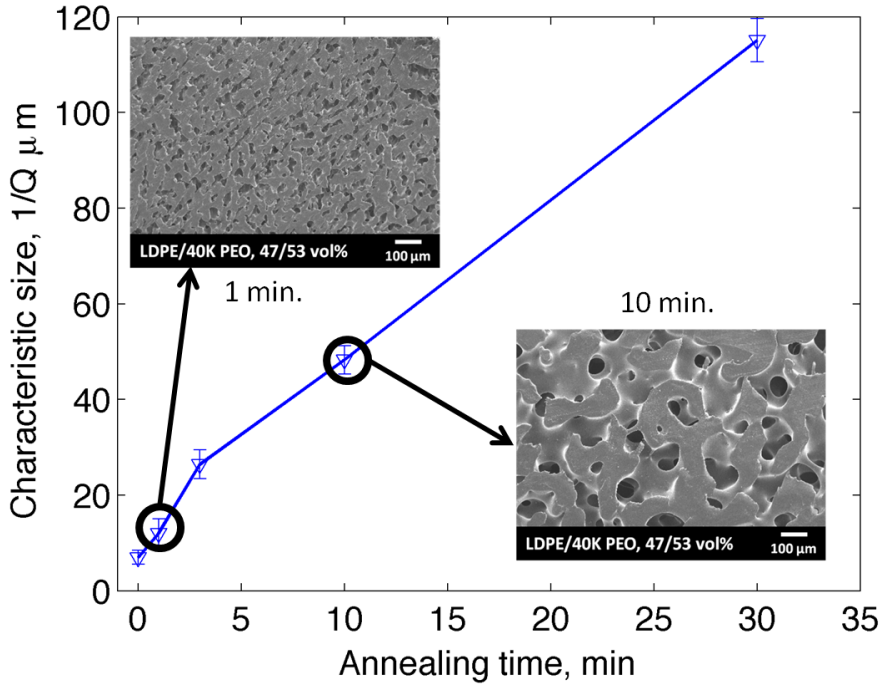

Figure 1.5. Characteristic phase size of a typical uncompatibilized LDPE/PEO cocontinuous blend as a function of annealing time at 150 °C. Inset SEM micrographs show the morphology undergoing self-similar coarsening.

The second challenge caused by the thermodynamic instability of cocontinuous polymer blends is the issue of coarsening. When a blend is heated above the glass transition temperatures of its components, the phase size of the morphology will increase due to self-similar coarsening, or the morphology will break up into dispersed droplets.[12,19,33-35] An example of self-similar coarsening can be seen in Figure 1.5, which shows the characteristic phase size of a cocontinuous blend as a function of annealing time. This coarsening is driven by the interfacial tension between the materials of the blend, which tries to minimize the interfacial area and curvature between the two phases.

In order to prevent or minimize the effects of coarsening during processing, cocontinuous blends are often compatibilized with an interfacial modifier. This can be either premade block copolymers,[7,35-37] or block and graft copolymers formed during melt processing via interfacial coupling reactions between functional polymers.[38-42] Blends may also be stabilized by interfacial localization of nanoparticles.[43-48] However, since the results of these stabilization techniques are also dependent on factors such as rheology and blending conditions, these represent more areas where further investigation is needed to develop a complete understanding of cocontinuous blends.

1.2 Overview of Thesis

As mentioned earlier, the control and determination of cocontinuity is predominantly influenced by four key factors: blend composition, blending conditions, rheological properties, and interfacial properties. However, in polymer melt processing, these factors are rarely independent. Processing conditions influence rheological behavior of shear thinning polymers. Changing the molecular weight of the components to control rheological behavior also affects the molecular weight of the interfacially located copolymers formed in reactive blending. Rheological and interfacial properties strongly influence what blend compositions are capable of forming cocontinuous blends. Finally, the shape of an interface is not determined exclusively by

interfacial properties, but also rheological properties of the blended polymers and the processing conditions. This provides the primary difficulty in predicting and controlling cocontinuous blend behavior – independent control of parameters is experimentally difficult to achieve.

This thesis aims to sort through these interrelated factors to shed light on some fundamental questions about cocontinuous blends. First, can a better understanding of blend stabilization be developed, particularly with how stabilization relates to rheological and interfacial phenomena? Second, can better intuition and methods be achieved for predicting the range of compositions that result in cocontinuity? Third, are there additional factors critical to the development of cocontinuity that merit investigation but have not previously been considered?

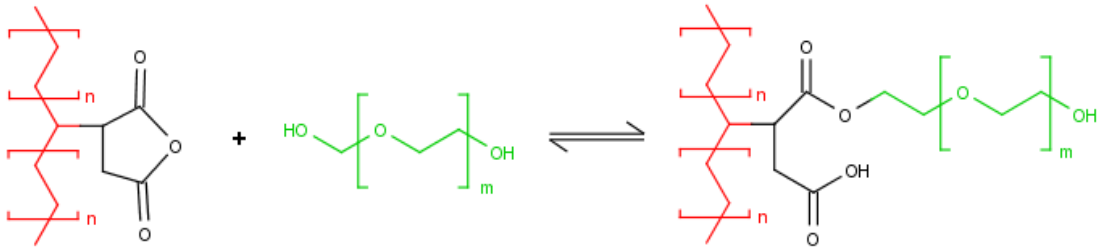

Figure 1.6. Reaction schematic between PE-g-MA and PEO.

Chapter 2 documents the work on interfacial stabilization by reactive blending, specifically exploring the interplay of bulk rheological properties, molecular weight of the components, and the interfacial properties of the resulting blends. The work here details blends prepared by melt mixing non-functional or maleic anhydride function polyethylene (PE) with polyethylene oxide (PEO) resins, comparing interfacial properties, blends size, and blend stability with varying the PEO molecular weight. Maleic anhydride grafted polyethylene (PE-g-MA) can react with the hydroxyl end functionality of PEO to form PE-g-PEO graft copolymers, as shown in Figure 1.6. These copolymers localize at the blend interface, lowering interfacial tension Γ and increasing interfacial elastic shear modulus β_s^*. Both Γ and β_s^* were observed to be dependent on the PEO molecular weight of the graft copolymer. The interfacial density of the graft copolymers was

quantified by x-ray photoelectron spectroscopy (XPS), and these results were related back to the measured interfacial properties in reactive systems. Reactively compatibilized systems also showed suppression of coarsening. This behavior was quantifiably linked back to the graft density and interfacial coverage of the graft copolymers, showing that cessation of coarsening was related to densification of the copolymer brush at the interface.

Chapter 3 presents a specific application of the results from Chapter 2 by developing a thin natural gas separation membrane from PE/PEO cocontinuous blends. The chapter focuses primarily on morphological control via processing conditions, comparing three separate melt blending procedures: small scale mixing in a recirculating batch microcompounder, and twin screw extrusion with both a low shear and high shear screw geometry. In particular, the study investigated the average characteristic size and characteristic size distribution of PE-g-MA/PEO blends that resulted from these different processing conditions. Ultimately, these parameters were used to design thin porous films from the blends that could be used in natural gas separation membranes, which required small pores and a narrow size distribution for the application.

Chapter 4 serves as a discussion and exploration on predicting the compositions that result in cocontinuity. While keeping processing conditions constant, the ranges of cocontinuity for polypropylene/polyethylene oxide (PP/PEO) blends as well as the blends produced in Chapter 2 were explored, comparing the effect of absolute viscosity, viscosity ratio, and interfacial reaction on the resulting morphology. Based on the observations on the ranges of cocontinuity, rules of thumb were developed in order to supplement the current literature with an improved and much-needed physical understanding of cocontinuity development and prediction. Various phase inversion models were also investigated, and it was found that models based on droplet packing behavior assuming deformable drops performed most successfully. When the viscosity ratio of the blend components was far from 1, the phase inversion composition could be best predicted by the same model modified to account for hard spheres instead of deformable particles.

Chapter 5 looks exclusively at rheological properties - namely the role that long chain branching of polymers plays in determining and controlling cocontinuity. Long chain branching is known to influence shear and, even more strongly, extensional rheological properties of polymers. The role of extensional rheology on the development of cocontinuity has never been previously explored. Comparing linear and branched versions of polyethylene (PE) and polylactic acid (PLA), it was found that blending with long chain branched polymers broadened the range of cocontinuous compositions. It is proposed that this is due to increased melt strength stabilizing elongated structures. These elongated features could more readily form cocontinuous networks. This improved the range of cocontinuity to a point, though excessive strain hardening due to branching was found to inhibit cocontinuous formation and lead to large characteristic sizes. We speculate that the very high extensional viscosity prevented the formation of thinner elongated structures and inhibited coalescence.

A final approach to interfacial and rheological modification of cocontinuous blends involved incorporating nanoparticulate clay, which is presented in Chapter 6. In these experiments, unmodified and organically modified montmorillonite were blended with LDPE/PEO cocontinuous blends. Localization was predicted by thermodynamics based on wetting parameters and interfacial tension, although discrepancies arose due to the kinetic effects of mixing disrupting the localization away from thermodynamic equilibrium. Organomodified clay was found to localize at the interface of these blends. This reduced characteristic size and suppressed coarsening. Clay was also incorporated into reactive PE-g-MA/PEO blends and was found to provide a synergistic effect to compatibilization, with blends stabilized both by graft copolymers and interfacially localized clay. Wetting parameter arguments were not successful in predicting clay localization in the reactive blend case. This was attributed to chemical compatibility between PE-g-MA and the clay that promoted dispersion in the PE-g-MA phase despite the thermodynamic drive of the clay to prefer PEO.

A summary and recommendations of future work in the area can be found in Chapter 7. The appendices are present to provide additional information concerning experimental methods and results beyond the scope of the chapters. Appendix A discusses and compares rheological methods of measuring interfacial tension within droplet-matrix polymer blends. Appendix B discusses methods of image analysis and compares results from 2D and 3D image analysis for cocontinuous blends. Since much of the present work featured blends of PEO, and PEO was found to contain nanoparticulate silica as a rheological modifier, Appendix C contains a rheological comparison of the commercial PEO used in the present work and specially synthesized silica-free PEO. Appendix D contains additional figures that are referred to throughout the thesis.

Chapter 2: Role of Molecular Weight in Reactive PE/PEO Cocontinuous Blends

2.1 Introduction

Melt blending of immiscible polymers is a relatively simple and effective way to create new materials with superior properties such as enhanced mechanical properties, improved processability, or reduced cost.[49-51] Blended polymers can also be used to continuously combine disparate properties such as mechanical toughness and electrical conductivity into a single material.[10,11] Most polymer pairs are immiscible and form macrophase separated structures due to the high molecular weight and large interfacial energy of the components.[1]

Binary immiscible polymer blends can adopt a variety of possible morphologies, including dispersed droplets, dispersed fibers, lamellar structures, and cocontinuous structures, as determined by rheological properties, interfacial tension between the components, blending conditions, and blend composition.[1-4] Of these morphologies, cocontinuous blends are of particular interest due to their unique ability to form continuous percolated networks of both blend components. Previous work has shown that cocontinuous blends can also be used to generate porous materials by solvent extraction or chemical etching of one of the phases, yielding a self-supporting scaffold of the remaining material.[4,12-15]

Cocontinuous morphologies are kinetically trapped, thermodynamically unstable structures that will coarsen during annealing. In order to reduce the characteristic size, prevent coarsening and coalescence, and improve interfacial adhesion in cocontinuous blends, the structures must be compatibilized.[12,13,19,34,35] Block copolymers are a common blend compatibilizer, and can be introduced to the blend either as pre-made block copolymers [7,35-37] or by forming block or graft copolymers during melt processing via interfacial coupling reactions between functional polymers.[38-42]

Molecular weight is also expected to play a significant role in morphology and stability. For non-compatibilized blends, interfacial tension is only weakly dependent on molecular weight.[52] For blends compatibilized by diblock copolymers, previous work has shown that interfacial tension goes through a minimum with diblock molecular weight.[35,36,53,54] A medium molecular weight diblock best balances the ability to localize at the interface with the improved compatibilizing effect of a longer, sufficiently entangled diblock.

For *in situ* formation of block copolymers via reactive blending, lower molecular weight polymers promote reaction due to a higher concentration of reactive end groups and an increased propensity for shorter chains to penetrate into the other polymer phase.[55,56] This is expected to increase graft density and reduce the phase size of dispersed domains.[57] However, reducing the molecular weight of the reactive component lowers the viscosity of the blend, and also results in fewer entanglements between graft copolymers and homopolymer.[58,59] This makes the actual effect on the morphology difficult to predict. The role of molecular weight on the morphology, stability, and interfacial tension of reactively compatibilized cocontinuous blends is still not fully understood.

The work shown here focused on the role of molecular weight on the ability to form and stabilize a cocontinuous structure during both reactive and nonreactive blending. The influence of molecular weight on blend interfacial tension and interfacial graft copolymer density was investigated, with the goal of minimizing domain sizes and resisting coarsening during annealing.

Blends were prepared using non-reactive low density polyethylene (LDPE), reactive maleic anhydride grafted polyethylene (PE-g-MA), and polyethylene oxide (PEO) to form LDPE/PEO and PE-g-MA/PEO blend systems with variable PEO molecular weight. Interfacial tension between the immiscible polymers was measured using the Palierne viscoelastic droplet model.[60-62] The interfacial tension results were verified qualitatively by a two-step blending process, which independently controlled the molecular weight of the interfacial grafted PEO and

the bulk phase PEO. The interfacial graft density for the reactive systems was estimated via X-ray photoelectron spectroscopy (XPS) of laminated PE-g-MA and PEO sheets. Blend stability was measured via coarsening studies, where domain size was measured as a function of annealing time using LSCM. The coarsening results were then explained based on the interfacial graft density results from XPS experiments.

2.2 Experimental Section

2.2.1 Materials

Two different polyethylene (PE) resins were used in the study: Low density polyethylene (LDPE) was provided by the Dow Chemical Company (LDPE 995l) and maleic anhydride grafted polyethylene (PE-g-MA) containing 1.6 wt% maleic anhydride by Chemtura (Polybond 3029). Polyethylene oxide (PEO) resins with number average molecular weights of approximately 40, 60, and 200 kg/mol (designated here as 40K, 60K, and 200K PEO, and supplied as Polyox N10, N80, and N3000, respectively), were provided by the Dow Chemical Company. Polyethylene oxide with 20 kg/mol number average molecular weight (designated 20K PEO) was purchased from Sigma Aldrich. Based on TGA measurements, all PEO contained 2 ± 0.5 wt% of fumed silica particles as a rheological modifier. A further discussion of the rheological effect of the fumed silica can be found in Appendix C. 2-Hydroxyethyl(methacrylate) (HEMA), azobisisobutyronitrile (AIBN), and Rhodamine B for fluorescence were purchased from Aldrich and used as received.

Table 2.1 shows the relevant material properties for the pure polymer materials. Melting temperature, T_m, was measured by dynamic scanning calorimetry (DSC, TA Instruments Q1000). Molecular weight of the PE was measured by high temperature gel permeation chromatography (GPC, Agilent PL-GPC 220 High Temperature GPC/SEC System) at 155 °C using 1,2,4-trichlorobenzene as the eluent and compared to polystyrene standards. Molecular weight of the PEO materials was measured by room temperature GPC (Wyatt Instruments) using 0.1M sodium

sulfate in 1% acetic acid aqueous solution as the eluent. PEO number average (M_n) and weight average (M_w) molecular weight were measured directly by light scattering (Wyatt HELEOS II) and refractive index (Wyatt Optilab rEX) using a d*n*/d*c* value of 0.1350. Density values were provided by the material suppliers.

Table 2.1. Melting temperature, molecular weight, and density for PE and PEO materials.

	Material	T_m (°C)	M_n (kg/mol)	M_w (kg/mol)	ρ (g/cm^3) @ 23 °C
PE	**LDPE**	105	12	59	0.92
	PE-g-MA	125	13	79	0.96
PEO	**20K PEO**	63	18	18	1.2
	40K PEO	65	37	80.	1.2
	60K PEO	65	59	120	1.2
	200K PEO	65	220	390	1.2

2.2.2 Rheology

Viscoelastic properties of the blend components were measured with an ARES rotational rheometer (TA Instruments) using 25 mm parallel plate geometry, except in the case of 20K PEO, where 50 mm parallel plates were used. Dynamic strain sweep tests at an oscillatory frequency of 1 rad/s were conducted on all materials to determine the critical strain, roughly 20% for each sample. Subsequent frequency sweep measurements were performed at strains below the critical strain to measure linear viscoelastic properties of the components and blends. Pure materials and blends were measured at 150 °C over a frequency range from 100 – 0.01 rad/s. In order to measure rheological properties of the pure materials at higher frequencies, measurements were repeated at temperatures just above T_m of the materials and plotted on a 150 °C master plot using time-temperature superposition. However, this was not done for the blends due to difference in shift factors between the blend components.

Complex viscosity profiles of the polymer materials were fit with the Cross model, given by:

$$\frac{\eta - \eta_\infty}{\eta_o - \eta_\infty} = \frac{1}{1 + (K\dot{\gamma})^n} \tag{2.1}$$

where η is the shear-rate dependent viscosity, η_o is the zero-shear viscosity, η_∞ is the infinite shear viscosity (assumed to be zero in all samples), K is the time constant of shear thinning, and n is the power law exponent. The Cox-Merz relation, which equates the oscillatory frequency dependent complex viscosity to the shear rate dependent viscosity for $\omega = \dot{\gamma}$, was assumed to apply for all materials.[63] Complex viscosity and Cross model fits are shown in Figure 2.1 for pure materials at 150 °C. Viscosity was reported to at least a shear rate of 400 s^{-1}, which was the approximate shear rate of blending used in this study.[64] Cross model parameters are shown in Table 2.2. A discussion on the relationship between PEO molecular weight and the rheological response can be found in Appendix C.

Table 2.2. Cross model parameters for PE and PEO pure materials. Measurements were conducted at 150 °C, the processing temperature for PE/PEO blends.

	Material	η_o (Pa s)	n	K (s)
PE	**LDPE**	2.15 x 10^4	0.419	3.48
	PE-g-MA	7.72 x 10^4	0.360	7.53
PEO	**20K PEO**	5.44	1.0	3760
	40K PEO	7.93 x 10^3	0.474	1.06
	60K PEO	2.70 x 10^4	0.431	1.44
	200K PEO	3.87 x 10^4	0.318	0.573

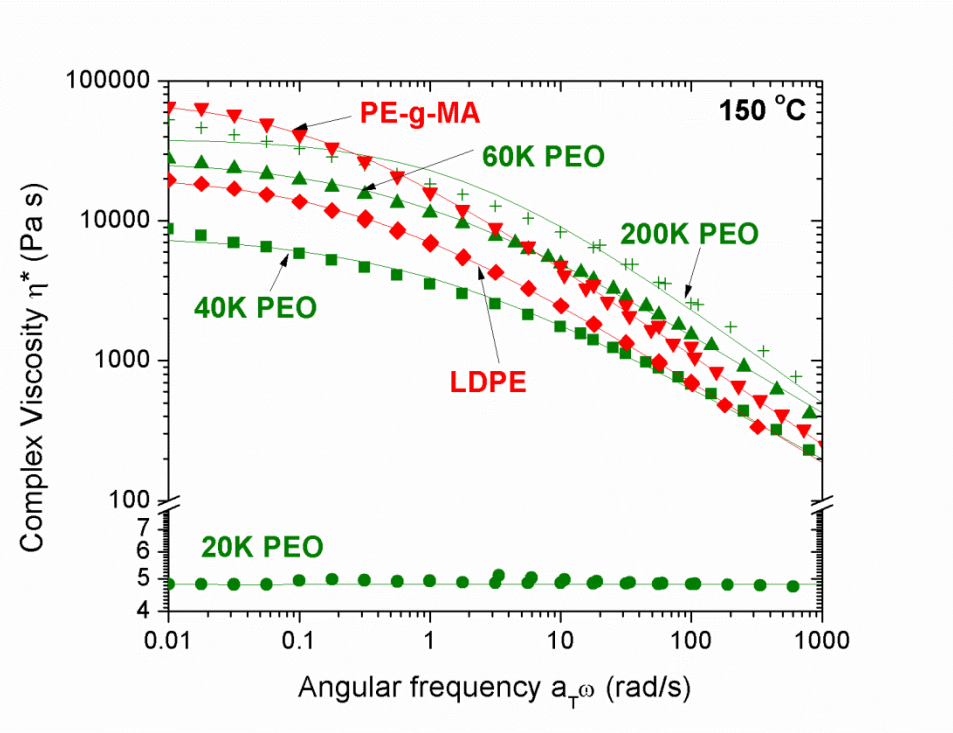

Figure 2.1. Complex viscosity versus frequency at 150 °C of PE and PEO materials. Viscosity at frequency >100 rad/s were collected by time-temperature superposition of data collected just above T_m of each material. The lines represent the Cross model fits, as described in Eq. 2.1.

2.2.3 Blend Preparation

Blends were prepared using a recirculating, batch microcompounder (DACA Instruments)[64] with a volume of 5 cm^3. All blends were prepared at 150 °C. Materials were loaded into the mixer and blended under nitrogen purge at 200 RPM for 6 minutes, at which point the recirculation channel was closed and the die opened to extrude the blended material. The extruded product was quenched in liquid nitrogen to freeze the morphology. Blends were made at compositions from 90/10 vol% PE/PEO to 10/90 vol% PE/PEO. However, this chapter will be limited to only those blends at the center of the ranges of cocontinuity, determined experimentally. Results and discussion on the cocontinuity ranges can be found in Chapter 4.

Additional reactively compatibilized blends were prepared in a "two-step" method, in order to independently tune the interfacially grafted and bulk PEO polymers. For the first step,

reactive PE-g-MA and PEO were blended with a composition of 20/80 wt% PE-g-MA/PEO in a 40 cm^3 batch microcompounder (Thermo-Haake Rheomix 600). A different molecular weight PEO was used for each first-step blend. These were blended at 150 °C for 6 minutes using a mixing speed of 200 RPM. After mixing, the material was removed from the mixing chamber and quenched in liquid nitrogen. The blends from this first mixing step formed PE-g-MA droplets, with grafted PEO chains of various molecular weight on the outside of the droplets.

For the second step, the blends from step one were washed in water to dissolve the PEO matrix. Each solution was vacuum filtered through a 220 nm filter to capture the PE-g-MA particles with grafted PEO on the outside of them. These particles were rinsed 4 times with distilled water to remove any free PEO. These rinsed PE-g-MA particles were then used as the feedstock for a second blending step. Each batch of surface-grafted PE-g-MA particles was blended with 40K PEO at 45/55 volume % PE-g-MA/PEO in the DACA microcompounder at 150 °C, 200 RPM, and 6 minutes. This resulted in blends that had the same bulk phase properties (since PE-g-MA and 40K PEO formed the bulk material in all cases), but the molecular weight of the interfacially grafted PEO differed according to the PEO used in the first mixing step.

2.2.4 Morphological Analysis

Morphology was investigated by imaging of two dimensional cross-sections via scanning electron microscopy (SEM, JEOL 6500), and in three-dimensional reconstructions via laser scanning confocal microscopy (LSCM, Olympus Fluo View 1000). For SEM imaging, smooth surfaces of the samples were prepared by cryo-microtome (Reichert UltraCut S Ultramicrotome) at -140 °C using a glass knife. Phase contrast of these surfaces was achieved by extracting PEO in a water bath overnight, leaving behind the PE matrix. These samples were sputter coated with 50 Å of platinum and imaged at an accelerating voltage of 5 kV and a working distance of 10 mm.

In order to create three-dimensional images of cocontinuous blends via LSCM, the

prepared samples needed to be optically transparent to allow the laser to penetrate the sample to a sufficient depth. Additionally, phase contrast must be generated by a difference in fluorescence between the phases.[12,13,65,66] To meet these imaging requirements, PEO was extracted from the blends. The resulting pores were filled with hydroxyethyl(methacrylate) (HEMA) with 0.01 wt% rhodamine B fluorescent dye. The samples were then heated at 80 °C for 10 minutes to polymerize the HEMA in the pores. The LSCM imaging technique and numerical analysis of 3D images to measure characteristic feature size of the cocontinuous blends followed the procedure described previously in work by Trifkovic *et al*,[13] and will be discussed in Chapter 3. Image analysis techniques used here are also described and compared in greater detail in Appendix B.

2.2.5 Interfacial Tension Analysis

Interfacial tension, Γ, and interfacial shear modulus, β_s^*, of each of the blends was estimated using the Palierne viscoelastic droplet model, which predicts the complex modulus of a droplet blend based on contributions from the viscoelastic properties of each blend component and a viscoelastic interface between them.[60,62] The model used for this study is described extensively in previous work by Jacobs *et al.*[62]

Blends of each PE/PEO system were prepared at 90/10 vol% PE/PEO. The droplet size of the dispersed PEO was measured via SEM. Cross sectional surfaces and images were prepared following the methods described above. The droplet size distribution of the blends was measured by tracing around the edge of the droplets using ImageJ software to improve contrast, and then running the images through an edge detection routine in MATLAB [67,68] to determine to size of each particle. This image analysis technique is described in Appendix B.

Using droplet histograms and rheological data for the blends and pure components, the Palierne viscoelastic droplet model was fit to G^* for each blend, using Γ and β_s^* as fitting parameters. For blends containing LDPE and PEO, $\beta_s^* = 0$, since there was no compatibilizer at

the interface. This simplification has been shown to be valid in previous studies.[69-72] For blends of PE-g-MA, a non-zero β_s^* was needed to accurately predict the viscoelastic behavior of the blends.[62] The model includes another parameter, β_d^*, the interfacial dilatation modulus, which describes changes in interfacial energy due to compression or expansion of the interface. For all studied blends, the interface was assumed to be purely elastic and β_d^* was zero. Rheological data, droplet size histograms of the PE/PEO droplet blends, and a more exhaustive description of the Palierne model used to calculate the interfacial tension can be found in Appendix A.

2.2.6 Reaction Graft Density Analysis

In order to compare reaction rates between PE-g-MA and PEO of varying molecular weight, sheets of PE-g-MA and PEO were prepared separately in a compression press at 150 °C for 10 minutes with an applied force of 9000 N, and were cooled in a separate water quenched compression press. These sheets were then laminated together by placing PE-g-MA samples on top of the PEO in the compression press and then annealing at 150 °C for 1 to 90 minutes. No pressure was applied, and a shim was used to ensure that there was no flow or compression of the materials during the lamination.

Laminated samples were placed into distilled water and stirred at room temperature for at least 4 hours. This was repeated 6 times with fresh water to ensure complete removal of all ungrafted PEO. Additionally, the 4th water bath was performed at 80 °C in order to disrupt the PEO crystallinity and remove unreacted PEO that had formed crystallites with grafted PEO.

Graft density of PEO at the PE-g-MA surface was measured by X-ray photoelectron spectroscopy (XPS, Surface Science SSX-100), using monochromatic Al K_α X-rays with an accelerating voltage of 10 kV, a current of 20 mA, an X-ray beam spot size of 800 μm, and a 35° takeoff angle. Since the samples were non-conductive, charge neutralization was provided by a metal mesh covering the samples and a low-energy electron gun set at 5-10 eV, tuned such that

electron release energies did not change with exposure time. Survey scans from 0-1100 eV were conducted prior to analysis of the samples to check for surface contamination.

The analysis method used by Boucher *et al*,[73,74] shown in Eq. 2.2, was used for determining the graft density of PEO on the laminated and washed surfaces. The graft density, Σ, gives the number of PEO grafts per area. The method seeks to quantify the surface PEO by comparing *O/C*, the normalized oxygen content of the laminated sample, to O_∞ / C_∞, the normalized oxygen content of pure PEO.

$$\Sigma = -\frac{N_a \rho \lambda \sin\theta}{M_{n,PEO}} \ln\left[1 - \left(\frac{O/C}{O_\infty/C_\infty}\right)\right] \tag{2.2}$$

where N_a is Avogadro's number, ρ is the density of the adhered phase (PEO), λ is the O1s electron inelastic mean free path of 16.9 Å,[75] θ is the electron take-off angle as determined by the instrument (35°), and $M_{n,PEO}$ is the number average PEO molecular weight. The O1s electron mean free path was used for λ in the analysis because the method is ultimately a comparison of normalized oxygen content. O and C are, respectively, the intensities for the O1s and C1s peaks in the laminated sample. O_∞ and C_∞ are the O1s and C1s peak intensities for pure PEO.

This analysis needed to be modified before use since PE-g-MA contained oxygen from the maleic anhydride. Directly measuring the intensity of the O1s peak would overestimate the amount of grafted PEO. For PE-g-MA/PEO laminated samples, the C1s peak could be resolved into two separate peaks: one peak representing C-C bonds at 284.6 eV, and another representing C-O bonds at 286.2 eV. High resolution C1s scans of the pure PEO showed that it only contributed to the C-O peak intensity, with negligible contribution to the C-C peak intensity. LDPE and PE-g-MA contributed only to the C-C peak intensity of the C1s peak, and did not contribute to the C-O peak intensity. Therefore, the C-O intensity was proportional to the contribution of PEO to the O1s peak intensity. Substituting the C-O intensity for *O* in Eq. 2.2 and

then recognizing that $(C-O)_\infty / C_\infty = 1$ results in:

$$\Sigma = -\frac{N_a \rho \lambda \sin\theta}{M_{n,PEO}} \ln\left[1 - \left(\frac{I_{C-O}}{I_{C-O} + I_{C-C}}\right)\right] \tag{2.3}$$

where $I_{C\text{-}O}$ is the intensity of the C-O peak at 286.2 eV and $I_{C\text{-}C}$ is the intensity of the C-C peak at 284.6 eV. Using this analysis method also resulted in the need to only perform the analysis from a single high-resolution scan of the C1s peak over a binding energy range from 266 to 286 eV. This range was selected to account for a shift in binding energy caused by the electron gun used for charge neutralization. The shifted C1s peak was fit with two Gaussian curves to represent C-C and C-O carbons, and the measured intensities were used to calculate PEO graft density by Eq. 2.3. Representative high resolution C1s scans for the pure materials and laminated samples can be found in Appendix D.

2.2.7 Coarsening

In order to study morphological stability of the PE/PEO blends, small pieces of extrudate were placed in a steel mold between two sheets of fluoropolymer-coated fabric (Premium 6 Mil, American Durafilm). These were held between heated plates of a compression press (Carver, Inc., Wabash, Indiana). All coarsening studies were performed at 150 °C with no applied pressure. After the desired coarsening time (between 1 and 30 minutes), the samples were quickly removed and cooled in a separate water-chilled compression press with no applied pressure. Blends used in the coarsening studies were selected from near the center of the range of cocontinuity. The cocontinuity results for these blends are reported in Chapter 4.

2.3 Results and Discussion

2.3.1 Interfacial Tension

PEO droplet size, interfacial tension Γ, and interfacial shear modulus β_s^* for 90/10 wt% PE/PEO blends are shown in Figure 2.2. The droplet size of the uncompatibilized blends showed

a strong dependence on viscosity ratio. Previous studies have shown that the droplet size of polymer blends decreases as the viscosity ratio $\eta_{matrix}/\ \eta_{droplet}$ (η_{PE}/η_{PEO} for this specific case) approaches a value of 6.5.[76,77] Blends composed of LDPE/40K PEO and LDPE/60K PEO, which had viscosity ratios approaching 6.5, showed a minimum droplet size, which is consistent with these studies. Droplets with a low viscosity such as those in LDPE/20K PEO were more prone to coalescence, and therefore resulted in larger droplets. Droplets with a high viscosity like those in LDPE/200K PEO resisted breakup into smaller features since the lower viscosity matrix was unable to effectively transfer stress to the dispersed phase,[77] again resulting in larger droplets.

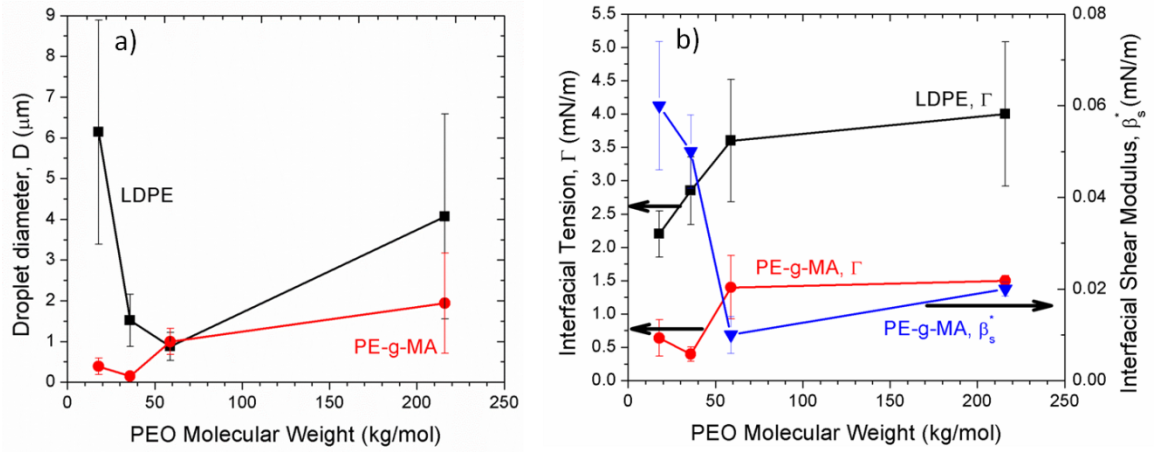

Figure 2.2. a) Droplet diameter for 90/10 wt% PE/PEO droplet blends. Points give the volume average droplet diameter, error bars give the standard deviation of the size distribution. b) Interfacial tension Γ and interfacial shear modulus β_s^* for 90/10 wt% droplet blends.

The interfacial tension between non-functional LDPE and PEO slightly increases with the molecular weight of the PEO. This is consistent with the study by Anastasiadis *et al*,[52] in which the interfacial tension in blends of PS and PMMA was measured as a function of PS molecular weight. While interfacial tension increased with increasing PS molecular weight, the effect was weaker than the dependence on PEO molecular weight observed here. Blends from LDPE and PEO all had an interfacial shear modulus β_s^* of zero, due to the absence of any interfacially localized materials.

Reactive PE-g-MA/PEO blends showed much smaller droplets, with a local minimum in droplet size and interfacial tension for 40K PEO. Droplet size and interfacial tension were well correlated for PE-g-MA containing blends. All PE-g-MA/PEO blends also showed a non-zero interfacial shear modulus β_s^*, which is indicative of the presence of an additional, interfacially localized material that bridges the interface and provides it with elastic stability. This suggests that PE-g-PEO graft copolymers were formed at the interface and are entangled with the PE-g-MA and PEO phases.[13]

Of particular interest is PE-g-MA/20K PEO, which shows a dramatically smaller droplet size compared to uncompatibilized LDPE/20K PEO blends. The presence of interfacial graft copolymers in the PE-g-MA/20K PEO blend resulted in a reduced interfacial tension and the highest interfacial shear modulus β_s^* measured here. The high value for β_s^* suggests the presence of a high density of interfacially localized graft copolymers which sterically hindered droplet coalescence.

Droplet blends of PE-g-MA/20K PEO and PE-g-MA/40K PEO showed similar Γ, β_s^*, and droplet sizes, suggesting that the extent of reactive compatibilization was similar between the two samples. Higher Γ and lower β_s^* for blends from PE-g-MA/60K PEO and PE-g-MA/200K PEO suggest a lesser extent of reactive compatibilization in these higher molecular weight systems. This argument will be revisited in the discussion of the graft density results by XPS, reported below in Section 2.3.4.

2.3.2 Initial Blend Characteristic Size

Blends from the center of the ranges of cocontinuity, determined from cocontinuity results reported in Chapter 4, were selected to compare initial characteristic size and coarsening stability (shown later in Section 2.3.5) as a function of PEO molecular weight. SEM images of the blends are shown in Figure 2.3. The characteristic sizes of the blends prior to any annealing,

as measured by LSCM images, are shown graphically in Figure 2.4.

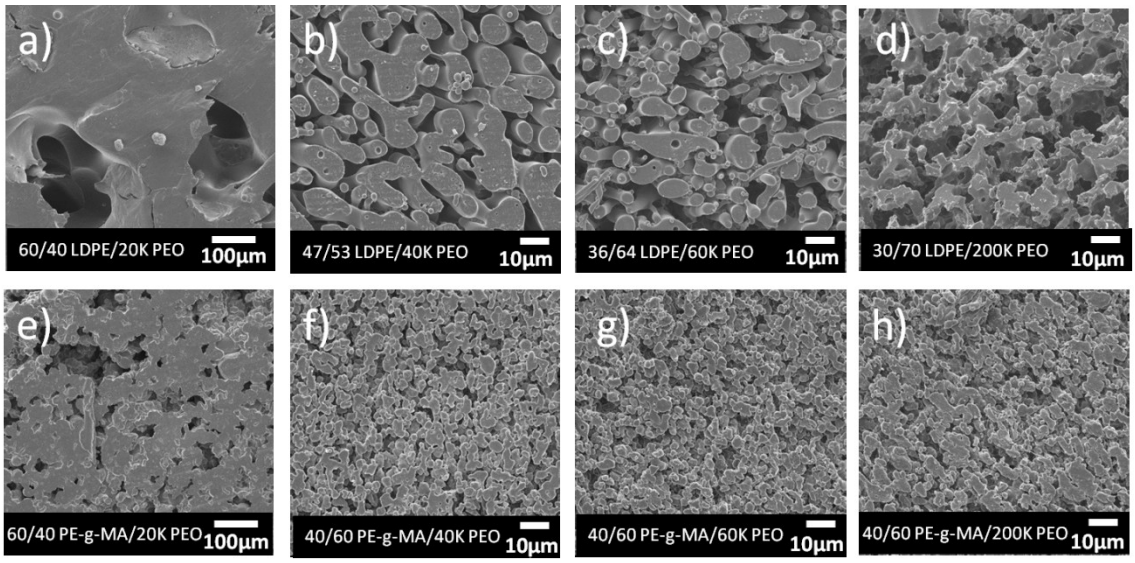

Figure 2.3. SEM images for PE/PEO blends. a) – d) LDPE/PEO blends. e) – h) PE-g-MA/PEO blends. All compositions listed represent volume fractions of the components.

For blends of LDPE/PEO with 40K, 60K, and 200K PEO materials, the characteristic size was on the order of 5 µm. In the case of LDPE/20K PEO blends, the low viscosity of 20K PEO did little to inhibit coarsening and coalescence, resulting in very large features with a characteristic size of 31 µm. LDPE/20K PEO cocontinuous blends also showed an irregular and poorly-mixed morphology in the cocontinuous region. These trends are largely consistent with the droplet sizes measured from 90/10 wt% LDPE/PEO blends. The exception is LDPE/200K, where the cocontinuous blend showed smaller features than those reported in the droplet blends. Increased viscosity is expected to resist breakup into smaller droplets, resulting in large droplet sizes. However, high viscosity also stabilizes the elongated and irregular features typical of cocontinuity by increasing the resistance to coarsening flows, which would result in smaller features. Unfortunately, while the literature has proposed models for feature size in droplet blends,[76,77] no such models exist at this time for predicting characteristic size of cocontinuous blends.

Characteristic size of the compatibilized cocontinuous blends was uniformly lower than

the non-compatibilized blends due to reduced interfacial tension. For the cocontinuous PE-g-MA/20K PEO blend, characteristic size was 12 μm. For PE-g-MA/PEO with 40K, 60K, and 200K PEO, the characteristic size was on the order of 2 μm.

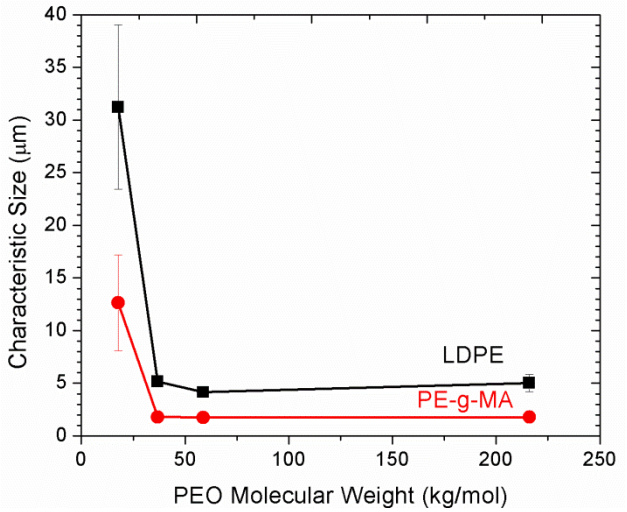

Figure 2.4. Characteristic phase size, as measured by LSCM images, of blended polymers as a function of PEO number average molecular weight. Size was analyzed for the blend compositions reported in Figure 2.3.

Of particular interest is the PE-g-MA/20K blend, where the feature size in the droplet blend was very small compared to the cocontinuous characteristic size. In the droplet blends, steric hindrance to droplet coalescence prevented the formation of large features. However, this effect is downplayed when features are already interconnected as they are in the cocontinuous blend. Since cocontinuous polymer blends are highly unstable structures, low viscosity provides little resistance to rapid coarsening into larger features.

This same line of reasoning can be applied to the PE-g-MA/PEO blends with 40K, 60K, and 200K PEO. Increasing the overall blend viscosity will promote the stability of elongated features and slow down the rate at which the morphology coarsens, producing smaller features.[19,34] However, this effect seems to be offset by an increase in interfacial tension for higher PEO molecular weight, resulting in similar characteristic sizes for these three blends.

2.3.3 Two-Step Blending

SEM images, interfacial tension, and characteristic size of the two-step blends prepared by the method described above are shown in Figure 2.5. The characteristic size as a function of the interfacial tension is also plotted in Figure 2.6. Interfacial tension was determined according to Figure 2.2b, based on the molecular weight of the interfacially localized PEO, as determined by the PEO used during the first step of mixing. For the second step of mixing in all cases, 40K PEO was blended with the PE-g-MA particles following extraction of the first PEO, in order to match bulk rheological properties of all blends. It should be noted that the characteristic size reported for these blends was determined by the perimeter per surface area as measured by 2D image analysis of SEM images. Error bars give the standard deviation of the characteristic size across four images. This image analysis technique is more fully described in Appendix B.

For each of the two-step blends studied, there is a positive correlation between the interfacial tension of the blends and the characteristic size, with decreasing characteristic size as interfacial tension decreases. This result is expected, as a reduction in interfacial tension will promote the generation of more interfacial area, due to the reduced energetic penalty. However, it should be noted that this method is not without potential issues – the possibility for reaction during the second step of mixing means that the true composition of the interfacial layer is not fully known, as new interface could be generated to react with the 40K PEO blended in the second step. Additionally, the bulk phase viscosity of these samples may not match if free PEO is not sufficiently rinsed from the surface of the precursor particles. However, assuming a reaction that proceeds to saturation (which the XPS results shown below in Figure 2.7 support), and assuming only small rheological changes from any free PEO left from the first step, the results here support the interfacial tension results. Furthermore, the method developed here represents a previously undocumented technique for preparing reactively compatibilized cocontinuous blends with independently tunable rheological and interfacial properties.

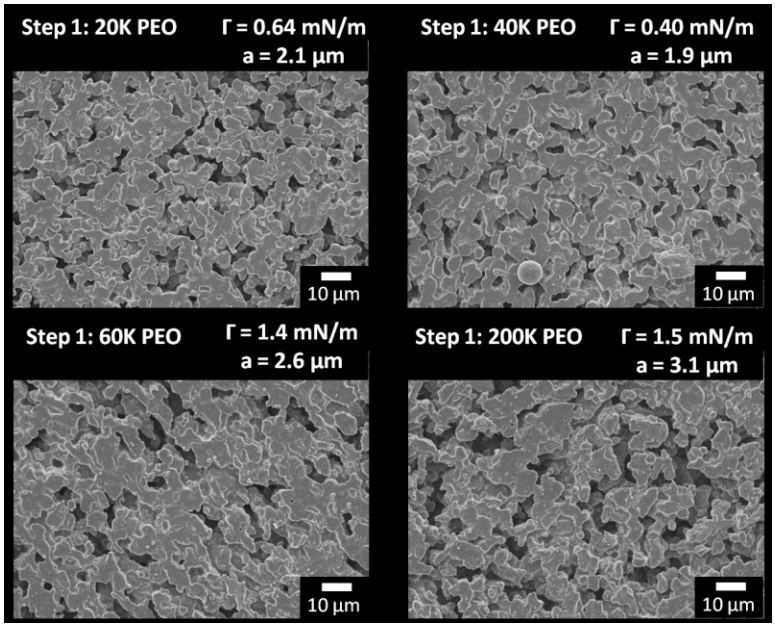

Figure 2.5. SEM micrographs of two-step blends with PE-g-MA and 40K PEO as the bulk materials, following bulk PEO extraction. The material labeled "Step 1" represents the molecular weight of the interfacially localized PEO, blended with the PE-g-MA and then extracted to pre-form the PE-g-PEO graft copolymers. For each image, Γ is the interfacial tension, and a is the characteristic pore size.

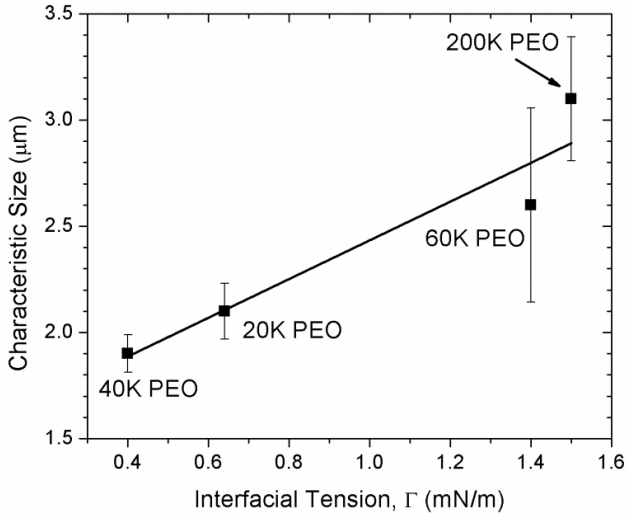

Figure 2.6. Characteristic pore size of cocontinuous blends from two-step blending using PE-g-MA and 40K PEO as the bulk materials. The labels show the molecular weight of the grafted PEO, as determined by the first step of mixing. The interfacial tension Γ is the value measured between PE-g-MA and the grafted PEO. The line is to guide the eye.

2.3.4 Graft Density

In order to further develop a better physical interpretation of the interfacial tension results of the PE-g-MA/PEO blends, the interfacial graft density of each of the blend systems was studied via XPS measurements of quiescently laminated bilayer samples. Figure 2.7 shows PEO graft density, calculated by Eq. 2.3, as a function of reaction time. Examples of the XPS data for which Eq. 2.3 was applied can be found in Appendix D. The reaction graft density increased rapidly within the first 10 minutes of reaction. After 10 minutes, the graft density remained constant, suggesting the surface rapidly reached saturation. These measurements were also conducted using non-functional LDPE. However, non-functional samples showed no adhesion after lamination, and a graft density of zero was measured in all cases.

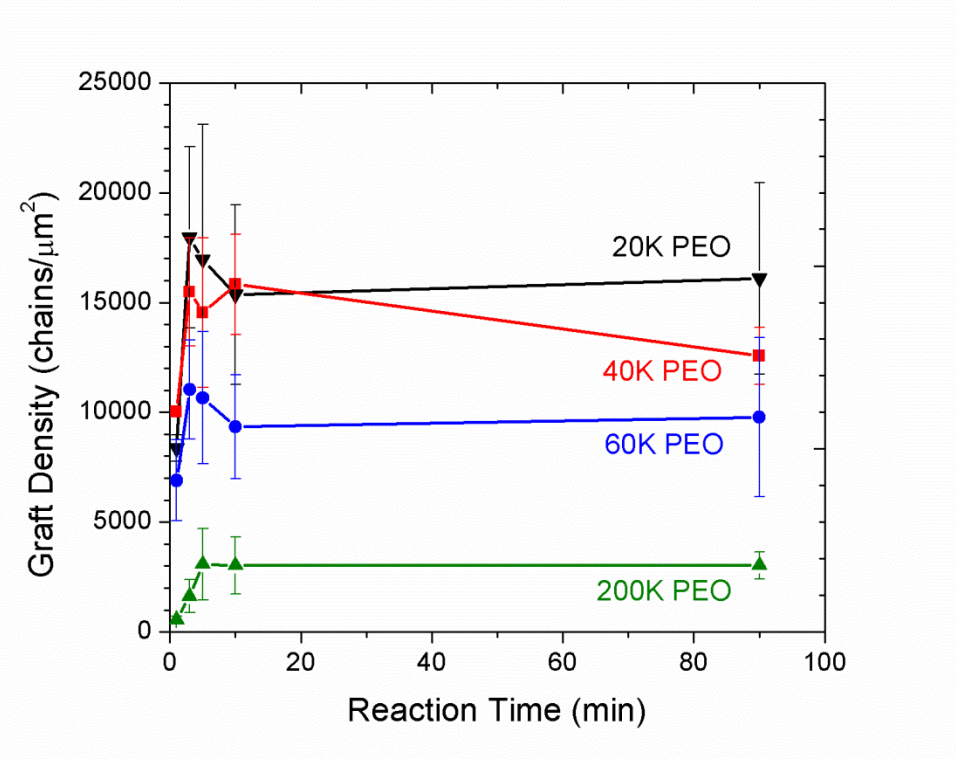

Figure 2.7. PEO graft density in bilayer lamination to PE-g-MA as a function of reaction time at 150 °C.

Figure 2.8 shows that the graft density of PEO to PE-g-MA after 90 minutes of annealing decreases with increasing PEO molecular weight. The reduction in graft density with increasing

molecular weight can be explained predominantly by a reduction in reactive hydroxyl end groups as molecular weight increases. A reduction in chain mobility and an increase in steric hindrance as molecular weight increases also contributed to the reduction in graft density.

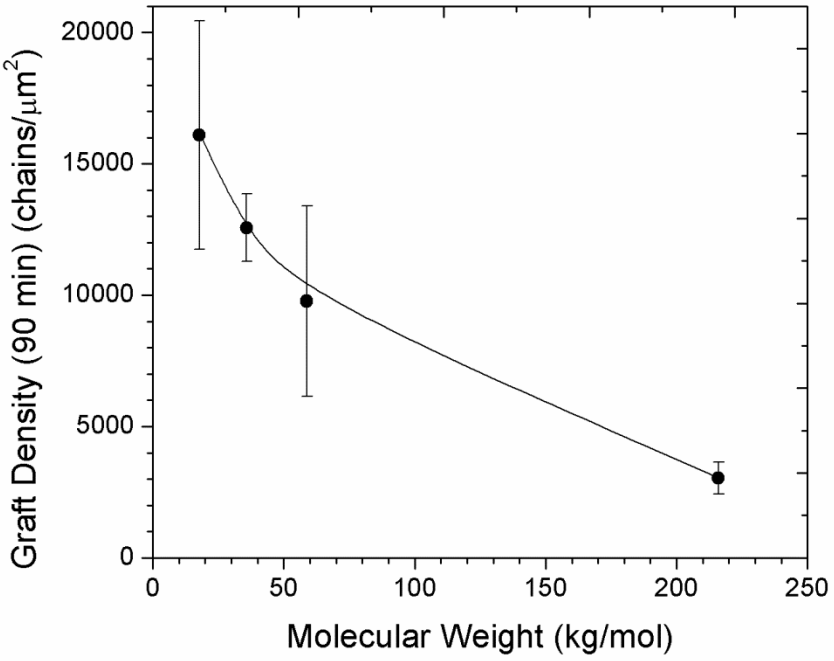

Figure 2.8. Graft density as a function of PEO number average molecular weight after annealing at 150°C for 90 minutes. The line is to guide the eye.

An alternative way to interpret the XPS results is to view them as fraction of the surface covered in PEO, calculated by normalizing the atomic fraction of oxygen in the laminated samples to the atomic fraction of oxygen in pure PEO. These results are shown in Figure 2.9. The fractional surface coverage approaches 60% as the molecular weight of the PEO increases, suggesting that this represents an upper limit to the possible PEO surface coverage. At this upper limit, a higher density of PEO grafts could not be achieved due to steric restrictions. The 60K and 200K PEO samples appear to be very near to this maximum surface coverage, and 40K PEO is approaching this limit with 50% coverage. The 20K PEO, however, shows a lower

normalized oxygen content at 32%, suggesting that it has reacted with all readily available maleic anhydride groups at the PE-g-MA surface.

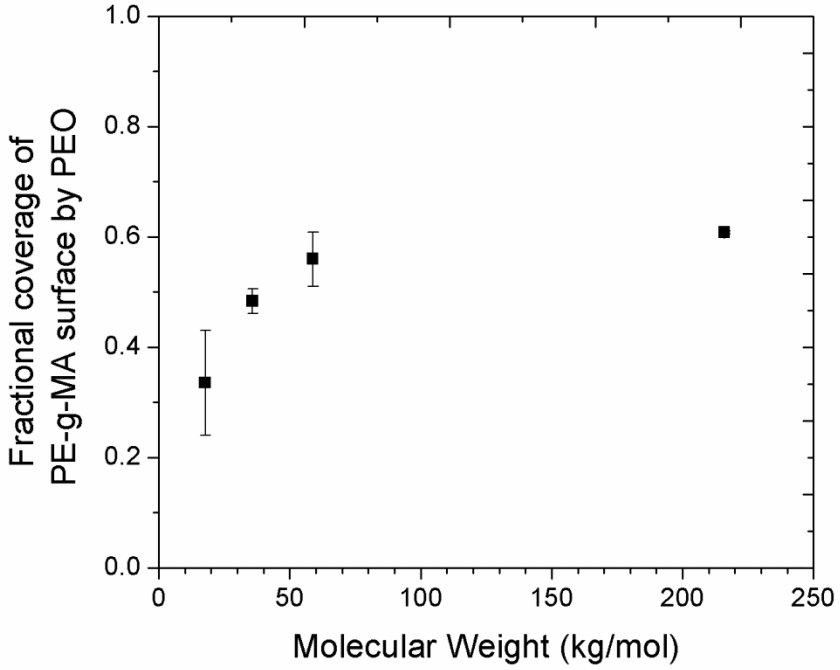

Figure 2.9. Fractional surface coverage by PEO as a function of PEO molecular weight in quiescent annealing at 150 °C for 90 minutes. The fractional coverage was calculated as atomic fraction of oxygen in the sample normalized by the atomic fraction of oxygen in pure PEO.

In light of the XPS results shown in Figure 2.7 through Figure 2.9, the interfacial tension results of PE-g-MA and PEO blends shown in Figure 2.2 can be interpreted in terms of graft density and oxygen content. First, this analysis assumes that the PE-g-PEO graft density in the droplet blends used to measure interfacial tension is equivalent to the time-independent graft density observed after lamination times greater than 10 minutes. Graft density is maximized when PE-g-MA is blended with 20K and 40K PEO. However, in the case of 20K PEO, the oxygen fraction is lower and the total surface coverage of the PE-g-PEO is less than that from 40K PEO, resulting in an unsaturated interface. This, when compared to the PE-g-MA/40K PEO blend, results in a slightly higher interfacial tension.

The blends containing 60K and 200K PEO, while having oxygen content equivalent to that of 40K PEO samples, showed an increased interfacial tension due to a lower graft density, meaning fewer copolymers bridge the interface and compatibilize the two immiscible phases. Lower graft density also resulted in a reduction in the interfacial shear modulus β_s^* as compared to the blends with lower molecular weight PEO. Elastic shear modulus of a bulk polymer phase is dependent on entanglement density.[78] Likewise, interfacial shear modulus should also be dependent on the density of chemical links across the interface. This is also comparable to the mechanism of polymer-polymer adhesion, in which the fracture energy of an interface depends on the graft density of the copolymers across that interface, but not the molecular weight of the copolymers.[79,80] These expectations based on shear modulus and adhesion are consistent with the present results.

2.3.5 Coarsening

Coarsening experiments were performed on blends selected near the center of the range of cocontinuity for each material system. The precise compositions used for coarsening experiments are the same as those reported in Figure 2.3. The characteristic size, measured via LSCM, as a function of quiescent annealing time at 150 °C is shown in Figure 2.10. Initial characteristic size was measured of the extruded sample with no annealing.

In the case of LDPE/PEO blends, shown in Figure 2.10a, higher molecular weight slowed the coarsening rate the most, though all blends showed no plateau after 30 minutes. LDPE/20K PEO blends coarsened very quickly, such that the features after 30 minutes of coarsening were too large to be analyzed by LSCM. Increasing PEO molecular weight increases zero shear viscosity and, more weakly, interfacial tension. The increased viscosity provided additional resistance to coarsening.

The LDPE/PEO coarsening studies showed more rapid coarsening during the first few minutes of annealing followed by a slight slowing of the rate of coarsening after about 10

minutes. The faster coarsening rate at the beginning is expected to be partially due to coalescence of dispersed droplets into the cocontinuous matrix and a "smoothing" of the interface as residual stress and shear alignment from extrusion are relieved. This occurs simultaneously with coarsening of the cocontinuous matrix. Once the coarsening rate slows, the blend is only undergoing self-similar coarsening. This is consistent with coarsening results observed in previous studies.[81-83]

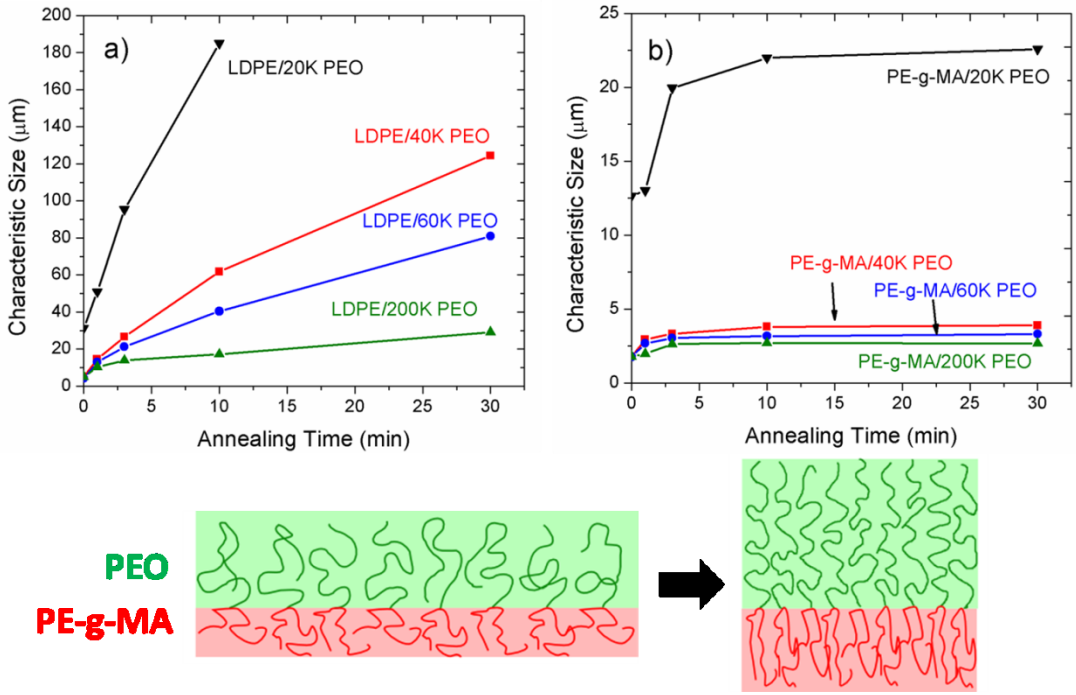

Figure 2.10. Characteristic phase size of blended polymers as a function of annealing time, as measured by LSCM imaging. a) Non-compatibilized LDPE/PEO blends. b) Reactively compatibilized PE-g-MA/PEO blends. The compositions of the blends tested here are reported in Figure 2.3. c) Schematic of the proposed mechanism for coarsening suppression observed in the reactively compatibilized blends. Interfacially localized graft copolymers are compressed as the interfacial area decreases, densifying the copolymer brush at the interface and preventing further loss of interface.

For reactively compatibilized cocontinuous PE-g-MA/PEO blends, shown in Figure 2.10b, the blends will coarsen for the first 10 minutes of annealing, after which the coarsening behavior is arrested and the characteristic size is constant with time. This is consistent with observations from previous studies.[13,35] The higher molecular weight PEO suppressed coarsening

the most, resulting in the smallest steady state characteristic size.

For interpreting the rate of coarsening, Previous work has shown that the coarsening rate of cocontinuous blends can be related to rate of breakup of elongated domains, and is proportional to the following relation.[19,81,84-86]

$$\left.\frac{da}{dt}\right|_{t=0} \propto \frac{\Gamma}{\eta_{blend}} \tag{2.4}$$

where a is the characteristic fiber radius (given as the initial characteristic size from when the coarsening rate was measured), Γ is interfacial tension, and η_{blend} is the effective zero shear blend viscosity, given by the volume fraction weighted log average viscosity of the blend components.[27]

$$\log \eta_{blend} = \sum_i \phi_i \log \eta_i \tag{2.5}$$

where ϕ_i is the volume fraction of component i in the blend, and η_i is the zero shear viscosity of component i in the blend.

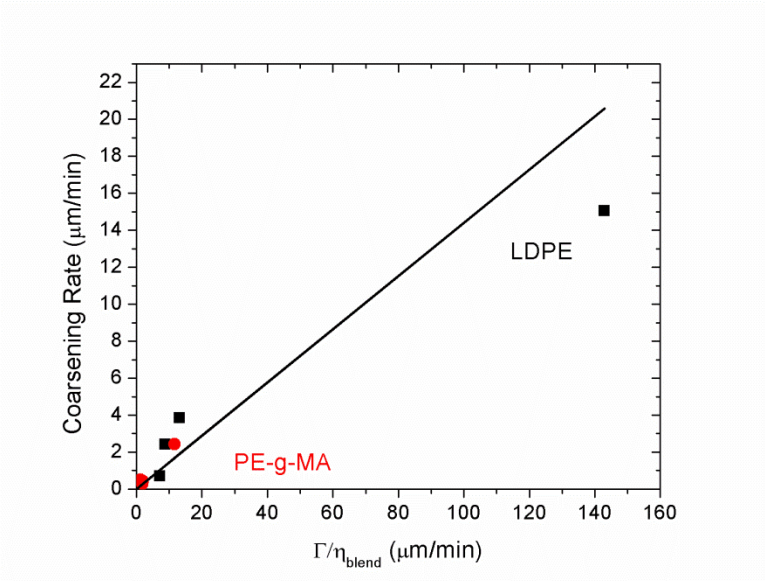

Figure 2.11. Coarsening rates of non-compatibilized LDPE/PEO (black squares) cocontinuous blends and compatibilized PE-g-MA/PEO (red circles) cocontinuous blends as a function of Γ/η_{blend}. The lines show a linear regression with a zero intercept, fit to both the reactive and non-reactive systems.

Some variations on this analysis also include Tomotika's function, Ω, which depends on the viscosity ratio of the dispersed phase to the continuous phase, η_{disp}/η_{cont}.[87] This approaches 1 when η_{disp}/η_{cont} is zero and approaches 0 when η_{disp}/η_{cont} is infinite. However, the work by Tomotika describes the breakup of a fiber in an infinite matrix, with only one phase subject to breakup. The cocontinuous blends examined here had no distinguishable dispersed phase, as each phase served the role of coarsening fiber and matrix. Since Ω could not be estimated without error, it was assumed to be constant.

The coarsening rate for LDPE/PEO blend systems was measured across all data points from 0 – 30 minutes. The initial coarsening rate for PE-g-MA/PEO blend systems were measured over 0-3 minutes of coarsening. The PE-g-MA/PEO blend sizes after 3 minutes of coarsening were not used for determining the coarsening rate due to the complete suppression of coarsening exhibited by all the studied reactive blends. These coarsening rates were plotted against Γ/η_{blend} in Figure 2.11. The linear fit for both material system shows that coarsening rate is roughly proportional to Γ/η_{blend} and independent of the presence of graft copolymers for early coarsening of compatibilized blends, suggesting that a simple reduction of interfacial tension is the main cause of the slowing of coarsening during the early coarsening times. However, this simple interpretation does not explain the tendency for these blends to cease coarsening after 3 minutes. The intercepts for the linear fit was fixed at zero, since zero interfacial tension or infinite viscosity would completely stop coarsening. A comparison to literature results for coarsening rates is reserved for Chapter 5.

In order to interpret the final size of the blends in which coarsening was arrested, two mechanisms were compared. By one mechanism, the copolymers at the interface exist as random coils, and coarsening will cease once these random coils are sufficiently constrained. At this point, interfacial pressure due to the entropic drive to restore the copolymers to a random coil reaches equilibrium with the coarsening rate driven by interfacial tension. The other mechanism

is that coarsening will cease when the macroscopic interfacial tension is effectively zero. This would occur when the copolymers at the interface form a dense monolayer with a graft density equal to that of lamellar diblock copolymers. A schematic of the copolymer brush at the interface during coarsening suppression is found in Figure 2.10c.

Table 2.3. Graft density of reactively compatibilized samples before and after coarsening of cocontinuous blends, assuming that the blending graft density equals the 90 minute lamination graft density from Figure 2.8. PE-g-MA density was assumed to be equivalent to PEO graft density. R_g for PE-g-MA was calculated to be 5.3 nm.

	20K PEO	**40K PEO**	**60K PEO**	**200K PEO**
M_n (PEO, kg/mol)	18	37	59	220
R_g (PEO, nm)	4.9	7.1	9.0	17
Σ_i, grafts/μm^2 (PEO, before coarsening)	1.6×10^4	1.3×10^4	9.8×10^3	3.0×10^3
Σ_f, grafts/ μm^2 (PEO, 30 min. coarsening)	2.9×10^4	2.7×10^4	1.8×10^4	4.6×10^3
grafts/πR_g^2 (PEO, before coarsening)	1.2	2.0	2.5	2.8
grafts/πR_g^2 (PEO, 30 min. coarsening)	2.2	4.3	4.6	4.2
grafts/πR_g^2 (PE-g-MA, before coarsening)	1.4	1.1	0.86	0.27
grafts/πR_g^2 (PE-g-MA, 30 min. coarsening)	2.5	2.4	1.6	0.40

Table 2.3 and Figure 2.12 show the interfacial graft density prior to coarsening and after 30 minutes of coarsening, in terms of chains per interfacial area, and chains per the area πR_g^2 of PE and PE-g-MA, the area occupied by the chain assuming a random coil conformation, where the radius of gyration R_g was defined by:[78]

$$R_g^2 = \frac{Nb^2}{6} \tag{2.6}$$

where N was the number average repeat units per PEO chain (based on M_n), and b was the statistical segment length, defined as 6.0 Å per PEO repeat unit and 5.9 Å per PE repeat unit.[78] The number of grafted chains occupying the area πR_g^2 of the relevant PEO or PE-g-MA gives a qualitative description of the graft density at the interface compared to cross sectional area that

the polymer chain would occupy as a random coil in the bulk phase. For these calculations, the graft density at the interface of the cocontinuous blends was assumed to be equal to the graft density after 90 minutes of lamination, as reported in Figure 2.8. Furthermore, the total number of graft copolymers present at the interface of the blend was assumed not to change with annealing time.

In the current study and for 40K, 60K, and 200K blends, this occurred at a surface density of 4 - 5 PEO chains per πR_g^2. In all these cases, the PEO radius of gyration was larger than that of PE-g-MA, so PEO would be expected to suppress coarsening first due to it forming the more saturated interface. At 4 - 5 PEO chains per πR_g^2, the chains are slightly elongated and compressed at the interface compared to the random walk configuration.

For the PE-g-MA/20K PEO blend, the final coarsened graft density was calculated as 2.2 grafts per πR_g^2. This result can be explained by the fact that the surface prior to coarsening was not completely saturated with PEO, as was demonstrated in by the XPS fractional surface coverage results in Figure 2.9. XPS results showed only 32% surface coverage for 20K PEO, compared to 60% for higher molecular weight PEO, which was attributed to saturation of the available maleic anhydride groups on the PE-g-MA.

Given that the initial surface of the 20K PEO blend was not PEO saturated, one would expect that the cessation of coarsening would coincide instead with densification of the PE-g-MA brush on the other side of the interface. Assuming the same graft density for PE-g-MA as was measured for 20K PEO, the initial normalized PE-g-MA graft density on 20K PEO was 1.4 grafts/ πR_g^2, and the coarsened graft density was 2.5 grafts/ πR_g^2. Furthermore, when decreasing molecular weight from 40K to 20K PEO, the final graft density of the PE-g-MA appears to approach a plateau at about 2.5 PE grafts/ πR_g^2. While this is still less than the previously measured 4 – 5 PEO grafts/ πR_g^2, this may reflect differences in PE-g-MA polymer architecture. Equating PEO and PE-g-MA graft density may not be appropriate for the multifunctional PE-g-

MA, which can react with PEO at several points along the backbone of a single molecule. Secondly, PE-g-MA is graft functional and not end functional like PEO, and this may influence the sterics of brush densification at the interface.

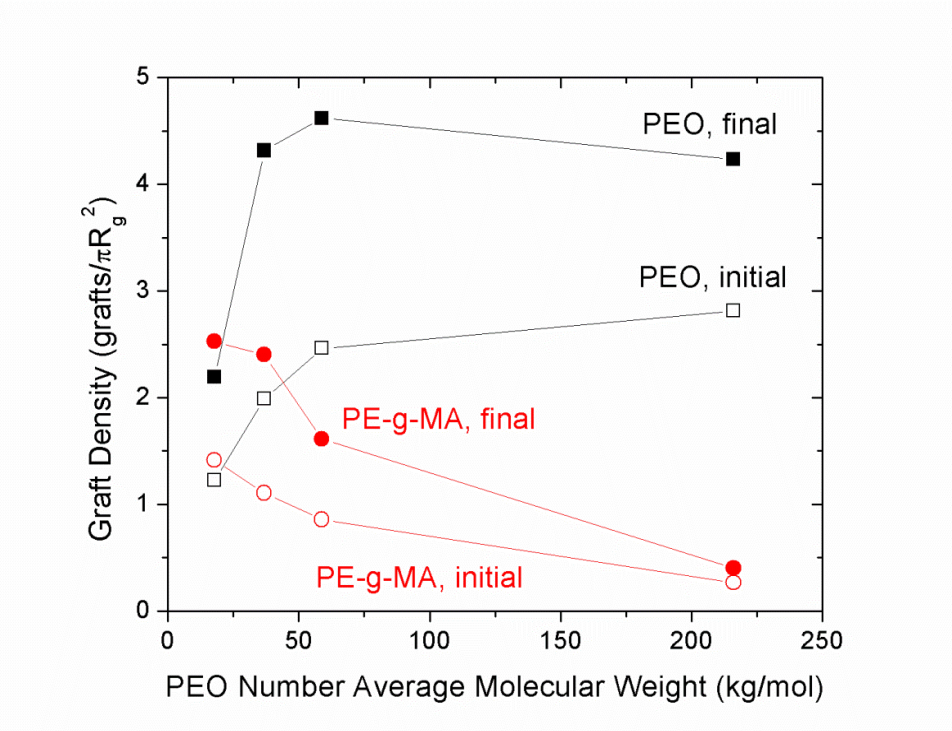

Figure 2.12. Graft density of PEO and PE-g-MA before and after coarsening. The graft density is normalized to πR_g^2, the area occupied by a random coil. The lines are to guide the eye.

For the other mechanism, where coarsening will be suppressed at a certain graft density relative to the maximum graft density of a lamellar diblock copolymer, first a maximum grafting density needs to be defined. Previous work has shown that this maximum graft density can be predicted by:

$$\Sigma_{max} = \frac{\Lambda/2}{M/\rho N_a} \tag{2.7}$$

where Λ is the lamellar spacing of the diblock copolymer, M is the molecular weight, ρ is the density, and N_a is Avogadro's number. Given that lamellar spacing Λ scales with $M_n^{2/3}$, then Σ_{max} is expected to scale with $M_n^{-1/3}$, whereas R_g^2 scaled linearly with M_n. As lamellar spacing Λ for

PE-PEO diblocks has not been previously measured, an estimated Σ_{max} of 0.25 grafts/nm^2 was used for the PE-g-MA/40K PEO system. The other systems were scaled appropriated based on Eq. 2.7. For the present arguments, an exact value of Σ_{max} was not as critical as the scaling of Σ_{max} with molecular weight.

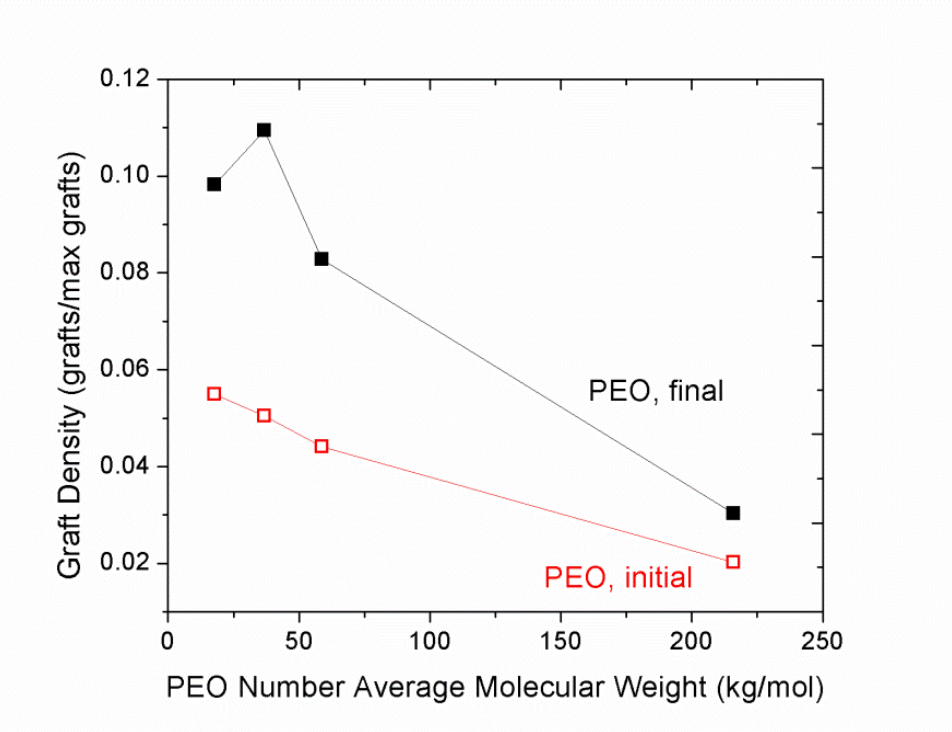

Figure 2.13. Graft density of PEO, normalized to the maximum graft density of a lamellar diblock copolymer, before and after coarsening. The lines are to guide the eye.

The results of the graft density normalized to Σ_{max} are shown in Figure 2.13. From these results, it is apparent that the scaling of final size of the coarsened compatibilized blends did not correlate with the maximum graft density as determined by a lamellar diblock copolymer, as the final normalized Σ/Σ_{max} shows a strong dependence on molecular weight, decreasing with increasing molecular weight. Therefore, it seems more likely that coarsening suppression occurs by the first proposed mechanism, where constraining an interfacial copolymer to an occupied area less than the area of its random coil creates an interfacial pressure that reaches equilibrium with the drive to compress the interfacial brush by interfacial tension. This would still have the

appearance of an effective zero interfacial tension for purposes of cocontinuous coarsening.

One caveat concerning a comparison of these potential mechanisms of coarsening suppression is that the graft density as a function of PEO molecular weight was measured on quiescently annealed samples rather than blends. However, flow is known to increase the rate of interfacial reactions, so the final graft density in the blends could be higher than those recorded here. However, this technique did have the advantage of avoiding the analytical difficulties of calculating graft density over a complex surface. Furthermore, these calculations were performed using the graft density after 90 minutes of annealing, at which point, the graft density had reached a plateau in all systems, suggesting that interfacial copolymer saturation is achieved quickly. Assuming that the graft density rapidly reaches a similar equilibrium in the blended system, the conclusions drawn from the prior analysis should still hold once corrected for the true graft density of the blended systems.

The graft density and suppression of coarsening results shown here were compared to existing results by Bell, *et al*,[35] for cocontinuous blends stabilized by premade diblock copolymers. The results are shown in Table 2.4. For these results, graft density was calculated based upon the total amount of copolymer added to the blend system. Generally, the graft density is much higher than the values observed in the present work. However, this is most likely a result of copolymers trapped in micelles away from the interface. This also explains why graft densities are observed in excess of the maximum graft density from a dense monolayer.

No immediately apparent trends emerge from this data due to the difficulty in interpreting the results in light of the micelle formation. However, the dilute cases, which contain 0.1 wt% of the added block copolymer, are the least likely to form extensive micelles. In each of these cases, coalescence suppression is observed at roughly 10 chains/ πR_g^2, which matches somewhat with the results reported here. Discrepancies could be explained by slight amounts of micelle formation and differences in copolymer architecture.

Table 2.4. Graft density in cocontinuous blends stabilized by premade diblock copolymers, from work by Bell, *et al*.[35] Final graft density represents the density after 30 minutes of annealing, after which time coarsening was suppressed.

System	wt% BCP	M_n BCP	Σ/Σ_{max} initial	Σ/Σ_{max} final	PS Chains/ πR_g^2 initial	PS Chains/ πR_g^2 final	Mtl. 2, Chains/ πR_g^2 init.	Mtl. 2, Chains/ πR_g^2 final
PS-PE	0.1	40	0.3	1	3.4	11	7.0	23
	0.3	40	0.6	1.3	6.8	15	14	30
	1	40	1.1	1.2	13	14	26	28
	1	6	12	92	38	290	79	610
	1	100	1.8	3.2	37	65	76	130
	1	200	1	3	34	100	70	210
PS-PMMA	0.1	100	0.2	1	2.7	13	2.2	11
	0.3	100	0.4	1.8	5.4	24	4.5	20
	1	100	1.1	1.8	15	24	12	20
	3	100	1.3	1.7	18	23	15	19
	1	42	1.6	1.8	12	14	10	11
	1	160	0.7	1.8	13	33	11	28
	1	260	0.9	1.7	23	44	19	36
PS-SAN	0.1	100	0.3	0.8	4	11	3.4	9
	0.5	100	0.9	2.1	12	28	10	24
	1	100	1.2	2.4	16	32	13	27
	5	100	1.6	4.3	22	58	18	48
	1	42	4	18.1	30	140	25	110
	1	74	1.6	5	18	55	15	46
	1	260	0.9	1.1	23	28	19	23
	1	900	0.6	1.2	35	70	29	58

The premade block copolymer results are also shown to be consistent with a final Σ/Σ_{max} of 1 for the dilute systems. This supports the conclusion that coarsening is suppressed by the formation of a dense monolayer, contrary to the reactive compatibilization results reported here. However, without more consistent trends across different molecular weights of premade block copolymer, it is difficult to draw more substantive conclusions on the mechanism of coarsening suppression.

2.4 Conclusions

Blends with maleic functional PE-g-MA showed significant reduction in the phase domain size compared to blends with non-functional LDPE, due to a reduction in the interfacial tension attributed to the presence of PE-g-PEO graft copolymers forming at the blend interface. No appreciable characteristic size difference was observed between blends with PE-g-MA and 40K, 60K and 200K PEO. This was due to a balancing effect between increased interfacial tension and better stabilization of elongated features as molecular weight increased. The exception was the PE-g-MA/20K PEO blend, which showed dramatically larger features in the cocontinuous blends, since the low viscosity provided little resistance to rapid coarsening within the interconnected PEO domains.

Of all the blends, PE-g-MA/40K PEO showed the lowest interfacial tension due to the high oxygen fraction, as shown in Figure 2.9, and the high number of graft copolymers formed. Lower molecular weight PEO was more reactive due to lower viscosity, more intermixing at the interface, and higher concentration of reactive hydroxyl end groups. However, 20K PEO showed slightly higher interfacial tension in the reactive system when compared to 40K PEO due to a reduced fractional surface coverage, as verified by XPS. Formation of fewer graft copolymers at the interface for higher molecular weight 60K and 200K PEO led to higher interfacial tension and lower interfacial shear modulus after reaction with PE-g-MA, despite having fractional surface coverage comparable to 40K PEO laminations.

The stability of these blends was observed via coarsening experiments, tracking the change in phase size with annealing time. All non-compatibilized blends showed no upper bound to the phase size, and higher molecular weight PEO slowed the rate of coarsening in these blends. The rate of coarsening was successfully shown to be proportional to Γ/η_{blend}, which was proposed as a modified version of the rate of fiber break up to account for the lack of a dispersed phase. Compatibilized PE-g-MA/PEO blends showed two distinct regions of coarsening behavior: a

small increase in phase size in the early stages of annealing, followed by a complete suppression of coarsening and constant phase size at longer annealing time. Again, blends with the highest viscosity suppressed the coarsening the most – a surprising result considering these blends also had the highest interfacial tension and lowest graft density of the studied PE-g-MA/PEO blends. This phenomenon of coarsening suppression suggests that during coarsening of cocontinuous blends, the reduction of interfacial area forces the block or graft copolymers at the interface to densify into an extended brush-like structure. The final grafting density of this brush was found to be 4-5 PEO chains per πR_g^2 when starting with a PEO-saturated interface, as was the case with 40K, 60K, and 200K PEO. The coarsening blend system reaches a steady state when the rate of reduction in interfacial are (driven by Γ) equals the rate at which grafted chains restore to a random walk, governed by conformational entropy.

Chapter 3: Cocontinuous PE/PEO Blends for Applications in Gas Separation [*]

3.1 Introduction

Melt blending of immiscible polymers is an effective way to obtain materials with enhanced properties, specifically processability, mechanical and electrical properties, and barrier behavior. A significant effort has been made to control the morphology of blends, which has been found to have a great impact on their properties. Most polymers used in blends are immiscible or partially miscible due to their high molecular weight and unfavorable interactions, and thus their blends macrophase separate into heterogeneous morphologies, including droplet/matrix, fiber, lamella, and cocontinuous.[1] The type of morphology formed during processing depends on the physical properties of the polymers (interfacial tension, viscosities and the ratio of these viscosities), their volume fractions and the processing conditions.[2] Of all possible morphologies, the cocontinuous morphology is of particular interest due to its ability to continuously combine the properties of both polymer components.[3]

A cocontinuous morphology is a non-equilibrium morphology defined by the coexistence of at least two continuous structures within the same volume. As such, it is an unstable morphology, and it starts changing through self similar coarsening, filament break-up, and retraction, as soon as the fluid blend comes out of the melt compounder. In order to maintain the desired cocontinuous morphology, the blend is quenched immediately after processing to freeze the morphology.

Interfacial modifiers called compatibilizers are often added to blends in order to stabilize

[*] Reproduced with minor modifications and including figures from supplemental information, with permission from M. Trifkovic, A. Hedegaard, K. Huston, M. Sheikhzadeh, and C. W. Macosko, "Porous Films via PE/PEO Cocontinuous Blends," *Macromolecules*, **45**, 6036−6044 (2012). Copyright 2012 American Chemical Society.

their morphology by suppressing coarsening [34,35,88] and improving interfacial adhesion. This also typically results in a significant size reduction in the phase domains of the blend. Typical compatibilizing molecules are block or graft copolymers, which contain a block miscible with each phase, often formed *in situ* during the mixing process via coupling reactions between functional groups at the interface of the two phases.[36,38,89,90] This *in situ* approach, called reactive compatibilization, is usually preferred in industry.[3]

Due to the irregular shape of the microstructure, quantitative morphological characterization of cocontinuous blends is a challenge. The interfacial area per unit volume is often used in modeling the evolution of interface shape and the characteristic phase size of the blend.[12,91] In most studies, interfacial perimeter per area of two-dimensional cross sections of blends, imaged by scanning electron microscopy (SEM) or transmission electron microscopy (TEM), is used to describe the interfacial shape. However, this often fails to describe the true morphology due to the nonuniformity of the blend. Recently, improvements have been made in three-dimensional imaging of polymer blends using various technologies including transmission electron microtomography (TEMT),[92,93] X-ray phase tomography,[82,94] three-dimensional nuclear magnetic resonance (NMR) imaging,[95] and laser scanning confocal microscopy (LSCM).[12,65] LSCM in particular has the advantages of fast and nondestructive image acquisition. However, in order to acquire a stack of 2D images, at least one of the phases must fluoresce, and the sample must be optically transparent to provide an adequate depth of field. To satisfy the fluorescence requirement, one of the polymers is usually polymerized with a small quantity of a fluorescent monomer.[12] However, this is not a feasible option for studies that employ most commercially available polymers. To satisfy the optically transparent requirement, the phases must match in terms of refractive index.

This chapter acts as an extension to the work shown in Chapter 2. It explores a specific application of porous polyethylene films derived from polyethylene/polyethylene oxide (PE/PEO)

cocontinuous blends as a mechanical support for gas separation membranes. This chapter focuses on LDPE/40K PEO and PE-g-MA/40K PEO as the specific blend system for the application. By extraction of one polymer phase, a porous network is formed. This porous network can then be filled in with a selectively permeable material such as an ionic liquid, which have been shown to possess high permeability and CO_2/CH_4 selectivity.[96-100] The PE/PEO polymer system was selected on the basis of ease of extraction of the PEO phase in water, the thermodynamic compatibility between PEO and the ionic liquid, and the solvent resistance, low cost, and toughness of PE.

This work reports the effect of functionalization of polyethylene, blend composition, and processing conditions on the blend morphology. Rheological characterization of droplet blends was fit to the Palierne viscoelastic droplet model [60,62] to quantify the equilibrium interfacial tension of PE/PEO blends. LSCM was used for 3D imaging and qualitative and quantitative analysis of cocontinuous blend morphology.

Gas separation membranes were prepared by solvent casting an acetone solution of poly(vinylidene fluoride-co-hexafluoropropylene) (p(VDF-HFP)) swollen with 1-ethyl-3-methylimidazolium bis(trifluoromethylsulfonyl)imide ([EMIM][TFSI]) into porous polyethylene films and tested in a gas diffusion cell.[100,101] To demonstrate the possibility of generating a cocontinuous structure on a large scale, the process was scaled-up from the 5 g batch microcompounder to a pilot-plant scale twin-screw extruder. For these continuously produced materials, the effects of processing conditions such as residence time, screw geometry, and composition were compared in terms of the resulting average characteristic size and characteristic size distribution, in order to determine the optimal processing method for the formation of the gas separation membrane supports.

3.2 Experimental Methods

3.2.1 Materials

Table 3.1 shows the molecular properties of the blend components. Low density polyethylene (PE) was provided by the Dow Chemical Company (LDPE 995l), maleic anhydride grafted polyethylene (PE-g-MA) containing 1.6 wt% maleic anhydride by Chemtura (Polybond 3029), and polyethylene oxide (PEO) was provided by the Dow Chemical Company (Polyox N10). Complex viscosity profiles of PE-g-MA, PE, and PEO, along with their Cross model fits are shown in Figure 3.1. The Cross model is given by the following equation:

$$\frac{\eta - \eta_\infty}{\eta_o - \eta_\infty} = \frac{1}{1 + (K\dot{\gamma})^n} \tag{3.1}$$

where η is the shear-rate dependent viscosity, η_o is the zero-shear viscosity, η_∞ is the infinite shear viscosity (assumed to be zero in all samples), K is the time constant of shear thinning, and n is the power law exponent. The corresponding Cross model parameters are shown in Table 3.2. In order to apply the Cross model fitting, the Cox-Merz relationship was assumed to hold, such that the measured frequency-dependent complex viscosity of the materials was equivalent to the shear rate-dependent viscosity for $\omega = \dot{\gamma}$.[63]

Table 3.1. Material properties of pure materials used for blending.

Material	M_w (kg/mol)	M_w/M_n	Functional groups/chain	η_o, (Pa s) @ 150 °C	η, (Pa s), @ 400 s^{-1}	Density, (g/cm^3) @ 23°C
PE	59	5.0	0	2.26 x 10^4	340	0.923
PE-g-MA	79	5.9	12.9	8.00 x 10^4	540	0.96
PEO	80	2.2	2	1.05 x 10^4	410	1.2

Molecular weights of the polyethylenes used in this study were measured by high

temperature gel permeation chromatography at 155° C using 1,2,4-trichlorobenzene as eluent and polystyrene standards. Density values in Table 3.1 were provided by the manufacturer. 2-Hydroxyethyl(methacrylate) (HEMA) monomer was purchased from Aldrich and was mixed with 1 wt% azobisisobutyronitrile, a thermally activated radical initiator, also purchased from Aldrich. Both were used as received.

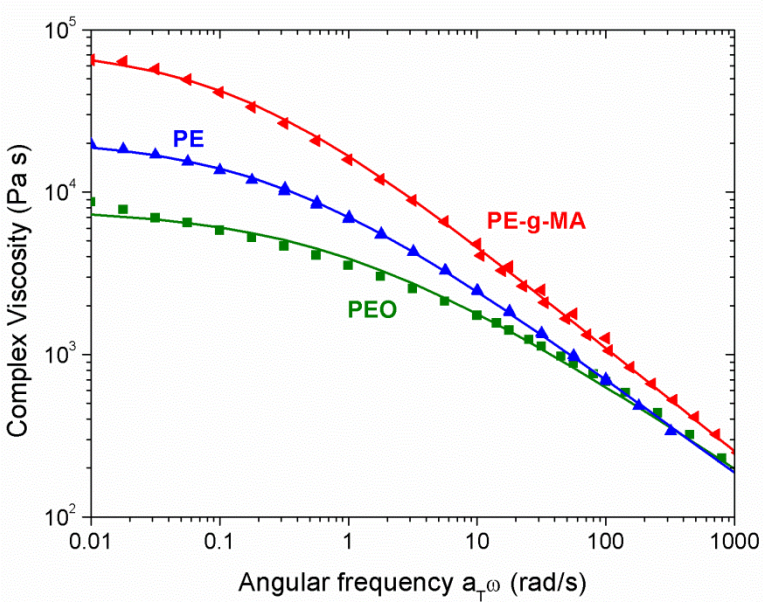

Figure 3.1. Complex viscosity of pure materials. Viscosity at frequency >100 rad/s were collected by time-temperature superposition of data collected just above T_m of each material. Lines represent Cross model fits, given by Eq. 3.1.

Table 3.2. Cross Model Parameters at 150 °C, fit using Eq. 3.1 to the shear rheology of the pure materials, as shown in Figure 3.1. Infinite shear viscosity, η_∞, was assumed to be zero for all materials.

Material	η_o, (Pa s)	n	K (s)
PE	2.15 x 10^4	0.419	3.48
PE-g-MA	7.72 x 10^4	0.360	7.53
PEO	1.05 x 10^4	0.474	1.06

3.2.2 Blend Preparation and Annealing

Blends were prepared by both batch and continuous melt mixing processes. Batch melt compounding of PE/PEO and PE-g-MA/PEO was performed in a recirculating, conical twin-screw extruder (Microcompounder, DACA Instruments) at a rotor speed of 200 RPM and 150 °C. The weight ratio of PE/PEO and PE-g-MA/PEO was varied between 55/45 to 45/55 wt%. Upon completion of batch mixing, the blends were rapidly quenched in liquid nitrogen to freeze the morphology.

Continuous melt mixing was performed in a pilot plant scale co-rotating twin-screw extruder (Leistritz, Neuremberg, Germany) with screw diameter of 27 mm, L/D of 48:1 and 12 individually heated/cooled zones. The extruder was operated with the total feed rate of 5 kg/hr, a barrel/die set temperature of 150 °C, and screw rotational speed of 200 RPM, while varying the weight ratio of PE/PEO (in the same fashion as for the batch process). Two gravimetric feeders (Brabender, Missisagua, Canada) with the feedrate range of 1-10 kg/hr and 0.5-3 kg/hr were used for feeding materials. Polyethylene resins were introduced to the extruder in Zone 1, at the beginning of the screw length. PEO was introduced at either Zone 1 or Zone 5, in order to vary the residence time of the mixture. Two different screw configurations were used to subject the molten blends to high-intensity and medium-intensity mixing conditions. The geometry of each of these screws is represented graphically in Figure 3.2. Residence time with the lower shear screw configuration was 80 s when PEO was added to Zone 1 and 50 s when PEO was added to Zone 5. For the higher shear configuration, residence time was 120 s when PEO was added to Zone 1 and 70 s when PEO was added in Zone 5. The extruded strands were quenched in liquid nitrogen. During experimental studies, sensors located on the extruder continuously measured processing conditions. A more detailed description of the extrusion experimental setup can be found in previous work by Trifkovic and co-workers.[102]

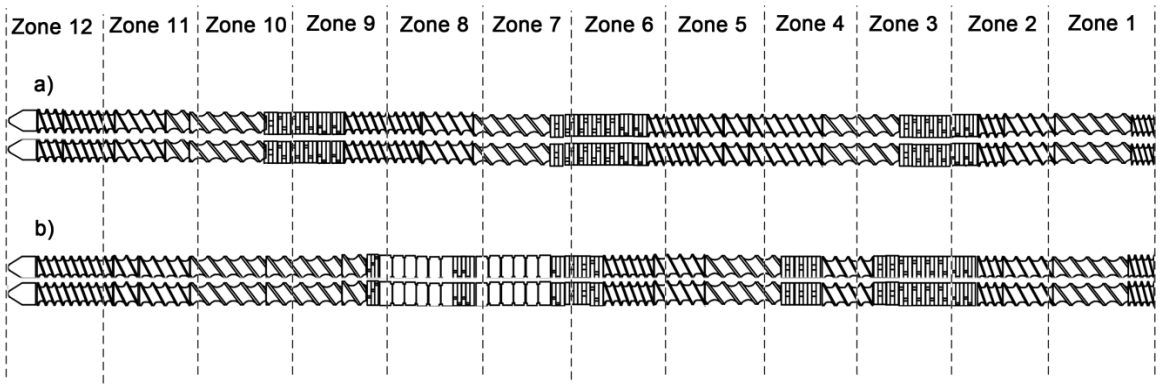

Figure 3.2. Screw geometry for a) Low shear screw configuration, b) high shear configuration. The high shear configuration includes a series of kneading elements in zones 7 and 8 for more intense mixing and a longer residence time.

Small pieces (0.7-1g) of the resulting blends were placed between two sheets of fluoropolymer coated fabric (Premium 6 Mil, American Durafilm) and then placed between the heated metal platens of a compression press (Carver, Inc., Wabash, Indiana). For morphology coarsening analysis, samples were annealed for various time intervals at 150 °C with no applied pressure. To obtain thin films with thickness of 100 μm, samples were pressed for no more than 3 minutes with one ton of force. After annealing, cold water was flushed through the press platens to cool the samples to room temperature.

3.2.3 Rheological Characterization

Rheological measurements of the blends and blend components were carried out at 150 °C using an ARES (TA Instruments) rheometer with a 25 mm parallel plate geometry. Prior to further rheological characterization, dynamic strain sweep tests were performed on all materials to determine the critical strain at which each material began to exhibit non-linear viscoelasticity. All subsequent tests were performed at strains within the linear viscoelastic region of the material. Small amplitude oscillatory shear tests were performed over a frequency range of 100 – 0.01 rad/s.

3.2.4 Morphology Analysis

Samples were cryo-microtomed (Reichert UltraCut S Ultramicrotome) at -140 °C using a glass knife. Phase contrast was generated by immersing the samples in water for 24 h and extracting the PEO phase, yielding porous PE samples. Samples were then sputter-coated with 50 Å of platinum. A scanning electron microscope (SEM, JOEL 6500) was used at an accelerating voltage of 5 kV and a working distance of 10 mm to study the morphology and phase dimensions after extraction.

Laser scanning confocal microscopy (LSCM, Olympus Fluo View 1000) was employed to obtain 3D images of cocontinuous polymer blends. In order to satisfy the LSCM requirements of specimen transparency and fluorescence of one phase, hydroxyethyl(methacrylate) (HEMA) with 0.01wt% rhodamine B dye was polymerized inside of the pores of the porous PE film at 80 °C for 10 minutes. An incident laser beam of wavelength of 563 nm excited fluorescence from the rhodamine dye dissolved in polyHEMA. A detector above the stage was set only to allow the rhodamine flourescense through the filter. Hence, the polyHEMA phase, which represents the previously extracted PEO phase, was identified as the bright phase under the LSCM. An oil-immersed 60 X objective lens was used with LSCM to obtain a stack of optical micrographs. The focal depth increment, Δz, was varied between 0.3 and 0.7 μm, depending on the average pore size of the sample.

The numerical models for the structural analysis were created in MATLAB 7 (The MathWorks Inc.) using the visualization toolbox. The LSCM images were imported, material pixels are separated from void pixels based on their grey values (tresholding), and a binary image representing the structure was obtained. A common practice for segmentation is to choose a simple global threshold. However, this procedure may lead to biases when one is trying to segment a stack of LSCM images. The distinction between the void and solid phases in images frequently changes throughout the stack of images since the laser's intensity is weakened as it

penetrates deeper into the sample. For this reason, the iterative selection thresholding method was used to perform segmentation of the cocontinuous blend images into pores and solid polymer material, where the threshold was adjusted as a function of depth into the sample to account for the reduced contrast.[103]

The 3D image was reconstructed using Avizo (v. 6.3, http://www.vsg3d.com/avizo) interactive visualization package. A marching cubes algorithm was applied for triangular mesh generation. Interfacial area per unit volume, Q, was obtained by adding the areas of all the triangles A_i of the generated mesh, and dividing the sum by the total volume of the sample, V.[66]

$$Q = \frac{1}{V}\sum_{i=1}^{N} A_i \tag{3.2}$$

Figure 3.3 shows a) the "solid model" of PE phase, and b) the interface between PEO and PE phase rendered and meshed (mesh generated by applying marching cubes algorithm).

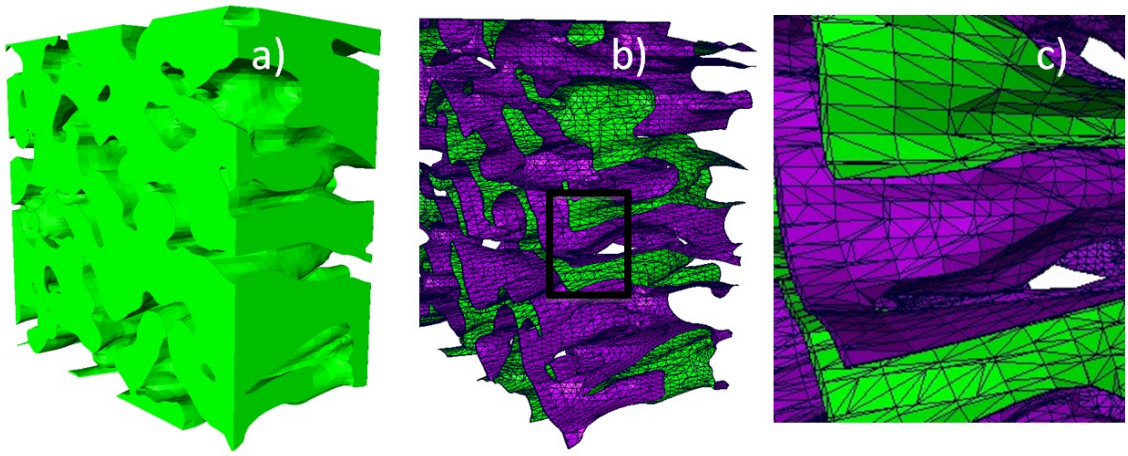

Figure 3.3. Rendered 3D microstructure for PE/PEO blend: a) solid model of the PE microstructure, b) interface between blend phases (purple facing toward the PEO phase and green towards PE phase, c) detail of the meshed interface (from the black square in b).

In addition to interfacial area, pore size distribution is another important descriptor of porous films derived from cocontinuous blends. Since the pores can be identified from contiguous white or black regions in a binarized image using MATLAB visualization toolbox, the pore size distribution can be estimated. For each 2D image, each individual pore could be selected and the

perimeter of each pore was calculated by identifying the set of pixels that belong to the pore and have at least one neighbor that interfaces with a polyethylene pixel. The area of the pores could be calculated based upon the total number of contiguous white polyHEMA pixels in each individual feature. Pore size distribution was calculated based on the equivalent pore diameter, which represents the diameter of a circle with the same area as the pore under consideration:[104]

$$D_{eq,i} = \frac{4A_{p,i}}{P_i} \tag{3.3}$$

where A_p is the pore area and P is its perimeter. The volume of each pore identified is calculated by multiplying the area of that pore by the constant slice thickness. By totaling the volume occupied by pores of a given equivalent diameter for all slices through the thickness, the overall pore size distribution for a sample can be obtained. At least 200 pores were sized for each distribution.

3.2.5 X-ray Photoelectron Spectroscopy

XPS was used for elemental analysis to detect grafted polymer at the surface of the blends. XPS spectra were collected using a SSX-100 spectrometer from Surface Science Instruments using monochromatic Al K_α X-rays with an accelerating voltage of 10 kV and a current of 20 mA. The X-ray beam spot size was 200 μm. A metal mesh and low-energy electron gun (energy output was tuned between 10-20 eV, dependent on the sample and spectra range) were used to provide charge neutralization during the experiment.

3.2.6 Contact Angle Measurement.

Static contact angle measurements were conducted using the captive air bubble method. The advantage of the captive bubble over the sessile drop method is complete immersion and hydration of the sample, and thus, the surface energy of interest between water and the film should not change with the time of measurement. Measurements were conducted on pressed smooth (non-porous) films of the unmixed polyethylene resins and on porous PE films, obtained

from thin film pressed blends which were subsequently subjected to PEO extraction in water. Films were placed in deionized water and air bubbles were released beneath the PE film using a J-shaped needle. The porosity of both porous samples was 50 volume% in this case. The bubble trapped under the surface of the film was imaged with a CCD camera and the tangent contact angle determined using FAMAS (v 3.1.3) analyzing software. A lower contact angle was representative of a more hydrophilic surface, where the surface was well-wetted by the water and the bubble retained more a spherical shape. The average static contact angles and 95% confidence intervals were obtained using at least 10 gas bubbles on each specimen, and are reported in Table 3.3. The solid (non-porous) PE and PE-g-MA films have much larger contact angles in comparison to their corresponding porous films. This happens since pores draw water in by capillary forces, resulting in Wenzel wetting.[105]

Table 3.3. Water contact angles for PE films.

	Smooth Films		**Porous Films**	
Material	PE	PE-g-MA	PE	PE-g-MA
Water Contact Angle (°)	81±3	63±2	27±2	18±2

3.2.7 Palierne Model

The Palierne model is used to obtain the interfacial tension between PE and PEO, as well as PE-g-MA and PEO, based on droplet blend rheology. The rheological behavior of immiscible polymer blends is generally complex, where the rheological properties depend strongly on composition and viscoelastic properties of the components. Under oscillatory shear flow or cessation of shear, the blend modulus, G^*, can be determined by contribution of each component and the interfacial tension:

$$G^* = G^*_{\text{components}} + G^*_{\text{interface}} \tag{3.4}$$

Palierne [60] suggested a model for droplet blends such that the modulus of a blend can be determined from that of each component. The model takes into account the size of the viscoelastic droplets dispersed in a viscoelastic matrix, the interfacial tension between the components, Γ, and interfacial shear modulus, β_s^*, and dilatation modulus, β_d^*.

$$G_{blend}^* = G_m^* \left(\frac{1+3\frac{\phi E}{D}}{1-2\frac{\phi E}{D}} \right) \tag{3.5}$$

$$\begin{aligned} E = &\left(G_d^* - G_m^*\right)\left(19G_d^* + 16G_m^*\right) + 24\beta_d^* \frac{\Gamma}{R_{avg}^{\ 2}} + 16\beta_s^* \frac{\Gamma + \beta_d^*}{R_{avg}^{\ 2}} + \\ &4\frac{\Gamma}{R_{avg}}\left(5G_d^* + 2G_m^*\right) + \frac{\beta_d^*}{R_{avg}}\left(23G_d^* - 16G_m^*\right) + \frac{2\beta_s^*}{R_{avg}}\left(13G_d^* + 8G_m^*\right) \end{aligned} \tag{3.6}$$

$$\begin{aligned} D = &\left(2G_d^* + 3G_m^*\right)\left(19G_d^* + 16G_m^*\right) + 48\beta_d^* \frac{\Gamma}{R_{avg}^{\ 2}} + 32\beta_s^* \frac{\Gamma + \beta_d^*}{R_{avg}^{\ 2}} + \\ &40\frac{\Gamma}{R_{avg}}\left(G_d^* + G_m^*\right) + \frac{2\beta_d^*}{R_{avg}}\left(23G_d^* + 32G_m^*\right) + \frac{4\beta_s^*}{R_{avg}}\left(13G_d^* + 12G_m^*\right) \end{aligned} \tag{3.7}$$

E and D are functions, which contain all model parameters. G^*_{blend}, G_d^*, G_m^* are the complex moduli of the blend, dispersed phase and matrix, respectively. φ is the volume fraction of droplets, and R_{avg} is the volume average radius of the droplets, as determined by image analysis of SEM micrographs of the droplet blends. The interfacial tension of dilute immiscible blends could be predicted by fitting the Palierne model to the blend rheological measurements. Compared to the original Palierne model,[60] the current model shown in Eqs. 3.5-3.7 contains the volume average radius of the droplets instead of droplet radius size distribution.

A simplified version of the Palierne model, which assumes that β_s^* and β_d^* =0, has successfully been applied to obtain morphological information of uncompatibilized blends by several researchers.[69-72] This simplified version was used to fit Palierne model to dynamic moduli

with previously calculated R_{avg}, to estimate a single parameter interfacial tension, Γ, of uncompatibilized PE/PEO blends.

For compatibilized PE-g-MA/PEO blends, the more general version of the Palierne model, which accounts for interfacial shear modulus, must be used.[62] The surface shear modulus is related to the presence of the compatibilizer at the interface. Therefore, the two-parameter (Γ and β_s^*) version of the Palierne model which assumes β_d^*=0, as discussed in detail by Van Hemelrijck *et al*,[61] is used in the present work. A more thorough discussion of the Palierne model can be found in Appendix A.

Knowing the droplet size distribution of the dispersed phase of the blends and the dynamic storage moduli *G'* of the blends and both components at 150 °C, it is possible to determine the interfacial tension using Eqs. 3.5-3.7. The droplet blend composition for PE/PEO and PE-g-MA/PEO was 90/10 wt%. To determine the droplet size, the droplet area was traced from SEM images using ImageJ software, and diameter was calculated from the corresponding droplet area, A_d. Typically, 200–300 particles were analyzed per sample. The volume average radius (R_{avg}) was calculated based on the particle size distribution.

3.3 Results and Discussion

3.3.1 Batch-mixed experiments: Comparing blends with PE vs. PE-g-MA.

Figure 3.4 shows a comparison of PE/PEO and PE-g-MA/PEO of cryomicrotomed extruded strands processed in the batch microcompounder under identical conditions (T=150 °C, RPM=200). Significant reduction in pore size is evident in the blend containing PE-g-MA. As the PEO used in this study is hydroxyl terminated on both ends, the possibility of reactive compatibilization as a consequence of reaction between maleic anhydride (MAH) groups randomly distributed along the PE backbone and OH groups at the ends of PEO chains was investigated. Tselios *et al* [106] reported reaction between MAH and OH groups in blends of

poly(ethylene-co-vinyl alcohol) and styrene-maleic anhydride (SMA) based on Fourier-transform infrared spectroscopy, differential scanning calorimetry, and extraction experiments. Flores *et al* [107] also observed similar functional group reaction from their investigation on blends of ethylene–vinyl acetate–vinyl alcohol and SMA.

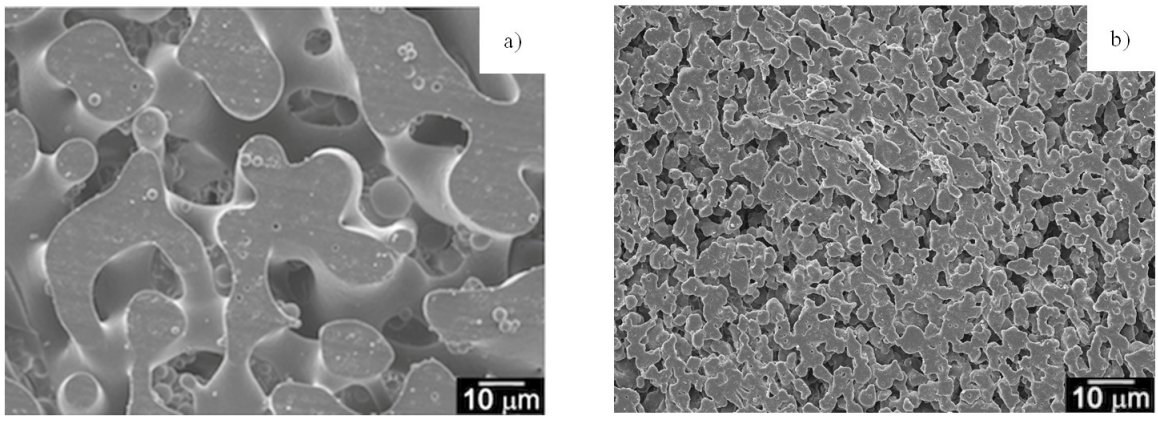

Figure 3.4. SEM micrographs of 50/50 vol% blends a) PE/PEO blend, b) PE-g-MA/PEO blend.

X-ray photoelectron spectroscopy (XPS) and the corresponding 3D images of porous PE and PE-g-MA films obtained after PEO extraction are shown in Figure 3.5. The XPS high-resolution spectra depicted the presence of carbon and oxygen for both films, with C/O ratio of 55/1 and 4/1 for porous PE and porous PE-g-MA films, respectively. The significant oxygen content (20%) on the surface of the porous polyethylene films derived from blends with PE-g-MA confirmed the formation of PE-g-PEO graft copolymer. This in turn explains the reduced contact angle (shown in Table 3.3) and the significant characteristic domain size reduction observed in blends using functionalized PE. The slight amount of oxygen present at the surface of porous PE film may be attributed to incomplete rinsing of PEO.

Figure 3.6 plots the characteristic length, $1/Q$, as a function of annealing time for 50/50 vol% blends of a) uncompatibilized PE/PEO and b) reactively compatibilized PE-g-MA/PEO, showing the effect of graft copolymer on suppression of coarsening during annealing. The stabilization of the interface is obvious in the case of the reactively compatibilized blend as the characteristic length increased from 1.5 to 2.5 µm in the first 5 minutes of annealing and then

stopped.

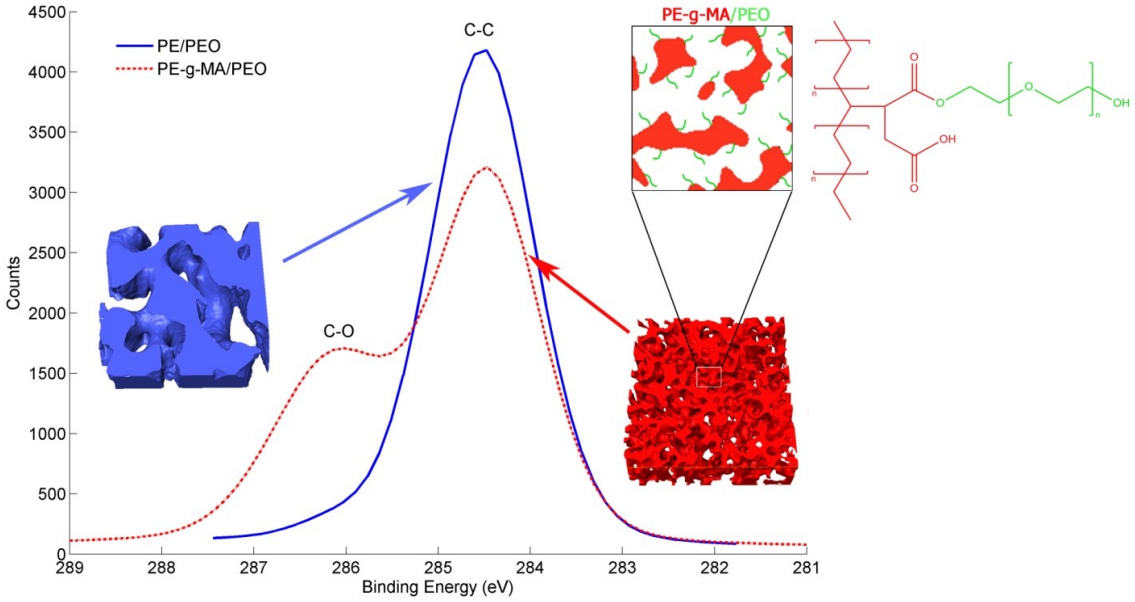

Figure 3.5. XPS spectra from cocontinuous blends after PEO extraction of 50/50 vol% PE-g-MA/PEO (right, C:O=4:1, 1.9 µm pore size) and PE/PEO (left, C:O=55:1, 11.1 µm pore size). The inset 3D images from laser scanning confocal microscopy (LSCM) show a 50x50x15 µm section of each porous film. The accompanying illustration of the PE-g-MA/PEO results shows the presence of the PE-g-PEO graft copolymers at the PE-g-MA surface following PEO extraction which resulted in the additional C-O peak at the higher binding energy.

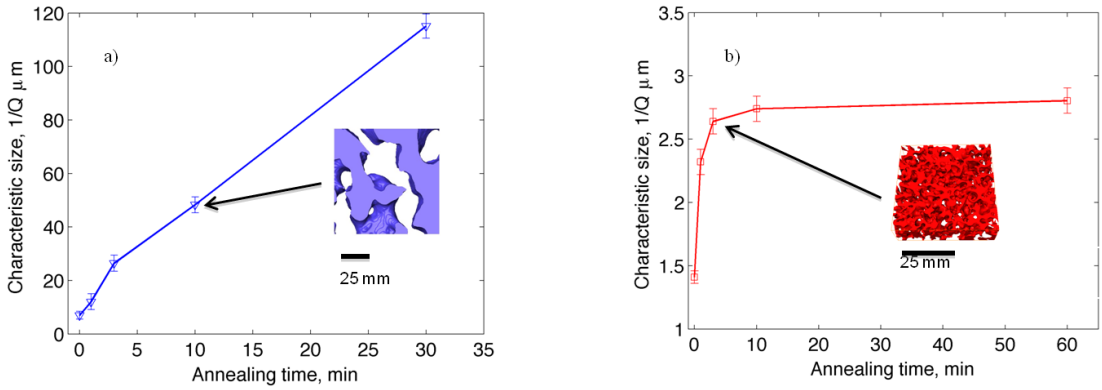

Figure 3.6. Characteristic size, defined as the inverse of interfacial area per unit volume (1/*Q*), vs. annealing time of 50/50 vol% blends. a) LDPE/PEO blend, b) PE-g-MA/PEO blend.

By contrast, the uncompatibilized blend shows an almost linear increase in the characteristic size. Similar differences between annealing of compatibilized and non-

functionalized cocontinuous blends has been observed previously.[35,88]

The rheology and morphology of droplet blends were investigated to determine interfacial tension. Figure 3.7 shows representative SEM micrographs of the droplet blends used in the rheological experiments. Image analysis, as described previously, of 4 such micrographs of each sample allowed the estimation of the volume average droplet radius for each sample. Figure 3.8 a) shows the frequency dependence of the storage moduli of pure polymers (PEO and PE) and the uncompatiblized PE/PEO droplet blend. The blend data were fit with the Palierne model using R_{avg}=1.02 μm (obtained from the SEM image analysis) and a single parameter, Γ, the interfacial tension. The estimated interfacial tension is 3 mN/m. In the case of the compatibilized PE-g-MA/ PEO blend, the results of fitting the data using R_{avg}=0.15 μm with the Palierne model using two parameters (Γ and β_s^*) is shown in Figure 3.8 b). The dynamic response of pure PE-g-MA, PEO, and the compatibilized blend subjected to the same shear history are added to these figures as well. The interfacial tension estimate is 0.4 mN/m and the corresponding interfacial shear modulus, β_s^*, is 0.05 mN/m. In the case of the compatibilized blend, the inclusion of the interfacial shear modulus was necessary to account for the existence of the generated PE-g-PEO graft copolymers at the interface, which, as a third component of the blend, will contribute an additional elastic response to the system. On the other hand, the absence of graft copolymers in uncompatibilized blend results in a zero interfacial modulus (β_s^*=0 mN/m).

From the values of contact angle in Table 3.3 for the pure PE and PE-g-MA films, it is evident that the presence of polar maleic anhydride groups increases the film's wettability, which is shown by a significant decrease in contact angle. Similarly, the porous films derived from cocontinuous blends with PE-g-MA resulted in improved wettability due to PEO grafted to the PE-g-MA surface acting with the polar maleic anhydride groups, and it was consequently easier to incorporate an ionic gel into the film pores during the solvent casting process.

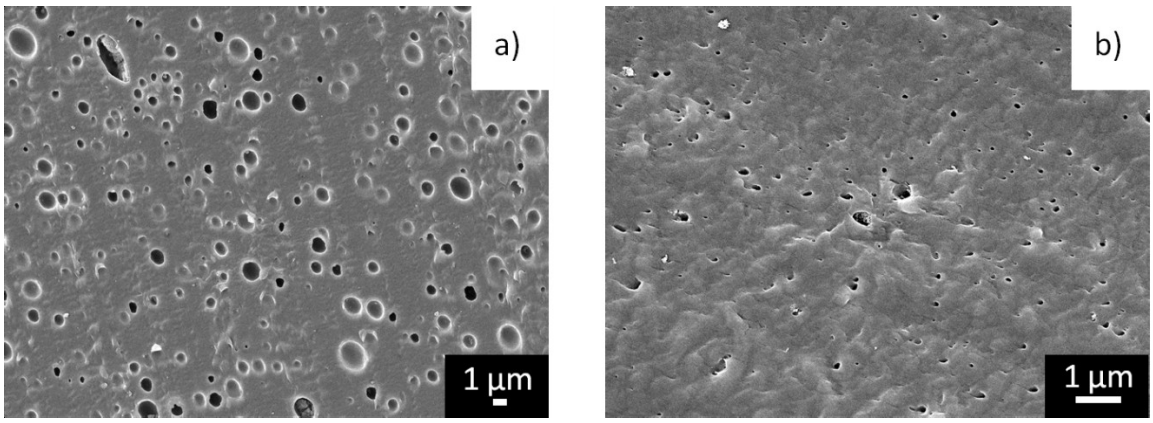

Figure 3.7. SEM micrographs of 92/8 vol% droplet blends after PEO extraction: a) PE/PEO, b) PE-g-MA/ PEO.

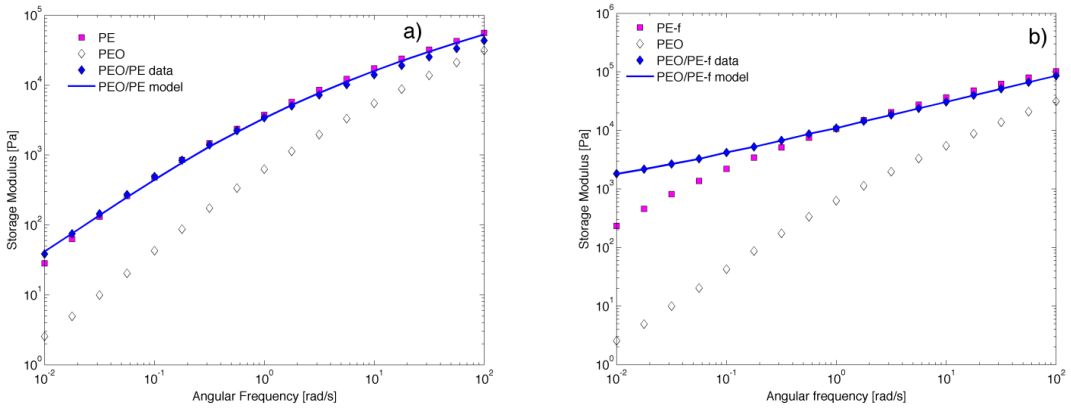

Figure 3.8. Storage modulus as a function of angular frequency for the pure polymers and 90/10 PE/PEO wt% blends. a) PE/PEO blend with R_{avg}= 1.02 µm, where Palierne model fitting gives Γ=3mN/m. b) PE-g-MA/PEO blend with R_{avg} = 0.15 µm, where Palierne model fitting gives Γ=0.4 mN/m and β_s^* = 0.05 mN/m.

From the above comparison of PE/PEO and PE-g-MA/PEO blends, it can be concluded that graft copolymers formed at PE-g-MA/PEO interfaces. This reactive coupling resulted in a significant decrease of interfacial tension and consequently smaller phase domains in cocontinuous blends and stabilization of interface during annealing at 150 °C. For the proposed application of the porous polyethylene films derived from cocontinuous blends as supports for gas separation membranes, compatibilized blends with PE-g-MA are better candidates: they have smaller, more stable pores and more wettable interfaces.

3.3.2 Extrusion experiments: Comparing processing conditions

The objective of twin-screw co-rotating extrusion experiments was to determine if the process could be scaled up from the microcompounder. The effect of blend composition, residence time and shear rate on the morphology of cocontinuous blends was investigated. Residence time was manipulated by introducing the PEO either in Zone 1 or Zone 5, which corresponded to 80s and 50s for lower shear configuration, and 120s and 70s for high shear configuration, respectively. Note that PE-g-MA was always introduced in Zone 1. Shear rate was altered by implementing two different screw configurations. The primary difference between the screw configurations was a block of high shear kneading elements after Zone 5 in the high shear screw, as opposed to a block of conveying elements in the low shear configuration.[102]

Figure 3.9 summarizes the effect of the aforementioned factors on the characteristic length, as calculated from 3D images and Eq. 3.2. As seen from Figure 3.9, 50/50 vol% blend compositions give the smallest characteristic size, $1/Q$.

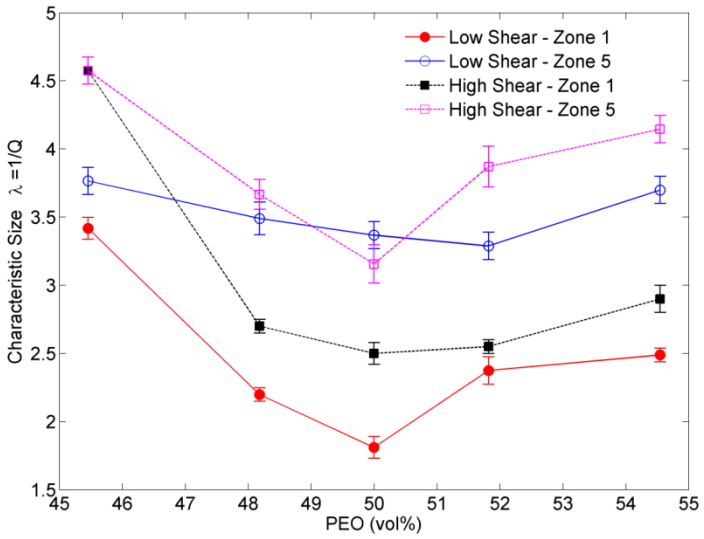

Figure 3.9. Characteristic size as a function of blend composition, shear rate and PEO zone introduction, as calculated by Eq. 3.2. Residence times were 80 s for low shear screw with PEO addition at Zone 1, 50 s for low shear screw and Zone 5 addition, 120 s for high shear screw and Zone 1 addition, and 70 s for high shear screw and Zone 5 addition.

On average the low shear configuration resulted in a smaller $1/Q$. For both low and high shear screws, error bars associated with the characteristic size of blends where PEO was added in Zone 5 were larger, suggesting that blend uniformity suffered as a result of the shorter residence time due to insufficient mixing to achieve a "steady state" cocontinuous morphology. The difference in the uniformity of the blends obtained by introducing PEO in Zone 1 vs. Zone 5 was obvious even by naked eye.

In order to quantify the uniformity of these blends, the pore size distribution was calculated using the stack of binarized 2D images acquired by LSCM by calculating the equivalent pore diameter by Eq. 3.3 for each 2D image according to the method described above. Figure 3.10 depicts the equivalent diameter pore size distribution of 50/50 vol% PE-g-MA/PEO blends obtained by the two different screws and residence times.

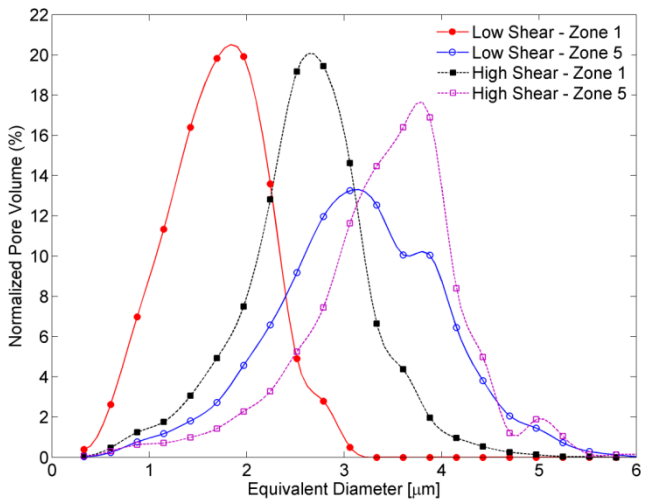

Figure 3.10. Equivalent diameter pore size distribution for 50/50 vol% PE-g-MA/PEO blend as a function of shear rate and PEO zone introduction, as calculated by Eq. 3.3. Residence times are the same as those shown in the caption of Figure 3.9.

It is evident that shorter residence times (when PEO is introduced in Zone 5) resulted in broader pore size distribution for both high and low shear screw configuration, again due to the shorter residence time which did not allow for extensive mixing and complete morphology

development. Also, high shear mixing resulted in larger pores for both residence times, despite that the residence time in the high shear screw geometry was longer than that for the low shear geometry. This can be attributed to shear induced coalescence, where intense mixing drives features to coalesce into larger features. It should be noted that the characteristic length, $1/Q$, calculated from 3D images was comparable to the average equivalent pore diameter, D_{eq}, obtained from the 2D LSCM images, suggesting that the two methods of analyzing these images give equivalent results. As previously mentioned, D_{eq} represents the diameter of a circle with the same area as the pore. Small quantitative differences between D_{eq} and $1/Q$ can be explained by the fact that the shapes of pores tend to be irregular in cocontinuous blends and can adopt a variety of shapes, from spherical to very elongated and irregular.

3.3.3 Burst Pressure Experiments

In order to study the mechanical robustness of the developed porous polymer films, the burst pressure of the gas separation membranes was tested in a diffusion cell. The membrane was placed between the two compartments of a diffusion cell, described previously.[108] The top chamber can be pressurized up to 10 atm and the bottom chamber is at atmospheric pressure at the beginning of the experiment.

Gas separation membranes were prepared by filling the pores of PE sheets with an ionic gel composed of 20/80 wt% of poly(vinylidene fluoride-co-hexafluoropropylene) (p(VDF-HFP)) swelled with (1-ethyl-3methylimidazolium bis(trifluoromethylsulfonyl) imide ([EMIM][TFSI]). This ionic gel possessed promising properties in gas separation of CO_2/CH_4 and CO_2/N_2 gas pairs, with the real selectivity being nearly the same as the ideal selectivity.[101] The procedure consisted of solvent casting an acetone solution of the ion gel into porous PE sheets followed by acetone evaporation under vacuum. The main purpose of the support layer is to provide mechanical strength and prevent the ionic gel being extruded out under the pressure difference. Therefore, small average pore size and uniform pore size distribution are desirable. Once the membrane was

prepared, it was clamped in the diffusion cell and both compartments were thoroughly flushed with CO_2 gas. The top chamber was pressurized and the bottom chamber was at atmospheric pressure at the beginning of the experiment. The pressure in the top chamber was increased in increments of 0.5 atm, and pressure in both chambers were continuously monitored in 1 s intervals. Burst pressure was defined as the applied pressure at which the pressure measured in both chambers rapidly equilibrated.

Typical examples of porous polyethylene sheets employed as support for gas separation membranes are depicted in Figure 3.11. Figure 3.11a) represents the SEM micrograph of porous PE film derived from the extruder blend with low shear configuration and longer residence time (PEO introduced in Zone 1), Figure 3.11b) shows the micrograph of porous PE film from the extruder blend with low shear configuration and shorter residence time (PEO introduced in Zone 5), and Figure 3.11c) presents the porous PE sheet generated from uncompatibilized blends (PEO introduced in Zone 1). Their corresponding measured burst pressures in the diffusion cell are >10, 4.5, and <1 atm, respectively. The results were in agreement with the previous characterization of extruder blends in terms of characteristic size (Figure 3.9), pore size distribution (Figure 3.10), and the morphology differences observed in Figure 3.11. Blends obtained with longer residence time in the extruder result in smaller average pore size, but also more uniform pore size distribution. Consequently, the membranes designed using these films as supports could withstand the maximum allowable gas pressure by the experimental setup and did not burst during experiments. However, blends with shorter residence time result in wider pore size distribution (Figure 3.10 and Figure 3.11b), and a significantly lower maximum gas pressure. Lastly, uncompatiblized blends result in large pore size, and no significant pressure difference could be applied without rupture of the membrane. Thus, the burst pressure is a function of average pore size as well as the coefficient of variation in pore size distribution – small pores are important for increasing the pressure needed to burst through the selective layer, but critical

failure will occur at the largest available pore. Therefore, a well-mixed blend with a narrow pore size distribution becomes important to creating a film without large pore defects that will compromise the function of membrane. Understanding the precise functionality of the burst pressure and the failure mechanism of the gas separation membranes will be the object of future experimental studies coupled with finite elements modeling.

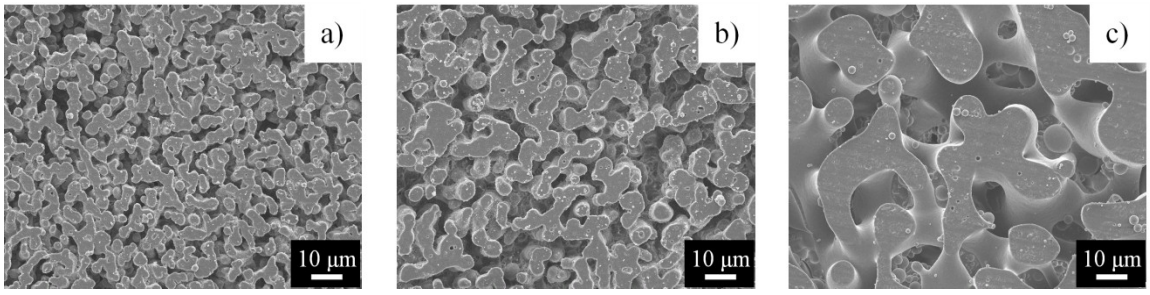

Figure 3.11. SEM micrographs of 50/50 vol% cocontinuous blends: a) PE-g-MA/PEO, Zone 1 PEO addition – 80s residence time (burst pressure >10atm), b) PE-g-MA/ PEO, Zone 5 PEO addition – residence time 40s, (burst pressure=4.5 atm), c) PE/PEO (non-functional), Zone 1 PEO addition– residence time 80s, (burst pressure<1 atm). All samples shown here were compounded continuous using the low shear screw configuration.

3.4 Conclusions

PE/PEO cocontinuous polymer blends were successfully prepared using a batch microcompounder and a twin-screw extruder and employed as a support layer for gas separation membranes. Blends prepared from PE-g-MA showed dramatically smaller phase sizes when compared to blends prepared from non-functional PE. Smaller phase size was attributed to reactive coupling of the OH end groups on PEO with the anhydride groups on PE-g-MA resulting in reduced interfacial tension.

The specific interfacial area was calculated from the triangular mesh data of interface between the two phases and a MATLAB code was developed for calculation of an average pore size from the 3D image data and a pore size distribution based on individual analysis of the 2D images used in the 3D reconstruction. Aside from the importance of minimizing the average pore size, pore size distribution was found to play a role in the performance of the derived porous

polymer films as supports in gas separation membranes. Decreasing the residence time in the twin-screw extruder by changing the PEO zone introduction (for both shear configurations) resulted in the broader pore size distribution, due to insufficient mixing time to achieve a steady state cocontinuous morphology. Consequently, these films could not withstand maximum allowable gas pressure in the diffusion cell. Additionally, a smaller average pore size was observed in blends produced using the lower shear rate screw geometry. This was attributed to an increased tendency towards shear induced coalescence in the higher shear screw geometry, which resulted in larger features. Longer residence time and a lower shear screw geometry allowed more effective blending of two polymers and yielded the smallest average pore size and narrower pore size distribution, making these most suitable for membrane applications.

Chapter 4: Effect of Viscosity Ratio and Interfacial Reaction on Cocontinuity

4.1 Introduction

Previous work in the field of immiscible polymer blends has observed that shear rheological properties of the blend components plays a vital role in the compositions that are capable of forming a cocontinuous morphology.[20,24-31] Many of these studies focus on predicting the occurrence of cocontinuity by way of the phase inversion composition, defined as the composition at which the blend inverts the major and minor phases. In blends of immiscible polymers, the morphology typically does not invert between opposite dispersed phases at a single composition. Rather, these blends adopt a cocontinuous morphology which occurs across a range of compositions centered on the phase inversion composition.

Many predictive models for determining the phase inversion composition have observed that it is strongly dependent on the viscosity ratio, *p*, of the immiscible blended polymers:

$$p = \frac{\eta_{PE}(\dot{\gamma}}{\eta_{PEO}(\dot{\gamma}} \tag{4.1}$$

where $\eta_{PE}(\dot{\gamma}$ is the shear rate dependent viscosity of the polyethylene (PE) phase and $\eta_{PEO}(\dot{\gamma}$ is the shear rate dependent viscosity of the polyethylene oxide (PEO) phase. It should be noted that all the models shown here are purported to be material system independent. The specific materials (PE and PEO) used in this study are listed in the equations here for clarity and ease of application to the current results.

Paul and Barlow [109] empirically observed that phase inversion in polymer-polymer blends occurred at a volume fraction ratio equal to the viscosity ratio *p*:

$$p = \frac{\phi_{PE,PI}}{\phi_{PEO,PI}} \tag{4.2}$$

where $\phi_{PE,PI}$ and $\phi_{PEO,PI}$ are the phase inversion volume fractions of the PE and PEO phases, respectively.

Work by Metelkin and Blecht [26] predicted the phase inversion of polymer-polymer blends by applying work by Tomotika [87] concerning the breakup of threads into droplets. The theory predicts phase inversion to occur when the deformation rate of stretching droplets into fibers is matched by the rate of fiber breakup into droplets.

$$\phi_{PEO,PI} = \left(1 + F(p) * p\right)^{-1} \tag{4.3}$$

$$F(p) = 1 + 2.25\log(p) + 1.8\left[\log(p)\right]^2 \tag{4.4}$$

This equation was derived using a LDPE/rubber blend. However, the original thread breaking work from Tomotika suggests that interfacial tension and thread size, which are not variables in the work presented by Metelkin and Blecht, play a key role in the rate of thread stretching and breakup, so there is dispute as to whether this model is generally applicable to other material systems.[3]

Work by Utracki [27] predicts that the phase inversion should depend on the packing of viscoelastic spheres into a continuous network of spherical particles. This model is derived from the Krieger-Dougherty equation for the rheology of monodisperse spheres,[110] modified such that the dispersed phase is initially composed of deformable droplets instead of hard spheres. Cocontinuity results at compositions when both phases would be capable of forming a percolated continuous network from the deformed droplets.

$$p = \left[\frac{\phi_m - \phi_{PEO,PI}}{\phi_m - \phi_{PE,PI}}\right]^{[\eta]\phi_m} \tag{4.5}$$

where $[\eta]$ is the intrinsic viscosity and ϕ_m is the maximum packing fraction of the dispersed phase. In the original analysis by Utracki, empirical values of $[\eta]$=1.9 and ϕ_m=0.84 were used to describe the behavior of deformable spherical particles. However, this chapter also investigates a

new application of this model assuming that the dispersed particles are hard spheres, using $[\eta]$=2.71 and ϕ_m=0.71 from the original Krieger-Dougherty equation.[110] Unique to this model is that ϕ_m defines the upper and lower bounds for phase inversion composition, which may limit the compositions that result in cocontinuity.

Despite this extensive work on predicting phase inversion by viscosity ratio, subsequent studies have found these models lacking in their general applicability to all blended polymer systems.[31,32,111] Other models have been proposed that go beyond just including shear viscosity to incorporate shear elasticity into the phase inversion prediction, particularly in work by Bourry and Favis.[32] These are based on an observation that a more elastic phase has a tendency to encapsulate a less elastic phase during mixing, due to a decrease in effective interfacial tension under dynamic conditions when the more elastic phase serves as the matrix.[111,112] This elastic dependence of the phase inversion can be described in terms of a ratio of *G'*:[32]

$$\frac{\phi_{PE,PI}}{\phi_{PEO,PI}} = \frac{G'_{PEO}}{G'_{PE}} \tag{4.6}$$

Similarly, the elastic dependence can also be described by a ratio of *tan(δ),* with the materials inverted compared to the *G'* ratio so as to retain the same dependency on *G'*:[32]

$$\frac{\phi_{PE,PI}}{\phi_{PEO,PI}} = \frac{\tan(\delta)_{PE}}{\tan(\delta)_{PEO}} \tag{4.7}$$

However, in true material systems and particularly in high viscosity polymer blends, cocontinuity occurs not only at a single phase inversion point but over a range of compositions empirically observed to be centered on the phase inversion composition. Phase inversion predictions do not give any information about the range of these cocontinuous compositions, which has been formally explored by only a few studies. Willemse *et al* [20,29] have proposed a model to predict the minimum volume fraction of the minor phase to form a continuous network, $\phi_{d,cc}$. It is based on an empirical model for percolation of stiff, randomly oriented rod-like

particles in a matrix and modified to account for the deformability of polymer droplets.

$$\frac{1}{\phi_{d,cc}} = 1.38 + 0.0213\left(\frac{\eta_m \dot{\gamma}}{\Gamma}\right) \tag{4.8}$$

where η_m is the shear viscosity of the major phase, $\dot{\gamma}$ is the mixing shear rate, Γ is the interfacial tension between the blend components, and R_o is the equivalent sphere radius of a droplet that is stretched into a rod-like shape and is dependent on the particulars of the blending process. The other limit of the range of cocontinuity is predicted by reversing the major and minor phase materials. Of note is the direct dependence on the major phase viscosity for determining the limit of minor phase percolation, with a notable lack of a direct dependence on minor phase viscosity (although it does factor implicitly into R_o.)

Compared to the listed phase inversion models, which depend only on intrinsic material properties that can be measured prior to melt processing, this model also depends on processing conditions and morphological characterization after blending. As such, it cannot be used to predict morphology *a priori*. The term R_o (i.e. the radius of the smallest pre-stretched droplet) can only be estimated after processing is complete. Such estimations are also prone to inaccuracy due to the cocontinuous blend existing in an elongated and irregular morphology where pre-stretched droplets are not directly observed. Additionally, while $\dot{\gamma}$ can be estimated within processing flows, it cannot be estimated to sufficient accuracy to be used in the model. Since the parenthetical term has an exponent of 4.2, it is apparent that even small errors to the estimated values of R_o or $\dot{\gamma}$ can drastically change the predicted range of cocontinuity.

The other major model used to describe the range of cocontinuity comes from work by Lyngaae-Jorgensen and Utracki,[113,114] in which the cocontinuity index Φ_I, which describes the fraction of a phase that is present in a continuous domain, can be described by percolation theory:

$$\Phi_I = k\left(\phi - \phi_{cr}\right)^{0.45} \tag{4.9}$$

where k is an empirical constant and φ_{cr} is the critical percolation composition at which continuous features begin to form (typically less than the composition at which complete phase continuity is exhibited). Numerical simulation suggests that for spherical droplets, $0.15 < \varphi_{cr} < 0.20$. This has been shown to hold for well-segregated PS/PMMA blends.[114] However, φ_{cr} is difficult to evaluate in a predictive measure, due to its dependence on interfacial stabilizing agents, thermal history, shearing history, and shape of the dispersed features prior to percolation.[32,113,115] Furthermore, previous studies have observed a wider variety of ranges of full cocontinuity, typically narrower than those predicted by Eq. 4.9.[4,5,29,32]

It is clear, then, that within the field of immiscible polymer blends, much work still needs to be done concerning the prediction of cocontinuity formation. In the present chapter, the phase inversion models will be explored in an attempt to address the disparities within the literature and to elucidate the extent of their applicability to the blends studied here and to general polymer blends. The models for predicting the range of cocontinuity will not be investigated here due to their experimental inaccessibility and limited value as predictive tools. However, experimentally measured ranges of cocontinuity will be discussed and compared with respect to the influence of shear viscosity and interfacial reaction, in the hope that a better logical and qualitative understanding of cocontinuity will aid in developing "rules of thumb" that will serve as a much-needed guide to experimental expectations and future quantitative predictions.

This chapter investigates the role of molecular weight, viscosity, and interfacial reaction on the compositions of immiscible polymer blends capable of forming cocontinuous structures. The work presented here specifically focuses on four blend systems. The first two blend systems are those first introduced in Chapter 2: low density polyethylene/polyethylene oxide (LDPE/PEO) blends and reactive maleic anhydride functional PE-g-MA/PEO. These systems are blended using variable molecular weight PEO to determine the influence of molecular weight, viscosity ratio, and reactive compatibilization on the compositions that result in cocontinuity. The other

two systems are reactive and non-reactive polypropylene/polyethylene oxide (PP/PEO) blends, which are investigated to explore cocontinuity in low viscosity blends. For the PP/PEO blends, the models listed in Eqs. 4.1 – 4.7 above can be used by replacing all instances of PE with PP.

For the experimental procedures of this study, PE/PEO and PP/PEO blends were produced via melt compounding in a batch mixer across a wide range of compositions. In order to determine the range of compositions which result in cocontinuity, the resulting morphology was characterized using gravimetric analysis via solvent extraction of the PEO and scanning electron microscopy (SEM). This chapter will focus exclusively on cocontinuity analysis: data and discussion concerning the stability and characteristic size of these blends can be found in Chapter 2.

4.2 Experimental Methods

4.2.1 Materials

In addition to the materials used in Chapter 2, three polypropylene (PP) resins were used: one non-functional PP (n-PP) provided by Huntsman (M135), and two maleic anhydride grafted polypropylenes of different viscosity, supplied by DuPont (designated here as the higher viscosity PP-g-MA-1 and the lower viscosity PP-g-MA-2, supplied under the names Fusabond ND211D and Fusabond P353, respectively).

Table 4.1. Melting temperature, molecular weight, and density for PP materials.

Material	T_m (°C)	M_n (kg/mol)	M_w (kg/mol)	ρ (g/cm^3) @ 23 °C
n-PP	163	33	390	0.95
PP-g-MA-1	162	28	210	0.95
PP-g-MA-2	140	18	59	0.95

Table 4.1 shows the relevant material properties for the pure PP materials. Melting temperature, T_m, was measured by dynamic scanning calorimetry (DSC, TA Instruments Q1000).

Molecular weight was measured by high temperature gel permeation chromatography (GPC, Agilent PL-GPC 220 High Temperature GPC/SEC System) at 160 °C using 1,2,4-trichlorobenzene as the eluent and compared to polystyrene standards. Density values were provided by the material suppliers. Material properties for the PE and PEO materials used in this study can be found by referring back to Table 2.1.

4.2.2 Rheology

Viscoelastic properties of the blend components were measured with an ARES rotational rheometer (TA Instruments) using 25 mm parallel plate geometry, except in the case of 20K PEO and PP-g-MA-2, where 50 mm parallel plates were used. Dynamic strain sweep tests at an oscillatory frequency of 1 rad/s were conducted on all materials to determine the critical strain, roughly 20% for each sample. Subsequent frequency sweep measurements were performed at strains below the critical strain to measure linear viscoelastic properties of the components and blends.

PE and PEO materials and blends were measured at 150 °C over a frequency range from 100 – 0.01 rad/s. PP and PEO materials used in PP/PEO blends were measured at 180 °C over a frequency range of 100 – 0.1 rad/s. All materials were also measured at lower temperatures, and using time-temperature superposition, this data was overlaid on the master curve at the processing temperature to record rheological properties at higher frequencies.

Complex viscosity profiles of the raw polymer materials were fit with the Cross model, as given by Eq. 3.1. The Cox-Merz relation was assumed to apply for all materials.[63] Complex viscosity, Cross model fits and Cross model parameters for PE and PEO materials at 150 °C can be found by referring back to Figure 2.1 and Table 2.2. Complex viscosity for the PP and PEO materials at 180 °C is shown in Figure 4.1. Cross model parameters for PP and PEO materials at 180 °C are shown in Table 4.2.

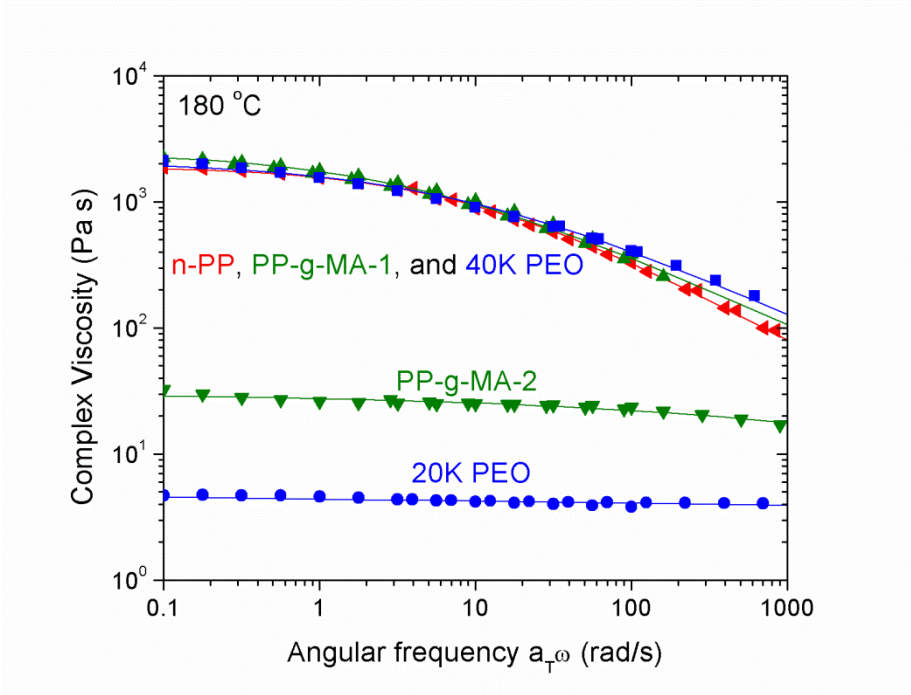

Figure 4.1. Complex viscosity versus frequency at 180°C for the PP and PEO materials used in PP/PEO blends. Viscosity at frequency >100 rad/s were collected by time-temperature superposition of data collected just above T_m of each material. The lines represent the Cross model fits, as described in Eq. 3.1.

Table 4.2. Cross model parameters for PP and PEO pure materials. Measurements were conducted at 180 °C. Cross model parameters for the remaining materials can be found in Table 2.2.

	Material	**η_o (Pa s)**	**n**	**K (s)**
PP	n-PP	1920	0.333	0.110
	PP-g-MA-1	2490	0.428	0.230
	PP-g-MA-2	30.4	0.716	0.00031
PEO	20K PEO	4.7	1	3760
	40K PEO	2090	0.439	0.129

From the rheological results, the relevant material parameters were selected to be used in

the phase inversion predictions from Eqs. 4.1 – 4.7. For these predictions, shear rate dependent viscosity η, elastic storage modulus *G'*, and phase angle *tan(δ)* were needed for each material at a rate representative of the mixing conditions, estimated to be 400 s^{-1}. Due to limitations of the instrumentation used, oscillatory measurements could only be conducted to a frequency of 100 rad/s. Therefore, time-temperature superposition of rheological data collected at lower temperatures was used to predict the response at high deformation rates. η(400 s^{-1}), *G'*(400 rad/s), and *tan(δ)*(400 rad/s) are shown above in Table 4.3.

Table 4.3. Rheological parameters used in phase inversion predictions for the studied blend systems, from Eqs. 4.1 – 4.7.

	Material	η(400 s^{-1}) (Pa s) †	*G'*(400 rad/s) (Pa) ‡	tan(δ) (400 rad/s) (Pa) ‡
PE and PP	**LDPE, 150 °C**	322	5.56 x 10^4	0.663
	PE-g-MA, 150 °C	455	1.84 x 10^5	0.604
	n-PP, 180 °C	143	4.70 x 10^4	0.716
	PP-g-MA-1, 180 °C	175	5.12 x 10^4	0.704
	PP-g-MA-2, 180 °C	19.6	1860	4.09
PEO	**20K PEO, 150 °C**	4.8	28.3	67.3
	40K PEO, 150 °C	316	1.02 x 10^5	0.886
	60K PEO, 150 °C	706	2.29 x 10^5	0.606
	200K PEO, 150 °C	928	3.85 x 10^5	0.500
	20K PEO, 180 °C	4.09	24.2	67.7
	40K PEO, 180 °C	206	6.08 x 10^4	1.06

† Measured via oscillatory shear rheometry. Shear rate dependence was assumed based the validity of the Cox-Merz relationship.

‡ Measured via oscillatory shear rheometry. Values at 400 rad/s were recorded using time-temperature superposition of measurements conducted at lower temperatures.

4.2.3 Blend Preparation

Blends were prepared using a recirculating, batch microcompounder (DACA Instruments)[64] with a volume of 5 cm^3. All blends were prepared under nitrogen purge at 200

RPM for 6 minutes, at which point the recirculation channel was closed and the die opened to extrude the blended material. PE/PEO blends were prepared at 150 °C, while PP/PEO blends were prepared at 180 °C. The extruded product was quenched in liquid nitrogen to freeze the morphology. Blends were made at compositions ranging from 90/10 vol% PE or PP/PEO to 10/90 vol% PE or PP/PEO.

4.2.4 Determination of Cocontinuity

Extruded blends were submerged in water overnight to extract the continuously interconnected PEO not trapped in droplets. The degree of PEO cocontinuity, Φ_{PEO}, was determined gravimetrically from the mass of PEO extracted in water:[4]

$$\Phi_{PEO} = \frac{m_i - m_f}{m_{PEO,i}} \tag{4.10}$$

where m_i is the initial mass of the blend, m_f is the final mass of the blend, and $m_{PEO,i}$ is the mass of PEO in the initial sample. Achieving $\Phi_{PEO} = 1$ suggested that all PEO initially present in the blend was extracted during the water bath, leaving only polyethylene or polypropylene behind. This is only possible in the case where all the PEO is continuously connected and no PEO is trapped in droplets. Blends with $\Phi_{PEO} \geq 0.9$ were defined to be continuous in the PEO phase. Some non-continuous PE or PP may be washed out of the structure after removal of the PEO, which will artificially increase the measured PEO continuity, potentially greater than $\Phi_{PEO} = 1$. Blends that remained self-supporting after PEO extraction were defined to be continuous in the PE or PP phase. The compositions which exhibited both phases achieved continuity according to the criteria listed above defined the range of cocontinuity.

4.2.5 Morphological Analysis

In order to aid in the interpretation of the degree of cocontinuity, the morphological transition from dispersed droplets to complete cocontinuity was qualitatively characterized by

scanning electron microscopy (SEM, JEOL 6500). Smooth cross sections of the extruded samples were prepared by cryo-microtome (Reichert UltraCut S Ultramicrotome) at -140 °C using a glass knife. Phase contrast was achieved by extracting PEO in a water bath overnight, leaving behind the PE or PP matrix. These samples were then sputter coated with 50 Å of platinum and imaged at an accelerating voltage of 5 kV and a working distance of 10 mm.

4.3 Results and Discussion

4.3.1 Cocontinuity of Non-reactive Blends

An overview of the cocontinuity results for each of the non-reactive blend systems, including the limiting compositions that achieved cocontinuity and the phase inversion compositions, can be found in Table 4.4. Also listed are the ratios for viscosity, storage modulus, and *tan(δ)*, that will be used in the subsequent section to discuss phase inversion predictions.

Table 4.4. Viscosity, *G'*, and *tan(δ)* ratios used to predict phase inversion by Eqs. 4.1 – 4.7, and ranges of cocontinuity, reported in terms of PEO volume fraction, for non-reactive LDPE and n-PP blended with PEO.

Blend System	$\eta_{PE/PP}$ / η_{PEO} ($400s^{-1}$)	G'_{PEO} / $G'_{PE,PE}$ (400 rad/s)	$\tan(\delta)_{PE/PP}$ / $\tan(\delta)_{PEO}$ (400 rad/s)	ϕ_{PEO} lower bound	ϕ_{PEO} upper bound	PEO Phase inversion, $\phi_{PEO,PI}$	Cocont. Range
LDPE / 20K PEO	67.1	2.89×10^{-4}	9.85×10^{-3}	0.38	0.45	0.405	0.07
LDPE / 40K PEO	1.02	1.04	0.748	0.38	0.69	0.535	0.31
LDPE / 60K PEO	0.456	2.34	1.09	0.47	0.81	0.64	0.34
LDPE / 200K PEO	0.347	3.94	1.33	0.54	0.85	0.695	0.31
n-PP / 40K PEO	0.694	1.29	0.676	0.44	0.62	0.53	0.18

What follows are observations and a discussion on the trends apparent in the cocontinuity results summarized in Table 4.4 as a function of absolute viscosity and viscosity

ratio. This discussion will be aided by plots showing degree of cocontinuity as a function of blend composition and SEM images representative of the morphological transitions from droplets to cocontinuous and back to droplets at the other end of the cocontinuity range. For the sake of clarity and brevity, continuity plots and SEM images will only be shown for selected blend systems. Such figures for all the blend systems studied here can be found in Appendix D.

As a specific example, the range of cocontinuity of blends composed of LDPE and 40K PEO is shown in Figure 4.2. This plot shows the degree of continuity for PEO, given by Eq. 4.10, as a function of PEO volume fraction in the blend. PEO continuity rapidly increases around 30 vol% PEO as the system transitions from dispersed PEO droplets to cocontinuity. Further increasing the PEO volume fraction through the range of cocontinuity eventually leads to breakup of the morphology into dispersed PE.

SEM micrographs of LDPE/40K PEO in Figure 4.3 illustrate the morphological transitions typically observed for blends with viscosity ratios near 1. These images show the transition with increasing PEO volume fraction from dispersed PEO droplets (Figure 4.3a) to the initial formation of continuous features at 33 vol% PEO (Figure 4.3b). Complete cocontinuity is clearly seen at 53 vol% PEO (Figure 4.3c) near the center of the range of cocontinuous compositions. The morphology undergoes a second transition from cocontinuous to dispersed LDPE at 67 vol% PEO (Figure 4.3d). Samples with PEO volume fractions greater than 69% PEO collapsed on the removal of the PEO matrix and were not able to be collected for imaging.

According to the cocontinuity of the non-reactive blends shown above in Table 4.4, the results show a trend towards a wider range of compositions that result in cocontinuity as the viscosity of the blend components increase. This is particularly noticeable in the case of LDPE/20K PEO, where the range has been reduced to a width of 0.07 PEO volume fraction, compared to the LDPE/200K PEO samples were the width of the range is 0.31 PEO volume fraction.

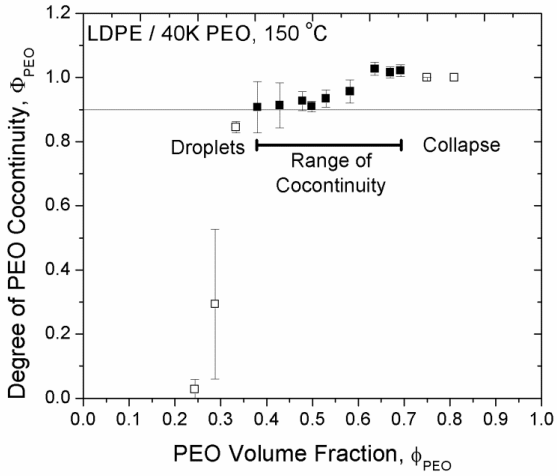

Figure 4.2. Degree of cocontinuity (Eq. 4.10) for blends containing LDPE and 40K PEO. Closed symbols indicate compositions of complete cocontinuity, while open symbols indicate dispersed morphologies. Error bars represent the standard deviation across 3 samples.

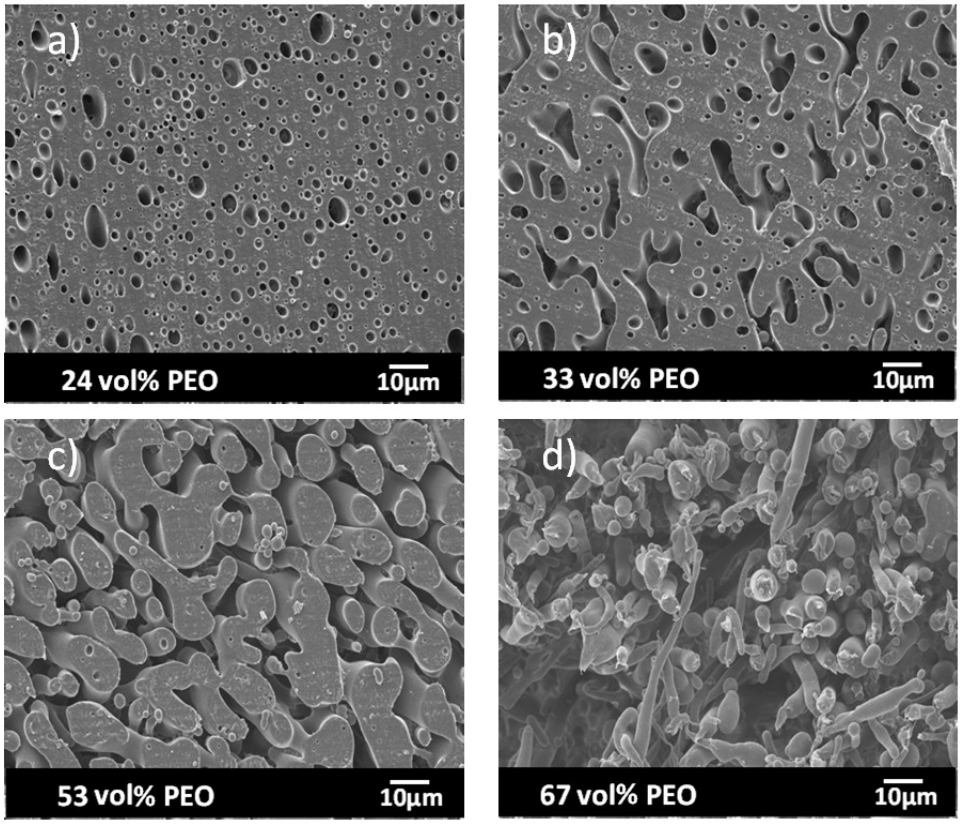

Figure 4.3. SEM micrographs of LDPE / 40K PEO blends following PEO extraction.

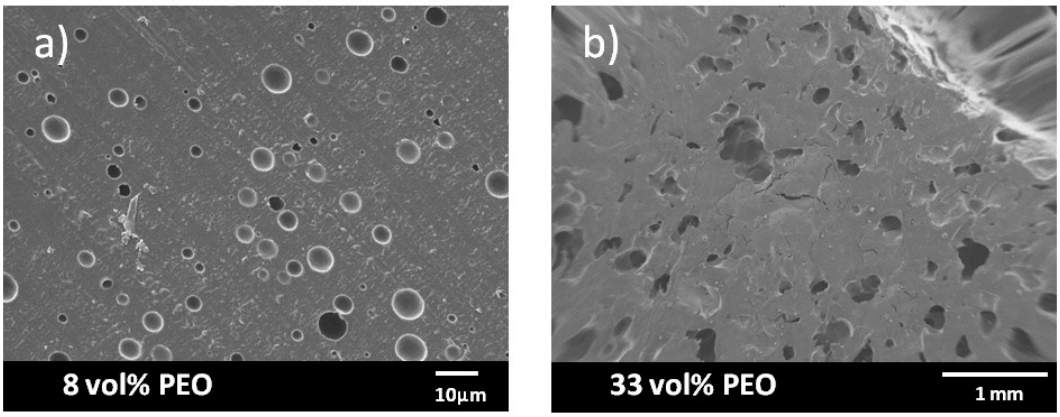

Figure 4.4. SEM micrographs of LDPE / 20K PEO blends following PEO extraction.

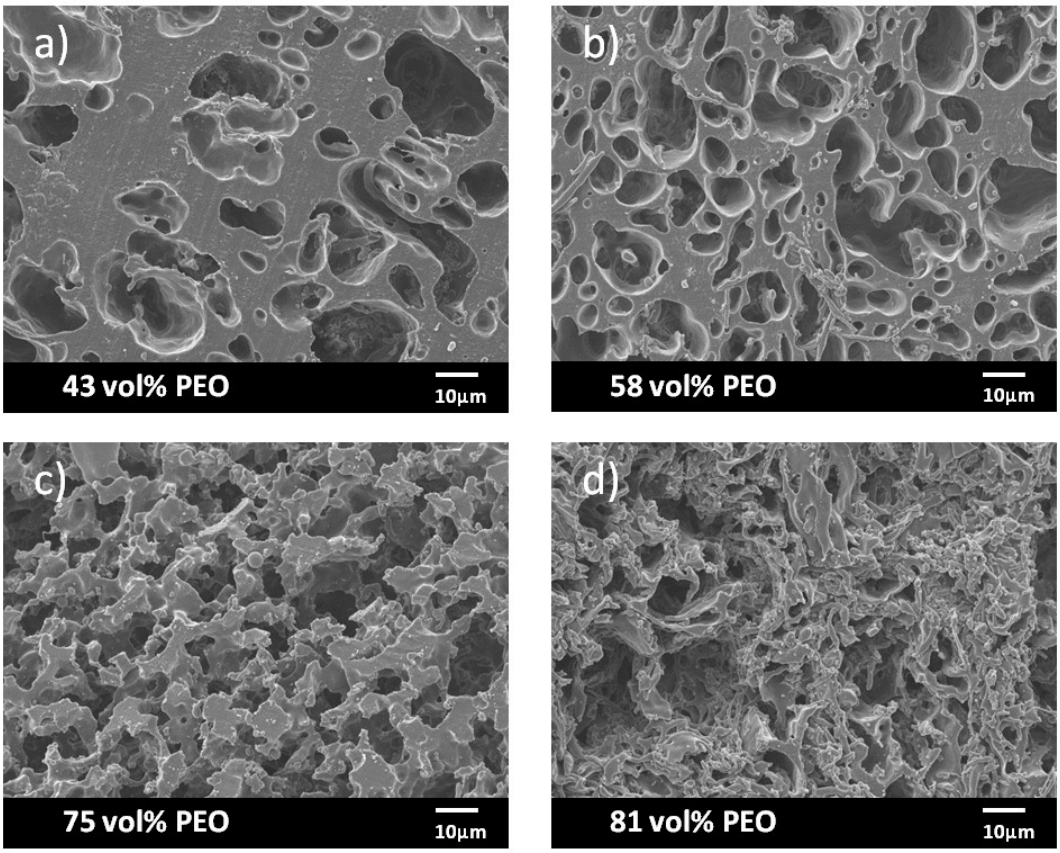

Figure 4.5. SEM micrographs of LDPE / 200K PEO blends following PEO extraction.

This assertion is further supported by comparing the range of cocontinuity for n-PP/40K PEO and LDPE/40K PEO, both of which have nearly identical viscosity ratios around 0.8 and measured phase inversion compositions of $\phi_{PEO,PI} = 0.53$. Having been processed at 180 °C, the

n-PP/40K PEO blend has the lower viscosity (as seen in the rheological results from Figure 2.1 and Figure 4.1). These blends resulted in a range of cocontinuity of only 0.18 volume fraction, narrower than that for the LDPE/40K PEO processed at 150 °C, which had a range of cocontinuity of 0.31 volume fraction. These observations are consistent with previous results from Sarazin and Favis,[116] where it was found that increasing the mixing temperature of polystyrene/polycaprolactone blends narrowed the range of cocontinuous compositions due to decreasing viscosity. This effect is likely caused by improved stability of elongated features with increasing viscosity. Higher viscosity features will break or restore to spherical droplets more slowly, promoting the formation of larger aspect ratio features which can more readily percolate into a continuous network.

However, in spite of observations that increased viscosity broadened the cocontinuity range, no increase in the range of cocontinuity was observed as the PEO molecular weight increased greater than the 40K PEO within the LDPE/PEO blends. This may be a result of differences in viscosity ratio. According to arguments made by Everaert and coworkers,[77] a lower viscosity major phase would not transfer stress effectively to a higher viscosity minor phase, resulting in difficulty extending the dispersed features into elongated structures that promote cocontinuity.

This is evident by comparing the SEM images from LDPE/20K PEO and LDPE/200K PEO, shown in Figure 4.4 and Figure 4.5 respectively, to the LDPE/40K PEO blends shown in Figure 4.3. Whereas LDPE/40K PEO promotes the formation of smooth and interconnected domains, both LDPE/20K PEO and LDPE/200K PEO blends showed an irregular and rough morphology in cocontinuous morphologies. This is particularly evident in the LDPE/200K PEO case nearer the limits of cocontinuous regime, such as in Figure 4.5 a) and b). These irregular domains would be expected to be less likely to percolate compared to elongated domains, which may explain the lack of broadening of the cocontinuity range despite the higher viscosity of

LDPE/200K PEO.

4.3.2 Cocontinuity of Reactive Blends

An overview of the cocontinuity results for each of the reactive blend systems, including the limiting compositions that achieved cocontinuity and the phase inversion compositions, can be found in Table 4.5. The viscosity, storage modulus, and *tan(δ)* ratios are listed as well, which will be used for phase inversion predictions in the following section. Similar to the previous section, the cocontinuity results and select SEM images will be discussed in order to determine further rules of thumb for determining cocontinuity, with an additional emphasis on the effect of compatibilization. Continuity plots and SEM images for all reactive blends can be found in Appendix D.

Table 4.5. Viscosity, *G'*, and *tan(δ)* ratios used to predict phase inversion by Eqs. 4.1 – 4.7, and ranges of cocontinuity, reported in terms of PEO volume fraction, for reactive PE-g-MA, PP-g-MA-1, and PP-g-MA-2 blended with PEO.

Blend System	$\eta_{PE/PP}$ / η_{PEO} ($400s^{-1}$)	G'_{PEO} / $G'_{PE/PP}$ (400 rad/s)	$\tan(\delta)_{PE/PP}$ / $\tan(\delta)_{PEO}$ (400 rad/s)	ϕ_{PEO} lower bound	ϕ_{PEO} upper bound	PEO Phase inversion, $\phi_{PEO,PI}$	Cocont. Range
PE-g-MA / 20K PEO	94.8	1.54×10^{-4}	8.98×10^{-3}	0.35	0.40	0.375	0.05
PE-g-MA / 40K PEO	1.44	0.554	0.682	0.44	0.71	0.575	0.26
PE-g-MA / 60K PEO	0.644	1.24	0.997	0.45	0.66	0.555	0.21
PE-g-MA / 200K PEO	0.490	2.09	1.21	0.5	0.66	0.58	0.16
PP-g-MA-1 / 40K PEO	0.847	1.19	0.664	0.44	0.65	0.545	0.21
PP-g-MA-2 / 20K PEO	4.79	0.0130	0.0604	--	--	0.45	0
PP-g-MA-2 / 40K PEO	0.095	32.7	3.86	0.48	0.58	0.53	0.10

With the reactive blends where the viscosity was relatively high and viscosity ratio was near 1, the samples showed similar morphological transformations compared to similar non-compatibilized systems. This is evident from SEM images of PE-g-MA/40K PEO, as shown in Figure 4.6. Similar to the case for LDPE/40K PEO blends shown in Figure 4.3, the blends go from droplets to the initial stages of cocontinuity with increasing PEO volume fraction. These initial stages of cocontinuity still retain the elongated, irregular shaped structures that form the continuous network of PEO. Full cocontinuity is achieved at the middle of the cocontinuity range, followed by dispersed PE as the PEO content increases further.

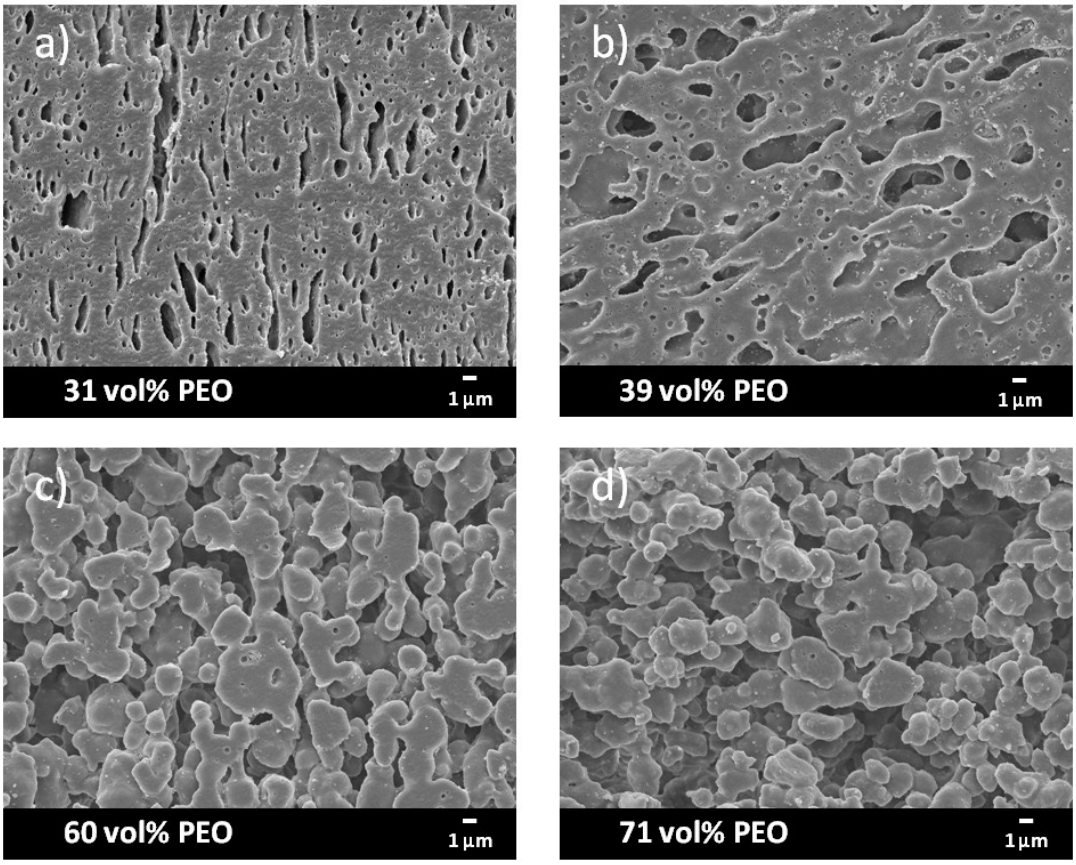

Figure 4.6. SEM micrographs of PE-g-MA / 40K PEO blends following PEO extraction.

For the reactively compatibilized blends, a similar trend to non-reactive blends exists with regards to low viscosity or high viscosity ratio systems. Low viscosity tends to prevent cocontinuity formation due to the instability of elongated features, which are prone to rapidly

breakup into droplets to form dispersed morphologies. High viscosity ratio results in poor stress transfer when the low viscosity material forms the major phase, resulting in poorly mixed or irregular features that are not conducive to percolation. Both of these trends are apparent in blends from PE-g-MA/20K PEO, shown in Figure 4.7, which are similar to the LDPE/20K blends. The influence of low viscosity is especially evident in the case of PP-g-MA-2/20K PEO, which was formed from the lowest viscosity materials. No completely cocontinuous blends from PP-g-MA-2/20K PEO were formed. A characteristic SEM image of this blend near the phase inversion point is shown in Figure 4.8. All other samples with higher PEO content collapsed after PEO extraction.

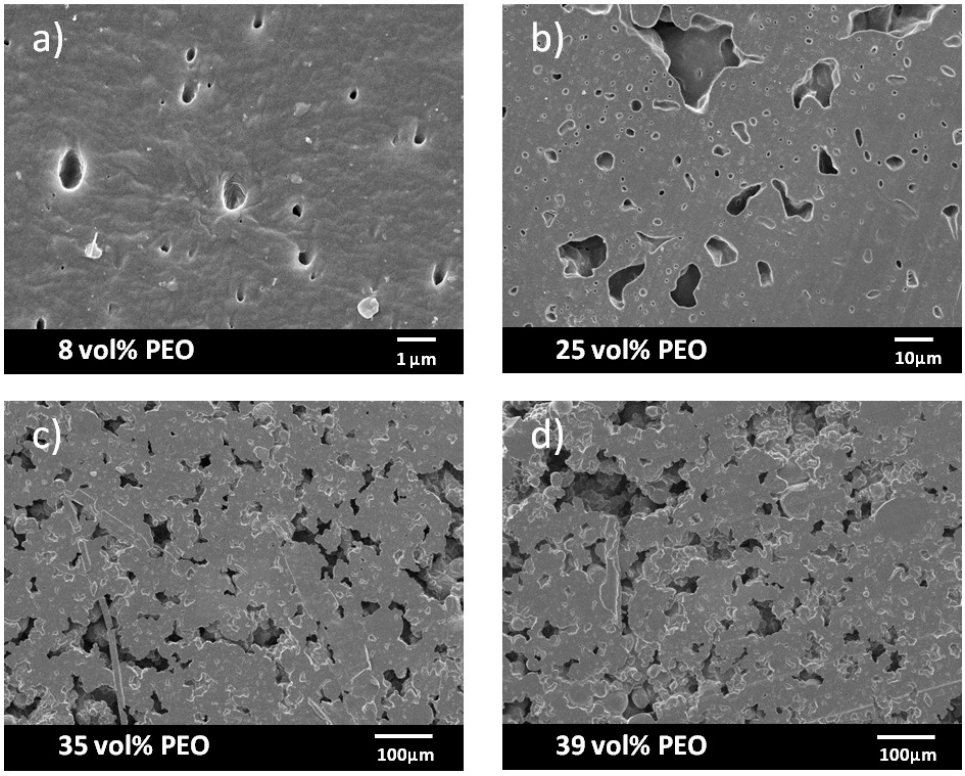

Figure 4.7. SEM micrographs of PE-g-MA / 20K PEO blends following PEO extraction.

Another trend is observed by comparing the data from Table 4.4 and Table 4.5, where it is observed that the ranges of cocontinuity for the reactively compatibilized blends have narrowed relative to their non-compatibilized counterparts. Furthermore, this degree to which the range

narrows appears to be dependent on PEO molecular weight. For example, blends such as n-PP/40K PEO and PP-g-MA-1/40K PEO, which are rheologically equivalent, show no statistically significant difference in cocontinuity range. However, with LDPE/200K PEO and PE-g-MA/200K PEO, another rheologically equivalent pair of blends but with higher overall viscosity and molecular weight, a much narrower range is seen in the reactive blend.

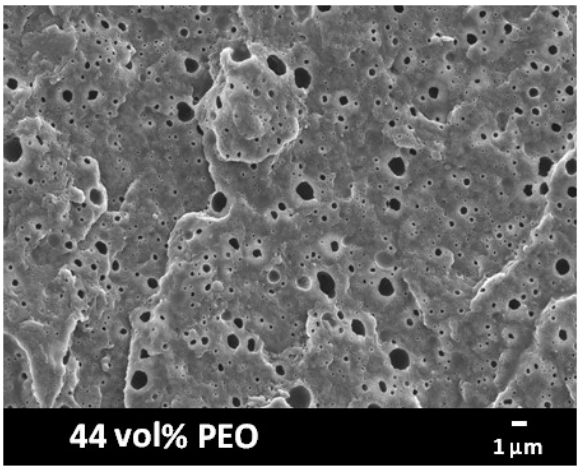

Figure 4.8. SEM micrograph of a PP-g-MA-2 / 20K PEO blend following PEO extraction. All other PP-g-MA-2 / 20K PEO blends with higher PEO content collapsed upon PEO extraction.

Considering the mechanism of fiber breaking, one would anticipate that lower interfacial tension would improve the stability of elongated features in the blend and widen the range of cocontinuity, due to a reduced thermodynamic drive to retract or break apart these features. This could at least partially explain why blends such as PE-g-MA/40K PEO had a wider range than PE-g-MA/60K PEO and PE-g-MA/200K PEO, as interfacial tension measurements from Chapter 2, shown in Figure 2.2, indicate a minimum in interfacial tension for PE-g-MA/40K PEO. However, this is insufficient for explaining why these blends showed a narrower range than non-compatibilized blends, which had much higher interfacial tension overall. In order to justify these results, one needs to consider steric arguments and particle coalescence – a reactively compatibilized blend will contain an interfacial layer of PE-g-PEO or PP-g-PEO graft copolymers. These graft copolymers form an interfacial "brush" which disrupt particle

coalescence and inhibit percolation of a cocontinuous network.[7,32,117,118] This effect is more pronounced with higher molecular weight due to a longer "brush" being formed at the interface, which further explains why PE-g-MA blends with higher PEO molecular weight decrease in cocontinuity range.

This suggests that for a reactively compatibilized blend, the widest cocontinuity range can be achieved with medium molecular weight polymers – high enough to stabilize elongated features through increased viscosity and reduced interfacial tension, but not so high as to inhibit coalescence due to a sterically bulky interfacial brush.

4.3.3 Phase Inversion Predictions for Non-reactive Blends

The ranges of cocontinuity for all non-functional PE/PEO and PP/PEO blends are shown plotted against the PE/PEO or PP/PEO viscosity ratio in Figure 4.9. The phase inversion points for each of these blends, defined as the center of the range of cocontinuity, are shown as open circles at the middle of each range bar. As the viscosity ratio of the blends decreases with increasing PEO viscosity, there is a general tendency for blends to form cocontinuous networks with larger volume fractions of PEO. The ranges of cocontinuity are also shown to depend on the viscosity ratio and the overall viscosity, as described above.

Figure 4.9 also shows the models for phase inversion composition based on the viscosity ratio (Eqs. 4.2-4.5), which aim to predict the center of the range of cocontinuity. The thread breaking model from Metelkin and Blekht [26] (Eqs. 4.3 and 4.4) predicts an even stronger dependence, which serves as evidence that the model as proposed may not be broadly applicable to all blend systems.

However, both the empirical model by Paul and Barlow [109] (Eq. 4.2) and the droplet packing model by Utracki [27] (Eq. 4.5), when using the empirical parameters $[\eta]$=1.9 and ϕ_m=0.84, appears to predict the phase inversion composition reasonably when the viscosity ratio is 0.2 – 2. Using the Utracki model with a hard sphere approximation with $[\eta]$=2.71 and ϕ_m=0.71 more

accurately predicts the phase inversion behavior LDPE/20K PEO, but tends to underestimate the effect of changing viscosity ratio on phase inversion when the viscosity ratio is near one.

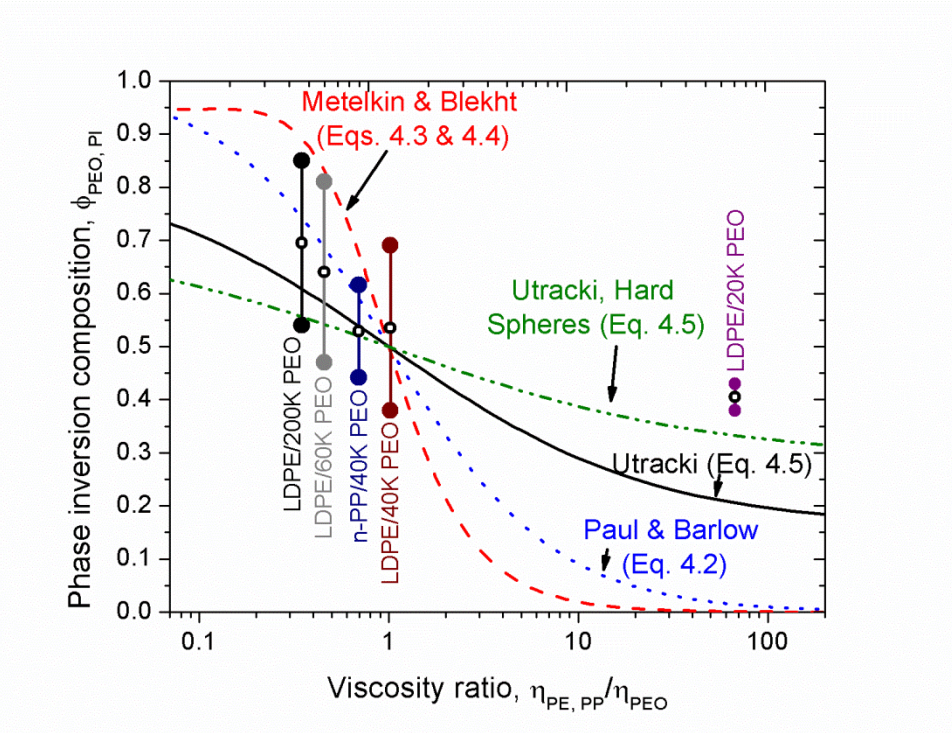

Figure 4.9. Range of cocontinuity for non-reactive LDPE/PEO and n-PP/PEO blends as a function of viscosity ratio. The curves show predictions for the phase inversion composition by on Paul and Barlow in Eq. 4.2, Metelkin and Blekht in Eqs. 4.3 and 4.4, and Utracki in Eq. 4.5 using $[\eta]$=1.9 and ϕ_m=0.84, and Eq. 4.5 assuming hard spheres, using $[\eta]$=2.71 and ϕ_m=0.71. Open circles mark the experimentally measured centers of the ranges of cocontinuity.

The relative success of Eq. 4.5 in predicting phase inversion suggests that the ability to form a percolated network of deformed viscoelastic droplets of one material in a matrix of the other is critical for cocontinuity, and that $[\eta]$ and ϕ_m, the conditions for percolation, are dependent on the viscosity ratio. With a viscosity ratio close to one, droplets can achieve a higher theoretical maximum packing fraction due to droplet deformability away from spherical shapes. In the case of blends containing 20K PEO, when the viscosity ratio is far from one, PE can be treated as a hard sphere inclusion that must approach the maximum packing fraction of hard spheres to percolate.

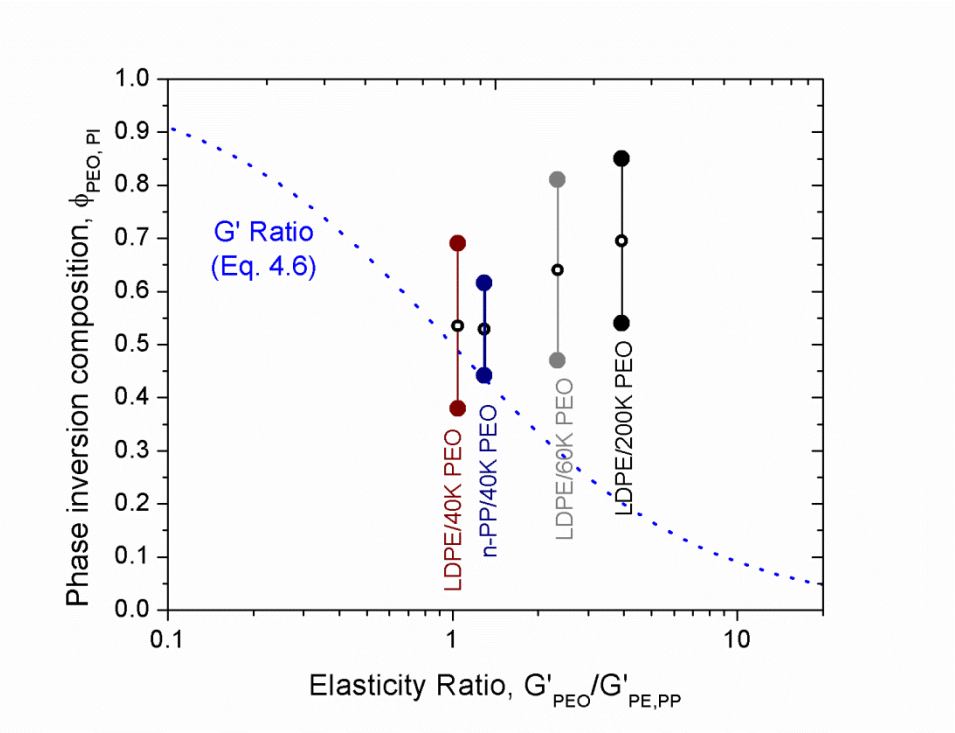

Figure 4.10. Range of cocontinuity for non-reactive LDPE/PEO and n-PP/PEO blends as a function of elasticity ratio. The dotted curve represents the phase inversion prediction based on elasticity ratio, shown in Eq. 4.6. Open circles mark the experimentally measured centers of the ranges of cocontinuity. The LDPE/20K PEO blend is omitted for clarity, as G'_{PEO}/G'_{PE} for this sample was less than 10^{-3}.

Ranges of cocontinuity for the non-reactive blends are shown compared to phase inversion predictions based on the ratio of *G'* (Eq. 4.6) and the ratio of *tan(δ)* (Eq. 4.7) in Figure 4.10 and Figure 4.11, respectively. The phase inversion composition appears to exhibit the inverse of the dependence suggested by these models. This suggests that the concept of the more elastic phase more easily encapsulating the less elastic phase, which the proponents of these models argue, is not the appropriate mechanism for the formation of cocontinuity.

A limitation to both of the elastic models, along with those from Paul and Barlow [109] (Eq.4.2) and Metelkin and Blekht [26] (Eqs. 4.3 and 4.4), is the lack of accounting for very dissimilar materials. None of these models could account for the high viscosity ratio present in LDPE/20K PEO, with the Utracki [27] model coming closest when making a hard sphere

assumption.

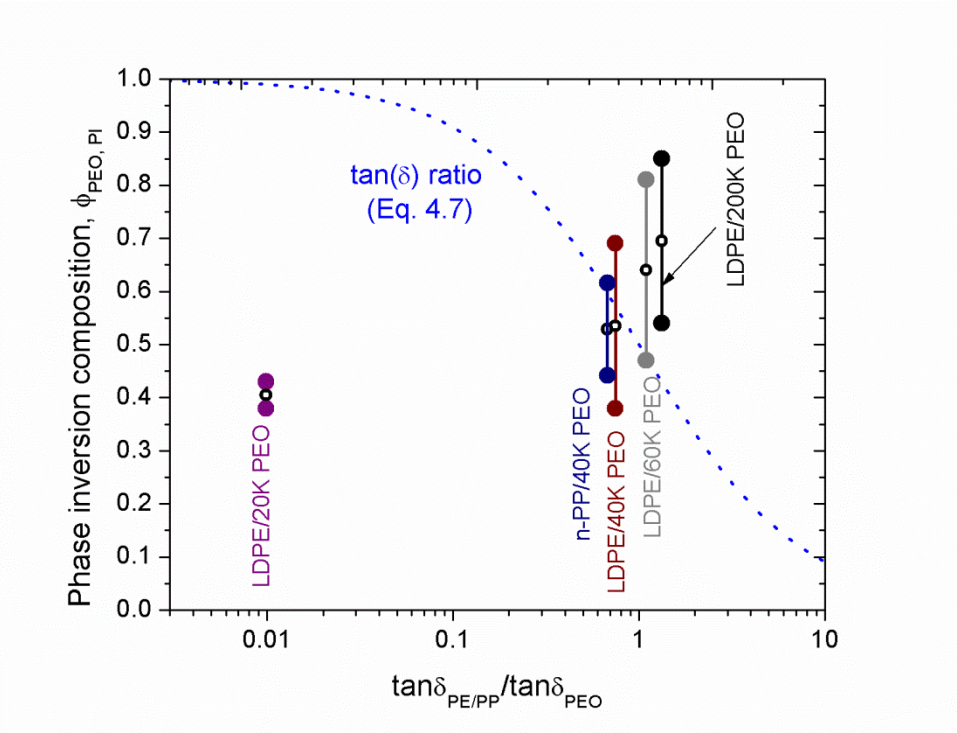

Figure 4.11. Range of cocontinuity for non-reactive LDPE/PEO and n-PP/PEO blends as a function of *tan(δ)* ratio. The dotted curve represents the phase inversion prediction based on *tan(δ)* ratio, shown in Eq. 4.7. Open circles mark the experimentally measured centers of the ranges of cocontinuity.

4.3.4 Phase Inversion Predictions for Reactive Blends

The ranges of cocontinuity for all reactive PE/PEO and PP/PEO blends are shown plotted against the viscosity ratio in Figure 4.12. A similar trend to the non-reactive blends is observed here where a decreasing viscosity ratio resulted generally in a higher volume fraction of PEO that could result in cocontinuity.

Similar to the results for the non-reactive blends, the Utracki model [27] (Eq. 4.5) best predicts the phase inversion behavior of the reactive blends. As the viscosity ratio deviates from 1, then the hard sphere Utracki model starts to perform better, although still with the similar deviations as was seen with LDPE/20K PEO. Both the models by Paul and Barlow [109] (Eq.4.2) and Metelkin and Blekht [26] (Eqs. 4.3 and 4.4) predict too strong of a dependence of the phase

inversion composition on viscosity ratio.

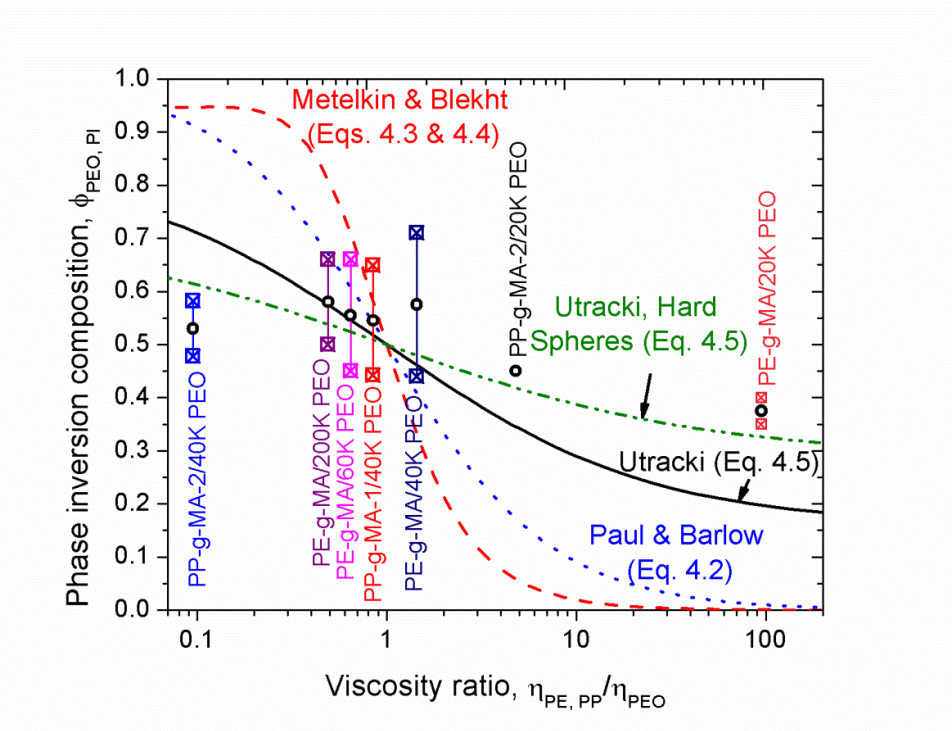

Figure 4.12. Range of cocontinuity for reactive PE-g-MA/PEO, PP-g-MA-1/PEO, and PP-g-MA-2/PEO blends as a function of viscosity ratio. The curves show predictions for the phase inversion composition by Paul and Barlow in Eq. 4.2, Metelkin and Blekht in Eqs. 4.3 and 4.4, and Utracki in Eq. 4.5 using $[\eta]$=1.9 and ϕ_m=0.84, and Eq. 4.5 assuming hard spheres, using $[\eta]$=2.71 and ϕ_m=0.71. Open circles mark the centers of the ranges of cocontinuity.

It should be noted, however, that despite some success with the Utracki model, it is still based on percolation of deformable droplets by droplet packing arguments only. It does not account for the nature of the interface of those droplets, which has been shown to disrupt coalescence and percolation. A further observation that is particularly highlighted by Figure 4.12 is that as the viscosity ratio decreases with increasing PEO viscosity relative to PE or PP, the upper limit of the range of cocontinuity actually decreases. This stands in contrast to the non-reactive results where the upper limit increased with higher molecular weight PEO.

This decrease in the maximum cocontinuous composition is easily explained by the steric arguments put forth in Section 4.3.2. However, it merits further discussion here due to relation to

the phase inversion point. If one considers a blend with a highly asymmetric interfacial copolymer, the copolymer density is expected to be limited by the maximum achievable density of the higher molecular weight end of the copolymer. This results in an interface with a difference in fractional interfacial coverage dependent on the side of the interface. A high molecular weight end may fully coat an interface, but this will prevent the lower molecular weight end from achieving the same. This was evident from the fractional interfacial coverage results in Figure 2.9, where 20K PEO could not saturate the interface with PE-g-MA.

These asymmetries will affect cocontinuity and percolation differently depending on which material is determined to form the major phase of the blend. If for example the high molecular weight material is the major phase, the dispersed phase will have a dense, high molecular weight brush on the outside of the droplets, which would strongly inhibit percolation. However, in the reverse case with the high molecular weight material as the dispersed phase, the outside interfacial brush will be short and not completely cover the surface, providing relatively less steric hindrance to percolation. This may result in an asymmetric narrowing of the cocontinuity range. This directly challenges the commonly accepted concept of defining the experimentally measured phase inversion composition as the center of the cocontinuity range. Rather, for compatibilized blends, the point of the phase inversion along the range of cocontinuity may be dependent on the relative interfacial coverage on both sides of the interface. However, since the phase inversion predictions do not account for the possibility of interfacial modification, model predictions are still insufficient for truly describing reactive blends.

Figure 4.13 and Figure 4.14 show the phase inversion predictions for the reactive blends based on the ratio of G' (Eq. 4.6) and $\tan(\delta)$ (Eq. 4.7), respectively. Consistent with the non-reactive results, both the ratios of G' and $\tan(\delta)$ fail to predict cocontinuity in any material system, instead predicting an inverted trend of the experimental observations.

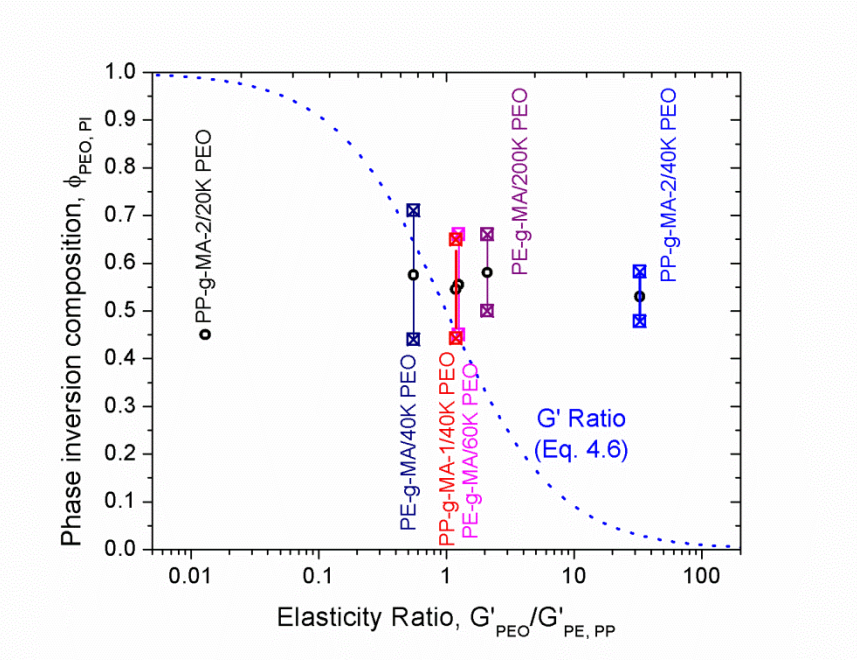

Figure 4.13. Range of cocontinuity for reactive blends as a function of elasticity ratio. The dotted curve represents the phase inversion prediction shown in Eq. 4.6. The PE-g-MA/20K PEO blend is omitted for clarity, as G'_{PEO}/G'_{PE} for this sample was less than 10^{-3}.

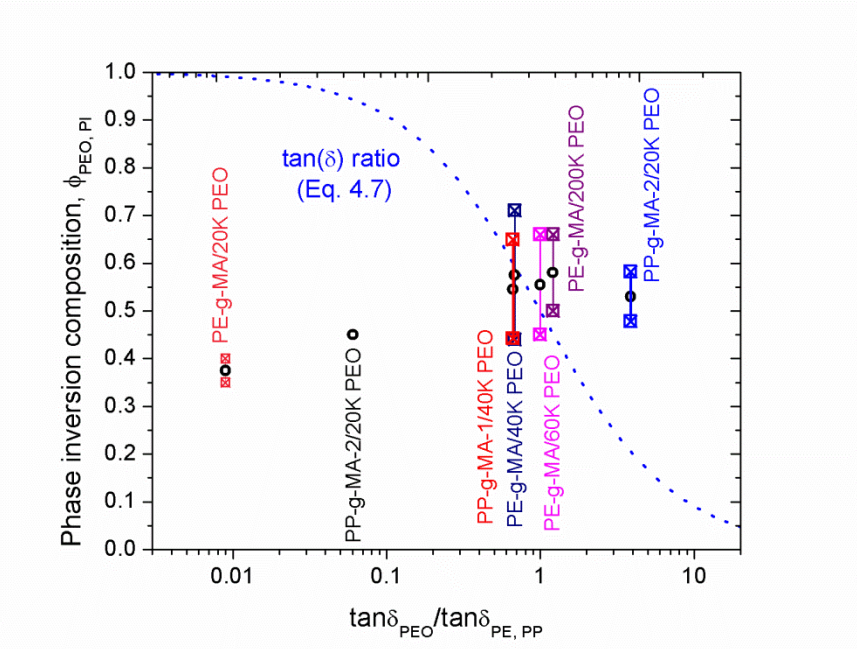

Figure 4.14. Range of cocontinuity for reactive blends as a function of *tan(δ)* ratio. The dotted curve represents the phase inversion prediction based on *tan(δ)* ratio, shown in Eq. 4.7.

4.4 Conclusions

From the study on the cocontinuous compositions of the various PE/PEO and PP/PEO blends, a number of "rules of thumb" were deduced in order to facilitate a better discussion and expectations within the literature of immiscible polymer blends. These rules of thumb were based upon a single, unified theme: that cocontinuity is promoted by the formation of elongated features which also must percolate into a continuous network.

First, as observed in both the non-reactive and reactive blend systems, higher viscosity materials are necessary for the stability of a cocontinuous morphology. Blends from lower viscosity materials tended to result in narrower ranges of cocontinuity, and in some cases were incapable of forming cocontinuity at all.

Second, if the viscosity ratio between the blended materials is far from one, the range of cocontinuous compositions will be narrower than with materials that are well matched. This is a result of poor stress transfer from the lower viscosity phase to the higher viscosity phase, particularly when the high viscosity phase is the minor phase. The lack of sufficient stress transfer results in irregular and poorly mixed morphologies that do not form the elongated structures that promote cocontinuity formation.

The third and fourth rules of thumb are more specific to reactive blends, and are difficult to interpret independently. The third rule states that lower interfacial tension will stabilize elongated features, so reactive blending should improve cocontinuity. However, a fourth rule complicates this prediction, as the copolymer "brush" at the blend interface inhibits coalescence, such that a percolated network is more difficult to form. Considered together with the interfacial tension results of Chapter 2, a medium molecular weight of interfacial copolymers appears to provide the widest range of cocontinuity for reactive polymers. Polymers tuned to the appropriate molecular weight will minimize interfacial tension, but provide too much steric bulkiness so as to prevent coalescence. Lower molecular weight copolymers would also sufficiently reduce interfacial

tension and provide little steric hindrance to percolation, but, when considered together with the first rule of thumb, will not provide the sufficiently high viscosity necessary to form cocontinuity in the first place.

The resulting phase inversion composition was best predicted when applying more realistic constraints, as outlined in the droplet packing model by Utracki.[27] Other models based on viscosity ratio were less successful at the predicting phase inversion composition. Models based on elasticity tended to predict an opposite trend in phase inversion to what was observed. At viscosity ratios near one, an empirical prediction of $[\eta]$ and ϕ_m for viscous droplets provided the best prediction of phase inversion. In the limiting cases of viscosity ratios far from one, the system was best modeled using the new modified version of the droplet packing model, using $[\eta]$ and ϕ_m of hard spheres. This suggests the consideration of a new model based on the existing droplet packing models but treating $[\eta]$ and ϕ_m as functions of the viscosity ratio.

These models are still imperfect predictors of cocontinuity, particularly at very high viscosity ratios or in blends with interfacial compatibilizers. Particularly challenging is the case of reactive blends with an asymmetric interfacial copolymer. In these cases, graft density is limited by the higher molecular weight reactive polymer. When the higher molecular weight side of the copolymer is in the major phase, droplets of the minor phase will be greatly restricted from coalescing. However, in the opposite case where the low molecular weight side is the major phase, a shorter brush will be on the outside of the droplets, and coalescence will be less inhibited. This would result in a range of cocontinuity which would be broader on one side of the phase inversion composition and narrower on the other, giving the appearance of a shifted phase inversion point. This observation challenges the validity of the commonly accepted notion that the phase inversion point coincides with the center the range of cocontinuity, particularly in compatibilized blends.

Despite these difficulties, the trends observed using these two forms of the droplet packing

model are still useful for roughly predicting the morphology *a priori*. Combined with the "rules of thumb" for the range of cocontinuity given above, one can approach blending of immiscible polymers with a better expectation of which compositions will result in cocontinuity.

Chapter 5: Effect of Extensional Viscosity on Cocontinuity of PE/PLA Blends

5.1 Introduction

Melt blending of immiscible polymers is a simple and straightforward method to create new materials with superior properties, such as improved mechanic toughness, ease of processing, tunable wettability, and reduced cost.[49-51] Blended polymers can adopt a variety of morphologies such as droplets, fibers, lamellae, and cocontinuous blends, based on the processing conditions, residence time, composition, rheological properties, and interfacial properties between the blend components.[1-4,21-23]

Of these possible morphologies, cocontinuous blends are of particular interest as both phases are continuously connected throughout the structure. Due to their microstructure, these blends lend themselves to a variety of applications, such as razor blade lubricating strips [9], mechanically robust conductive polymer blends,[10,11] and porous polymers if one continuous phase is extracted or etched by a solvent.[4,8,12-15] These blends are thermodynamically unstable and will coarsen during annealing,[12,19,34] and so they are frequently compatibilized with block copolymers which act as surfactants at the polymer-polymer interface and can be added either as pre-made [7,35-37] or made *in situ* via reactive blending.[13,38,40-42,119]

The available literature on immiscible polymer blends has explored predictions of cocontinuity and phase inversion, which were reviewed and compared in Chapter 4. These models have been limited only to predictions based on shear rheological properties. However, it is well known that melt processing flows in a device like a twin-screw extruder are complex and cannot be modeled as simple shear flow. Extensional flows factor heavily in real mixing processes and the extensional rheological properties of a material can deviate dramatically from their shear flow counterparts. This is especially true in the case of polymers with long-chain

branching (LCB) which, when subjected to extensional flows, show significant strain hardening (often related to the concept of melt strength), increasing the extensional viscosity, denoted here as η_u, well above that predicted by Trouton's ratio where $\eta_u = 3\eta$.[120-127]

When compared to linear polymers, branched polymers also tend to demonstrate other superior processing properties such as higher zero-shear viscosity with stronger shear thinning,[122,128-130] reduced wall slip in extrusion,[131,132] and resistance to necking in extensional processes like fiber or sheet formation.[125,133] While many industrial applications already take advantage of these superior processing properties of branched polymers, the influence LCB has on polymer blend morphology, and particularly how it relates to blend cocontinuity, has not been previously explored.

In order to explore the role of extensional viscosity on the mechanism and ability to form cocontinuous structures, the present study investigates the effect of increased extensional viscosity and strain hardening due to LCB on the range of compositions that can generate a cocontinuous microstructure, as well as the characteristic size and stability of the microstructure. Blends were prepared from linear and branched versions of polyethylene (PE) and polylactic acid (PLA). Effort was made to select materials for which LCB would modify the extensional viscosity but only minimally influence the shear rheological behavior at shear rates typically observed in melt processing flows (>10 s^{-1}). Materials were characterized rheologically in shear using small amplitude oscillatory shear and capillary rheometry. Extensional flow properties were characterized using counter-rotating drums [134] and Cogswell's analysis of entrance pressure drop from capillary rheometry.[63,135,136] Blend morphology was analyzed gravimetrically via solvent extraction of the PLA phase, and imaged by scanning electron microscopy (SEM) and laser scanning confocal microscopy (LSCM), the latter of which was used to generate 3D reconstructions of the cocontinuous microstructure for use in characteristic size analysis. The dependence of blend stability on long chain branching was investigated by using LSCM to

measure characteristic size as a function of quiescent annealing time.

5.2 Methods

5.2.1 Materials

For the present study, two polyethylene (PE) resins supplied by the Dow Chemical Company were used: linear high-density polyethylene (HDPE, Dow 4452N), and branched low-density polyethylene (LDPE, Dow 9955i). Two polylactic acid (PLA) resins were used: a linear PLA (L-PLA, Natureworks Materials 2003D), and a branched PLA (B-PLA) derived from the supplied linear PLA with long-chain branching added by free radical chemistry, performed by Interfacial Solutions, LLC (IP 1406-1).[137]

The relevant material properties are shown in Table 5.1. Melting temperature, T_m, was measured by dynamic scanning calorimetry (DSC, TA Instruments Q1000). Molecular weight of the PE materials was obtained by the method described in Chapter 2. Molecular weight of PLA samples were measured using a room temperature GPC (SpectraSYSTEM AS 1000, Thermo Separation Products) using tetrahydrofuran as the eluent and compared to polystyrene standards. Density values were provided by the material suppliers.

Table 5.1. Melting temperature, molecular weight, and density for PE and PLA materials.

	Material	T_m (°C)	M_n (kg/mol)	M_w (kg/mol)	ρ (g/cm^3) @ 23 °C
PE	**LDPE**	105	12	59	0.92
	HDPE	120	18	90	0.954
PLA	**L-PLA**	165	140	230	1.24
	B-PLA	165	130	330	1.18

A third PLA sample (henceforth referred to as "Mixed PLA") was produced with an intermediate amount of LCB by blending together linear and branched PLA at 75/25 wt% L-PLA/B-PLA, using a lab-scale 16-mm co-rotating twin screw extruder (PRISM Model CS/16-V2)

at 180 °C. L-PLA and B-PLA were fed into the extruder at a rate of 500g/hr, with a screw speed of 50 RPM. The product was extruded from a circular die, cooled in a recirculating water trough, and pelletized.

Due to moisture sensitivity, all PLA materials were stored long-term by vacuum sealing the materials into glass containers. Prior to experimental use, the necessary amount of PLA was removed from long-term storage and dried in a vacuum oven at 80 °C overnight. All PE materials were stored at room temperature in sealed containers.

For 3D imaging of the blends in confocal laser scanning microscopy (LSCM), 2-hydroxyethyl(methacrylate) (HEMA), azobisisobutyronitrile (AIBN), and Rhodamine B fluorescent dye were purchased from Aldrich and used as received.

5.2.2 Small Amplitude Oscillatory Shear (SAOS)

The linear viscoelastic properties under shear flow of all pure materials were measured via SAOS on an ARES rheometer. Measurements were conducted at 180 °C, using 25-mm parallel plates. Pellets of the pure materials were loaded onto the plates and pressed into the desired shape using a melt ring around the plates and a fixed axial load of 500 g of force. Strain sweep tests were conducted on all materials at a frequency of 1 rad/s to determine the critical strain at which materials exhibited non-linear behavior. Frequency sweeps over a range of 100 – 0.01 rad/s were then conducted for each material, using strains below the measured critical strain.

5.2.3 Capillary Rheometry

All materials were measured via capillary rheometry using a 15-mm diameter twin-bore capillary rheometer (Rosand RH-7, Malvern Instruments) in order to characterize the shear and extensional rheological properties at higher deformation rates. Pressure drop as a function of piston speed was measured independently in both barrels. In one barrel, pressure drop was measured across a capillary die with 16 mm length, 1 mm diameter, and 180° entrance angle, using a 10,000 psi pressure transducer. In the other barrel, the same material was run and

pressure drop was measured across a 0.25 mm length, 1 mm diameter, and 180° entrance angle capillary die, using a 1,500 psi pressure transducer. Entrance pressure and capillary pressure were calculated using the Rosand Flowmaster software package, which constructed a Bagley plot [138] of pressure drop as a function of die length, treating the 0.25 mm length die as an effective zero-length die. The true shear rate in the die was calculated by applying the Rabinowitsch correction to account for non-Newtonian flow behavior of the material, and the shear viscosity was calculated from the capillary pressure drop. The extensional viscosity and an estimated extensional rate were calculated based on the entrance pressure drop, following Cogswell's analysis.[63,135,136]

5.2.4 Extensional Viscosity

Extensional viscosity of the PLA materials was measured on an ARES-G2 rheometer (TA Instruments) using the extensional viscosity fixture (EVF), based on the counter-rotating barrel design by Meissner.[134] Rectangular samples with dimensions 25x5x1 cm were prepared in advance using a compression press (Carver, Inc., Wabash, Indiana) at 180 °C and 2 tons of force. Materials were tested by clipping a rectangular bar onto the two posts of the fixture, then closing the oven to heat the sample to 180 °C. The sample was briefly annealed at 180 °C for 20 seconds to allow the temperature to equilibrate. Following annealing, a pre-stretch was applied to a Hencky strain of 0.035 at a strain rate of 0.01 s^{-1} to ensure that the sample was adhered tightly to the posts prior to extension. Any residual stress from the pre-stretch was allowed to relax by annealing for another 20 seconds. The sample was then stretched at strain rates between 0.1 and 10 s^{-1} to a total Hencky strain of 5. Due to the design of the fixture, the material began to overlap at a Hencky strain of around 3, and so extensional viscosity data at a total strain between 0 and 3 was reported.

To compare the extensional response to the linear viscoelastic limit, the pure materials were also tested in start-up of steady shear at a shear rate of 0.1 s^{-1} for all materials except B-

PLA, which was measured at 0.01 s^{-1} instead due to excessive torque on the rheometer at higher rates, on an ARES rheometer (TA Instruments), using a 25 mm cone and plate with an angle of 0.1. The measured shear viscosity from these tests was multiplied by 3, based on Trouton's ratio of $\eta_u = 3\eta$ for Newtonian fluids, to predict the linear viscoelastic limit of the materials under extensional flow.

The extensional viscosity of the PE materials was not measured in this way due to their lower melting point and zero-shear viscosity, which resulted in sagging during the pre-stretch annealing. This compromised the accuracy of these results, and so extensional viscosity of the PE materials will only be reported as measured by entrance pressure drop in capillary rheometry.

5.2.5 Blending Experiments

Blends of PE and PLA were prepared using a recirculating, conical twin-screw batch microcompounder (DACA Instruments) with a mixing volume of 5 cm^3. All blends were prepared at 180 °C with a rotation speed of 200 RPM, which correlated to a shear rate of approximately 400 s^{-1}.[64] After 6 minutes of mixing, the recirculation channel was opened to extrude the product from a circular die. This was immediately quenched in liquid nitrogen to freeze the morphology. Blends were produced across compositions ranging from 10/90 wt% PE/PLA to 90/10 wt% PE/PLA.

5.2.6 Determination of Cocontinuity

The extruded blend products were soaked in chloroform for 48 hours in order to dissolve all continuously connected regions of PLA that contacted the outside surface of the extrudate. The degree of PLA continuity, Φ_{PLA}, a measure of the fraction of PLA in the blend that is continuously connected, was measured gravimetrically:[4]

$$\Phi_{PLA} = \frac{m_i - m_f}{m_{PLA,i}} \tag{5.1}$$

where m_i is the initial mass of the blend, m_f is the final mass following extraction in chloroform, and $m_{PLA,i}$ is the initial mass of the PLA in the blend. A degree of PLA continuity of 1 was indicative of a completely continuous PLA phase, whereas a degree of continuity approaching zero was indicative of a PLA phase composed of dispersed droplets. For the purposes of this study, $\Phi_{PLA} \geq 0.9$ was treated as a fully continuous PLA phase. Polyethylene continuity was determined by the ability of the blend to remain self-supporting after PLA extraction. A blend that collapsed following the chloroform wash indicated a discontinuous PE phase. Therefore, a cocontinuous blend was defined as one with $\Phi_{PLA} \geq 0.9$ which remained self-supporting following the chloroform wash. The range of cocontinuity of a material system was defined as the range of compositions that displayed these properties.

5.2.7 Coarsening

In order to determine blend stability, cocontinuous blends from each material system were annealed at 180 °C on a compression press (Carver, Inc., Wabash, Indiana) with no applied pressure. Samples were annealed for between 1 and 30 minutes. Upon completion of annealing, the samples were immediately transferred to a separate chilled compression press for rapid cooling to freeze the final morphology.

5.2.8 Scanning Electron Microscopy

Cross-sections normal to the machine direction of the blends were imaged by scanning electron microscopy (SEM, JEOL 6500). Prior to imaging, smooth cross-sections of the blends were prepared by cryo-microtome (Reichert UltraCut S Ultramicrotome) at -140 °C using a diamond knife. Blends were then soaked in chloroform for 48 hours to extract the PLA from the surface of the blend, leaving behind a PE matrix. Each PE matrix was dried in a vacuum oven overnight and then sputter coated with 50 Å of platinum to create a conductive surface, and then was imaged at an accelerating voltage of 5 kV and a working distance of 10 mm.

5.2.9 Laser Scanning Confocal Microscopy

For the purposes of characteristic size analysis, cocontinuous blends were imaged in 3D using laser scanning confocal microscopy (LSCM, Olympus Fluo View 1000). In order to image blends by LSCM, they need to be optically transparent to allow the laser to penetrate to the interior of the sample and have fluorescent contrast between the phases. The PE/PLA blends were not optically transparent, due to a difference between the refractive index of each component, and were not fluorescent. In order to generate optically clear samples, thin slices (~100 μm thick) were prepared with a razor blade and then soaked in chloroform overnight to extract the continuous PLA. The slices were placed between a glass slide and coverslip, and this space was filled by pipette with 2-hydroxyethyl(methacrylate) (HEMA) containing 0.01wt% Rhodamine B fluorescent dye and 1 wt% azobisisobutyronitrile (AIBN) radical initiator, allowing the HEMA to fill the pores of the PE slice. The slides were then placed in an oven at 80 °C for 10-15 minutes, until the refractive index of the polymerized HEMA matched that of PE and the sample appeared optically transparent, with the fluorescent HEMA replacing the extracted PLA phase in the imaging. It should be noted that due to the requirement of PLA extraction prior to imaging, this technique could only be used for cocontinuous samples and not for blends consisting of dispersed droplets.

A series of 2D images were taken at different focal depths through the sample, and an iterative thresholding method developed in MATLAB was used to binarize the images, with black representing the non-fluorescent PE and white the fluorescent HEMA (indicative of the continuous PLA domains). Using Avizo (v. 6.3, http://www.vsg3d.com/avizo), these binarized images were then reconstructed into a stack of images, which generated a 3D reconstruction of the structure. A triangular mesh was applied along the PE-HEMA interface using a marching cubes algorithm included in the Avizo software package. From these 3D images, a characteristic size of the blends could be calculated:[66]

$$a = V \Big/ \sum_{i=1}^{N} A_i \tag{5.2}$$

where a is the characteristic pore size of the cocontinuous blend, V is the total volume of the analyzed sample, and A_i is the area of a single triangle of the interfacial triangular mesh.

5.3 Experimental Results

5.3.1 Rheology

Figure 5.1 shows the results of shear viscosity collected by both SAOS and capillary rheometry. Data points with closed symbols show the complex viscosity versus the oscillatory frequency from a frequency range of 0.01 – 100 s^{-1} collected from SAOS. Data points with open symbols show the shear viscosity versus the Rabinowitsch-corrected shear rate as collected by capillary rheometry. The overlapping data from SAOS and capillary rheometry in the range of 10-100 s^{-1} suggest that the two methods are in agreement, and that the Cox-Merz rule, which equates the frequency dependent complex viscosity to the shear rate dependent viscosity when $\omega = \dot{\gamma}$, was applicable for all pure materials.[63] The solid lines show the Cross model fit to the combined data for each material, given by Eq. 3.1 from Chapter 3. The Cross model coefficients are shown in Table 5.2.

Table 5.2. Cross model parameters for PE and PLA materials at 180 °C.

	Material	**η_o (Pa s)**	**n**	**K (s)**
PE	HDPE	2610	0.244	0.0204
	LDPE	6300	0.387	0.560
PLA	L-PLA	6620	0.189	0.0369
	B-PLA	1.43×10^5	0.370	15.24
	"Mixed PLA" 75/25 wt% L/B PLA	1.07×10^4	0.283	0.136

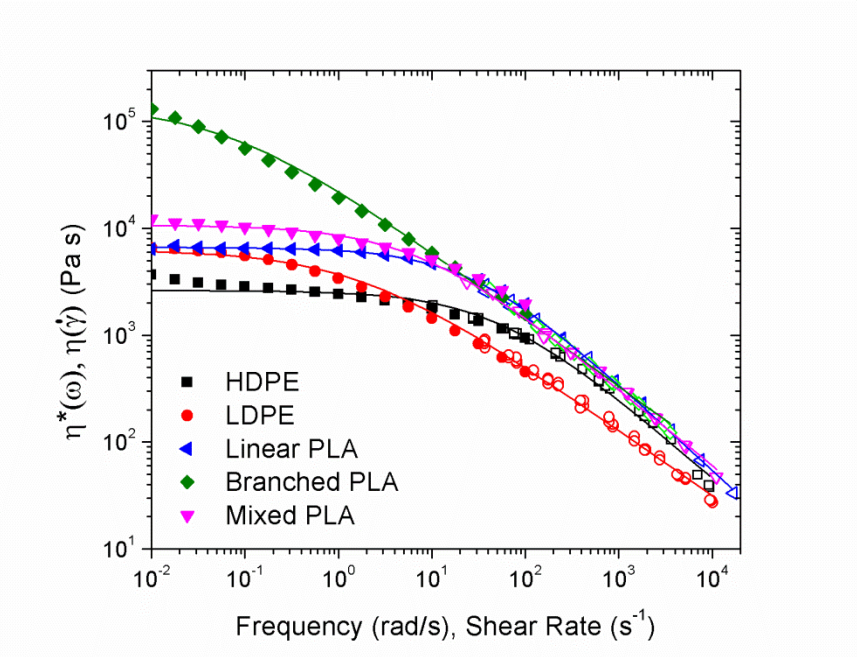

Figure 5.1. Shear viscosity of PE and PLA materials at 180 °C. Closed symbols from shear rates 0.01 – 100 s^{-1} are complex viscosity $\eta^*(\omega)$ collected by parallel plate SAOS rheology. Open symbols for shear rates greater than 10 s^{-1} are $\eta(\dot{\gamma})$ collected by capillary rheometry. Lines show Cross model fits from Eq. 3.1, using the fitting parameters shown in Table 5.2.

Table 5.3. Shear rheological parameters used for phase inversion predictions for the studied blend systems at 180 °C. Phase inversion predictions are shown in Eqs. 4.1 – 4.7.

	Material	**η(400 s^{-1}) (Pa s) †**	***G'*(400 rad/s) (Pa) ‡**	**tan(δ) (400 rad/s) (Pa) ‡**
PE	HDPE	444	1.39 x 10^5	1.01
	LDPE	220	6.39 x 10^4	0.728
PLA	L-PLA	671	2.89 x 10^5	0.598
	B-PLA	575	2.71 x 10^5	0.531
	Mixed PLA	589	3.25 x 10^5	0.525

† Measured via oscillatory and capillary shear rheometry.
‡ Measured via oscillatory shear rheometry. Values at 180 °C and 400 rad/s were collected by time-temperature superposition of viscoelastic data at lower temperatures.

The shear viscosity at 400 s^{-1}, the estimated shear rate of mixing at 200 RPM in the DACA microcompounder,[64] elastic storage modulus *G'* at 400 rad/s, and *tan(δ)* at 400 rad/s, are

shown on Table 5.3. These values were used for the phase inversion predictions shown in Eqs. 4.1 – 4.7 from Chapter 4.

Figure 5.2 shows the extensional viscosity of each pure material used in blending, as measured by capillary rheometry and estimated using Cogswell's analysis. The strain hardening factor, X_e, a measure of the degree of strain hardening the material undergoes during extensional deformation, is given by:[120]

$$X_e \left(\quad \right) \quad \text{when} \quad \quad (5.3)$$

The case were X_e is one represents the Newtonian case. The results of X_e as measured by capillary rheometry are given in Figure 5.3.

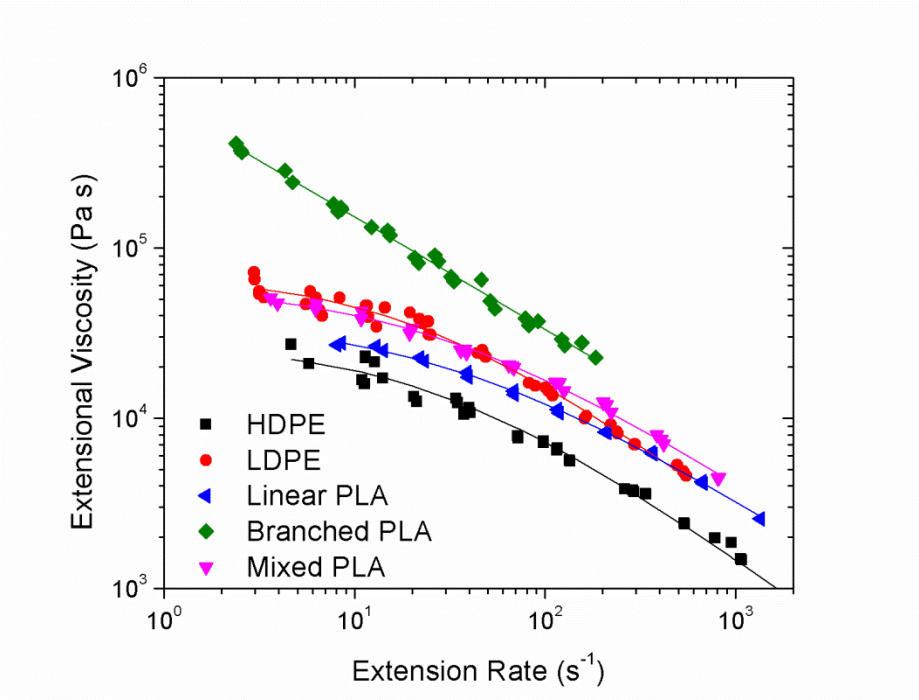

Figure 5.2. Extensional viscosity of pure materials, as measured by Cogswell's analysis for entrance pressure drop in capillary rheometry. The lines are to guide the eye.

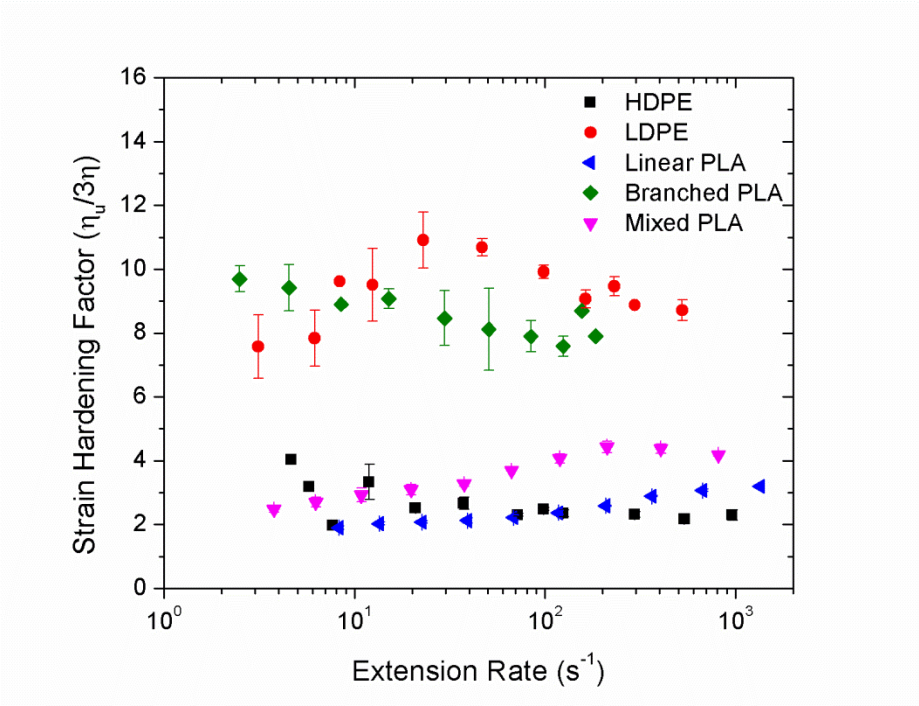

Figure 5.3. Strain hardening factor, defined as the ratio of the extensional viscosity to 3 times the shear viscosity (Trouton's ratio), as predicted by capillary rheometry.

From Figure 5.1 through Figure 5.3, a number of conclusions can be drawn concerning the various materials studied. First, from Figure 5.1, the presence of long-chain branching in the mixed and branched PLA shows a strong influence on the shear rheology of the material, but only in the long time regime at shear rates less than 10 s^{-1}. A higher degree of branching in the PLA was observed to increase the zero-shear viscosity and the time constant K, so that materials with a higher degree of branching showed an onset of shear thinning behavior at lower shear rates. However, at shear rates greater than 10 s^{-1}, the shear viscosity of the studied PLA materials were nearly indistinguishable, suggesting that at higher shear rate mixing such as that used in the blending conditions for the present study, long chain branching does not significantly influence the shear flow behavior. This behavior is consistent with results reported previously [122,123,129]. The shear viscosity of the PE materials follows a similar trend. Between HDPE and LDPE, the shear viscosity at high shear rates does not match as consistently as was observed among the PLA

materials, but the branched LDPE does show a higher zero-shear viscosity, while the viscosity at shear rates greater than 10 s^{-1} is lower than that of HDPE. However, this discrepancy may arise due to the fact that all PLA materials studied here were derived from the same base material (L-PLA), which was not the case for the studied PE. To emphasize the most critical observation, when processing these materials (particularly the PLA) under conditions of shear rate greater than 10 s^{-1}, the shear rheological response of these materials is nearly identical, and so rheological differences observed during the blending process must be attributed to differences in extensional viscosity.

From Figure 5.3, it is observed that B-PLA and LDPE showed the strongest strain hardening response at all rates, with strain hardening factors around 9 times that predicted by the Trouton ratio. Mixed PLA showed slight strain hardening behavior compared to the linear polymers. This strain hardening behavior is roughly independent of extension rate (within experimental error), such that the branched materials show higher extensional viscosity than their linear counterparts at all rates. This suggests that LCB, while only influencing shear viscosity at low rates, increases the extensional viscosity at all measured rates due to strong chain entanglement in extensional flow, and that a higher degree of branching amplified this effect.

Figure 5.4 shows the transient extensional viscosity of the PLA materials at extension rates between 0.1 and 10 s^{-1}, as measured by EVF. As mentioned in the experimental methods, EVF results for PE materials are not reported here, due to their tendency to sag when attached to the fixture. The figure also shows the linear viscoelastic limit of the transient response of each material under extension, given as 3 times the time-dependent shear viscosity, as measured by start-up of steady shear experiments.

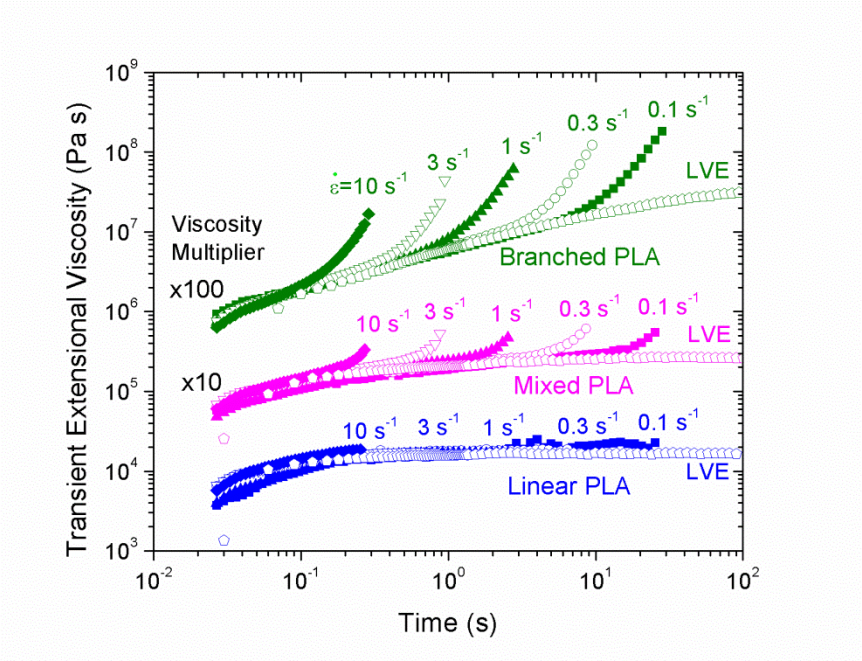

Figure 5.4. Transient extensional viscosity of PLA, as measure by EVF. The LVE limit reported is measured by three times the startup of steady shear using 25-mm cone and plate. The data have been vertically offset by the reported viscosity multipliers for clarity.

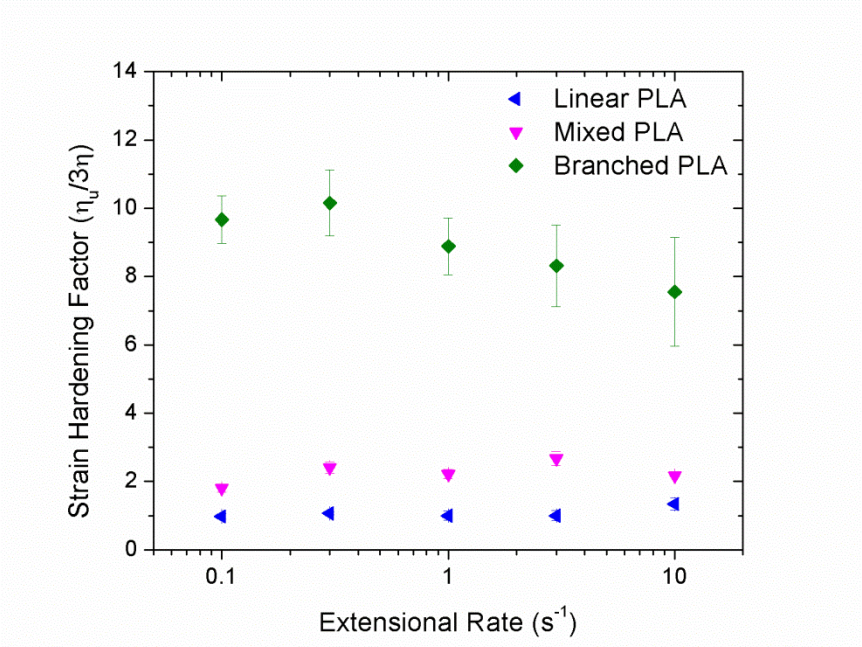

Figure 5.5. Strain hardening factor for PLA materials as measured by EVF, with extensional viscosity evaluated at a Hencky strain of 2.7, and steady state shear viscosity evaluated from SAOS measurements.

Figure 5.5 shows the strain hardening factor X_e from Eq. 5.3, and is analogous to Figure 5.3. However, since measurements of extensional viscosity by EVF are transient and, for the strain hardening materials, did not reach a steady state extensional viscosity before sample overlap or breakage, $\eta_u(\dot{\varepsilon}$ was evaluated at a Hencky strain of 2.7 and $\eta(\dot{\gamma}$ was evaluated from the complex shear viscosity as determined by SAOS measurements (again, applying the Cox-Merz rule).

These results confirm the observations from Figure 5.2 and Figure 5.3 that the branched materials, including the Mixed PLA, show strain hardening, with more dramatic strain hardening observed with a higher degree of LCB. According to EVF measurements, L-PLA showed no strain hardening behavior, which contrasts with observations from capillary rheometry where L-PLA was reported to have a strain hardening factor of 2. However, strain hardening factor results for B-PLA appear consistent between the EVF and capillary tests. Discrepancies observed can be attributed to the different nature of the experiments – capillary rheometry is an indirect measure of extensional viscosity, calculated by the steady-state pressure drop due to entrance flow into an orifice, while EVF is a transient and direct measurement of η_u by uniaxial extension. However, the consistency of X_e for B-PLA when measured both by EVF and capillary rheometry suggests that extensional viscosity calculated by Cogswell's analysis relates to a Hencky strain of approximately 2.7. This observation is consistent with previous results by Padmanabhan.[139]

5.3.2 Range of Cocontinuity

Figure 5.6 shows the degree of PLA continuity, as calculated by Eq. 5.1, as a function of PLA volume fraction for each blend system. The symbols give the measure of PLA continuity, while the ranges shown at the bottom of the figure indicate all compositions that met the criteria of cocontinuity, $\Phi_{PLA} \geq 0.9$ and a self supporting PE phase following extraction in chloroform, for each material system.

The filled black circles along the ranges show the predicted phase inversion point, which is expected to coincide with the center of the range of cocontinuity. It is given by the following model by Utracki, derived from the packing of viscoelastic spheres to create a continuous network:[27]

$$\frac{\eta_{PE}(;}{\eta_{PLA}(;} \quad {}_{n} - \frac{\phi_{PLA,PI}}{\left(1-\phi_{PLA,PI}\right)}\Bigg]^{[\eta]\phi_m} \tag{5.4}$$

where $\eta_{PE}(;$ and $\eta_{PLA}(;$ are shear viscosity of the PE and PLA, respectively, at the shear rate of mixing, $\phi_{PLA,PI}$ are the predicted phase inversion volume fraction for the PLA phase, and ϕ_m is the maximum packing fraction deformable spheres and $[\eta]$ is the intrinsic viscosity of deformable viscoelastic spheres. Values of $[\eta]$=1.9 and ϕ_m=0.84, empirically derived in previous studies when the viscosity ratio is near unity,[27] were used to describe this droplet packing behavior assuming deformable spherical particles. This model was specifically explored first due to its relative success in predicting phase inversion in the PE/PEO and PP/PEO blends from Chapter 4.

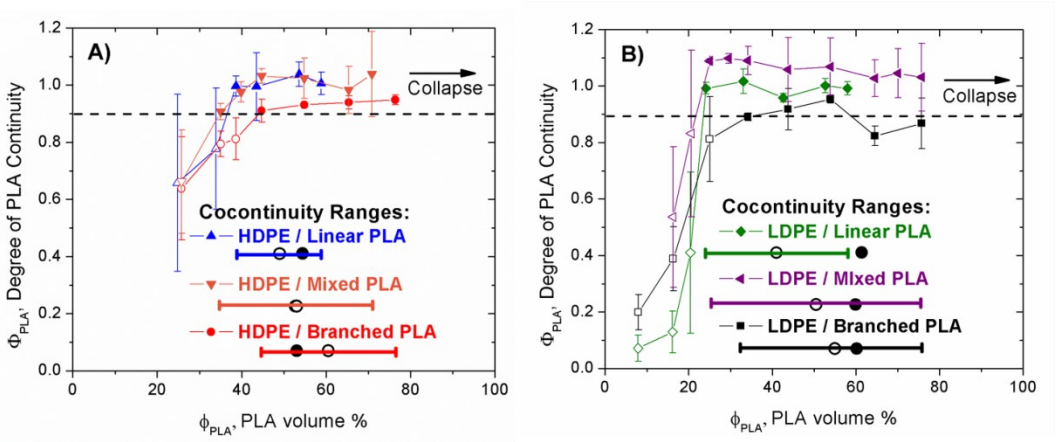

Figure 5.6. Degree of cocontinuity and range of cocontinuity for A) HDPE/PLA blends and B) LDPE/PLA blends. For the degree of cocontinuity data, the closed symbols represent fully cocontinuous blends. Open symbols were not completely cocontinuous and contained dispersed PLA droplets. The horizontal bars show the range of cocontinuous compositions. Along the ranges, the closed circles show the phase inversion composition as predicted by Eq. 5.4. The open circles show the center of each range.

Table 5.4 tabulates the range of cocontinuity results, as well as the experimentally

observed phase inversion compositions (defined as the center of the range of cocontinuity), the phase inversion compositions predicted by Eq. 5.4, and the deviation between the experimentally measured phase inversion values and the predicted values from Eq. 5.4.

Table 5.4. Tabulated values for the upper and lower bound of PLA volume % for the range of cocontinuity, with a comparison of the experimentally observed phase inversion point to the phase inversion point as predicted by Eq. 5.4. All values represent PLA volume percent.

Material System	**ϕ_{PLA}, lower bound**	**ϕ_{PLA}, upper bound**	**$\phi_{PLA\text{-}PI,exp}$, experimental phase inversion**	**$\phi_{PLA\text{-}PI,pred}$, predicted phase inversion, Eq. 5.4**	**Deviation: $\phi_{PLA\text{-}PI,exp} - \phi_{PLA\text{-}PI,pred}$**
HDPE/ L-PLA	39	59	49	54.4	-5.4
HDPE/ Mixed PLA	35	71	53	52.7	0.3
HDPE/ B-PLA	45	76	60.5	53.0	7.5
LDPE/ L-PLA	24	58	41	61.4	-20.4
LDPE/ Mixed PLA	25	76	50.5	59.9	-9.9
LDPE/ B-PLA	34	76	55	60.2	-5.2

From the ranges of cocontinuity, it was observed that when blending with branched polymers, the blends were capable of forming cocontinuous networks containing a larger volume fraction of the branched polymer, or alternatively, formed cocontinuous blends with increasingly less of the other phase. This broadening of the range occurred despite no apparent increase in the shear viscosity at the blending shear rate when using branched polymers. The HDPE/L-PLA system, in which both phases were composed of linear polymers, showed the narrowest range of cocontinuous compositions, between 39-59 vol% PLA. However, by replacing the linear PLA with a strain hardening material such as the mixed PLA or B-PLA, the upper limit of PLA continuity can be extended from 59 vol% PLA to as high as 76 PLA vol% PLA. Adding a branched PLA resulted in only minimal deviation in the lower limit of cocontinuity, which

remained at 40±5 vol% PLA.

Likewise, by substituting branched LDPE in place of the linear HDPE, the lower limit of PLA continuity is extended to as low as 24 vol% PLA. This is particularly evident when comparing the case of HDPE/L-PLA to LDPE/L-PLA, where the upper bound of cocontinuity (58 vol% PLA) remained unchanged, while the lower bound of continuity changed from 39 vol% PLA for linear HDPE to 24 vol% PLA for branched LDPE. In the case where both phases are branched and display strain hardening, the range of cocontinuity is extended in both directions, resulting in the widest ranges of cocontinuity, as seen in the LDPE/mixed PLA system.

Further support of the observation of an asymmetric extension of the range of cocontinuity when adding a single branched phase can be found from the estimates of the phase inversion composition. In cases where the two phases are most similar in branching content and overall strain hardening coefficient (as is the case in the HDPE/L-PLA, HDPE/mixed PLA, and LDPE/B-PLA systems), the predictions from Eq. 5.4 coincide most closely with the observed phase inversion compositions, within an error of 5 vol% PLA. However, more significant deviations are observed when the blend phases are unlike in branching content and strain hardening coefficient (as in the case of HDPE/B-PLA, LDPE/L-PLA, and LDPE/mixed PLA), all with deviations greater than 7 vol% and as high as 20 vol% in the LDPE/L-PLA case.

The causes for failure in the model are two-fold: first, defining the phase inversion composition as the center of the cocontinuous compositions is a limited definition that fails to capture the asymmetric extension of the range of cocontinuous compositions when branching is introduced to a single phase. A similar observation was made in Chapter 4 for other asymmetric blends, in that case blends with interfaces stabilized by asymmetric block or graft copolymers. Both of these instances underscore the importance of considering range of cocontinuity independently for either side of the phase inversion composition.

Second, this model attempts to describe phase inversion only by shear viscosity. Other

models have been proposed that incorporate shear elasticity into the phase inversion prediction, particularly in work by Bourry and Favis.[32] These models are given by Eq. 4.6 and Eq. 4.7 in Chapter 4, and are based on an observation that a more elastic phase has a tendency to encapsulate a less elastic phase during mixing.[111,112]

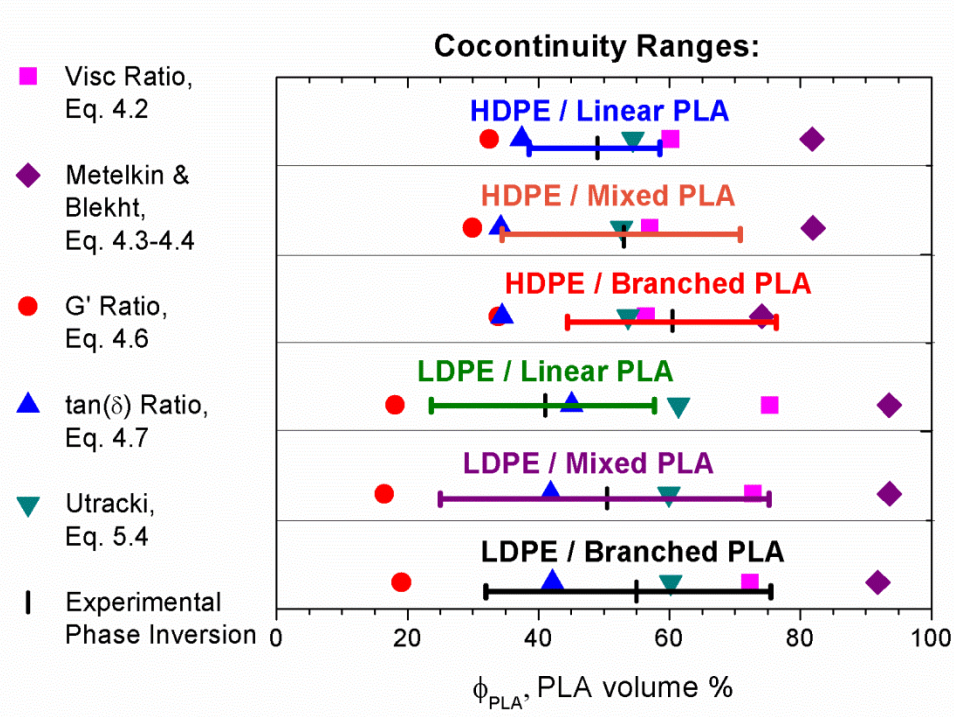

Figure 5.7. Phase inversion predictions from different literature-reported models, relative to the ranges and centers of cocontinuity for each blend system. The Utracki model (Eq. 5.4) [27] and the ratio of tan(δ) (Eq. 4.7) [32] predicted the behavior most successfully, but inconsistently, showing large deviations for blends with dissimilar branching architecture between the phases.

While previous studies have reported better predictions of phase inversion from Eqs. 4.6 and 4.7 than from models that only incorporate shear viscosity,[31,32,111] no such improvement was observed here, as shown in Figure 5.7. This figure shows graphically the range of cocontinuity and phase inversion composition of each blend system compared to the all the phase inversion predictions from Chapter 4. The accuracy of the predictions is shown graphically in Figure 5.8, and was evaluated by plotting the model-predicted phase inversion points against the experimentally observed results. Between the predictions incorporating elasticity, the one based

on the ratio of *tan(δ)* performed nearer to the observed phase inversion results. However, it was inconsistent for blends containing HDPE, and was in general not as accurate as the Utracki model. Figure 5.8 particularly shows that predictions based on *tan(δ)* also predicted that the PLA phase inversion composition decreased with increased PLA branching, which was opposite of the experimentally observed trend, confirming a need for incorporating extensional rheological effects into predictions of cocontinuity. An attempt to do so by way of arguments on the mechanism of cocontinuity formation and the rheological influence of strain hardening will be undertaken in the Discussion section below.

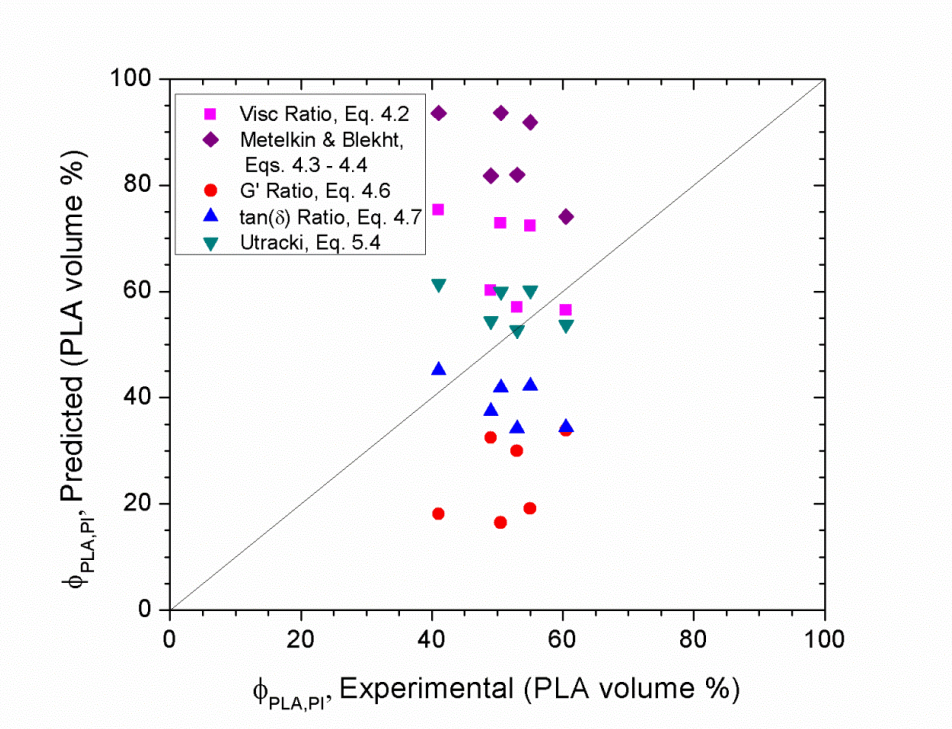

Figure 5.8. Evaluation of the accuracy of phase inversion predictions. The diagonal line represents agreement between the measured results and the model predictions.

5.3.3 Size Analysis

Figure 5.9 shows representative SEM micrographs of the blends following PLA extraction in chloroform, each with a volume fraction of 45/55 vol% PE/PLA. As is observed in Figure 5.6, all of the samples at this composition possess a cocontinuous morphology, and the

SEM images qualitatively support this claim, being composed of continuously connected regions and what appear to be droplets. It is important to keep in mind that the appearance of droplet-like features is not necessarily indicative of a dispersed droplet morphology. Since the extruded samples are cross sectioned perpendicular to the machine direction, round features may in fact be elongated droplets or fibers normal to the imaged surface. The characteristic size of the blend, *a*, as calculated by Eq. 5.2 using LSCM images of the same samples, is reported with each image in Figure 5.9, and shown graphically in Figure 5.10.

From Figure 5.10, a minimum of the domain size is observed for blends with an intermediate amount of branching, while HDPE/Linear PLA with no branching and LDPE/Branched PLA with a large amount of branching in each phase showed the largest characteristic size.

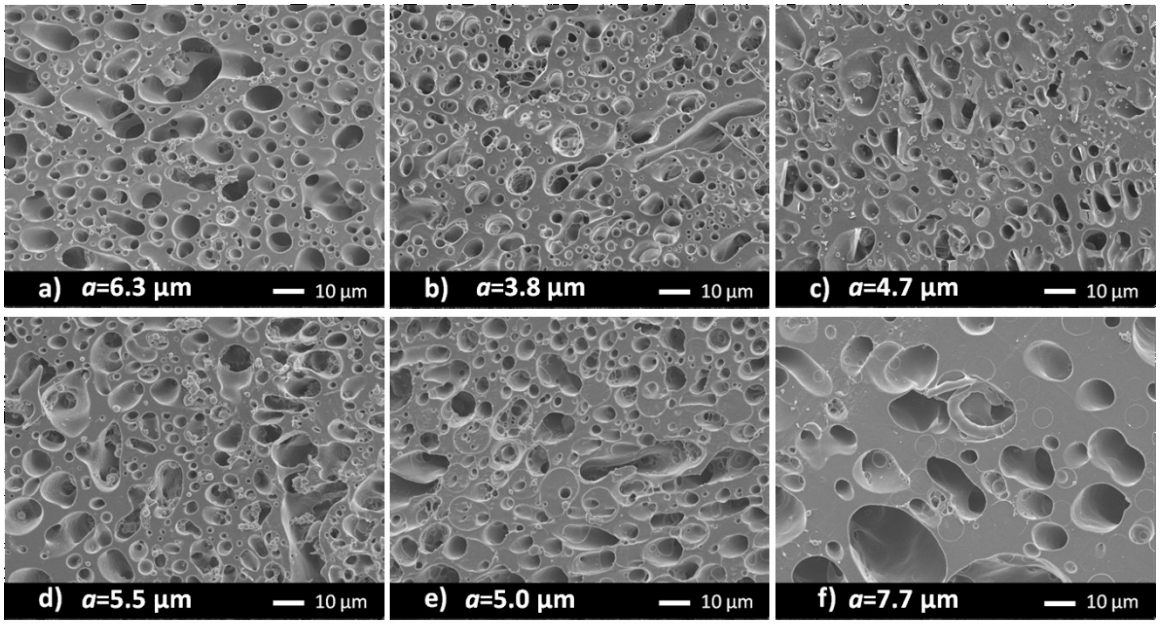

Figure 5.9. SEM images of PLA extracted PE/PLA blends at 45/55 volume % of a) HDPE/Linear PLA, b) HDPE/Blended PLA, c) HDPE/Branched PLA, d) LDPE/Linear PLA, e) LDPE/Blended PLA, and f) LDPE/Branched PLA. All scale bars are 10 µm.

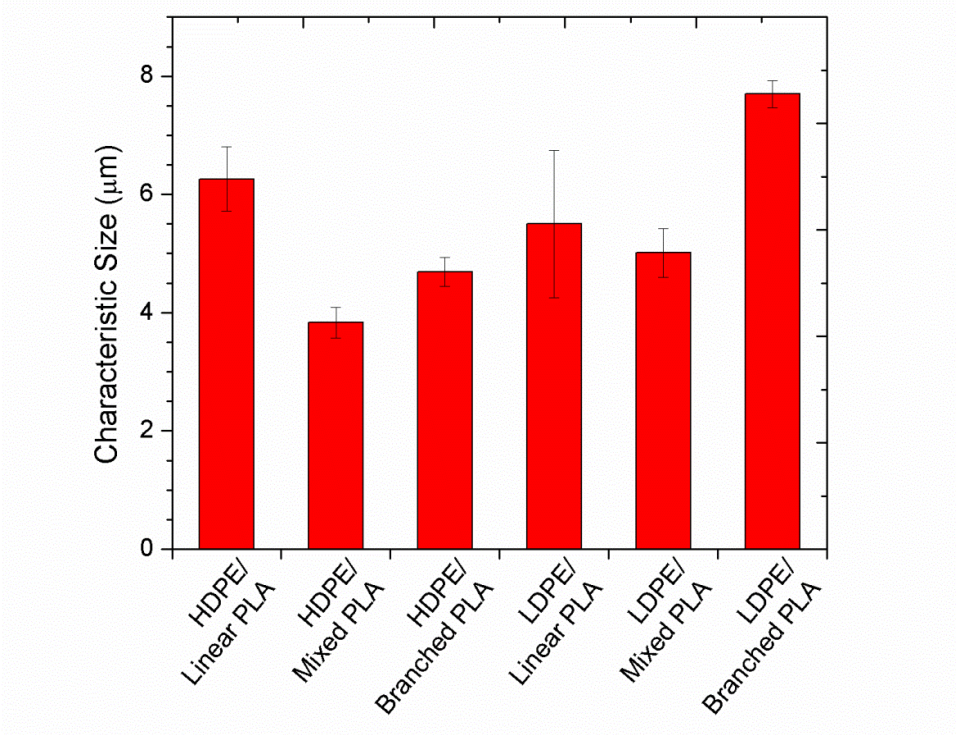

Figure 5.10. Initial characteristic size for 45/55 vol% PE/PLA blends. Overall branching content increases from left to right.

5.3.4 Stability Analysis via Coarsening

In order to investigate the blend stability, blends at 45/55 volume% PE/PLA were also subjected to coarsening at 180 °C for up to 30 minutes. The coarsening results in terms of characteristic size as a function of time for each blend are shown in Figure 5.11. All the blends studied here showed a continuous increase of characteristic size with annealing time with no apparent plateau, indicative of an uncompatibilized cocontinuous blend undergoing self-similar coarsening.

Theory predicts [19,81,84-86] that the rate of coarsening of a cocontinuous blend should be analogous to work done by Tomotika [87] which predicts the rate of breakup of a viscous fiber in an infinite matrix of another viscous material. The rate of cocontinuous coarsening has been given by the equation:

$$\left.\frac{da}{dt}\right|_{t=0} \propto \frac{\Gamma\Omega}{\eta_{blend}} \tag{5.5}$$

where a is the blend characteristic size at the beginning of coarsening, Γ is the interfacial tension between the two phases, η_{blend} is the overall blend viscosity, given as the log volume average of the zero-shear viscosity η_o of the blend components,[27] and Ω is a tabulated function referred to as Tomotika's function, which describes the growth rate of the disturbance and is dependent on the viscosity ratio between the dispersed and continuous phase, η_{disp}/η_{cont}. The value of Ω approaches 1 as η_{disp}/η_{cont} becomes 0, and approaches 0 as η_{disp}/η_{cont} becomes infinite. For the present analysis, the interfacial tension Γ was measured following the Palierne viscoelastic droplet model, described more fully in Appendix A and in other publications,[13,60,62] and was measured to be around 11 mN/m for all combinations of PE and PLA.

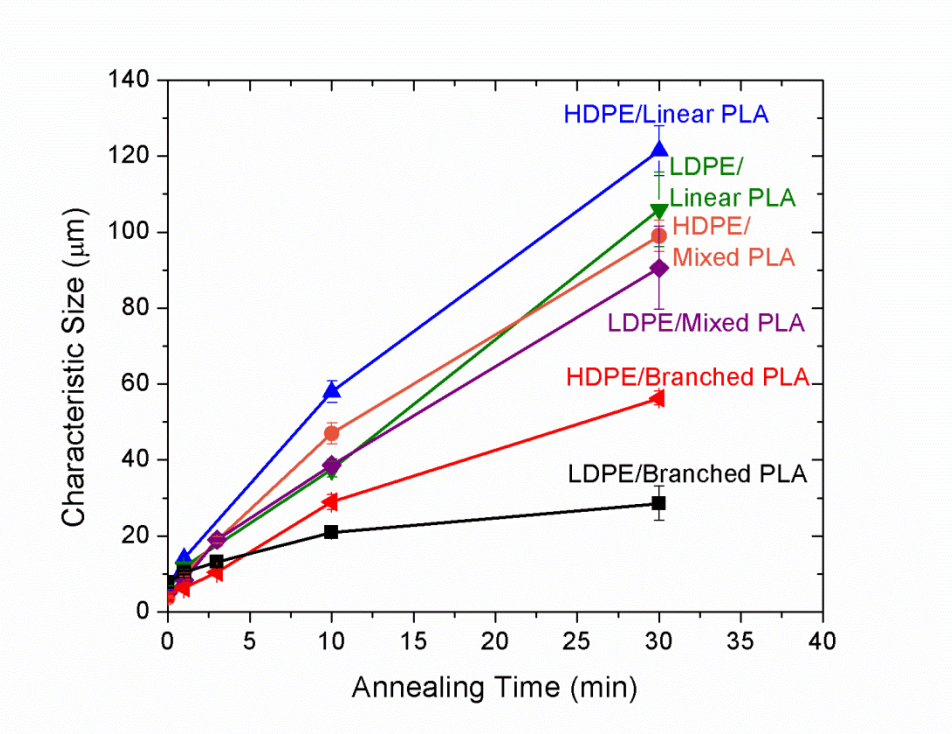

Figure 5.11. Characteristic phase size of cocontinuous blended polymers as a function of annealing time at 180 °C.

Coarsening of cocontinuous blends poses a unique problem for evaluating Ω, in that there

is no discernible dispersed and continuous phase: the assumption of an infinite matrix fails, as both phases exhibit both continuity and coarsening behavior, such that each phase simultaneously satisfies the definition of both matrix and "breaking thread." This complicates the mathematical analysis as well, as the viscosity ratio η_{disp}/η_{cont} becomes indeterminate when no phase uniquely fulfills the role of dispersed or continuous phase. Hence, the value of Ω becomes indeterminate, and so for the present analysis, Ω was assumed to be constant.

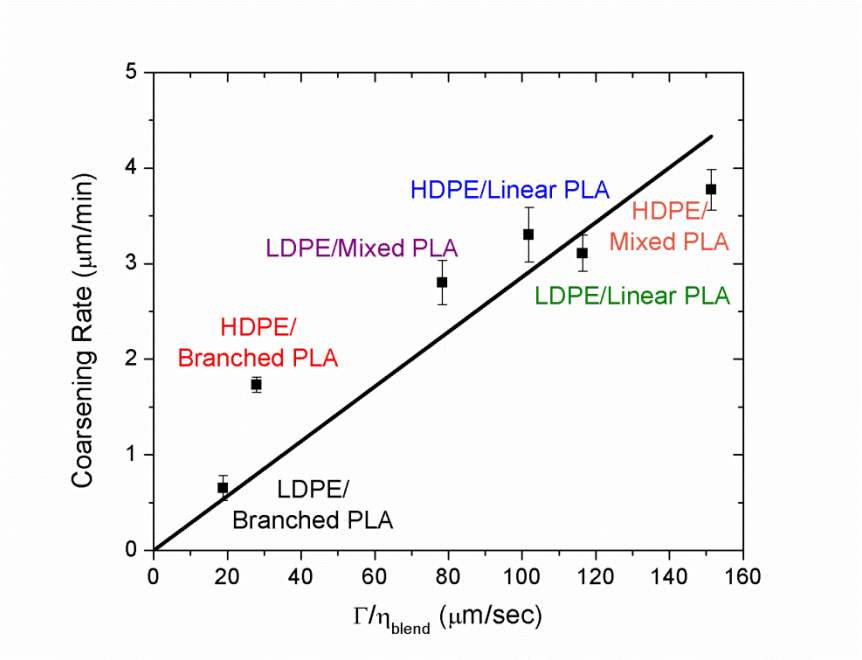

Figure 5.12. Coarsening rate of PE/PLA cocontinuous blends from 1-30 minutes of coarsening, as a function of Γ/η_{blend}. The line shows a linear regression with a zero intercept.

The rate of coarsening was measured as the linear increase of the characteristic size from 1 – 30 minutes of annealing time. The characteristic size at 1 minute of coarsening was used as the initial condition to limit the effect of anisotropy in the initial sample – samples that had not undergone any coarsening were still shear aligned from the extrusion, which complicated assumptions of self-similar coarsening during the first minute of annealing. The results for coarsening rate plotted against Γ/η_{blend} (with the Ω term treated as a constant) are shown in Figure 5.12. These results were linearly fit with an intercept of zero, since infinite viscosity or zero

interfacial tension would result in no coarsening.

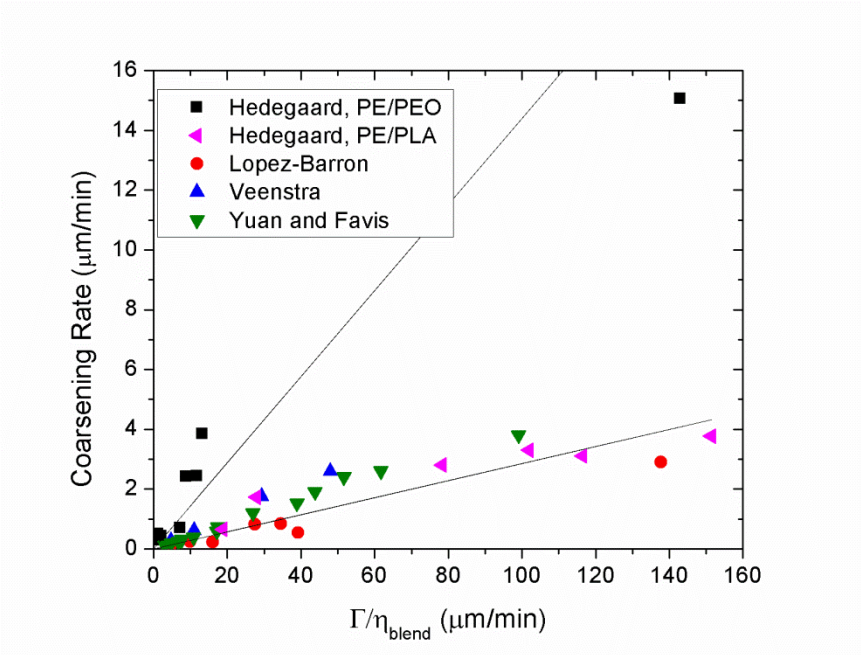

Figure 5.13. Coarsening rates of PE/PEO and PE-g-MA/PEO blends, PE/PLA blends, and coarsening rate data from studies by Lopez-Barron,[81] Veenstra,[19] and Yuan and Favis,[34] plotted against Γ/η_{blend}. The lines show linear regressions with zero intercept, the upper line fit PE/PEO and PE-g-MA/PEO blends and the lower line fit to the PE/PLA blends.

As can be seen in Figure 5.12, the rate of coarsening correlates linearly to the term Γ/η_{blend}, as predicted by Eq. 5.5 when excluding Ω from the analysis. Figure 5.13 shows these same results, but with the similar coarsening rate results for the LDPE/PEO and PE-g-MA/PEO blends from Chapter 2, as well as coarsening results from previous studies.[19,34,81] In each case, it is apparent that the linear relationship between coarsening rate and Γ/η_{blend} holds. According to the comparison between PE/PLA and the additional literature data, the proportionality constant between the coarsening rate and Γ/η_{blend} is independent of the material system, suggesting that the present relationship is both general and sufficient when no interfacial species are present.

However, a different proportionality is observed with PE/PEO when compared to the other blend systems. This discrepancy is likely due to a number of potential factors. First, PEO within the PE/PEO blends can degrade rapidly during mixing, which would decrease viscosity of

the blend relative to what was measured prior to mixing, as shown in Appendix C. Second, PE/PEO blends were known to contain nanoparticulate fumed silica, and the role of these nanoparticles on coarsening behavior is unclear. Lastly, droplet coalescence during interfacial tension measurements, particularly with lower viscosity 20K and 40K PEO, can result in an interfacial tension that appears lower, as interfacial tension in the Palierne model is always expressed as Γ/R, where R is the droplet radius.

The analysis here also suggests that coarsening of the blend's morphology during quiescent annealing is resisted primarily by the zero shear viscosity of the blend, and not by the strain hardening behavior of the constitutive polymers. Given that LDPE and B-PLA exhibited strain hardening factors on the order of 9, if the quiescent coarsening rate were governed by extensional viscosity one would expect to see a dramatic deviation from linearity with Γ/η_{blend}. This result suggests that either the flow during coarsening of a cocontinuous blend is dominated by shear flow, or that extensional flow is present but at a sufficiently low rate such that the materials behave in a linear viscoelastic fashion and thus fail to exhibit any strain hardening. Further experiments or flow simulations would be required to further distinguish the nature of the coarsening flow.

5.4 Discussion

Based on the observations shown here concerning the range of cocontinuous compositions and the initial phase size of these blends, it is evident that the shear rheology of the constituent materials, even when including elastic effects, is insufficient for determining when a cocontinuous structure is formed, and extensional flow is influential in the processing and formation of a cocontinuous polymer blend. Due to the complex nature of flow in twin-screw extrusion and melt mixers, the flow is not simple shear but a combination of shear and extensional flow over a wide range of rates. Therefore, the "rules of thumb" devised in Chapter 4 are not sufficient conditions for predicting ranges of cocontinuity on their own, and further

conclusions are needed to improve morphological predictions. However, for the discussion to remain relevant and consistent with the conclusions from Chapter 4, this discussion must also keep in mind the central tenet of cocontinuity – that it is promoted by the formation and stability of elongated features which must then percolate into a continuous network.

Based on the asymmetric widening of the cocontinuity range when blending with a single branched phase, strain hardening of the major phase appears to stabilize the existence of elongated or interconnected structures of the minor phase. However, no change was observed in the range of cocontinuous compositions when increasing PLA branching content from mixed PLA (25% branched PLA) to 100% branched PLA. In order to more fully explain this phenomenon, a deeper understanding of the mechanism of cocontinuity formation must be developed. To aid in this discussion, SEM images for blends of HDPE/L-PLA, HDPE/B-PLA, LDPE/L-PLA, and LDPE/B-PLA at various compositions can be found in Figure 5.14 through Figure 5.17, respectively. All of the blends shown in these figures are cocontinuous according to gravimetric solvent extraction experiments.

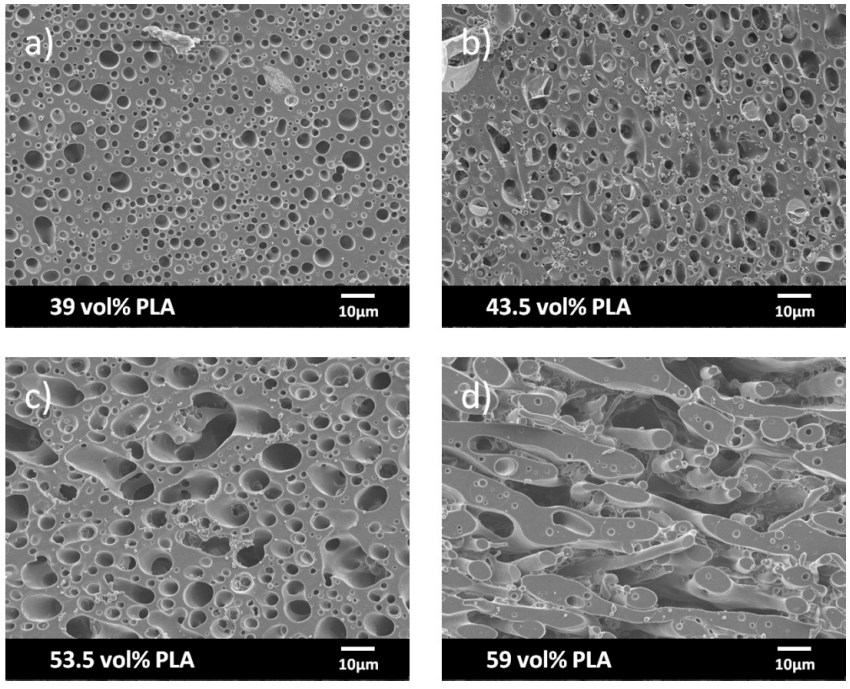

Figure 5.14. Cocontinuous blends of HDPE/L-PLA across the range of cocontinuity.

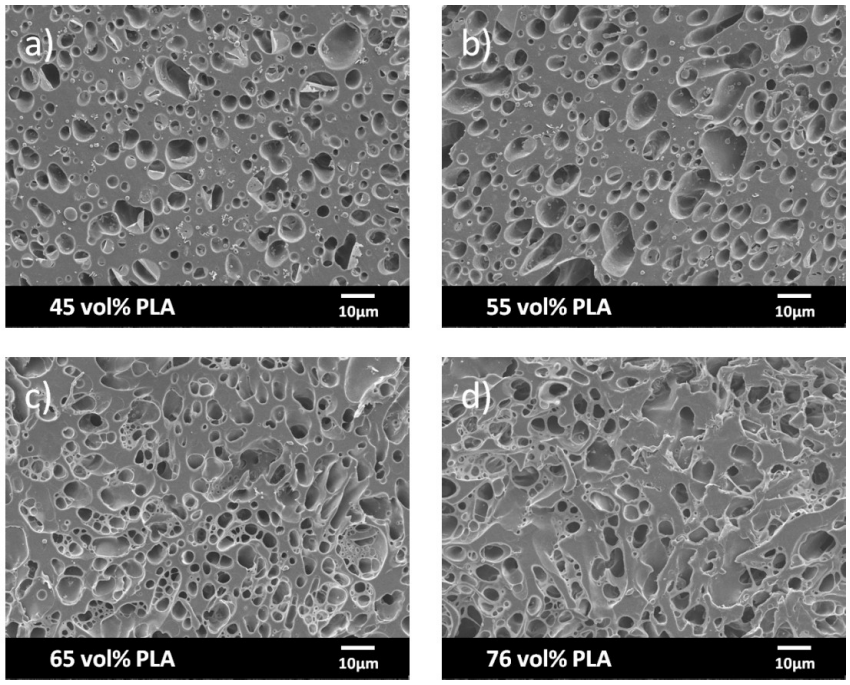

Figure 5.15. Cocontinuous blends of HDPE/B-PLA across the range of cocontinuity.

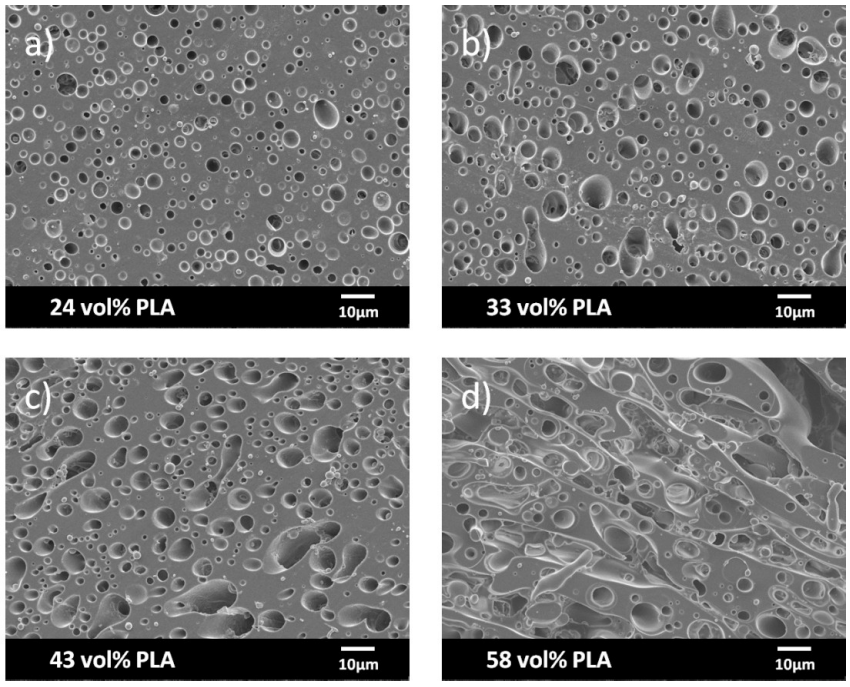

Figure 5.16. Cocontinuous blends of LDPE/L-PLA across the range of cocontinuity.

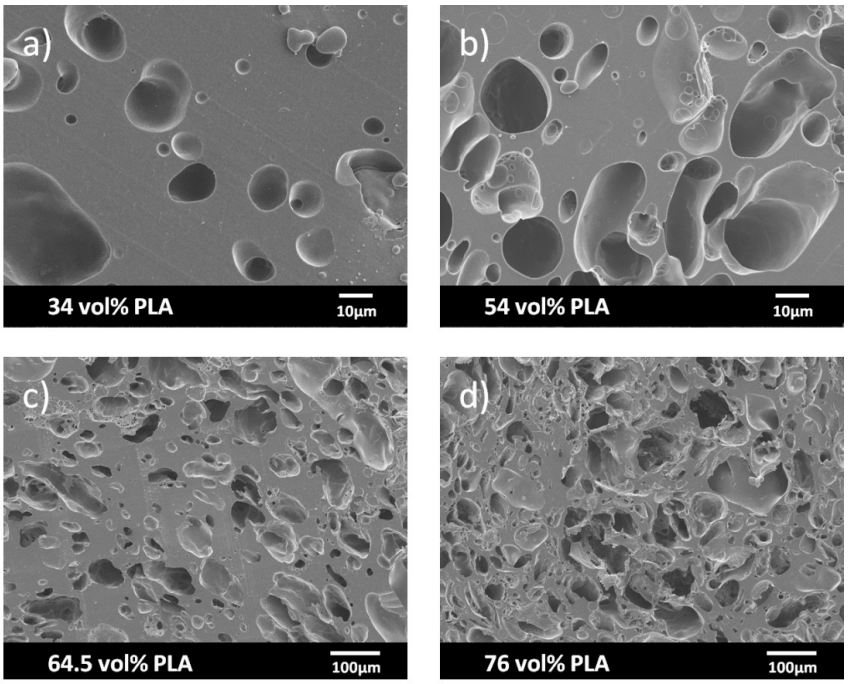

Figure 5.17. Cocontinuous blends of LDPE/B-PLA across the range of cocontinuity.

Work by Li *et al* [7] suggests a potential mechanism for cocontinuity formation, based on either fiber-fiber or droplet-droplet flow-induced coalescence of the minor phase into a continuous network. Coalescence occurs when dispersed features (either droplets or fibers) approach each other, thereby displacing the major-phase fluid between them in draining flow until the film of the major phase ruptures, allowing contact and percolation of the dispersed features. This coalescence is limited by the rate at which the film can be drained – if the features are allowed to flow past each other before the major phase film can rupture, no coalescence will occur. A schematic of droplet coalescence accompanied by draining flow is shown in Figure 5.18.

The role of long-chain branching in flow-induced coalescence has not been explored in the current literature, though the role of long-chain branching during foam extrusion has been previously studied, and parallels can be drawn between the draining flows observed in both flow-induced coalescence and foaming processes. Previous work has shown that including long-chain branching in extrusion-foamed polymers reduces cell coalescence. This was attributed to the

strain hardening of the branched polymer, which prevented rupture of the continuous polymer phase as it was squeezed by expanding cells.[123,127] Therefore, it would be anticipated that as dispersed features approach one another in flow-induced coalescence, the continuous phase between them will be squeezed out of the interstitial space, and so a strain hardening major phase would be expected to prevent coalescence of the minor phase.

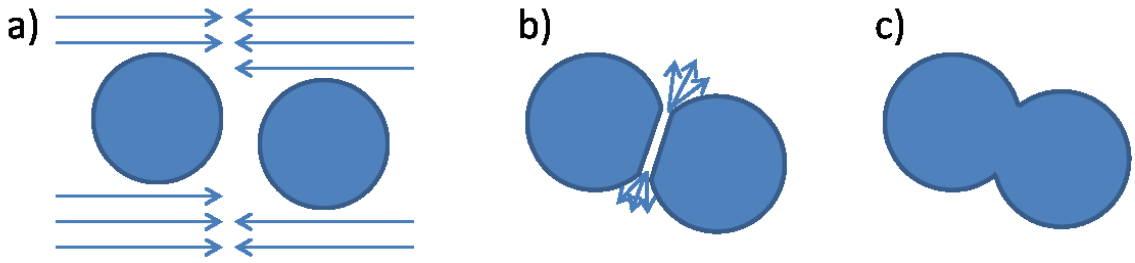

Figure 5.18. Schematic of the mechanism of droplet coalescence. a) Droplets in a matrix flow towards each other. b) The droplets collide, but the matrix fluid must be squeezed out of the space in draining flow. c) The draining film of the matrix fluid ruptures, and the droplets coalesce. It is expected that a strain hardening matrix fluid will resist the draining flow is step b, thereby reducing coalescence of features.

However, this expectation is opposite of what is observed from the cocontinuity results presented here, where the general trend is that a strain hardening major phase *promotes* percolation of the minor phase, allowing percolation into a continuous network with less minor phase material. This suggests that naively applying the mechanism of coalescence and percolation to predict cocontinuity is not sufficient for describing conditions for cocontinuity.

An alternative mechanism of cocontinuity has been proposed in work by Sundararaj *et al*,[140,141] in which cocontinuity is a blending transition state resulting from sheet formation during initial stages of mixing. The sheets break up irregularly to form an interpenetrating transition state over a broad range of compositions. This transition state can continue to develop either to "steady state" cocontinuity or break up into dispersed droplets.

Based on this mechanism, the conditions for cocontinuity are less influenced by the ability of the minor phase to coalesce and percolate, and more influenced by the stability of the

sheets, elongated particles, and irregularly shaped features during complex flow. Considering the case of a strain hardening major phase and a non-strain hardening minor phase, the strain hardening phase would serve two purposes to stabilizing cocontinuity. First, the viscosity of the major phase would increase during extensional flows. This would encourage the minor phase to more readily form a continuous network as it attempts to encapsulate the higher viscosity material, as is observed in typical blending processes. Second, the increased major phase viscosity during extensional flows would promote stress transfer to the minor phase, promoting extension of the phase into elongated features. This is shown schematically in Figure 5.19. These elongated features would more readily percolate into a continuous network, as is shown schematically in Figure 5.20.

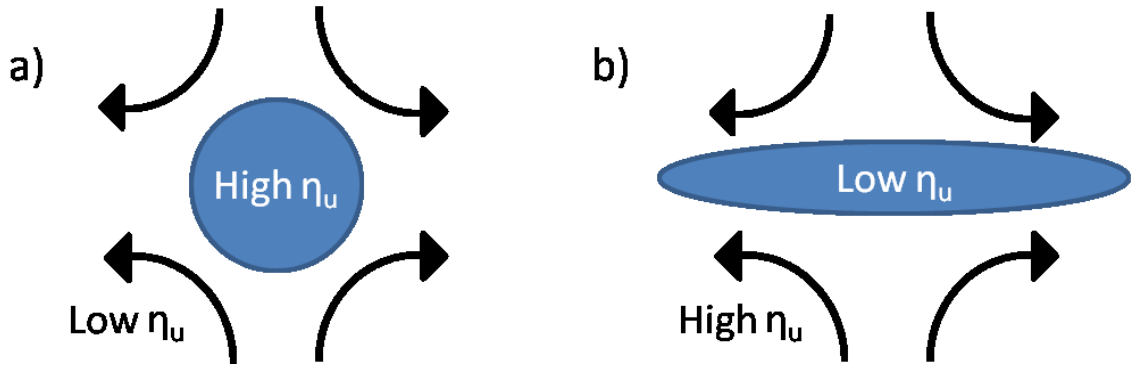

Figure 5.19. Droplet stretching in elongational flow. a) A low viscosity matrix and high viscosity droplet resists stretching due to poor transfer of stress to the dispersed phase. b) A high viscosity matrix stretches the droplet due to effective stress transfer.

Third, and perhaps most importantly, the idea that a higher extensional viscosity stabilizes elongated features to broaden the range of cocontinuity is consistent with results observed in Chapter 4, where the range of cocontinuity broadened with increasing shear viscosity. Even without an increase of shear viscosity at higher shear rates, the increase in extensional viscosity will still similarly increases the resistance to the flow observed in melt mixing, especially in the presence of extensional flows.

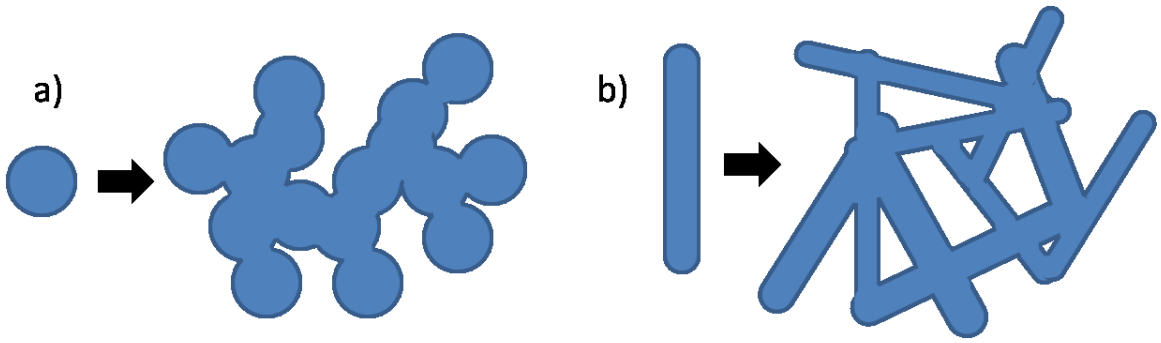

Figure 5.20. Schematic comparing percolation of a) spherical droplets to b) elongated features. Elongated features will more readily form a percolated network, and therefore promote cocontinuity. It is expected that strain hardening will stabilize elongated features due to increased melt strength, superior stress transfer to the minor phase, and higher extensional viscosity promoting fiber formation and inhibiting fiber breakup.

Evidence of stabilized elongated features of a linear minor phase with a branched major phase are seen in the LDPE/L-PLA blends of Figure 5.16, where the onset of stable elongated features of the linear PLA (represented by the holes in the blend) can already be seen at only 33 vol% PLA (Figure 5.16b), with a greater probability of elongated features as L-PLA content increases. Meanwhile, HDPE/B-PLA blends shown in Figure 5.15 exhibit droplet-like behavior of the PLA phase for higher amounts of PLA, with extended droplets not seen until 55 vol% B-PLA (Figure 5.15b).

The results reported here seem to suggest a combined mechanism of cocontinuity formation based on both coalescence and stabilized irregular features will predict the observed behavior best. The trend of strain hardening matrices to promote percolation of their minor phase with less of the minor phase suggests that the second mechanism of the stabilization of complex or elongated features formed early during mixing must be taken into account, as theories of coalescence and percolation alone suggest an opposite outcome.

However, coalescence theory is still needed to explain the lack of improvement of the cocontinuity range between higher degrees of strain hardening, particularly when considering that blends containing mixed PLA tended to outperform those containing B-PLA when comparing the

range of cocontinuity. Further increasing extensional viscosity of the PLA phase would inhibit coalescence and percolation by inhibiting draining flows, as observed previously in extrusion foaming,[123,127] which would explain the lack of improvement when using a fully branched PLA.

The competing role of strain hardening to both resist flow and stabilize features can also serve to explain the dependence of the characteristic size of the blends on the stain hardening properties of the constitutive polymers, where characteristic size was minimized when blending with slightly strain hardening materials, and maximized when blending with two highly-branched materials or with two materials with no strain hardening. A fiber under extensional flow can experience necking, a flow instability which results in an uneven rate of deformation over the length of an elongated feature, with faster deformation within the necking region than outside of it. The presence of strain hardening behavior will increase the viscosity within the necking region, stabilizing that region so that strain hardening materials can achieve a higher degree of total elongation without breaking,[133,142] promoting the formation of narrower features as "fibers" within the matrix are able to be stretched further without breaking. However, a dramatically increased extensional viscosity due to a high degree of branching will resist extensional flow such that elongated features are formed more slowly, allowing retraction into larger diameter features to occur.

Unfortunately, existing literature provides insufficient experimental evidence to form a more thorough understanding of both the complete mechanism of cocontinuity formation and the role of strain hardening matrices on the fluid dynamics of a viscoelastic dispersed phase. To address this, further experimental studies are needed where viscoelastic fibers are embedded into a viscoelastic matrix with varying degrees of branching, and are then subjected to shear and extensional flow conditions to determine the role of strain hardening of the matrix on the stability of embedded fibers. This would be similar to prior work by Ramaswamy and Leal,[143,144] but with dispersed fibers instead of droplets and the strain hardening of the matrix as an experimental

variable. Further experiments directly investigating flow-induced droplet coalescence as a function of the degree of branching of the major and minor phases would also be essential to elucidating the role strain hardening plays in the coalescence of continuous networks in polymer blends. These experiments, however, are beyond the scope of the current study.

5.5 Conclusions

A rheological investigation of the linear and branched counterparts of PE and PLA showed that the presence of long-chain branching served to dramatically increase both the extensional viscosity and the zero-shear viscosity of the polymers, while leaving the shear viscosity relatively unchanged at $\dot{\gamma}$. These materials gave the present study the basis to explore the role of strain hardening in the formation of cocontinuous polymer blends, as the extensional flow properties could be tuned independently while leaving shear flow properties at processing-relevant shear rates unchanged.

When blending with strain hardening materials, the range of compositions of complete cocontinuity was asymmetrically expanded to include more of the strain hardening material and less of the other dispersed phase while still retaining cocontinuity. The Utracki model for predicting the phase inversion point based on percolation theory succeeded in cases where each phase showed similar strain hardening behavior, but broke down when applied to systems of one linear and one highly branched phase, due to its inability to predict the influence of extensional flow properties like strain hardening on phase inversion and cocontinuity.

The expansion of the range of cocontinuity was attributed to the stabilizing effect of a strain hardening matrix on dispersed fibers and irregular features within that matrix. However, further increases in strain hardening when blending with B-PLA rather than a mixed PLA did not further expand the cocontinuous range, suggesting that draining flows and extension of the dispersed phase into elongated features were suppressed due to the increased extensional viscosity. This suggested a dual-mechanism for the formation of cocontinuity, based

simultaneously on the requirements of stability of elongated, irregular sheets formed early in the blending process coupled with the requirement of percolation and coalescence of dispersed phase. This also supplements the "rules of thumb" developed in Chapter 4 by adding one more to this list: strain hardening materials can expand the range of cocontinuity, to a point up until they inhibit draining flows during coalescence of the dispersed phase.

The initial characteristic size of the blends was minimized when blending with materials that showed slight amounts of strain hardening, and was maximized when blending with two linear, non-strain hardening materials or with two strongly strain hardening materials with X_e>9. This supports the earlier assertions that some strain hardening can stabilize thinner elongated features in the blend, but excessive strain hardening resists the formation of these thinner features. While long-chain branching did serve to slow down the rate of coarsening of these blends during post-processing annealing, this was not a result of strain hardening but of increased zero-shear viscosity. This was confirmed by the linear dependence of the coarsening rate on Γ/η_{blend}, related only to linear viscoelastic shear rheology and not to extensional properties.

Chapter 6: Stabilization of PE/PEO Cocontinuous Blends by Interfacial Nanoclays

6.1 Introduction

The stabilization of immiscible fluids by colloidal particles can be traced back to work by Pickering over a century ago, where he reported that fine solid particles could stabilize emulsions made from two immiscible, low-viscosity liquid phases.[145] Since then, Pickering emulsions have become key ingredients in wastewater treatment, cosmetic formulations, and in the recovery, separation, and cleaning of oil.[146] In recent years, applying the phenomenon of particles adsorbed at fluid-fluid interfaces to immiscible polymer blends has received a great deal of interest from scientific and industrial communities.[43-48]

Polymer blends represent an inexpensive route to develop materials with enhanced properties. The final properties of a blend are strongly influenced by its morphology which can be tuned by varying the composition, processing conditions, and the chemistry and rheology of the blended polymers.[147] Of all possible polymer blend morphologies, cocontinuous blends are of particular interest due to their unique property within the field of blended polymers of possessing two continuous phases. This property allows cocontinuous blends to be used for novel applications such as conductive polymer blends.[10,11] Furthermore, extraction of a single continuous phase results in a porous structure, which can be used in materials that either require pores or large amounts of interfacial area, such as membranes and scaffolds for tissue engineering applications.[14,15,148] However, cocontinuous morphologies are not in thermodynamic equilibrium. They are kinetically trapped and, during annealing, their features will coarsen into larger sizes as coalescence occurs, and may eventually break up into dispersed morphologies. These transformations are driven by the high interfacial tension between the two polymer phases.

The interface is commonly compatibilized either by addition of premade block copolymers

or generation of graft copolymers via *in situ* coupling reaction at the interface.[35,149-151] The extent of compatibilization for both strategies is directly related to the amount of copolymers present at the interfacial region. Higher block copolymer content reduces interfacial tension and stabilizes the desired morphology. Premade block copolymers added to the blend must be carefully designed in chemistry, molecular weight, and chain architecture to localize at the blend interface, although even well-designed block copolymers can form micelles which lessen the effectiveness of the additive by reducing the amount of interfacially active copolymer. Reactive compatibilization is a complex and not fully characterized phenomenon controlled by the interplay of polymer chemistry, chain architecture (e.g. molecular weight of the reactants, linear versus branched, end-functional versus graft-functional), reaction kinetics, reaction equilibria, flow conditions, and the thermal properties of the reactive ingredients and their products. These factors must be tuned to maximize the probability of functional groups reacting with each other during short processing times in a heterogeneous reaction environment. Therefore, both of these compatibilization strategies are experimentally exhaustive, and the additives or reactive polymers involved are often blend-specific.

On the other hand, nanofillers as compatibilizers have the potential to be used as a more generic, low cost approach to compatibilization of polymer blends: a single nanofiller has the potential to behave as an effective compatibilizer for multiple polymer blends, based on the relative wettability of a polymer-polymer interface compared to nanoparticle-polymer interfaces. In addition, incorporation of nanofillers in polymer blends can result in significant improvements of mechanical, electrical, gas barrier, and flame retardant properties.[152-155]

Previous work on polymer blends with nanoparticles have reported that compatibilization was attributed to a decrease in interfacial tension by interfacial localization of nanoparticles, an increase in viscosity upon addition of nanoparticles, or a combination of those two effects.[45,47,156-159] Selective localization at the interface is the desired mechanism so that compatibilization can

be achieved with significantly fewer particles relative to those needed to sufficiently increase the viscosity using randomly distributed particles throughout the polymer. However, accomplishing this often poses significant challenges due to the complex and little understood interplay of particle compatibility, transport behavior and rheology. Kinetic and thermodynamic effects are both important in this respect. While the equilibrium aspects of particle-polymer interactions (wetting coefficient) are known and serve to guide the choice of polymers and particles, often the morphology/structure of the polymer blend nanocomposite is far from the expected one, due in part to the role of viscosity in particle localization during non-equilibrium processes like melt mixing.[160]

For this chapter, three compatibilization routes were explored: selective localization of nanoclays at phase interfaces, reactive compatibilization, and the synergistic action of the two. These were compared across various processing conditions in terms of their effect on blend morphology and properties. Two polymer blend systems, a non-reactive polyethylene (LDPE)/polyethylene oxide (PEO) and reactive maleic anhydride functional polyethylene (PE-g-MA)/PEO were investigated. Non-modified montmorillonite (Cloisite Na^+), and organically modified montmorillonite (Cloisite 15A, Cloisite 20A, Cloisite 10A, and Cloisite 30B, in order of ascending hydrophilicity) have been chosen to study the effect of molecular structure and concentration of the organomodifier on the location and dispersion of the clay in polymer blends. The resulting morphology was characterized using scanning electron microscopy (SEM), transmission electron microscopy (TEM) and laser scanning confocal microscopy (LSCM). The interface between the two immiscible polymer phases was characterized using 3D reconstructions from LSCM image data, in order to compare different loadings of organomodified clay by an estimation of mean curvature based on surface patch parameterization. The effect of polymer functionality and clay chemistry on the wettability of porous polyethylene films (formed by extraction of PEO from the cocontinuous blends) was investigated by contact angle

measurements. Thermogravimetric analysis (TGA) measurements of porous PE films allowed quantification of the amount of clay present in PE phase. Blend stability was investigated through measurement of characteristic size as a function of annealing time. The chapter closes with a comparison between the observed morphology and the theoretical predictions of nanoclay localization given by wetting coefficient evaluation, with a discussion on the validity of the wetting coefficient evaluation for selection of suitable polymer and nanoparticle candidates.

6.2 Experimental Methods

6.2.1 Materials

The low density polyethylene (LDPE) used for this study was provided by the Dow Chemical Company (LDPE 9955i), maleic anhydride grafted polyethylene (PE-g-MA) containing 1.6 wt % maleic anhydride by Chemtura (Polybond 3029), and poly(ethylene oxide) (PEO) by the Dow Chemical Company (Polyox N10). The PEO contained 1-2 wt% of fumed silica particles as a rheological modifier, which can be seen in the TEM images of the blends. Table 6.1 shows the polymer resin properties.

Table 6.1. Polymer resin properties

Polymer	Mw (kg/mol)	Functionality groups/chains	η_0(Pa s) at 150 °C	η(Pa s) at 400 s^{-1}
LDPE	59	0	2.15 x 10^4	320
PE-g-MA	79	12.9	7.72 x 10^4	450
PEO	80	2	7.93 x 10^3	320

One pristine unmodified montmorillonite (Cloisite Na^+) and four organically modified clays, (Cloisite 15A, Cloisite 20A, Cloisite 10A and Cloisite 30B) were used in these blends, and were provided by Southern Clay Products, Inc., USA. Table 6.2 shows the chemical structure of the intercalating cations and the structural information of the nanoclays, provided by the material supplier. The clays are listed in order from highest d-spacing (and most hydrophobic) to lowest

d-spacing (and most hydrophilic). Note that Cloisite 15A and Cloisite 20A have the same organomodifier but with different concentrations, resulting in different d-spacing between the clay layers. 2-Hydroxyethyl methacrylate (HEMA) monomer, azobisisobutyronitrile (AIBN) and a fluorescent dye, Rhodamine B, which were used in preparing samples for imaging by laser scanning confocal microscopy, were purchased from Aldrich and used as received.

Table 6.2. Structural information of nanoclays, including chemical structure of the interlayer cation, the capacity of the cation (similar to a concentration), and the d-spacing between the clay layers. Clays are listed in order of ascending hydrophilicity and descending d-spacing.

Nanoclay	**Interlayer cation**	**Cationic exchange capacity (meq/100g clay)**	**Basal spacing d_{001} (nm)**
Cloisite 15A	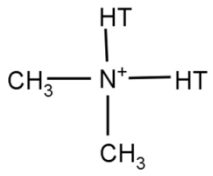	125	3.15
Cloisite 20A	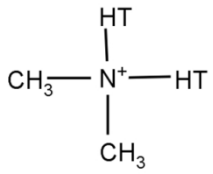	95	2.42
Cloisite 10A	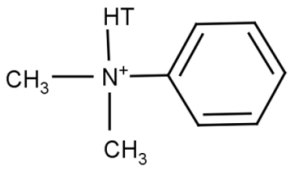	125	1.92
Cloisite 30B	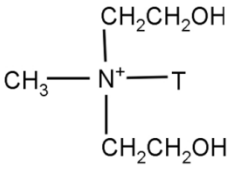	90	1.85
Cloisite Na^+	Na^+	92.6	1.17

T=tallow: linear alkyl chains (C18 (65%), C16 (30%), C14 (5%)); HT=hydrogenated tallow.

6.2.2 Rheology

Viscoelastic properties of the blend components were measured using an ARES shear rheometer (TA Instruments) using 25 mm parallel plate geometry. Frequency sweep measurements were performed at strains below the critical strain to measure linear viscoelastic properties of the components and blends at 150 °C over a frequency range from 100 – 0.1 rad/s.

6.2.3 Melt compounding

Two blending methods (batch and continuous) were employed to study the effect of mixing conditions on the location and dispersion of nanoclays and the morphology of the resulting blends. The batch melt compounding was performed in a recirculating, batch microcompounder (DACA instruments). Blends were mixed at a rotor speed of 200 RPM and temperature of 150 °C for 6 minutes under a continuous nitrogen purge. The extruded products were rapidly quenched in liquid nitrogen to freeze the morphology. The weight ratio of PE/PEO and PE-g-MA/PEO was set to the center of their cocontinuity range under the same processing conditions, as determined in previous work [13] and shown in Chapters 2 and 3.

A co-rotating Leistritz twin-extruder (screw diameter of 27 mm, L/D of 48:1), equipped with gravimetric feeders (Brabender, Missisagua, Canada), was employed for continuous melt blending. A screw speed of 150 RPM, feed rate of 5 kg/h and temperature of 150 °C were used for all runs. The clay and the PEO powder were dry mixed prior to melt mixing and fed together into the extruder via one of the two gravimetric feeders. The second gravimetric feeder was used for feeding polyethylene resins. All the materials were introduced to the beginning of the mixing barrel of the extruder through Zone 1 to maximize residence time. The extruded strands were quenched in liquid nitrogen. Two different screw configurations, a low-shear and high shear screw geometry (as shown in Figure 2.2), were used to subject the molten blends to high-intensity and medium-intensity mixing conditions. A more detailed description of the extrusion experimental setup can be found elsewhere.[161]

6.2.4 Coarsening

Small pieces of the extruded blends were annealed at 150 °C in a Wabash hydraulic press with no applied pressure. The samples were placed between two sheets of fluoropolymer-coated fabric (Premium 6 Mil, American Durafilm) in a steel mold. Annealing time was varied between 1 and 30 minutes.

6.2.5 Morphological Analysis

The blend morphology was examined by scanning electron microscopy (SEM, JOEL 6500), transmission electron microscopy (TEM, FEI Tecnai Spirit Bio-Twin) and laser scanning confocal microscopy (LSCM, Olympus Fluo View 100). SEM imaging was conducted in order to qualitatively evaluate the effectiveness of the blending and the nature of the blend morphology. Samples were prepared via cryo-microtome (Leica EM UC6 Ultramicrotome) at -160 °C using a diamond knife. The PEO phase was selectively extracted overnight in water, and the remaining PE matrix was sputter coated with 5 nm of platinum. Samples were imaged at an accelerating voltage of 5 kV and a working distance of approximately 10 mm.

TEM imaging was employed in order to visually determine nanoparticle localization within the blends. Samples were ultrathin-sectioned (approximately 50 nm thick) at -160 °C via cryo-microtome (Leica EM UC6 Ultramicrotome) equipped with a diamond knife. The ultrathin sections were transferred via eyelash onto Formvar-coated copper grids. The TEM was operated at an accelerated voltage of 120 kV. Image contrast was improved by employing both the condenser aperture and the 120 μm diameter objective aperture. No staining was required, as sufficient phase contrast could be generated without. The PEO phases tended to be brighter (white in the images), where PE phases tended to be darker (gray in the images). Clay was evident as thin black particles.

LSCM imaging was used to generate 3D images of the blends in order to qualitatively evaluate the characteristic pore size as a function of processing conditions and blend composition,

via the interfacial area per volume of the samples. Thin slices approximately 100 μm in thickness were prepared by razor blade. After overnight extraction of PEO phase in water, slices were dried and placed on microscope slides. Following PEO extraction, the samples were white and opaque. 2-Hydroxyethyl(methacrylate) (HEMA) containing 0.01 wt% Rhodamine B fluorescent dye and 1 wt% azobisisobutyronitrile (AIBN) radical initiator was dropped via pipette onto the slices, and was allowed to flow into the pores of the PE. The cover slip was placed on top of the filled samples, and then the slides were placed into an oven at 80 °C for 10-15 minutes to allow the HEMA to polymerize. At this point, the refractive index of the polymerized HEMA matched that of PE. This produced transparent slices which possessed the fluorescent phase contrast necessary for acquiring stacks of 2D images. The samples were imaged with 60x oil immersion objective and 525 nm laser excitation in order to generate a stack of 2D images at different focal depths through each sample. It should be noted that the fluorescent contrast was limited to only between the PE phase and the HEMA phase – the clay nanoparticles were not fluorescently labeled and therefore were not visible under LSCM. However, an indirect measure of interfacial clay localization could be obtained based on the curvature of the PE/PEO interface, following the method described below in Section 6.2.8.

6.2.6 Thermogravimetric Analysis

For cocontinuous blends containing organoclays, all of the continuously connected PEO could be extracted out by water bath, leaving behind a PE matrix containing any clay localized within the PE phase. TGA was used to determine the clay content residing in the PE matrix. Sample mass was measured as a function of temperature during heating from 50 °C to 590 °C with a heating rate of 10 °C/min in a nitrogen environment using a Pyris Diamond TG/DTA by Perkin Elmer Instruments. At least five repetitions of each sample were taken to avoid errors arising from non-uniform distribution of clay in polymer blends.

6.2.7 Contact Angle Measurement

To measure the water-wettability of the final porous products, static contact angle measurements were conducted on porous PE films obtained by pressing blends using a heated hydraulic press, then extracting the PEO via a water bath. Porous films were placed in deionized water and air bubbles were released beneath the LDPE or PE-g-MA film using a J-shaped needle. The bubble trapped under the surface of the film was imaged with a contact angle meter DM-CE1 (Kyowa, Japan) and the tangent contact angle (the angle between the bubble and the surface, measured on the outside of the bubble) was determined using built-in FAMAS (v 3.1.3) analyzing software. A lower contact angle indicated greater water wettability. Measurements of contact angle were taken with at least 10 gas bubbles on each specimen.

6.2.8 3D Image Analysis

The stacks of 2D images acquired by LSCM were thresholded in MATLAB and reconstructed into 3D images using Avizo (v. 6.3, http://www.vsg3d.com/avizo) interactive visualization package. A triangular mesh was generated along the interface of the 3D images using a marching cubes algorithm included in the Avizo software package. Interfacial area was calculated by summing the areas of all the triangles, A_i of the generated mesh. Dividing volume of the sample, V, by the total interfacial area gives a characteristic size, a:

$$a = V \Big/ \sum_{i=1}^{N} A_i \tag{6.1}$$

The shape of the interface was quantified via computation of local interfacial curvature from the reconstructed 3D images. The mean curvature distribution for each sample was calculated based on the mean curvature, H, at all points of interest along the interface, given by:

$$H = \frac{\kappa_1 + \kappa_2}{2} \tag{6.2}$$

where κ_1 and κ_2 are the minimum and maximum curvature (the so-called principal curvatures) at

a particular point of interest. Each point of interest is selected by generating a triangular mesh over the interface, and analyzing curvature at the vertices. Local curvature was calculated using a coordinate transformation method. Details of this calculation procedure are published elsewhere.[12,81]

6.3 Results and Discussion

6.3.1 Thermodynamic prediction of clay localization

At thermodynamic equilibrium, the location of filler in a polymer blend can be predicted by the minimization of the interfacial energy. According to Young's equation, it is possible to find the equilibrium position of the filler by evaluating the wetting coefficient ω_a.

$$\omega_a = \frac{\gamma_{organoclay-PE} - \gamma_{organoclay-PEO}}{\gamma_{PE-PEO}} \tag{6.3}$$

where each γ represents the interfacial energy for all potential interfaces within the blend – the clay-PE interface, the clay-PEO interface, and the PE-PEO interface. If the wetting coefficient is >1, the clay is predicted to be in the PEO phase, since the interfacial tension of the clay-PE interface is high and the interfacial tension of the clay-PEO phase is very low. If ω_a has a value <-1, the clay will preferentially be located in PE since the clay-PE interfacial tension is much lower than the clay-PEO interfacial tension. The wetting coefficient will be between -1 and 1 when the difference between the clay-PE and clay-PEO interfacial tension is less than the PE-PEO interfacial tension. In this case, the clay will localize at the PE-PEO interface to minimize the interfacial tension.

Due to the experimental difficulty in accurately evaluating interfacial tension between nanoparticle and a molten polymer, interfacial tension was estimated from known surface energies of the components. The surface energy of a single blend component is characterized by the sum of the dispersive and polar contribution. The interfacial tension between two blend

components can then be evaluated based on the surface energies of the components and the harmonic mean of the dispersive and polar contributions:[162]

$$\gamma_{12} = \gamma_1 + \gamma_2 - 2\left(\sqrt{\gamma_1^d \gamma_2^d} + \sqrt{\gamma_1^p \gamma_2^p}\right) \quad (6.4)$$

where γ_1 and γ_2 are the surface energies of components 1 and 2; γ_1^d and γ_2^d are the dispersive parts of the surface tension of components 1 and 2; and γ_1^p and γ_2^p are the polar parts of the surface tension of components 1 and 2. The values of the surface energy of polymers and clays at the processing temperature have been extrapolated from values reported in literature[163-166] and are summarized in Table 6.3.

Table 6.3. Total surface energy and the dispersive and polar components for polymers and clays.

Material	Temperature coefficient -dγ/dT (mN/m)	Dispersive component at 150 °C (mN/m)	Polar component at 150 °C (mN/m)	Total surface energy at 150 °C (mN/m)
LDPE [163]	0.057	28.29	0	28.29
PE-g-MA [164]	0.057	30.42	0.94	31.36
PEO [163]	0.076	23.78	9.23	33.02
Cloisite 15A [165]	0.1	22.2	7.76	29.84
Cloisite 20A [165]	0.1	22.2	7.17	29.38
Cloisite 10A [166]	0.1	24.16	8.53	32.7
Cloisite 30B [165]	0.1	24.76	10.88	35.65
Cloisite Na^+ [166]	0.1	28.73	19.37	48.1

The calculated values for the interfacial tension between each pair of blend components, as well as the wetting parameter and the predicted location of the clays in the studied polymer blends are reported in Table 6.4. In general, these predictions suggest that interfacial localization will be achieved with the most hydrophobic clays (Cloisite 15A, 20A, and 10A) for both PE/PEO and PE-g-MA/PEO blends. For the more hydrophilic clays (Cloisite Na+ and 30B), the clay is predicted to be randomly dispersed within the PEO phase for both LDPE/PEO and PE-g-

MA/PEO blends, primarily due to the very high interfacial tension between the clay and the PE.

Table 6.4. Clay localization predictions based on wetting coefficients.

Polymer/clay blend	Interfacial tension, γ_{12} (mN/m)	Wetting coefficient, ω_a	Location prediction
LDPE/PEO/Cloisite 15A	$\gamma_{LDPE/PEO}$=9.43 $\gamma_{c15A/PEO}$=2.95 $\gamma_{c15A/LDPE}$=8.14	0.55	Interface
LDPE/PEO/Cloisite 20A	$\gamma_{LDPE/PEO}$=9.43 $\gamma_{c20A/PEO}$=0.15 $\gamma_{c20A/LDPE}$=7.54	0.78	Interface
LDPE/PEO/Cloisite 10A	$\gamma_{LDPE/PEO}$=9.43 $\gamma_{c10A/PEO}$=0.01 $\gamma_{c10A/LDPE}$=8.69	0.92	Interface
LDPE/PEO/Cloisite 30B	$\gamma_{LDPE/PEO}$=9.43 $\gamma_{c30B/PEO}$=0.08 $\gamma_{c30B/LDPE}$=10.99	1.15	PEO
LDPE/PEO/Cloisite Na+	$\gamma_{LDPE/PEO}$=9.43 $\gamma_{cNa+/PEO}$=2.08 $\gamma_{cNa+/LDPE}$=19.36	1.83	PEO
PE-g-MA/PEO/Cloisite 15A	$\gamma_{PE\text{-}g\text{-}MA/PEO}$=4.69 $\gamma_{c15A/PEO}$=2.95 $\gamma_{c15A/PE\text{-}g\text{-}MA}$=3.97	0.21	Interface
PE-g-MA /PEO/Cloisite 20A	$\gamma_{PE\text{-}g\text{-}MA/PEO}$=4.69 $\gamma_{c20A/PEO}$=0.15 $\gamma_{c20A/PE\text{-}g\text{-}MA}$ =3.57	0.72	Interface
PE-g-MA /PEO/Cloisite 10A	$\gamma_{PE\text{-}g\text{-}MA/PEO}$=4.69 $\gamma_{c10A/PEO}$=0.01 $\gamma_{c10A/PE\text{-}g\text{-}MA}$=4.17	0.88	Interface
PE-g-MA /PEO/Cloisite 30B	$\gamma_{PE\text{-}g\text{-}MA/PEO}$=4.69 $\gamma_{c30B/PEO}$=0.08 $\gamma_{c30B/PE\text{-}g\text{-}MA}$=10.99	1.20	PEO
PE-g-MA/PEO/Cloisite Na+	$\gamma_{PE\text{-}g\text{-}MA/PEO}$=4.69 $\gamma_{cNa+/PEO}$=2.08 $\gamma_{cNa+/PE\text{-}g\text{-}MA}$=11.81	2.07	PEO

These theoretical predictions are not without limitations. The first major limitation of the model is in predicting the interfacial tension between PE-g-MA and PEO. The theoretical prediction of interfacial tension based upon Eq. 6.4 does not bring into consideration any

additional interfacial species such as block copolymers, and so cannot account for the formation of PE-g-PEO graft copolymers in the PE-g-MA/PEO blend. In results presented in Chapters 2 and 3, the interfacial tension of the PE-g-MA/PEO blend decreased by a factor of about 5 compared to the PE/PEO blends, whereas Eq. 6.4 predicts only a two-fold decrease in interfacial tension. It should be noted that values of interfacial tension predicted here compared to Palierne model results are expected to differ based upon differences in the method of prediction.

Secondly, this model is limited to arguments of thermodynamic equilibrium, and assumes that the system has sufficient time and ability to achieve equilibrium. However, in the experimental blended systems, this may not necessarily be the case, due to the blends being frozen in a non-equilbrium state after extrusion. Furthermore, this does not consider the potential kinetic effects of other interfacially localized species, like the PE-g-PEO graft copolymers, which could disrupt the clay's ability to reach the PE-PEO interface. The effects on particle localization caused by the brush-like nature of the PE-g-PEO graft copolymers and the elasticity of an interface covered with such a brush cannot be considered by the current model. The veracity of these predictions and the extent of these limitations will be evaluated based upon the blending results below, first evaluating the non-reactive LDPE/PEO case, and then exploring the reactive PE-g-MA/PEO blends.

6.3.2 LDPE/PEO blends with clay

6.3.2.1 Unmodified versus organomodified clay

The effect of incorporating pristine Cloisite Na^+ and organically modified Cloisite 20A on the morphology of LDPE/PEO blend is shown Figure 6.1. SEM micrographs show the LDPE/PEO 55/45wt% blend with no clay (Figure 6.1a), and with 5 wt% of Cloisite Na^+ and Cloisite 20A (Figure 6.1b,d), respectively. With addition of Cloisite Na^+, the characteristic size, *a*, (calculated from reconstructed 3D images) changes from 7.2 to 4.9 μm. It can be also observed

that phase domains appear more elongated and the blend morphology looks less uniform. However, Cloisite 20A depicts a clear compatibilization effect with characteristic size reduction to 2.0 μm. TEM micrographs depict that Cloisite Na^+ (Figure 6.1c) is primarily located in the PEO phase with little interfacial localization, while Cloisite 20A (Figure 6.1e) is located at the interface between LDPE and PEO domains. This is consistent with the prior predictions based on the interfacial wetting coefficient. In both TEM images, fumed silica, which is added to PEO to improve processing, can also be seen.

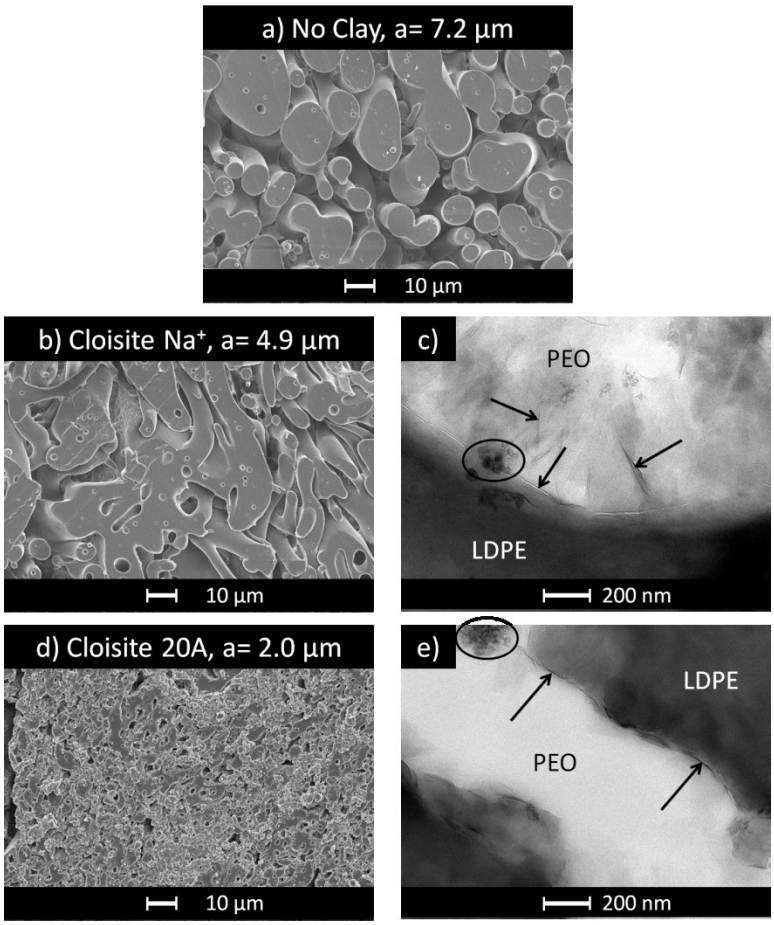

Figure 6.1. SEM and TEM micrographs of LDPE/PEO with clay, from batch mixing: a) LDPE/PEO; b,c) LDPE/PEO/Cloisite Na^+; d,e) LDPE/PEO/Cloisite 20A. For the TEM images in c and e, the darker phase is LDPE and the lighter phase is PEO. Clay showed up as elongated dark particles. Fumed silica, and additive to the PEO, is circled and can be seen as clustered dark particles. Characteristic size, *a*, is shown for each sample. Arrows point to the clay platelets.

The polar interactions between the Na^+ cation and PEO are favorable, which results in

intercalation and apparent exfoliation of Cloisite Na^+ in this phase. In the absence of significant interfacial localization of Cloisite Na^+, the slight decrease in characteristic size is most likely due to the increase in viscosity of the PEO phase. With two bulky tallow groups, the ammonium cations present in the Cloisite 20A are very hydrophobic and consequently have a relatively larger affinity for the interface and LDPE phase. Similar behavior of Cloisite 20A preferentially segregating to the interface with some clay dispersed in the matrix was previously reported in polypropylene/ethylene–propylene rubber (EPR)/ clay nanocomposites.[167]

Coarsening experiments were performed to examine the effect of clay on the morphological stability. The characteristic pore size, measured via LSCM, as a function of quiescent annealing time at 150 °C is shown in Figure 6.2. As expected, LDPE/PEO with no clay coarsened very quickly and showed no plateau after 30 min of annealing.

The blend containing Cloisite Na^+ showed a dramatic increase in characteristic size during the first three minutes of annealing, followed by a slower rate of coarsening. No plateau in characteristic size was observed for these samples, suggesting that the mechanism of coarsening was similar to that of the LDPE/PEO blends without clay. However, the exfoliated clay particles increased the viscosity, which served to slow the rate of coarsening relative to the no-clay LDPE/PEO blend, without completely stopping coarsening. The significant slowing of the rate of coarsening after long times is likely due to small amounts of interfacially localized Cloisite Na^+, which can be expected to eventually jam the interface after sufficient reduction in interfacial area.

Alternatively, the blend containing interfacially localized Cloisite 20A showed suppression of coarsening during annealing. In this case, the clay is expected to be thermodynamically confined to the interface, as removing clay from the interface and dispersing it randomly into either phase would incur an energetic penalty due to the creation of new energetically unfavorable PE/PEO interface. Because the particles are confined, any reduction in

the interfacial area due to coarsening would quickly cause the particles to jam into each other, preventing further reduction in the interfacial area. This is similar to results for reactively compatibilized cocontinuous blends shown in Chapter 2 and observed previously,[13,35] where jamming of the interfacially localized graft copolymers prevented coarsening during annealing. This suggests that the two compatibilization processes share a similar stabilization mechanism. These results show that simple presence of clay randomly dispersed through the blend is not sufficient for arresting coarsening, and that the clay must be localization at the interface in order to reap the stabilizing effects.

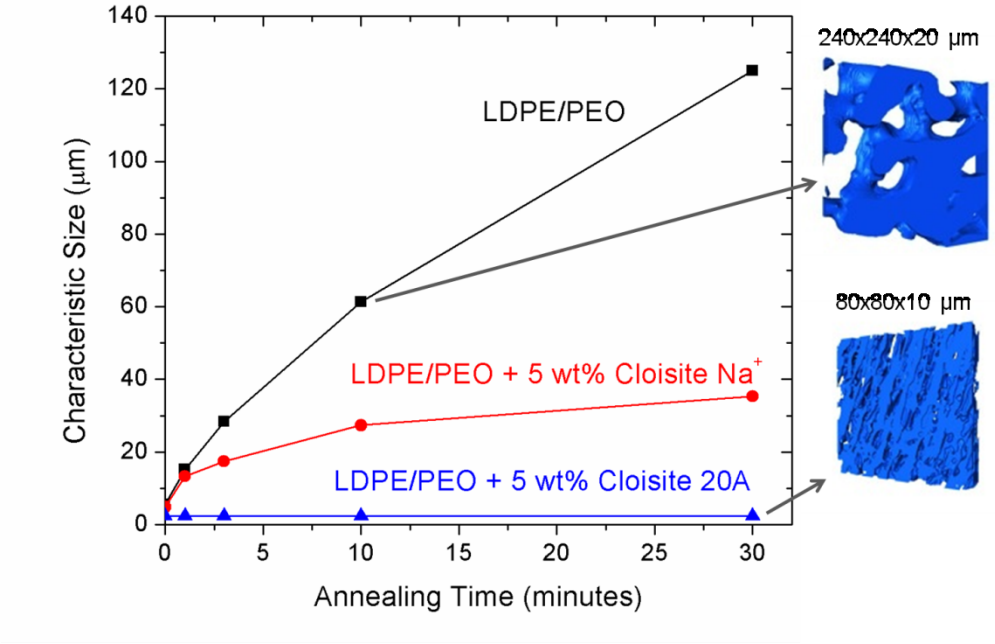

Figure 6.2. Characteristic phase size as a function of annealing time at 150 °C for batch-blended LDPE/PEO with clay. Representative LSCM images are shown with the outer dimensions of each image.

6.3.2.2 Concentration dependence of stabilization and interfacial curvature

In order to determine the minimum amount of clay required to completely suppress coarsening during annealing, five blends of LDPE/PEO were prepared by varying the amount of Cloisite 20A between 0.25 and 5 wt%. The coarsening rates of these blends are shown in Figure

6.3. No plateau of characteristic size was observed during the course of the experiment when blending with only 0.25 wt% Cloisite 20A. This seems to indicate that at this loading, insufficient clay was present at the interface to provide complete stabilization. However, if some degree of interfacial localization is present, an eventual suppression may be expected, although not observed here, once there is sufficiently little surface area so as to be completely jammed with clay. By increasing the clay loading to 0.5 wt% Cloisite 20A, the coarsening behavior reaches a plateau after 10 minutes at a size of roughly 11 μm, after which the characteristic size of the blends ceased to increase with further annealing. Further increasing the loading of Cloisite 20A beyond 0.5 wt% completely suppressed coarsening at a progressively smaller characteristic size, with an almost immediate onset of plateau behavior.

However, only a limited amount of additional stabilization is gained when increasing the clay content above 1 wt%. This suggests that at some point, the blend can no longer create more interfacial area between the two phases, even in the presence of additional compatibilizing agent. There are two interpretations for this phenomenon. The first is that the amount of interfacial area that can be generated during mixing can reach a steady state point, where the rate of area creation during mixing (based on the mixing properties and rheology) achieves equilibrium with the rate of loss of interface (based on the interfacial tension of the components). Similar trends to this were observed in the results of PE-g-MA/PEO blends from Chapter 2 and 3, which did not show complete conversion of all available reactive groups and an ever increasing interface with mixing time despite the opportunity to create continually more stabilized interface with PE-g-PEO copolymers at that new interfaces.

The second interpretation is based on the size and stiffness of the particles. The particles have a finite bending modulus and size, and can therefore not conform to an interface with an arbitrarily small feature size and radius of curvature, and so a practical limit is set based on particle size. This interpretation is supported by work by Rafailovich and coworkers, who studied

droplet blends compatibilized with interfacially localized functional clays. They found that due to the high bending energy of the clay platelets, droplet sizes could not be reduced to smaller than the length of the clay platelets.[48] Further experiments are needed to deduce which interpretation dominates this lack of significant improvements to stabilization with high clay loading. However, based on either interpretation, the small decrease in characteristic size with >1 wt% clay are likely be attributed to an increase in blend viscosity in a blend system with an interface that is already saturated with particles.

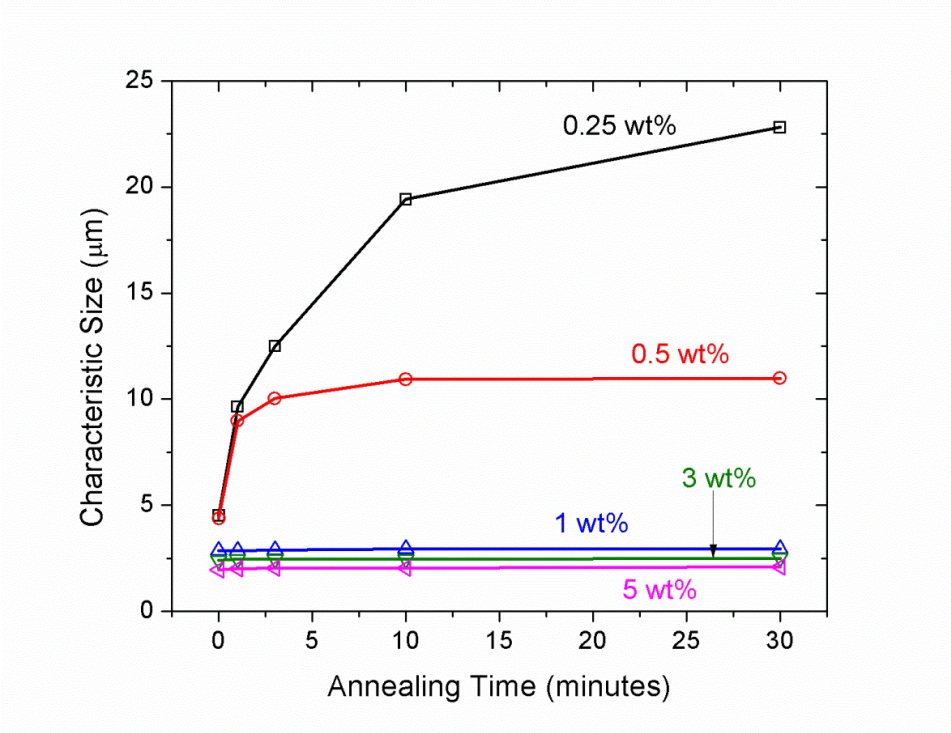

Figure 6.3. Characteristic size as a function of annealing time at 150 °C for LDPE/PEO/Cloisite 20A, with varying amounts of Cloisite 20A loading.

Table 6.5. Interfacial coverage of Cloisite 20A before and after 30 minutes of coarsening. Clay is assumed to be 10 layers thick on average.

Clay wt%	a, initial (μm)	a, final (μm)	Coverage, initial ($A_{clay}/A_{interface}$)	Coverage, final ($A_{clay}/A_{interface}$)
0.25 wt%	4.5	23	0.28	1.4
0.5 wt%	4.4	11	0.54	1.4
1 wt%	2.9	3.0	0.71	0.73

3 wt%	2.4	2.5	1.8	1.9
5 wt%	2.0	2.1	2.4	2.6

The final characteristic size of the annealed blends could be correlated to the total amount of clay in the blend. Assuming that all clay localized at the interface, a fractional coverage could be calculated by the total interfacial area of the clay divided by the interfacial area of the blend:

$$Coverage = \frac{\phi_{clay} a}{N d_{001}} \tag{6.5}$$

where ϕ_{clay} is the volume fraction of the clay in the blend, a is the characteristic blend size, N is the number of layers in a single clay tactoid (estimated to be 10 based on observation of TEM micrographs), and d_{001} is the interlayer spacing of the clay. The coverage results are shown in Table 6.5. The final coverage after 30 minutes of annealing varies between 0.7 – 1.4 for the blends with 1 wt% or less of clay. This suggests that coarsening of the blends is suppressed once the entire interface is covered by clay, thereby jamming the clay together and preventing further reduction in interfacial area. The blends with >1 wt% clay have coverage values above 1, even prior to coarsening. This suggests that more clay is present than is needed to stabilize the interface, and much of the clay exists within the bulk polymer phases and not at the interface.

The effect of Cloisite 20A loading on the mean curvature distribution of these blends was obtained from differential geometry of 3D images and is presented in Figure 6.4. It is expected that as the interfacial area increases with addition of more Cloisite 20A, the width of the mean curvature distribution increases as well. However, the symmetry and shape of the distribution can reveal information about curvature uniformity and interfacial surface properties. The mean curvature for LDPE/PEO interface is symmetrical and centered around zero. However, as the Cloisite 20A loading increases, the distribution gets wider and also loses its symmetry. This can be attributed to the fact that when rigid platelet-like particles saturate the interface, bending energy along the interface increases making the phase domains more irregular in shape. This may

be particularly notable cases where the clay is interfacially localized but still shows a slight thermodynamic preference for one phase over the other. According to the wetting parameter results from Table 6.4, the clay was interfacially localized with a slight preference for localizing in PEO over LDPE. A preference to favor one "side" of the interface will have a tendency to create more asymmetry in the curvature due to the stiffness of the clay particles, preventing the interface from adopting arbitrarily small concave radii of curvature towards the side containing the clay. This is the case for Cloisite 20A in PE/PEO blends, as the clay still has a lower interfacial tension with PEO. These results suggest that with further experimental and mathematical development, the mean curvature could be potentially used for quantification of interfacially localized clay. [66]

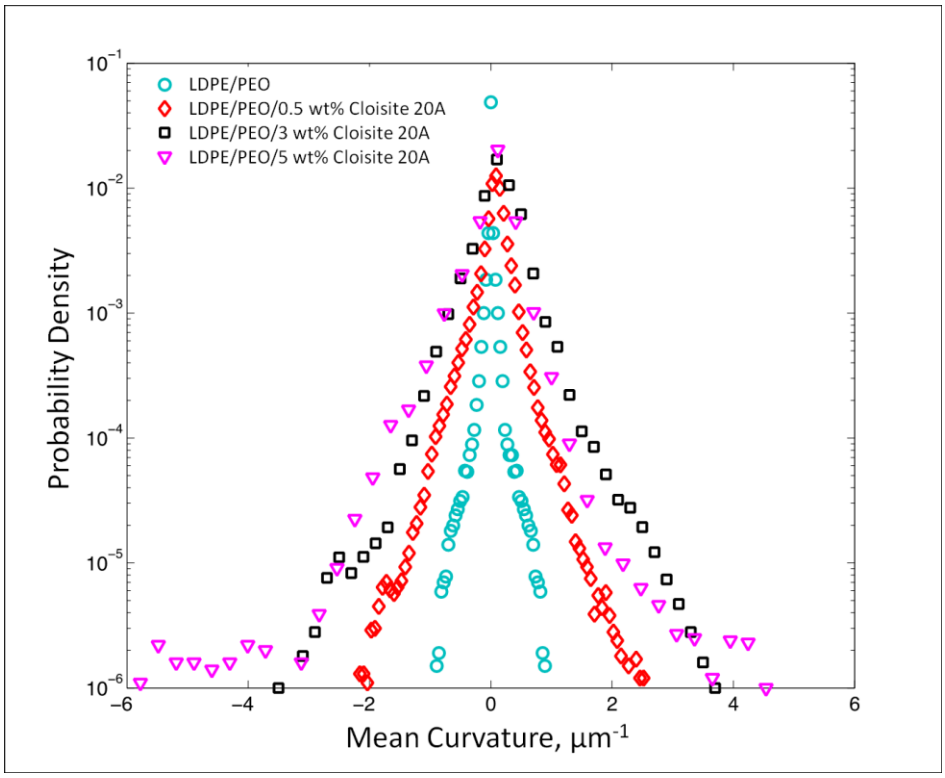

Figure 6.4. Curvature of LDPE/PEO/Cloisite 20A blends as a function of Cloisite 20A loading.

6.3.2.3 Comparison of modified clays in low-shear mixing

Extrusion experiments were performed to examine the effect of the type of processing on

the clay location and distribution in the non-reactive and reactive blends of interest. Since bench scale experiments confirmed that Cloisite Na^+ was not a suitable compatibilizer for these blends, it was excluded from this set of experiments. Instead, this study compared the organically modified clays to probe the effect of different organomodifier on clay localization and the resultant blend morphology. The ratio of LDPE/PEO was set to 40/60 wt% and clays were added at 5 wt% loading. Mixing for these experiments was performed using the low shear screw configuration (see Figure 2.2) in the twin screw extruder.

Figure 6.5 shows the effect of the different organoclays on morphology of non-reactive LDPE/PEO blends with the low shear screw configuration applied. As can be seen from the SEM images, compatibilization is readily evident in all blends prepared using the organically modified clays. The TEM images show that all clays localized at the interface between the LDPE and PEO phases. This is consistent with all results from the wetting coefficient predictions, except for the case of Cloisite 30B, where the clay was predicted to localize in the PEO phase. However, the wetting coefficient for Cloisite 30B in LDPE/PEO is 1.15, close to 1. Given the possibility of error in the predictions, some interfacial localization could be expected.

Results from coarsening experiments, shown in Figure 6.6, depict the ability of each type of clay to stabilize the morphology of LDPE/PEO blends. It is clear that the coarsening mechanism is similar for all clays, and the final characteristic size is mainly dependent on the initial blend characteristic size. Cloisite 30B, the most hydrophilic clay with the smallest d-spacing, resulted in the largest phase size domains. This could be attributed both to an increased propensity to localize in the PEO phase based on wetting parameter predictions, or to greater difficulties in achieving exfoliation due to the smaller d-spacing.

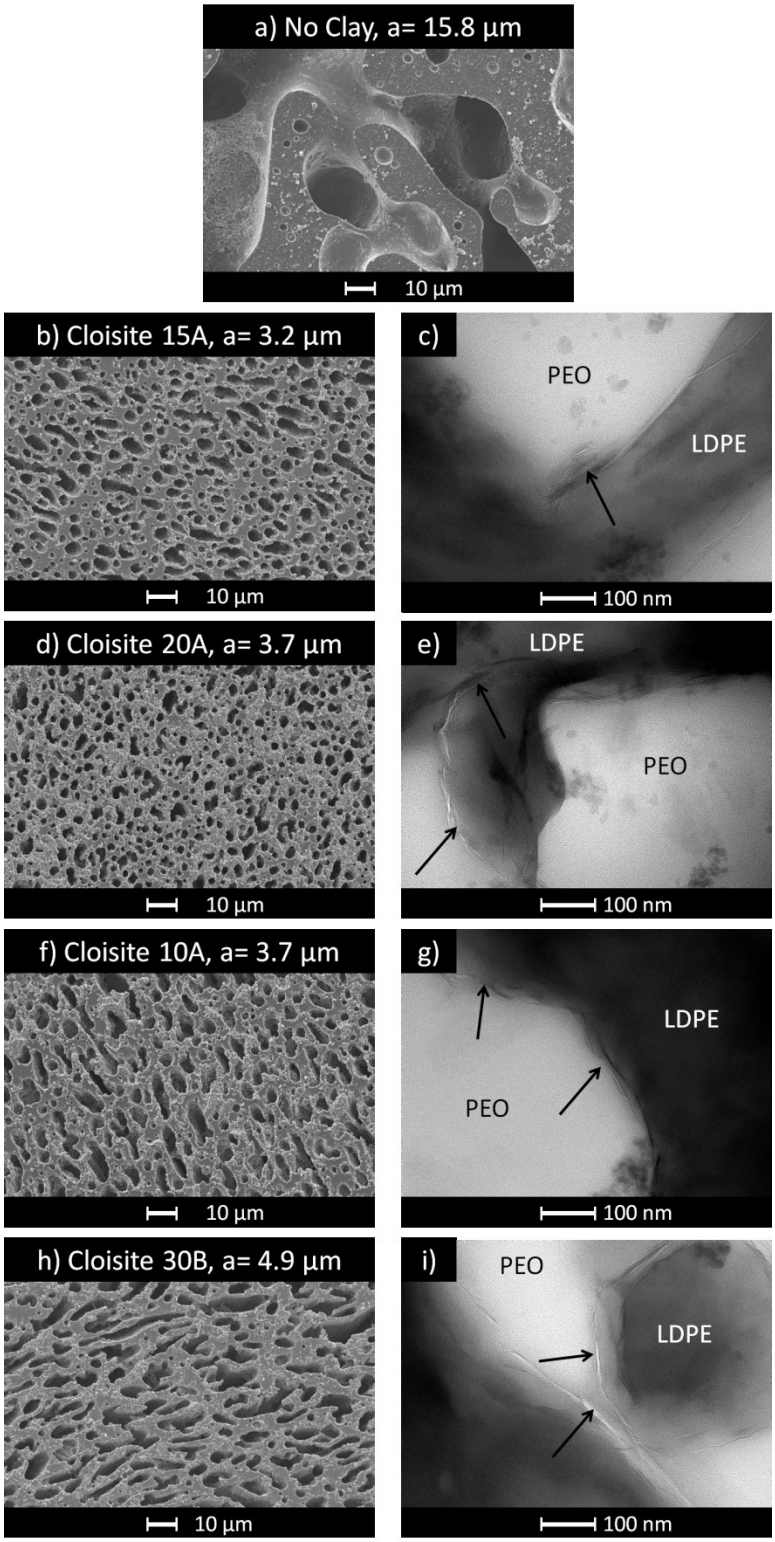

Figure 6.5. SEM and TEM micrographs of LDPE/PEO with organoclay, prepared by extrusion using the low shear screw geometry. a) LDPE/PEO; b,c) LDPE/PEO/Cloisite 15A; d,e) LDPE/PEO/Cloisite 20A; f,g) LDPE/PEO/Cloisite 10A; h,i) LDPE/PEO/Cloisite 30B.

On the other hand, Cloisite 15A resulted in the smallest phase size. This could be attributed to it having the largest interlayer spacing and two bulky hydrophobic tallow groups in the organomodifier. The large interlayer-spacing would allow polymer chains to more easily intercalate the layers, ultimately improving exfoliation and increasing the clay's surface area per volume, allowing it to more readily cover an interface. Its hydrophobic cation also makes it more compatible with LDPE chains than the other organically modified clay. Of the LDPE/PEO blends, LDPE/PEO/Cloisite 15A had a wetting coefficient nearest to zero, suggesting relatively less preference for one phase over another and more thermodynamic inclination to localize at the interface. The end result was highly exfoliated particles with a strong interfacial localization.

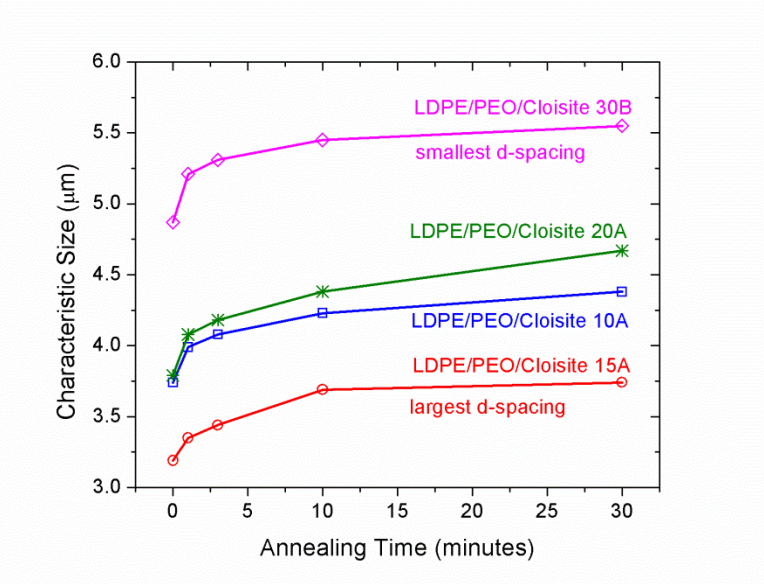

Figure 6.6. Characteristic size as a function of annealing time at 150 °C for LDPE/PEO/5 wt% organoclay blends, prepared by twin screw extrusion using the low-shear screw geometry.

It is also important to note that much smaller characteristic sizes were obtained from blends prepared in the DACA microcompounder, as is evident when comparing LDPE/PEO blends and LDPE/PEO/5 wt% Cloisite 20A blends prepared by each method. It is estimated that the shear rate in the low-shear screw geometry extruder is higher than in the batch microcompounder. An increased shear rate would be expected to increase shear-induced

coalescence of the polymer phases, resulting in larger characteristic size. A higher shear rate would also reduce the viscosity of the polymer material, which would actually serve to reduce the ability to transfer stress to the clay particles – this may reduce the amount of exfoliation observed. A lower overall viscosity would also likely create larger cocontinuous features, consistent with results from Chapters 2 and 5. Finally, the higher shear rate may actually do more to disrupt the system from equilibrium, which may lead to random particle distributions within the phases instead of interfacially localized particles.

In order to gain more insight about the location of clays in the prepared blends, thermogravimetric and rheological analyses were performed using the LDPE matrix. This was obtained by water extraction of the continuous PEO phase, followed by melting and pressing of the remaining LDPE to remove the pores. The TGA profiles and storage modulus of the LDPE phases of the blends are shown in Figure 6.7. These rheology and TGA results are complementary: higher clay content in LDPE phase, as measured in TGA, corresponded to an increase in storage modulus. However, blends containing Cloisite 15A, which was the most successful compatibilizer for LDPE/PEO blends, showed the lowest amount of clay in the LDPE phase. However, this is inconsistent with the previous predictions based on wetting coefficients, where Cloisite 15A should be the most thermodynamically compatible with LDPE. A deeper explanation for this observation is not clear, but an initial hypothesis is that it may be due to the most hydrophobic clay having a stronger driving force to the interface, such that it is more prone to delamination from the interface during PEO extraction, resulting in the appearance of less clay according to rheology and TGA. Conversely, the more hydrophilic clays show little interfacial preference, and so in the final morphology that has been frozen in place away from thermodynamic equilibrium, their localization was more strongly determined by kinetic and rheological effects. This is supported by the rheological data of the pure polymers (shown in Chapter 2, Figure 2.1), where the LDPE viscosity decreases faster than PEO viscosity with

increasing shear rate, and LDPE viscosity is lower than PEO viscosity at shear rates greater than 100 s^{-1}. This is consistent with work by Feng and coworkers,[160] who observed that nanoparticles have a higher probability to be found in the lower viscosity phase during mixing processes where particle localization will be far from thermodynamic equilibrium.

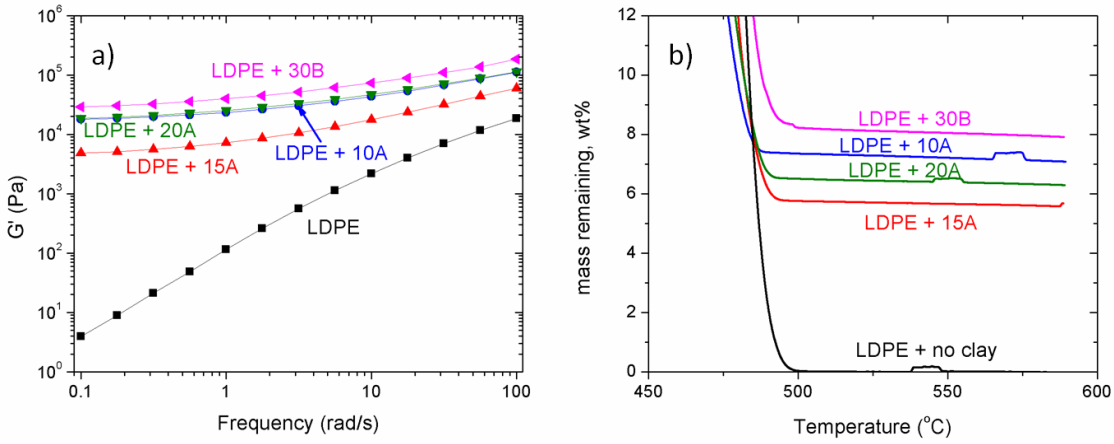

Figure 6.7. a) Storage modulus and b) TGA analysis of LDPE/Clay, obtained after extraction of PEO phase in water and then pressing the remaining LDPE phase to remove the pores.

6.3.2.4 Comparison of modified clays in high-shear mixing

To further investigate the effect of flow on migration of particles and the resultant morphology, a higher mixing intensity screw configuration was applied on the non-reactive and reactive blends. Again in this case, since the unmodified Cloisite Na^+ was previously shown to be a poor compatibilizer, only the organically modified clays were used in this experiment. The morphology of LDPE/PEO with different clays subject to mixing with the high-shear screw geometry is shown in Figure 6.8.

The phase domain size is larger for all blends in comparison to low shear extrusion experiments, which is consistent with the comparison between the batch mixed and low-shear mixed blends. In each case, a higher mixing shear rate caused greater amounts of shear induced coalescence, resulting in larger domain sizes. Numerical values of the domain sizes will be summarized at the end of the chapter in Table 6.6.

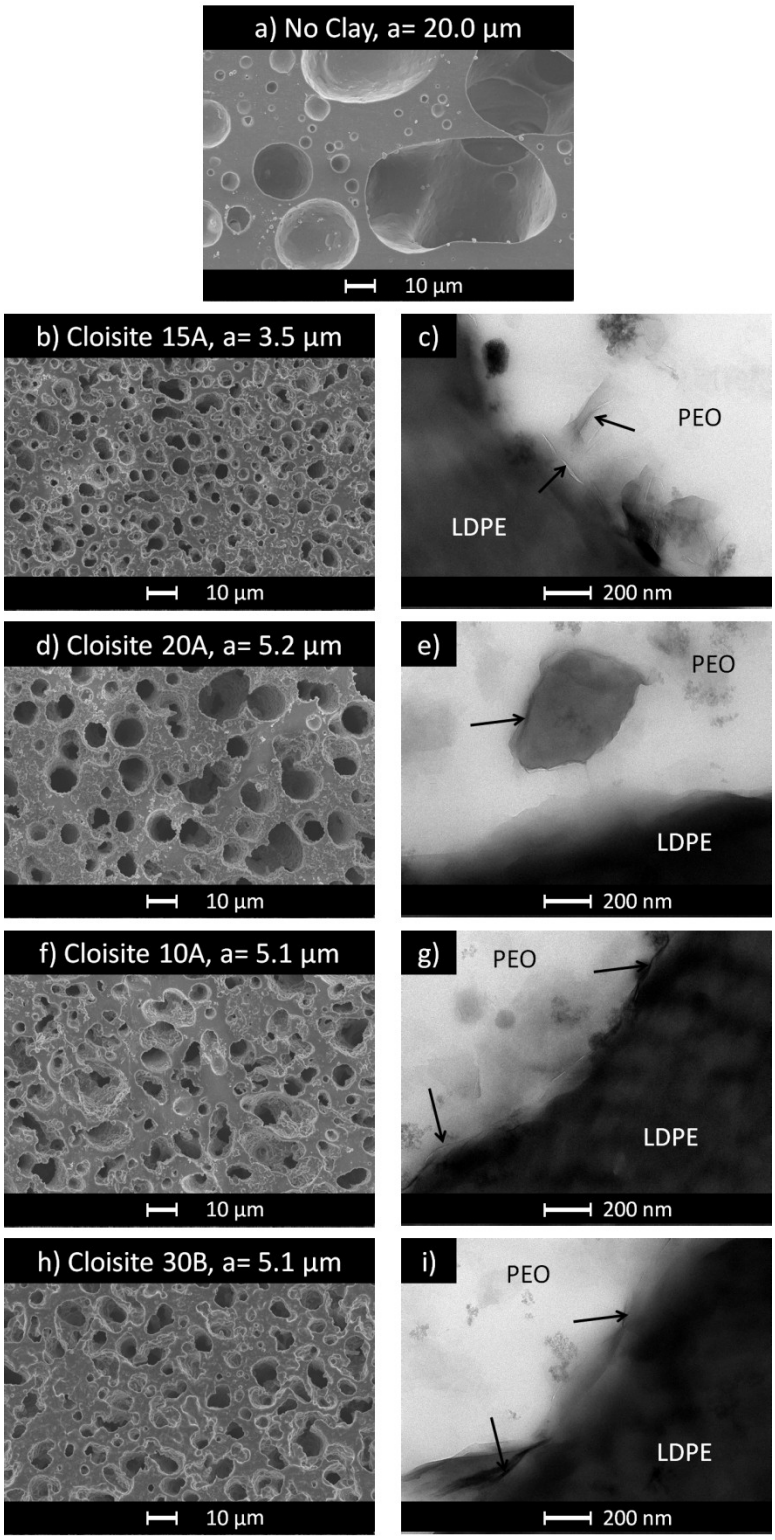

Figure 6.8. SEM and TEM micrographs of LDPE/PEO with organoclay, prepared by extrusion using the high shear screw geometry. a) LDPE/PEO; b,c) LDPE/PEO/Cloisite 15A; d,e) LDPE/PEO/Cloisite 20A; f,g) LDPE/PEO/Cloisite 10A; h,i) LDPE/PEO/Cloisite 30B.

TEM images still show clay particles localized along the LDPE/PEO interface, along with clay distributed randomly in each phase, suggesting again that the final morphology is kinetically trapped away from thermodynamic equilibrium. However, Cloisite 15A remained the most successful compatibilizer for high shear LDPE/PEO system, as it was in the low shear experiments, which is again consistent with wetting parameter predictions. This suggests that the thermodynamic predictions have some value in predicting nanoparticle behavior, even when the system is subject to very high rate mixing and kinetic mixing effects are dominant.

6.3.3 PE-g-MA/PEO blends with clay

6.3.3.1 Unmodified versus organomodified clay

Reactively compatibilized 40/60 wt% PE-g-MA/PEO and the corresponding blends containing 5 wt % Cloisite Na^+ and Cloisite 20A were prepared by batch microcompounder. The morphology is shown in the SEM and TEM images of Figure 6.9. Significant pore size reduction for the PE-g-MA/PEO blend in comparison to non-reactive LDPE/PEO blend (see Figure 6.1a) is evident, which is consistent with the results reported in Chapters 2 and 3. However, PE-g-MA/PEO blends processed with Cloisite Na^+ do not show any decrease in the characteristic size relative to PE-g-MA/PEO blends with no clay. SEM and TEM images of these blends (Figure 6.9b and c) depict large aggregates of Cloisite Na^+, which explains its lack of additional compatibilizing effect – without exfoliation, the clay cannot contain sufficient interfacial area to stabilize the morphology. These aggregates appear to localize at the interface within the PE-g-MA phase, which is contrary to the prediction based on wetting parameters, which suggest that the Cloisite Na^+ should be dispersed in the PEO phase. The reason for the observed PE localization and the lack of exfoliation compared to the LDPE/PEO/Cloisite Na^+ case, where Cloisite Na^+ was well exfoliated and dispersed in the PEO phase, is not yet fully understood. However, it is possible that due to the ionic nature of the clay, the polar functional groups on PE-

g-MA may interact at the charged clay surface, reducing exfoliation by preventing polymers from intercalating the clay layers.

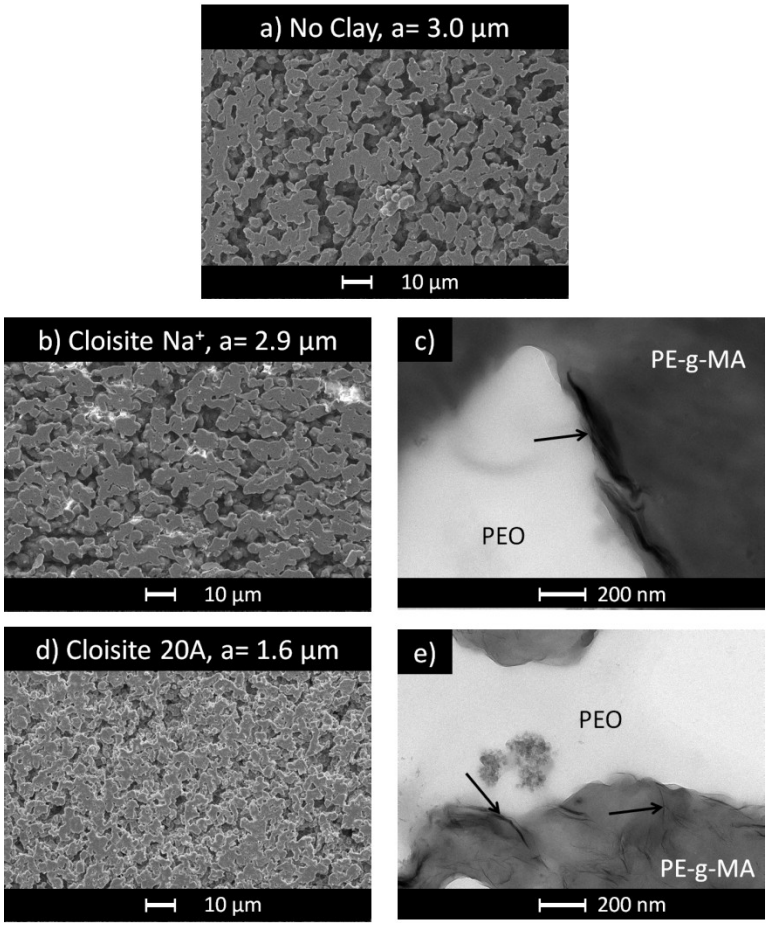

Figure 6.9. SEM and TEM micrographs of PE-g-MA/PEO with Cloisite Na^+ and Cloisite 20A: a) PE-g-MA/PEO. b,c) PE-g-MA/PEO/Cloisite Na+. d,e) PE-g-MA/PEO/Cloisite 20A. For the TEM images in d and e, the darker phase is PE-g-MA and the lighter phase is PEO. Clay showed up as long, dark particles. Clay platelets are highlighted with arrows. Fumed silica, a rheological modifier present in PEO, appears as dark clusters.

Addition of organomodified Cloisite 20A (see Figure 6.9d and e) reduces the characteristic size of the blend relative to PE-g-MA/PEO with no clay. The TEM image also confirms the presence of intercalated Cloisite 20A present at the interface and PE-g-MA phase. The interfacial localization is expected in this case according to the wetting parameters, though the presence of clay within the PE-g-MA phase is not, due Cloisite 20A possessing a lower interfacial energy with PEO. This PE-g-MA localization supports the previous hypothesis of an

additional polar or ionic interaction between PE-g-MA and the montmorillonite structure.

Previous work has investigated the effect of Cloisite 20A on the morphology of PP/PS and PP-g-MA/PS blends in 80/20 and 50/50 ratios.[168] With 50/50 wt% PP/PS, the addition of 2 wt% of Cloisite 20A had no effect on the morphology, but with 5 wt%, there was a noticeable decrease of phase size. With PP-g-MA/PS, the decrease in phase size is seen at both 2 wt% and 5 wt%. However, in their TEM results, clay localized at the interface in the non-functional PP/PS system, but was predominantly dispersed in the PP-g-MA phase of the functional blends, citing maeic anhydride interactions with clay hydroxyl groups as the cause for improvements in compatibilization. Rheological analysis and interfacial tension measurement via the drop deformation method indicated that this effect was due to the decrease in interfacial tension rather than increase in blend viscosity.

These previous results can aid in understanding the present comparison between LDPE/PEO and PE-g-MA/PEO blends with clay. The observation of clay localization within PP-g-MA is similar to the present results showing higher clay compatibility with functional PE-g-MA than thermodynamics initially suggest. In this study, the characteristic size decrease in LDPE/PEO blend was observed even with 0.25 wt% of Cloisite 20A, whereas with 1 wt% the morphology was completely stabilized during annealing. Given that the interfacial tension between LDPE and PEO will be much higher than that of PP/PS, it is unsurprising that the organoclays show better localization and compatibilizing effect, and can coat the interface with less material. Additionally, the viscosity of the present system is much higher – the work by Utracki[168] reported viscosities measured at a shear rate of 50 s^{-1} on the order of 10-100 Pa-s, whereas the viscosity of the present PE/PEO systems is on the order of 1000 Pa-s for the same shear rate. This increased viscosity will increase exfoliation, again promoting compatibilization with less clay.

6.3.3.2 Comparison of modified clays in low-shear mixing

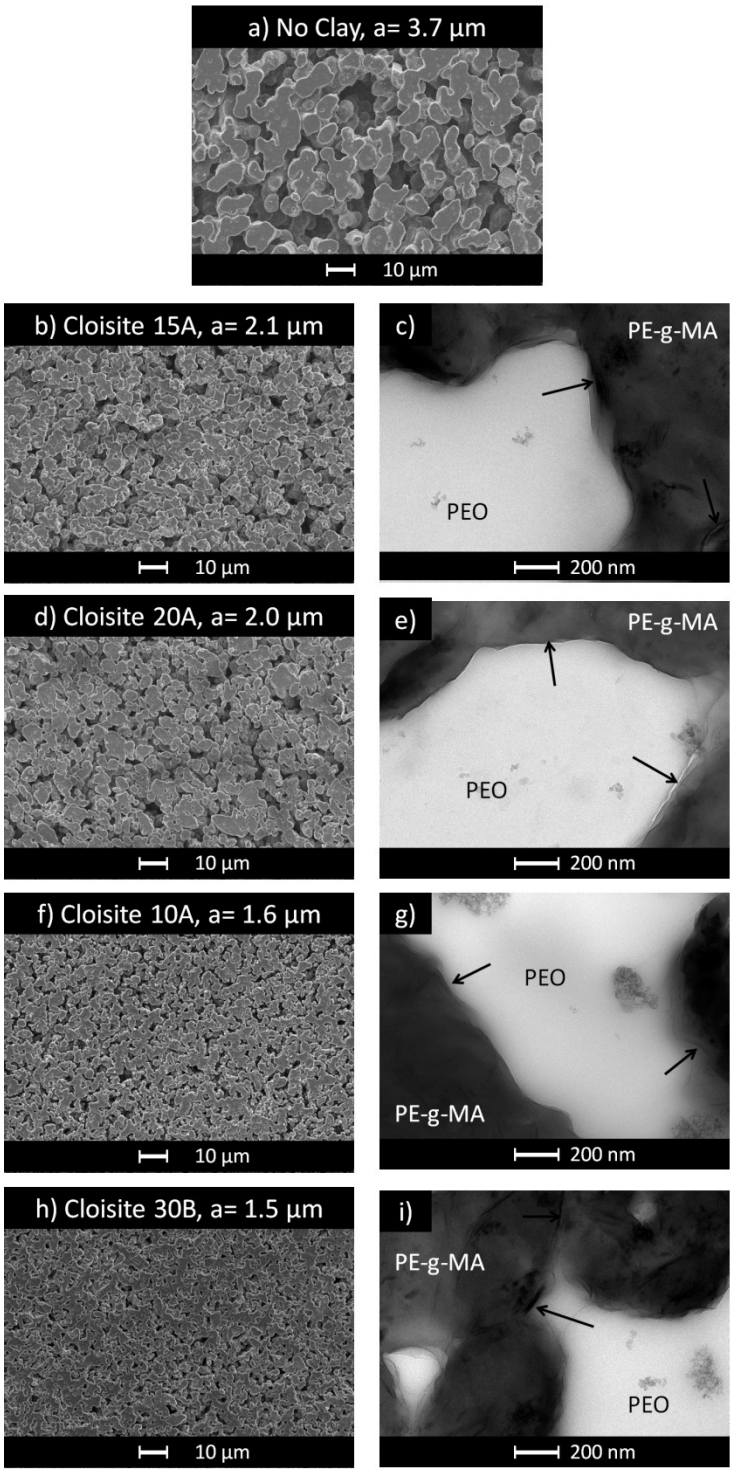

Figure 6.10. SEM and TEM micrographs of PE-g-MA/PEO with clays, prepared using the low shear screw geometry. a) PE-g-MA/PEO; b,c) PE-g-MA/PEO/Cloisite 15A; c,g) PE-g-MA / PEO / Cloisite 20A; d,h) PE-g-MA / PEO / Cloisite 10A; e,i) PE-g-MA / PEO / Cloisite 30B.

Following the batch experiments, extrusion experiments were performed using PE-g-MA/PEO and clay to compare the compatibilizing effect of the organically modified clays. Again, since Cloisite Na+ was shown previously to be a poor compatibilizer due to lack of exfoliation, this sample was excluded from the current experimental comparison.

The morphology of reactive PE-g-MA/PEO blend as well as its composites with the clays is shown in Figure 6.10. For these extrusion experiments, similar to the batch mixed samples, reactive compatibilization from reactive PE-g-MA and PEO served to compatbillize the blends even without clay. It is also evident that all the blends containing organoclay result in smaller phase domains in comparison to the pure PE-g-MA blend, which confirms the synergistic action of *in situ* formed block copolymers and clay in compatibilization of these blends that was observed in the batch compounding experiments. TEM micrographs show that all the clays located at the interface and the PE-g-MA phase. Interfacial localization was expected in all cases except for Cloisite 30B according to the wetting parameters, though with a slight preference for the PEO phase over the PE-g-MA phase. Again, this PE-g-MA preference can be attributed to chemical compatibility between the maleic anhydride and the clay surface.

From this set of experiments, the smallest characteristic size resulted from blends containing 5 wt% Cloisite 10A and 30B - incidentally, the most hydrophilic organoclays tested here. The order of effectiveness of organoclays for compatibilization in the reactive PE-g-MA/PEO blends is reversed from the LDPE/PEO blends. Based on thermodynamic arguments, an increase in hydrophilicity would push the clay more into the PEO phase, as is would be expected based on the wetting coefficient results. However, if the clay is chemically compatible with the PE-g-MA, which can be expected based on the TEM observations of PE-g-MA localization and the previous results by Utracki and coworkers,[168] than what may be occurring is that the clay is bound to the PE-g-MA but being thermodynamically driven towards the PEO phase, causing it to better locate at the interface than if it were more hydrophobic and had less

thermodynamic drive to leave the PE-g-MA phase. Further support of this hypothesis is based on the chemical functionality of the Cloisite 30B interstitial organic cation, which contains a hydroxyl group that could undergo a similar graft reaction to the PE-g-MA and PEO graft reaction previously observed, thereby greatly improving compatibility between PE-g-MA and Cloisite 30B. Such a reaction would also encourage intercalation and exfoliation due to this reaction occurring between clay layers. Consequently, it was more efficient in saturating the interface and compatibilizing the blend.

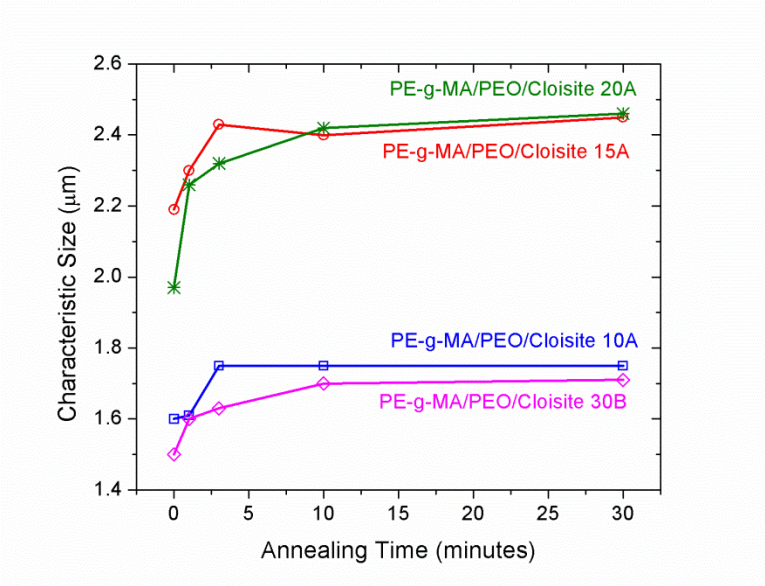

Figure 6.11. Characteristic size as a function of annealing time at 150 °C for PE-g-MA/PEO/5 wt% organoclay blends, prepared using the low-shear screw geometry in extrusion experiments.

Coarsening experiments confirm the morphology obtained by TEMs of the reactive PE-g-MA with clay and are presented in Figure 6.11. All the blends show the stable morphology, with characteristic sizes that reached a plateau by 10 minutes of coarsening. These results support the SEM results which show increased compatibilization for the more hydrophilic clays, and are consistent with the stabilization mechanism observed before with PE-g-MA/PEO blends with no clay and LDPE/PEO blends with interfacially localized organoclay. In this case, however, the combined mechanism results in greater degrees of compatibilization.

6.3.3.3 Comparison of clays in high-shear mixing

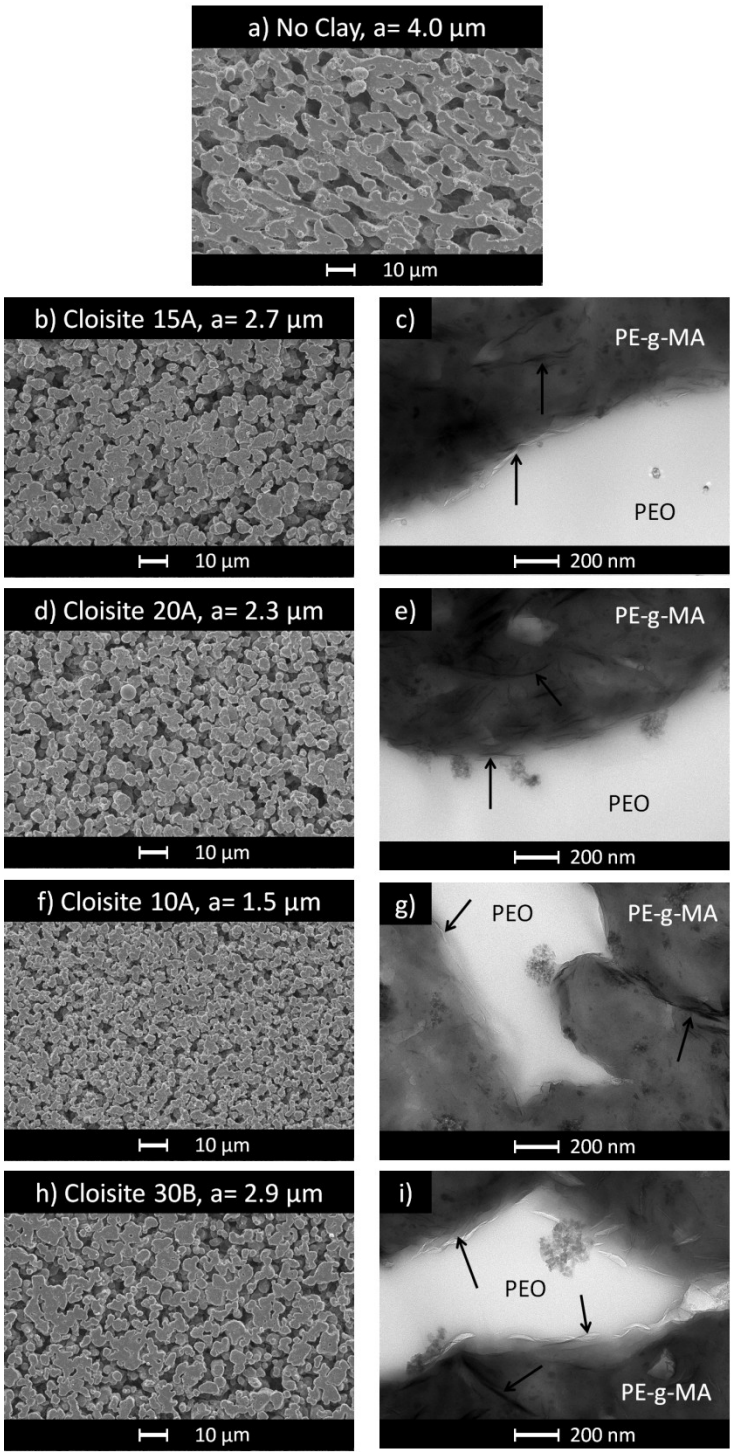

Figure 6.12. SEM and TEM micrographs of PE-g-MA/PEO with clays, prepared using the high shear screw geometry. a) PE-g-MA/PEO; b,c) PE-g-MA/PEO/Cloisite 15A; c,g) PE-g-MA / PEO / Cloisite 20A; d,h) PE-g-MA / PEO / Cloisite 10A; e,i) PE-g-MA / PEO / Cloisite 30B.

The morphology of the reactive PE-g-MA/PEO blends with the clays, processed by extrusion using the high-shear screw geometry, is shown by SEM and TEM in Figure 6.12. The results observed here can be similarly compared to the LDPE/PEO high shear results, such that the characteristic size for all blends is larger than the same blends prepared by the low-shear screw geometry, suggesting again that shear induced coalescence resulted in larger feature sizes. For these experiments, the most effective compatibilizer was Cloisite 10A, whereas Cloisite 30B did not perform as well as it did in low-shear experiments. This is mostly consistent with the results from the low-shear mixing in that more hydrophilic clay performed better as a compatibilizer than the more hydrophobic clays. However, Cloisite 30B is an exception in this case due in part to the intense mixing environment which lowers the possibility of bond formation between hydroxyl group on Cloisite 30B and maleic anhydride. Also, the Cloisite 30B had the smallest interstitial space of the organoclays, which when combined with the lower viscosity of the polymers at the higher shear rate may have reduced the ability of the Cloisite 30B to effectively exfoliate, despite better chemical compatibility.

6.3.4 LDPE versus PE-g-MA, comparison and discussion

6.3.4.1 Comparison of flow conditions

What follows is an overview and comparison of the effectiveness of compatibilization for blending LDPE or PE-g-MA with PEO and organoclay across the three blending methods: batch mixing, low shear extrusion, and high shear extrusion. Previous work has investigated the morphological and rheological evolution of PP/PS/Cloisite 20A with 70/30 PP/PS ratio and 5 wt% of clay loading in both batch and continuous melt mixing processes.[169] TEM image analysis indicated clay localization at the interface, which resulted in the size reduction of the dispersed phase, morphological stabilization, and the reinforcement of the rheological properties for both types of processing. However, X-ray analysis revealed that basal spacing between clay layers (which indicates the extent of the clay intercalation) was higher in blends obtained by continuous

processing, suggesting that better exfoliation was achieved by extrusion.

In the current study, image analysis indicates that higher shear resulted in larger phase domains for blends with and without clay, such that batch mixing showed the smallest characteristic size and high shear extrusion showed the largest. This is consistent with previous findings of shear induced pore coalescence in cocontinuous blends,[13] due to the reduced blend viscosity and increased chance to feature collisions that lead to coalescence. Therefore, to quantify the extent of compatibilization for each method employed in this study, the characteristic size of the control sample (LDPE/PEO) will be compared to the reactive blend (PE-g-MA/PEO) and the corresponding blends with 5wt% of Cloisite 20A, obtained in the three different shear environments. These results are shown in Table 6.6.

For all the blends, higher shear results in larger characteristic size. However, comparing the characteristic size of non-reactive blends with Cloisite 20A to the control sample shows that Cloisite 20A has similar compatibilization effect in all three processing environment. The extent of reactive compatibilization appears to increase with increasing shear, suggesting that in the absence of clay more intense mixing improves the interfacial reaction between PE-g-MA and PEO by faster flow rates and lower viscosity of the reactive components. However, since the molecular weight and rheological behavior of LDPE and PE-g-MA are different, this increase is a result of reactive coupling can also be attributed to viscosity differences in the blend components. Finally, the synergistic action of clay and reactive compatibilization further decreases characteristic size for all processing environments, showing superior compatibilization to either mechanism applied independently.

These results show that higher shear induces pore coalescence, resulting in higher characteristic size. Clay reduced the characteristic size equivalently in all shear environments. Synergistic action of reactive coupling and clay is the most efficient compatibilization method.

Table 6.6. Characteristic size and characteristic size percent decrease in different processing environments.

Type of processing	Characteristic Size (μm)				Percent decrease in characteristic size (%)		
	LDPE / PEO (control)	LDPE / PEO / Cloisite 20A	PE-g-MA / PEO	PE-g-MA / PEO / Cloisite 20A	Clay only	Reactive Compatibilization only	Synergistic action
DACA Batch Mixer	7.2	2.0	3.0	1.6	72	59	78
Low Shear Extrusion	15.8	3.8	3.7	2.0	76	77	88
High Shear Extrusion	20	5.2	4.0	2.3	74	80	88

6.3.4.2 Wettability

Previously work reported in Chapter 3 showed high wettability of porous PE-g-MA films obtained after PEO extraction due to the presence of PEO chains at the pore wall. In order to examine how the presence of clay in these blends alters the wettability of pores, contact angle experiments were conducted on porous PE films, obtained by pressing films of the blend extrudate from the low-shear extrusion experiments, followed by PEO extraction. The measurements of the contact angle were performed using captive air bubble method, as described in Section 6.2.7.

As expected, porous PE-g-MA films are more wettable than the porous LDPE films. However, the presence of clay at the pore wall and surface of the film alters the wettability of these films. Porous LDPE was significantly more wettable when blended with Cloisite 30B, which was expected considering that Cloisite 30B is the most hydrophilic organomodified clay in the clay portfolio. On the other hand, the addition of clay only minimally increased the wettability of PE-g-MA porous films. This would imply that PEO chains present at the pore wall or

intercalated between silicate layers are still the key drivers of wettability of these films, and that interfacially localized clay did not significantly inhibit the overall interfacial PEO coverage. The synergistic action of hydrophilic Cloisite 30B and PEO chains is present here as well, making this the most wettable film, suggesting that the combined effect of hydrophilic clay and PEO were better able to completely saturate the interface than either component alone.

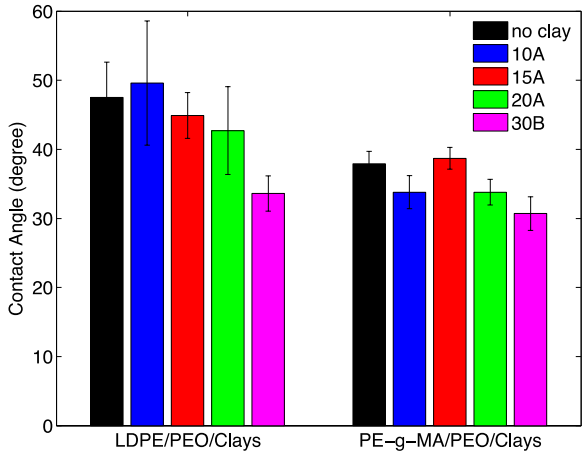

Figure 6.13. Contact angle on porous LDPE and PE-g-MA films obtained after PEO extraction

6.4 Conclusions

From the results and discussion above, it is evident that organically modified clays can serve as an effective compatibilizer for PE/PEO blends. Thermodynamic predictions based on wetting coefficients, calculated from the surface energies of the blend components, was largely successful in predicting the clay localization behavior of non-functional LDPE/PEO blends for the various organically modified clay. The unmodified Cloisite Na^+ clay, predicted to exist in the PEO phase and not at the interface, only provided minimal blend compatibilization even with 5 wt% clay loading. However, organically modified clays localized at the interface as predicted and provided complete suppression of coarsening, even with as little as 1 wt% organoclay, in a mechanism similar to that observed in reactively compatibilized blends stabilized by graft copolymers. The effectiveness of the compatibilizer increased as the wetting coefficient of the blend system approached zero and as the d-spacing of the clay increased, confirming that clays

with a higher interfacial affinity and a higher likelihood to exfoliate performed best. In this sense, nanoparticles can be considered a "generic compatibilizer," so long as the clay can sufficiently exfoliate and is selected to produce an appropriate wetting coefficient. TGA and rheology results, however, showed that thermodynamic predictions were not completely sufficient for predicting where the clay locates in the blends when the morphology is frozen and kinetically trapped in a state away from thermodynamic equilibrium, as the clay tended to localize more in LDPE due to the lower LDPE viscosity, despite higher interfacial tension. Therefore, for applying a clay as a generic compatibilizer, wetting coefficient serves more as a guide to compatibility, but not as the ultimate prediction of particle localization. Increasing the shear rate of mixing appeared to cause shear induced coalescence, which increased the characteristic size of the LDPE/PEO/clay blends, although compatibilization effects were still observed at all processing conditions.

For the reactively compatibilized PE-g-MA/PEO systems, the overall trend is less obvious, as the most hydrophilic clays, those with high affinity for PEO and wetting coefficients approaching 1, were the ones that performed the best for compatibilization. This was under the condition that the d-spacing of the clay was sufficiently large to enable exfoliation. Such was not the case for Cloisite Na^+, and so no additional compatibilization was gained with that clay. However, for organoclays that could be exfoliated, chemical compatibility between the surface of the clay and PE-g-MA caused the clay to be trapped in the PE-g-MA phase. Therefore, the clays with the strongest thermodynamic drive to enter the PEO phase showed the best compatibilization, contrary to the LDPE/PEO results. The nature of the clay/PE-g-MA chemical interaction is still not fully understood, and will require further experiments to verify. Increasing the shear rate of mixing increased the degree of shear induced coalescence, similar to the LDPE/PEO blends. In the case of Cloisite 30B, the most hydrophilic organoclay with small d-spacing, the clay performed the best in low shear mixing, but not as well in high shear mixing, suggesting that increasing the mixing shear rate disrupted the ability of the clay to act as a

compatibilizer, either by lower viscosity reducing exfoliation or by faster flow rate pulling the blend further from the desired equilibrium state. The synergistic effect of clay compatibilization combined with interfacial graft copolymer reactions served to stabilize blends better than either method applied independently, and also improved the water wettability of the final films.

Chapter 7: Summary and Outlook

7.1 Summary

Cocontinuous blends are interpenetrated structures from blended immiscible polymers. While these are simple to create and scale-up from a materials processing point of view, the fundamental understanding of the formation of cocontinuous structures is a complex problem existing at the intersection of rheology, processing parameters, and the thermodynamics of interfaces. Due to this complexity, the scientific background on predicting blend morphology has so far been empirical and often contradictory. From the standpoint of application design, the thermodynamic instability of the structure requires further research into methods of compatibilization that are well characterized and, if they are to be adopted for industrial applications, inexpensive. This purpose of this thesis was to aid in a fundamental understanding of both interfacial stabilization and morphological prediction of cocontinuous blends.

Much of this thesis focused on immiscible blends produced from polyethylene (PE) and polyethylene oxide (PEO), due to the toughness of PE and the wettability of PEO. These blends, however, were highly incompatible, resulting in large features and coarsening during annealing. Reactive blending was explored in Chapter 2 as a compatibilization method, with a specific focus on determining the effect of varying the molecular weight of the reactive PEO. The effectiveness of the compatibilization was quantified by a suite of techniques, including interfacial tension measurements by shear rheometry of droplet blends, XPS of laminated materials, two-step blends, and coarsening. It was found that a medium molecular weight PEO, such as the 40K PEO measured, minimized the blend interfacial tension. This was due to maximizing both surface coverage (which increased with increasing molecular weight) and graft density (which decreased with increasing molecular weight), as reported by XPS. This was confirmed by two-step blending, which showed the smallest domain size with a 40K PEO interface. All blends with a

saturated interface showed cessation of coarsening once the graft density reached 4-5 grafts/πR_g^2. This confirmed that coarsening suppression resulted from the densification of the copolymer brush at the interface.

Chapter 3 explored a specific application of the reactive blending experiments from Chapter 2. Here, gas separation membranes were prepared from PE and 40K PEO blends made by twin-screw extrusion. Processing techniques which varied by residence time and mixing intensity were compared, and it was found that a medium shear rate screw geometry with a sufficiently long residence time minimized the characteristic blend size and narrowed the size distribution. The higher shear screw geometry resulted in larger features due to shear induced coalescence. The PEO was extracted from these blends, and the resulting pores were filled with an ionic gel. These films were used in a diffusion cell to test burst pressure, and it was found that small, wettable pores with a narrow pore size distribution maximized the burst pressure.

In order to review and improve upon the literature on cocontinuous blend morphology predictions, Chapter 4 investigated the range of cocontinuous compositions for the blend systems from Chapter 2, in addition to polypropylene (PP)/PEO blends. Continuity data was analyzed with respect to several phase inversion predictions found in the literature. The best prediction of the center of the cocontinuity ranges when the viscosity ratio of the components was close to 1 was found using the phase inversion prediction by Utracki,[27] which was derived from a droplet packing model assuming deformable spheres. This model as originally described could not predict the behavior of blends with viscosity ratio far from 1, though it was successful under these conditions when modified to treat the droplets as hard spheres. From the cocontinuity ranges, a set of rules of thumb were derived to provide better intuition for cocontinuity range than have been previously recorded in one place. These rules of thumb were based around a single central concept that cocontinuity requires elongated features that also must percolate into a network. In general, high viscosity, viscosity ratios near 1, and lower interfacial tension are all expected to

broaden the range of cocontinuity, due to promoting the formation and stability of elongated features. However, large interfacially localized copolymers narrow this range, due to steric hindrance of the coalescence necessary to form a continuous network.

Chapter 5 extended this discussion on the range of cocontinuity to investigate the role of branched polymer chain architecture on cocontinuity, specifically studying blends from branched and linear PE and polylactic acid (PLA). Branched polymers were found to exhibit significant strain hardening under extensional flow. This strain hardening served to broaden the range of compositions that could achieve cocontinuity, specifically when the strain hardening material formed the major phase. This suggested that strain hardening promoted stress transfer to the minor phase, encouraging formation and stability of elongated features which could form a continuous network. However, excessive strain hardening, as shown in blends of branched LDPE/branched PLA, slowed down coalescence due to inhibition of draining flows, and so the range was not improved further with increasing branching content.

Finally, a second method of interfacial modification was explored in Chapter 6, where PE and PEO were blended with nanoclays. In non-reactive LDPE/PEO blends, thermodynamic wetting coefficients predicted with reasonable success the localization the nanoclays, with the organically modified nanoclays localizing at the interface. This interfacial localization was found to suppress coarsening in a similar manner to the reactive blending shown in Chapter 2. Blending clays with reactive polymers, however, disrupted the thermodynamic predictions due to chemical compatibility between the clay and the PE-g-MA. However, reactive blends with organomodified clays still showed an overall decrease in blend characteristic size compared to reactive blends with no clay, despite the difficulty in predicting clay localization. Also, in general, the wetting coefficients could not account for the influence of mixing and rheology, which served to disrupt the system away from the thermodynamic predictions.

7.2 Future Directions

7.2.1 Reactive Blending

Further work in the area of reactive blending can help to answer questions not addressed in the present work. Perhaps the most critical question arises from the optimal performance of the medium molecular weight PEO: is there a particular molecular weight that achieves a local minimum in interfacial tension? The success of the 40K PEO can potentially be attributed also to maximized interfacial coverage on both sides of the interface, due to well balanced radii of gyration between the reactive polymers. This may require XPS analysis of both sides of the interface to measure graft density and interfacial coverage independently. The present experiments were only capable of investigating graft density on one side of the interface due to the inability to solvent extract PE, though other reactive systems could be derived to circumvent this limitation.

Also of interest is the role of copolymer architecture on compatibilization. Due to the interplay of reaction kinetics and rheology, different architecture would be expected to form different types of interfacial brushes. Subsequent studies could investigate the difference in cocontinuous stability for end-to-end reactive polymers compared to the graft copolymers used here. Additionally, end-functional reactive branched polymers would also be expected to influence the nature of an interfacial brush in unexpected ways. These experiments could be coupled with numerical simulations of interfacial copolymer brushes with various architectures to verify the coarsening limits exhibited by each system.

Finally, a simple experiment could be to extend the two-step blending procedure to introduce only non-reactive polymers during the second step, to eliminate the possibility of reactions from the second set of materials. This would provide better experimental control, allowing this method to be used more quantitatively for size and interfacial tension predictions.

7.2.2 Membrane Processing

Better techniques for membrane preparation would be valuable for improving the applicability of cocontinuous blends to thin film applications such as membranes. Particularly in the area of gas separation membranes, thin selective layers are needed, which excludes the filled-pore solvent casting design used here. However, multilayer coextrusion of cocontinuous blends with a selectively permeable material could be used to generate laminated membranes from melt processing alone. Previous work in the Macosko group has explored multilayer coextrusion,[170-172] and this expertise could be combined with knowledge of cocontinuous blends to develop structures similar to the one seen in Figure 7.1.[173] A sacrificial phase such as PEO would be washed from the cocontinuous layers to provide the porous support. Such an experiment would also present ample opportunity for studying adhesion between cocontinuous blends and other laminated materials, and the stability of cocontinuity during annealing near an interface.

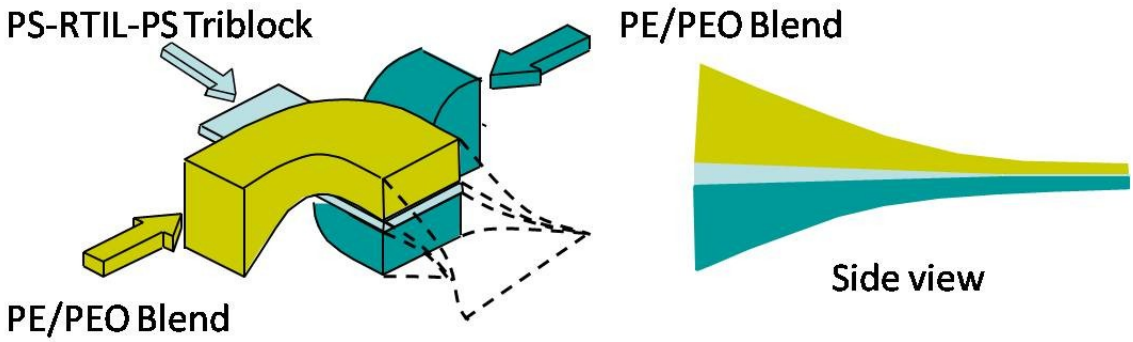

Figure 7.1. Multilayer coextrusion for a laminated membrane, formed by layers of cocontinuous blends and a selectively permeable polymer.[173] PS-RTIL-PS represents a polystyrene-room temperature ionic liquid-polysytrene triblock copolymer as the selective layer.[100,174]

Another option for forming thin films of cocontinuous blends would be film blowing of the blended product. This would present an opportunity to form thin films continuously from melt processing, which could then be immersed in a solvent to create a porous film. This processing also consists largely of extensional flows, so the role of branched polymers on the morphology and mechanical properties of blown films from cocontinuous blends would be

experimentally valuable for improving potential industrial applications.

7.2.3 Cocontinuity Formation

The discussions on cocontinuity formation here were unfortunately but necessarily limited to empirical observations and models, due to the complexity of mixing flows and cocontinuity formation. However, certain fundamental experiments would be invaluable for further verifying the central claim of Chapters 4 and 5 that cocontinuity is promoted by elongated features that are capable of coalescing into a continuous network.

First would be an investigation of droplet coalescence, following experiments similar to those used by De Bruyn and coworkers.[175] This previous work investigated droplet coalescence within confined shear flow, using a shear rheometer and optical imaging equipment. By tuning the parameters of both the matrix phase and droplet phase, this experiment could form comparisons of coalescence between polymers of different molecular weights, degrees of long chain branching, or reactive functionality. This could serve to directly observe differences in coalescence behavior between various materials, which could be correlated to their ability to achieve cocontinuity.

Furthermore, these experiments could be modified to change the geometry of the rheometer to explore extensional flows. These could be used to observe extension of droplets into fibers and the stability of those fibers when varying the matrix and dispersed phase molecular weight and branching content. These experiments, along with similar studies under shear flow, could be used to determine the formation and stability of elongated features within different material systems, which could then be related back to the cocontinuity of such systems.

7.2.4 Cocontinuous Blends and Nanoparticles

Taking advantage of the results from the present work where nanoparticles were successfully localized at the interface of a cocontinuous blend, future experiments could produce cocontinuous blends containing graphene. Previous work has shown that graphene

nanocomposites can be used to create conductive polymers, although this requires a percolated network of graphene.[176-178] However, if the graphene can be confined to the interface of a cocontinuous blend which already exists as a 2D percolated structure, then graphene percolation can be achieved with very low graphene loading.

Bibliography

1. Scott, C. E.; Macosko, C. W. "Morphology development during the initial stages of polymer-polymer blending," *Polymer* **1995**, *36*, 461-470.

2. Tucker, C. L.; Moldenaers, P. "Microstructual Evolution in Polymer Blends," *Annu. Rev. Fluid Mech.* **2002**, *34*, 177-210.

3. Pötschke, P.; Paul, D. R. "Formation of Co-continuous Structures in Melt-Mixed Immiscible Polymer Blends," *J Macromol Sci C, Polym Rev* **2003**, *C43*, 87-141.

4. Galloway, J. A.; Koester, K. J.; Paasch, B. J.; Macosko, C. W. "Effect of sample size on solvent extraction for detecting cocontinuity in polymer blends," *Polymer* **2004**, *45*, 423-428.

5. Galloway, J. A.; Macosko, C. W. "Comparison of methods for the detection of cocontinuity in poly(ethylene oxide)/polystyrene blends," *Polym. Eng. Sci.* **2004**, *44*, 714-727.

6. Galloway, J. A.; Montminy, M. D.; Macosko, C. W. "Image analysis for interfacial area and cocontinuity detection in polymer blends," *Polymer* **2002**, *43*, 4715-4722.

7. Li, J.; Ma, P. L.; Favis, B. D. "The Role of the Blend Interface Type on Morphology in Cocontinuous Polymer Blends," *Macromolecules* **2002**, *35*, 2005-2016.

8. Riscanu, D.; Favis, B. D.; Feng, C.; Matsuura, T. "Thin-film membranes derived from co-continuous polymer blends: preparation and performance," *Polymer* **2004**, *45*, 5597-5609.

9. Ramachandran, R.; Dinunzi, S. A. US Patent #5589545 A, 1994.

10. Lu, Q.; Meltzer, D. A.; Eckstein, Y. US Patent #2011/0092648 A1, 2010.

11. RTP Company Permastat® Compounds Providing Permanent Antistatic Protection - Conductive and Antistatic Plastic Compounds. http://www.rtpcompany.com/products/conductive/permastat.htm (accessed March 7, 2013).

12. Lopez-Barron, C.; Macosko, C. W. "Characterizing Interface Shape Evolution in Immiscible Polymer Blends via 3D Image Analysis," *Langmuir* **2009**, *25*, 9392-9404.

13. Trifkovic, M.; Hedegaard, A.; Huston, K.; Sheikhzadeh, M.; Macosko, C. W. "Porous Films via PE/PEO Cocontinuous Blends," *Macromolecules* **2012**, *45*, 6036-6044.

14. Sarazin, P.; Roy, X.; Favis, B. D. "Controlled preparation and properties of porous poly(l-lactide) obtained from a co-continuous blend of two biodegradable polymers," *Biomaterials*

2004, *25*, 5965-5978.

15. Washburn, N. R.; Simon, C. G.; Tona, A.; Elgendy, H. M.; Karim, A.; Amis, E. J. "Co-extrusion of biocompatible polymers for scaffolds with co-continuous morphology," *J. Biomed. Mater. Res.* **2002**, *60*, 20-29.

16. Ellison, C. J.; Meuler, A. J.; Qin, J.; Evans, C. M.; Wolf, L. M.; Bates, F. S. "Bicontinuous Polymeric Microemulsions from Polydisperse Diblock Copolymers," *J Phys Chem B* **2009**, *113*, 3726-3737.

17. Hillmyer, M. A.; Maurer, W. W.; Lodge, T. P.; Bates, F. S.; Almdal, K. "Model Bicontinuous Microemulsions in Ternary Homopolymer/Block Copolymer Blends," *J Phys Chem B* **1999**, *103*, 4814-4824.

18. Matsen, M. W.; Bates, F. S. "Unifying Weak- and Strong-Segregation Block Copolymer Theories," *Macromolecules* **1996**, *29*, 1091-1098.

19. Veenstra, H.; Van Dam, J.; Posthuma de Boer, A. "On the coarsening of co-continuous morphologies in polymer blends: effect of interfacial tension, viscosity and physical cross-links," *Polymer* **2000**, *41*, 3037-3045.

20. Willemse, R. C.; Posthuma de Boer, A.; van Dam, J.; Gotsis, A. D. "Co-continuous morphologies in polymer blends: the influence of the interfacial tension," *Polymer* **1999**, *40*, 827-834.

21. Kwon, O.; Zumbrunnen, D. A. "Progressive morphology development to produce multilayer films and interpenetrating blends by chaotic mixing," *J Appl Polym Sci* **2001**, *82*, 1569-1579.

22. Lee, J. K.; Han, C. D. "Evolution of polymer blend morphology during compounding in an internal mixer," *Polymer* **1999**, *40*, 6277-6296.

23. Lee, J. K.; Han, C. D. "Evolution of polymer blend morphology during compounding in a twin-screw extruder," *Polymer* **2000**, *41*, 1799-1815.

24. Paul, D. R.; Barlow, J. W. "Polymer Blends," *Poly. Rev.* **1980**, *18*, 109-168.

25. Jordhamo, G. M.; Manson, J. A.; Sperling, L. H. "Phase continuity and inversion in polymer blends and simultaneous interpenetrating networks," *Polym. Eng. Sci.* **1986**, *26*, 517.

26. Metelkin, V. I.; Blekht, V. P. *Colloid Journal of the USSR* **1984**, *46*, 425.

27. Utracki, L. A. "On the viscosity-concentration dependence of immiscible polymer blends," *J. Rheol.* **1991**, *35*, 1615-1637.

28. Utracki, L. A. *Polym. Mater. Sci. Eng.* **1991***, 65*, 50.

29. Willemse, R. C.; Posthuma de Boer, A.; van Dam, J.; Gotsis, A. D. "Co-continuous morphologies in polymer blends: a new model," *Polymer* **1998***, 39*, 5879-5887.

30. Steinmann, S.; Gronski, W.; Friedrich, C. "Quantitative rheological evaluation of phase inversion in two-phase polymer blends with cocontinuous morphology," *Rheo. Acta* **2002***, 41*, 77-86.

31. Steinmann, S.; Gronski, W.; Friedrich, C. "Cocontinuous polymer blends: influence of viscosity and elasticity ratios of the constituent polymers on phase inversion," *Polymer* **2001***, 42*, 6619-6629.

32. Bourry, D.; Favis, B. D. "Cocontinuity and phase inversion in HDPE/PS blends: Influence of interfacial modification and elasticity," *J Polym Sci Pol Phys* **1998***, 36*, 1889-1899.

33. Lopez-Barron, C. R.; Macosko, C. W. *Morphology and Rheology of Cocontinuous Blends;* 2008; Vol. 1027, pp 523-525.

34. Yuan, Z.; Favis, B. D. "Coarsening of immiscible co-continuous blends during quiescent annealing," *AICHE J.* **2005***, 51*, 271-280.

35. Bell, J. R.; Chang, K.; Lopez-Barron, C. R.; Macosko, C. W.; Morse, D. C. "Annealing of Cocontinuous Polymer Blends: Effect of Block Copolymer Molecular Weight and Architecture," *Macromolecules* **2010***, 43*, 5024-5032.

36. Galloway, J. A.; Jeon, H. K.; Bell, J. R.; Macosko, C. W. "Block copolymer compatibilization of cocontinuous polymer blends," *Polymer* **2005***, 46*, 183-191.

37. Maric, M.; Macosko, C. W. "Block copolymer compatibilizers for polystyrene/poly(dimethylsiloxane) blends," *Journal of Polymer Science Part B: Polymer Physics* **2002***, 40*, 346-357.

38. Baker, W.; Scott, C.; Hu, G. H. *Reactive Polymer Blending;* Hanser Publishing: 2001.

39. Jones, T. D.; Macosko, C. W.; Moon, B.; Hoye, T. R. "Synthesis and reactive blending of amine and anhydride end-functional polyolefins," *Polymer* **2004***, 45*, 4189-4201.

40. Jeon, H. K.; Zhang, J.; Macosko, C. W. "Premade vs. reactively formed compatibilizers for PMMA/PS melt blends," *Polymer* **2005***, 46*, 12422-12429.

41. Macosko, C. W.; Jeon, H. K.; Hoye, T. R. "Reactions at polymer–polymer interfaces for blend compatibilization," *Prog Polym Sci* **2005***, 30*, 939-947.

42. Maric, M.; Ashurov, N.; Macosko, C. W. "Reactive blending of poly (dimethylsiloxane) with nylon 6 and poly (styrene):Effect of reactivity on morphology," *Polymer Engineering & Science* **2001***, 41*, 631-642.

43. Vermant, J.; Cioccolo, G.; Golapan Nair, K.; Moldenaers, P. "Coalescence suppression in model immiscible polymer blends by nano-sized colloidal particles," *Rheologica Acta* **2004***, 43*, 529-538.

44. Zhang, W.; Lin, M.; Winesett, A.; Dhez, O.; Kilcoyne, A. L.; Ade, H.; Rubinstein, M.; Shafi, K. V. P. M.; Ulman, A.; Gersappe, D.; Tenne, R.; Rafailovich, M.; Sokolov, J.; Frisch, H. L. "The use of functionalized nanoparticles as non-specific compatibilizers for polymer blends," *Polym. Adv. Technol.* **2011***, 22*, 65-71.

45. Baudouin, A.; Devaux, J.; Bailly, C. "Localization of carbon nanotubes at the interface in blends of polyamide and ethylene–acrylate copolymer," *Polymer* **2010***, 51*, 1341-1354.

46. Thareja, P.; Velankar, S. "Particle-induced bridging in immiscible polymer blends," *Rheologica Acta* **2007***, 46*, 405-412.

47. Thareja, P.; Moritz, K.; Velankar, S. "Interfacially active particles in droplet/matrix blends of model immiscible homopolymers: Particles can increase or decrease drop size," *Rheologica Acta* **2010***, 49*, 285-298.

48. Si, M.; Araki, T.; Ade, H.; Kilcoyne, A. L. D.; Fisher, R.; Sokolov, J. C.; Rafailovich, M. H. "Compatibilizing Bulk Polymer Blends by Using Organoclays," *Macromolecules* **2006***, 39*, 4793-4801.

49. Xie, H.; Xu, J.; Zhou, S. "Polymer blends with two kinds of elastomeric ionomers," *Polymer* **1991***, 32*, 95-102.

50. Hara, M.; Sauer, J. A. "Synergism in Mechanical Properties of Polymer/Polymer Blends," *Journal of Macromolecular Science, Part C* **1998***, 38*, 327-362.

51. Paul, D. R.; Bucknall, C. B. *Polymer Blends: Formulation. ;* Wiley: New York, 2000.

52. Anastasiadis, S. H.; Gancarz, I.; Koberstein, J. T. "Interfacial tension of immiscible polymer blends: temperature and molecular weight dependence," *Macromolecules* **1988***, 21*, 2980-2987.

53. Retsos, H.; Margiolaki, I.; Messaritaki, A.; Anastasiadis, S. H. "Interfacial Tension in Binary Polymer Blends in the Presence of Block Copolymers:â€‰ Effects of Additive MW," *Macromolecules* **2001***, 34*, 5295-5305.

54. Chang, K.; Macosko, C. W.; Morse, D. C. "Ultralow Interfacial Tensions of Polymer/Polymer

Interfaces with Diblock Copolymer Surfactants," *Macromolecules* **2007***, 40*, 3819-3830.

55. Broseta, D.; Fredrickson, G. H.; Helfand, E.; Leibler, L. "Molecular weight and polydispersity effects at polymer-polymer interfaces," *Macromolecules* **1990***, 23*, 132-139.

56. Reiter, J.; Zifferer, G.; Olaj, O. F. "Monte Carlo studies of the interface between two polymer melts," *Macromolecules* **1990***, 23*, 224-228.

57. Koning, C.; Ikker, A.; Borggreve, R.; Leemans, L.; Möller, M. "Reactive blending of poly(styrene-co-maleic anhydride) with poly(phenylene oxide) by addition of α-amino-polystyrene," *Polymer* **1993***, 34*, 4410-4416.

58. Washiyama, J.; Kramer, E. J.; Hui, C. Y. "Fracture mechanisms of polymer interfaces reinforced with block copolymers: transition from chain pullout to crazing," *Macromolecules* **1993***, 26*, 2928-2934.

59. Washiyama, J.; Kramer, E. J.; Creton, C. F.; Hui, C. "Chain Pullout Fracture of Polymer Interfaces," *Macromolecules* **1994***, 27*, 2019-2024.

60. Palierne, J. F. "Linear rheology of viscoelastic emulsions with interfacial tension," *Rheo Acta* **1990***, 29*, 204-214.

61. Van Hemelrijck, E.; Van Puyvelde, P.; Velankar, S.; Macosko, C. W.; Moldenaers, P. "Interfacial elasticity and coalescence suppression in compatibilized polymer blends," *J. Rheol.* **2004***, 48*, 143-158.

62. Jacobs, U.; Fahrlander, M.; Winterhalter, J.; Friedrich, C. "Analysis of Palierne's emulsion model in the case of viscoelastic interfacial properties," *J. Rheol.* **1999***, 43*, 1495-1509.

63. Macosko, C. W. *Rheology Principles, Measurements, and Applications;* Wiley, VHC: New York, 1994.

64. Maric, M.; Macosko, C. W. "Improving polymer blend dispersion in mini-mixers," *Polym Eng Sci* **2001***, 41*, 118-130.

65. Verhoogt, H.; Dam, J. V.; de Boer, A. P.; Draaijer, A.; Houpt, P. M. "Confocal laser scanning microscopy: a new method for determination of the mophology of polymer blends," *Polymer* **1993***, 34*, 1325-1329.

66. Lopez-Barron, C. R.; Macosko, C. W. "Direct Measurement of Interface Anisotropy of Bicontinuous Structures via 3D Image Analysis," *Langmuir* **2010***, 26*, 14284-14293.

67. Montminy, M. D.; Tannenbaum, A. R.; Macosko, C. W. "New Algorithms for 3-D Imaging and Analysis of Open-Celled Foams," *Journal of Cellular Plastics* **2001***, 27*, 501-515.

68. Montminy, M. D.; Tannenbaum, A. R.; Macosko, C. W. "The 3D structure of real polymer foams," *J. Colloid Interface Sci.* **2004***, 280*, 202-211.

69. Gramespacher, H.; Meissner, J. "Interfacial tension between polymer melts measured by shear oscillations of their blends," *J. Rheol.* **1992***, 36*, 1127-1141.

70. Lacroix, C.; Bousmina, M.; Carreau, P. J.; Favis, B. D.; Michel, A. "Properties of PETG/EVA blends: 1. Viscoelastic, morphological and interfacial properties," *Polymer* **1996***, 37*, 2939-2947.

71. Mekhilef, N.; Carreau, P. J.; Favis, B. D.; Martin, P.; Ouhlal, A. "Viscoelastic properties and interfacial tension of polystyrene-polyethylene blends," *J. Polym. Sci., Part B: Polym. Phys.* **2000***, 38*, 1359-1368.

72. Xing, P.; Bousmina, M.; Rodrigue, D.; Kamal, M. R. "Critical Experimental Comparison between Five Techniques for the Determination of Interfacial Tension in Polymer Blends: Model System of Polystyrene/Polyamide-6," *Macromolecules* **2000***, 33*, 8020-8034.

73. Boucher, E.; Folkers, J. P.; Hervet, H.; Leger, L.; Creton, C. "Effects of the Formation of Copolymer on the Interfacial Adhesion between Semicrystalline Polymers," *Macromolecules* **1996***, 29*, 774-782.

74. Laurens, C.; Creton, C.; Leger, L. "Adhesion Promotion Mechanisms at Isotactic Polypropylene/Polyamide 6 Interfaces: Role of the Copolymer Architecture," *Macromolecules* **2004***, 37*, 6814-6822.

75. Tanuma, S.; Powell, C. J.; Penn, D. R. "Calculations of electorn inelastic mean free paths. II. Data for 27 elements over the 50–2000 eV range," *Surf. Interface Anal.* **1991***, 17*, 911-926.

76. Favis, B. D.; Chalifoux, J. P. "The effect of viscosity ratio on the morphology of polypropylene/polycarbonate blends during processing," *Polym. Eng. Sci.* **1987***, 27*, 1591-1600.

77. Everaert, V.; Aerts, L.; Groeninckx, G. "Phase morphology development in immiscible PP/(PS/PPE) blends influence of the melt-viscosity ratio and blend composition," *Polymer* **1999***, 40*, 6627-6644.

78. Hiemenz, P. C.; Lodge, T. P. *Polymer Chemistry;* CRC Press: Boca Raton, FL, 2007.

79. Brown, H. R. "The Adhesion Between Polymers," *Annu Rev Mater Sci* **1991***, 21*, 463-489.

80. Song, J.; Ewoldt, R. H.; Hu, W.; Craig Silvis, H.; Macosko, C. W. "Flow accelerates adhesion between functional polyethylene and polyurethane," *AIChE J.* **2011***, 57*, 3496-3506.

81. Lopez-Barron, C. R.; Macosko, C. W. "A new model for the coarsening of cocontinuous morphologies," *Soft Matter* **2010***, 6*, 2637-2647.

82. Pyun, A.; Bell, J. R.; Won, K. H.; Weon, B. M.; Seol, S. K.; Je, J. H.; Macosko, C. W. "Synchrotron X-ray Microtomography for 3D Imaging of Polymer Blends," *Macromolecules* **2007***, 40*, 2029-2035.

83. Omonov, T. S.; Harrats, C.; Groeninckx, G.; Moldenaers, P. "Anisotropy and instability of the co-continuous phase morphology in uncompatibilized and reactively compatibilized polypropylene/polystyrene blends," *Polymer* **2007***, 48*, 5289-5302.

84. McMaster, L. P. "Aspects of Liquid-Liquid Phase Transition Phenomena in Multicomponent Polymeric Systems." *Advances in Chemistry* **1975**; Vol. 142, pp 43-65.

85. Siggia, E. D. "Late stages of spinodal decomposition in binary mixtures," *Phys. Rev. A* **1979***, 20*, 595-605.

86. Elemans, P. H. M.; Janssen, J. M. H.; Meijer, H. E. H. "The measurement of interfacial tension in polymer/polymer systems: The breaking thread method," *J. Rheol.* **1990***, 34*, 1311-1325.

87. Tomotika, S. "On the Instability of a Cylindrical Thread of a Viscous Liquid Surrounded by Another Viscous Fluid," *P Roy Soc Lond A Mat* **1935***, 150*, 322-337.

88. Lopez-Barron, C.; Macosko, C. W. "Morphology and Rheology of Cocontinuous Blends," *Macromol. Symp.* **2009***, 283-284*, 348.

89. Guo, H.; Packirisamy, S.; Mani, R.; Aronson, C.; Gvozdic, N.; Meier, D. "Compatibilizing effects of block copolymers in low-density polyethylene/polystyrene blends," *Polymer* **1998***, 39*, 2495.

90. Asthana, H.; Jayaraman, K. "Rheology of Reactively Compatibilized Polymer Blends with Varying Extend of Interfacial Reaction," *Macromolecules* **1999***, 32*, 3412.

91. Doi, M.; Ohta, T. "Dynamics and rheology of complex interfaces. I," *J. Chem. Phys.* **1991***, 95*, 1242-1248.

92. Jinnai, H.; Nishikawa, Y.; Spontak, R. J.; Smith, S. D.; Agard, D.; Hashimoto, T. "Direct Measurement of Interfacial Curvature Distributions in a Bicontinuous Block Copolymer Morphology," *Phys. Rev. Lett.* **2000***, 84*, 518.

93. Sengupta, P.; Noordermeer, J. W. M. "Three-Dimensional Structure of Olefinic Thermoplastic Elastomer Blends Using Electron Tomography," *Macromol. Rapid Commun.* **2005***, 26*, 542.

94. Momose, A.; Fujii, A.; Kadowaki, H.; Jinnai, H. "Three-dimensional observation of polymer blend by X-ray phase tomography," *Macromolecules* **2005***, 38*, 7197.

95. Koizumi, S.; Yamane, Y.; Kuroki, S.; Ando, I.; Nishikawa, Y.; Jinnai, H. "Three-Dimensional observation of phase-separated poly(methyl methacrylate)/poly(styrene-ran-4-bromostylene blends by 3D NMR microscopy with X-ray microscopy," *J. Appl. Polym. Sci.* **2007***, 103*, 470.

96. Lu, J.; Yan, F.; Texter, J. "Advanced applications of ionic liquids in polymer science," *Prog Polym Sci* **2009***, 34*, 431-448.

97. Bara, J. E.; Carlisle, T. K.; Gabriel, C. J.; Camper, D.; Finotello, A.; Gin, D. L.; Noble, R. D. "Guide to CO2 Separations in Imidazolium-Based Room-Temperature Ionic Liquids," *Ind Eng Chem Res* **2009***, 48*, 2739-2751.

98. Camper, D.; Scovazzo, P.; Koval, C.; Noble, R. "Gas Solubilities in Room-Temperature Ionic Liquids," *Ind Eng Chem Res* **2004***, 43*, 3049-3054.

99. Camper, D.; Becker, C.; Koval, C.; Noble, R. "Diffusion and Solubility Measurements in Room Temperature Ionic Liquids," *Ind Eng Chem Res* **2006***, 45*, 445-450.

100. Gu, Y.; Lodge, T. P. "Synthesis and Gas Separation Performance of Triblock Copolymer Ion Gels with a Polymerized Ionic Liquid Mid-Block," *Macromolecules* **2011***, 44*, 1732.

101. Jansen, J. C.; Friess, K.; Clarizia, G.; Schauer, J.; Izak, P. "High Ionic Liquid Content Polymeric Gel Membranes: Preparation and Performance," *Macromolecules* **2011***, 44*, 39.

102. Trifkovic, M.; Sheikhzadeh, M.; Choo, K.; Rohani, S. "Model predicitive control of a twin-screw extruder for thermoplastic vulcanizate (TPV) applications," *Comput. Chem. Eng.* **2012***, 36*, 247.

103. Ridler, T.; Calvard, S. "Picture thresholding using an iterative selection method," *IEEE Trans. Syst., Man, Cybernetics* **1978***, 8*, 630.

104. Mather, M. L.; Morgan, S. P.; White, L. J.; Tai, H.; Kockenberger, W.; Howdle, S. M.; Shakesheff, K. M.; Crowe, J. A. "Image-based characterization of foamed polymeric tissue scaffolds," *Biomed. Mater.* **2008***, 3*, 1.

105. Wenzel, R. N. "Resistance of solid surfaces to wetting by water," *Ind. Eng. Chem.* **1936***, 28*, 988.

106. Tselios, C.; Bikiaris, D.; Prinos, J.; Panayiotou, C. "Structure and properties of blends of poly(ethylene-co-vinyl alcohol) with poly(styrene-co-maleic anhydride)," *J Appl Polym Sci* **1997***, 64*, 983.

107. Flores, M.; Hernandez, G.; Escobar, A.; Cardoso, J.; Palma, A.; Maciel, A.; Sanchez, E.; Manero, O. "Synthesis and processing of the (ethylene-vinyl acetate-vinyl alcohol) terpolymer and its blends with a polyamide and styrene copolymers," *J Appl Polym Sci* **1998**, *67*, 1071.

108. Phillip, W. A.; Rzayev, J.; Hillmyer, M. A.; Cussler, E. L. "Gas and water liquid transport through nanoporous block copolymer membranes," *J. Membr. Sci.* **2006**, *286*, 144.

109. Paul, D. R.; Barlow, J. W. *J. Macrom. Sci. , Rev. Macromol. Chem.* **1980**, *C18*, 108-168.

110. Krieger, I. M.; Dougherty, T. J. "A Mechanism for Non-Newtonian Flow in Suspensions of Rigid Spheres," *Transactions of the Society of Rheology* **1959**, *3*, 137-152.

111. Favis, B. D.; Chalifoux, J. P. "Influence of composition on the morphology of polypropylene/polycarbonate blends," *Polymer* **1988**, *29*, 1761-1767.

112. Vanoene, H. "Modes of dispersion of viscoelastic fluids in flow," *J. Colloid Interface Sci.* **1972**, *40*, 448-467.

113. Lyngaae-Jørgensen, J.; Rasmussen, K. L.; Chtcherbakova, E. A.; Utracki, L. A. "Flow induced deformation of dual-phase continuity in polymer blends and alloys. Part I," *Polymer Engineering & Science* **1999**, *39*, 1060-1071.

114. Lyngaae-Jørgensen, J.; Utracki, L. A. *Makromol. Chem. , Macromol. Symp.* **1991**, *48/49*, 189.

115. Mekhilef, N.; Favis, B. D.; Carreau, P. J. "Morphological stability, interfacial tension, and dual-phase continuity in polystyrene-polyethylene blends," *J. Polym. Sci.: Part B: Polym. Phys.* **1997**, *35*, 293.

116. Sarazin, P.; Favis, B. D. "Influence of temperature-induced coalescence effects on co-continuous morphology in poly(ε-caprolactone)/polystyrene blends," *Polymer* **2005**, *46*, 5966-5978.

117. Lyu, S.; Jones, T. D.; Bates, F. S.; Macosko, C. W. "Role of Block Copolymers on Suppression of Droplet Coalescence," *Macromolecules* **2002**, *35*, 7845-7855.

118. Willis, J. M.; Caldas, V.; Favis, B. D. "Processing-morphology relationships of compatibilized polyolefin/polyamide blends," *J. Mater. Sci.* **1991**, *26*, 4742-4750.

119. Jones, T. D.; Macosko, C. W.; Moon, B.; Hoye, T. R. "Synthesis and reactive blending of amine and anhydride end-functional polyolefins," *Polymer* **2004**, *45*, 4189-4201.

120. Auhl, D.; Stange, J.; Munstedt, H.; Krause, B.; Voigt, D.; Lederer, A.; Lappan, U.; Lunkwitz, K. "Long-Chain Branched Polypropylenes by Electron Beam Irradiation and Their

Rheological Properties," *Macromolecules* **2004***, 37*, 9465-9472.

121. Bubeck, R. A. "Structure–property relationships in metallocene polyethylenes," *Materials Science and Engineering: R: Reports* **2002***, 39*, 1-28.

122. Lohse, D. J.; Milner, S. T.; Fetters, L. J.; Xenidou, M.; Hadjichristidis, N.; Mendelson, R. A.; Garcia-Franco, C. A.; Lyon, M. K. "Well-Defined, Model Long Chain Branched Polyethylene. 2. Melt Rheological Behavior," *Macromolecules* **2002***, 35*, 3066-3075.

123. Spitael, P.; Macosko, C. W. "Strain hardening in polypropylenes and its role in extrusion foaming," *Polymer Engineering & Science* **2004***, 44*, 2090-2100.

124. Wei, X.; Collier, J. R.; Petrovan, S. "Shear and elongational rheology of polyethylenes with different molecular characteristics. II. Elongational rheology," *J Appl Polym Sci* **2007***, 104*, 1184-1194.

125. Inkson, N. J.; McLeish, T. C. B.; Harlen, O. G.; Groves, D. J. "Predicting low density polyethylene melt rheology in elongational and shear flows with ``pom-pom" constitutive equations," *J. Rheol.* **1999***, 43*, 873-896.

126. Stange, J.; Uhl, C.; Münstedt, H. "Rheological behavior of blends from a linear and a long-chain branched polypropylene," *Journal of Rheology (1978-present)* **2005***, 49*, 1059-1079.

127. Stange, J.; Münstedt, H. "Effect of Long-chain Branching on the Foaming of Polypropylene with Azodicarbonamide," *Journal of Cellular Plastics* **2006***, 42*, 445-467.

128. Yan, D.; Wang, W.; Zhu, S. "Effect of long chain branching on rheological properties of metallocene polyethylene," *Polymer* **1999***, 40*, 1737-1744.

129. Lehermeier, H. J.; Dorgan, J. R. "Melt rheology of poly(lactic acid): Consequences of blending chain architectures," *Polymer Engineering & Science* **2001***, 41*, 2172-2184.

130. Larson, R. G. "Combinatorial Rheology of Branched Polymer Melts," *Macromolecules* **2001***, 34*, 4556-4571.

131. Kim, J.; Kim, D. H.; Son, Y. "Rheological properties of long chain branched polyethylene melts at high shear rate," *Polymer* **2009***, 50*, 4998-5001.

132. Delgadillo-Velázquez, O.; Hatzikiriakos, S. G. "Processability of LLDPE/LDPE blends: Capillary extrusion studies," *Polymer Engineering & Science* **2007***, 47*, 1317-1326.

133. Larson, R. G. "Instabilities in viscoelastic flows," *Rheologica Acta* **1992***, 31*, 213-263.

134. Meissner, J. "Development of a Universal Extensional Rheometer for the Uniaxial Extension

of Polymer Melts," *Trans. Soc. Rheol.* **1972***, 16*, 405-420.

135. Cogswell, F. N. "Converging flow of polymer melts in extrusion dies," *Polymer Engineering & Science* **1972***, 12*, 64-73.

136. Cogswell, F. N. "Measuring the Extensional Rheology of Polymer Melts," *Trans. Soc. Rheol.* **1972***, 16*, 383-403.

137. Cernohous, J. J.; Van Gordon, G. S. "Biobased Polymer Compositions," **2010**.

138. Bagley, E. B. "End Corrections in the Capillary Flow of Polyethylene," *J. Appl. Phys.* **1957***, 28*, 624-627.

139. Padmanabhan, M.; Macosko, C. W. "Extensional viscosity from entrance pressure drop measurements," *Rheologica Acta* **1997***, 36*, 144-151.

140. Sundararaj, U.; Dori, Y.; Macosko, C. W. "Sheet formation in immiscible polymer blends: model experiments on initial blend morphology," *Polymer* **1995***, 36*, 1957-1968.

141. Sundararaj, U.; Macosko, C. W.; Shih, C. K. "Evidence for Inversion of Phase Continuity During Morphology Development in Polymer Blending," *Polym. Eng. Sci.* **1996***, 36*, 1769.

142. McKinley, G. H.; Sridhar, T. "Filament-stretching rheometry of complex fluids," *Annu. Rev. Fluid Mech.* **2002***, 34*, 375-415.

143. Ramaswamy, S.; Leal, L. G. "The deformation of a viscoelastic drop subjected to steady uniaxial extensional flow of a Newtonian fluid," *J. Non Newtonian Fluid Mech.* **1999***, 85*, 127-163.

144. Ramaswamy, S.; Leal, L. G. "The deformation of a Newtonian drop in the uniaxial extensional flow of a viscoelastic liquid," *J. Non Newtonian Fluid Mech.* **1999***, 88*, 149-172.

145. Pickering, S. U. "Emulsions," *J. Chem. Soc. , Trans.* **1907***, 91*, 2001-2021.

146. Tambe, D. E.; Sharma, M. M. "The effect of colloidal particles on fluid-fluid interfacial properties and emulsion stability," *Adv. Colloid Interface Sci.* **1994***, 52*, 1-63.

147. Robeson, L. M. *Polymer Blends*. Carl Hanser Verlag GmbH & Co. 2007; pp I-XII.

148. Munch Elmér, A.; Jannasch, P. "Gel electrolyte membranes derived from co-continuous polymer blends," *Polymer* **2005***, 46*, 7896-7908.

149. Gani, L.; Tencé-Girault, S.; Milléquant, M.; Bizet, S.; Leibler, L. "Co-continuous Nanostructured Blend by Reactive Blending: Incorporation of High Molecular Weight

Polymers," *Macromolecular Chemistry and Physics* **2010**, *211*, 736-743.

150. Bhadane, P. A.; Tsou, A. H.; Cheng, J.; Ellul, M.; Favis, B. D. "Morphology and continuity development in highly reactive nanoscale polymer blends," *Polymer* **2011**, *52*, 5107-5117.

151. Pu, G.; Luo, Y.; Wang, A.; Li, B. "Tuning Polymer Blends to Cocontinuous Morphology by Asymmetric Diblock Copolymers as the Surfactants," *Macromolecules* **2011**, *44*, 2934-2943.

152. Bose, S.; Bhattacharyya, A. R.; Bondre, A. P.; Kulkarni, A. R.; Pötschke, P. "Rheology, electrical conductivity, and the phase behavior of cocontinuous PA6/ABS blends with MWNT: Correlating the aspect ratio of MWNT with the percolation threshold," *Journal of Polymer Science Part B: Polymer Physics* **2008**, *46*, 1619-1631.

153. Lee, M. H.; Dan, C. H.; Kim, J. H.; Cha, J.; Kim, S.; Hwang, Y.; Lee, C. H. "Effect of clay on the morphology and properties of PMMA/poly(styrene-co-acrylonitrile)/clay nanocomposites prepared by melt mixing," *Polymer* **2006**, *47*, 4359-4369.

154. Ray, S. S.; Bousmina, M.; Maazouz, A. "Morphology and properties of organoclay modified polycarbonate/poly(methyl methacrylate) blend," *Polymer Engineering & Science* **2006**, *46*, 1121-1129.

155. Elias, L.; Fenouillot, F.; Majeste, J. C.; Cassagnau, P. "Morphology and rheology of immiscible polymer blends filled with silica nanoparticles," *Polymer* **2007**, *48*, 6029-6040.

156. Voulgaris, D.; Petridis, D. "Emulsifying effect of dimethyldioctadecylammonium-hectorite in polystyrene/poly(ethyl methacrylate) blends," *Polymer* **2002**, *43*, 2213-2218.

157. Hong, J.; Kim, Y.; Ahn, K.; Lee, S.; Kim, C. "Interfacial tension reduction in PBT/PE/clay nanocomposite," *Rheologica Acta* **2007**, *46*, 469-478.

158. Göldel, A.; Kasaliwal, G.; Pötschke, P. "Selective Localization and Migration of Multiwalled Carbon Nanotubes in Blends of Polycarbonate and Poly(styrene-acrylonitrile)," *Macromolecular Rapid Communications* **2009**, *30*, 423-429.

159. Cao, Y.; Zhang, J.; Feng, J.; Wu, P. "Compatibilization of Immiscible Polymer Blends Using Graphene Oxide Sheets," *ACS Nano* **2011**, *5*, 5920-5927.

160. Feng, J.; Chan, C.; Li, J. "A method to control the dispersion of carbon black in an immiscible polymer blend," *Polymer Engineering & Science* **2003**, *43*, 1058-1063.

161. Trifkovic, M.; Sheikhzadeh, M.; Choo, K.; Rohani, S. "Experimental and statistical study of the effects of material properties, curing agents, and process variables on the production of thermoplastic vulcanizates," *J Appl Polym Sci* **2010**, *118*, 764-777.

162. Owens, D. K.; Wendt, R. C. "Estimation of the surface free energy of polymers," *J Appl Polym Sci* **1969***, 13*, 1741-1747.

163. Bicerano, J. *Surface Tension and Interfacial Tension*. CRC Press: 2002.

164. Xiang, F.; Wang, Y.; Shi, Y.; Huang, T.; Chen, C.; Peng, Y.; Wang, Y. "Morphology and mechanical property changes in compatibilized high density polyethylene/polyamide 6 nanocomposites induced by carbon nanotubes," *Polym. Int.* **2012***, 61*, 1334-1343.

165. Kamal, M. R.; Calderon, J. U.; Lennox, B. R. "Surface Energy of Modified Nanoclays and Its Effect on Polymer/Clay Nanocomposites," *J. Adhes. Sci. Technol.* **2009***, 23*, 663-688.

166. Gomari, S.; Ghasemi, I.; Karrabi, M.; Azizi, H. "Organoclay localization in polyamide 6/ethylene-butene copolymer grafted maleic anhydride blends: the effect of different types of organoclay," *Journal of Polymer Research* **2011***, 19*, 1-11.

167. Mehta, S.; Mirabella, F. M.; Rufener, K.; Bafna, A. "Thermoplastic olefin/clay nanocomposites: Morphology and mechanical properties," *J Appl Polym Sci* **2004***, 92*, 928-936.

168. Sinha Ray, S.; Pouliot, S.; Bousmina, M.; Utracki, L. A. "Role of organically modified layered silicate as an active interfacial modifier in immiscible polystyrene/polypropylene blends," *Polymer* **2004***, 45*, 8403-8413.

169. Cho, S.; Hong, J. S.; Lee, S. J.; Ahn, K. H.; Covas, J. A.; Maia, J. M. "Morphology and Rheology of Polypropylene/Polystyrene/Clay Nanocomposites in Batch and Continuous Melt Mixing Processes," *Macromolecular Materials and Engineering* **2011***, 296*, 341-348.

170. Zhao, R.; Macosko, C. W. "Slip at polymer--polymer interfaces: Rheological measurements on coextruded multilayers," *J. Rheol.* **2002***, 46*, 145-167.

171. Dooley, J.; Costeux, C.; Wrisley, R.; Schlader, A. In *Multilayer Rheology Effects in Coextruded Structure Design;* 2008; pp 202-206.

172. Lee, P. C.; Park, H. E.; Morse, D. C.; Macosko, C. W. "Polymer-polymer interfacial slip in multilayered films," *J. Rheol.* **2009***, 53*, 893-915.

173. Macosko, C. W. "MRSEC Proposal: Multilayer Coextrusion," **2008**.

174. He, Y.; Boswell, P. G.; Buhlmann, P.; Lodge, T. P. "Ion Gels by Self-Assembly of a Triblock Copolymer in an Ionic Liquid," *J Phys Chem B* **2007***, 111*, 4645-4652.

175. De Bruyn, P.; Cardinaels, R.; Moldenaers, P. "The effect of geometrical confinement on coalescence efficiency of droplet pairs in shear flow," *J. Colloid Interface Sci.* **2013***, 409*, 183-

192.

176. Pang, H.; Chen, T.; Zhang, G.; Zeng, B.; Li, Z. "An electrically conducting polymer/graphene composite with a very low percolation threshold," *Mater Lett* **2010***, 64*, 2226-2229.

177. Liao, K.; Qian, Y.; Macosko, C. W. "Ultralow percolation graphene/polyurethane acrylate nanocomposites," *Polymer* **2012***, 53*, 3756-3761.

178. Kim, H.; Abdala, A. A.; Macosko, C. W. "Graphene/Polymer Nanocomposites," *Macromolecules* **2010***, 43*, 6515-6530.

Appendix A: Measuring interfacial tension by shear rheology of droplet blends

A.1 Introduction

Between two immiscible phases exists a positive, non-zero interfacial tension, Γ, which characterizes the energetic penalty involved in the creation of the interface. This interaction is enthalpic in nature, and will drive the system to a state where interfacial area between the phases is minimized in order to minimize the free energy of the system. This parameter is valuable for characterizing the nature of immiscible polymer blends, as it contributes to the size of domains of the blend (since a lower energetic penalty means interfacial area is easier to create, resulting in breakup of large domains into smaller particles) and the stability of the blend when subjected to post-processing or annealing.

One of the important features of interfacial tension is its tendency to create spherical droplets of a dispersed phase, due to that particular shape minimizing the interfacial area for a given volume. Droplets that are deformed away from a spherical shape will be restored to their spherical shape due to interfacial tension according to the following droplet relaxation time:

$$\lambda_d = \frac{a\eta_s}{\Gamma} \tag{A.1}$$

where a is the radius of the spherical droplet, η_s is the viscosity of the surrounding fluid, and Γ is the interfacial tension. This relaxation time introduces a variety of rheological complexities to the system, particularly due to droplets disturbing flow streamlines through the surrounding fluid [Bartok and Mason, 1958] and deformation of the droplets [Goldsmith and Mason, 1967]. The droplet recovery will impart an additional elastic response to the blend, such that the overall viscoelastic response of the blend can be interpreted conceptually as the sum of response from the matrix phase, the response from the dispersed phase, and the additional contribution due to the interface between them.

The viscoelastic response of dispersed droplets in a matrix is further complicated in the case where an interfacial phase is present, usually in the form of a block copolymer surfactant or an interfacially confined nanoparticle [Hong 2007]. This interfacial phase contributes to an interfacial elastic modulus, resulting in additional rigidity and resistance to droplet deformation. This can be further characterized by a second relaxation time of the droplet, λ_β, [Jacobs 1999] which corresponds to the interfacial elasticity. Deformation of droplets with surfactant at the interface can also result in a dilution of the surfactant as new surface area is created. The result is that interfacial tension increases with increased deformation, and this behavior is captured in a dilatation modulus.

By measuring the viscoelastic response of a polymer blend composed of droplets of one material contained in a matrix of another, and by knowing the viscoelastic properties of the blend components and the size of the dispersed droplets, the rheological results can be interpreted to calculate an interfacial tension between the two polymers, based on the relaxation time of the droplets. In cases where there is an interfacially localized phase, the rheological response can also be interpreted to calculate an interfacial shear modulus. In this appendix, two such approaches are shown and compared – one method, from work by Palierne and expounded upon by Jacobs [Palierne 1990, Jacobs 1999], where the complex modulus and a distribution of droplet sizes is used to characterize the response, and a second method from work by van Hemelrijck [Van Hemelrijck 2004] which uses a single average droplet size and the storage modulus.

A.2 Methods

A.2.1 Materials

While interfacial tension analysis by shear rheology of droplet blends can be conducted on any blend composed of two highly immiscible phases, this appendix will focus on the three distinct blend systems presented in Chapters 3 and 4 – non-compatibilized PE/PEO blends, compatibilized PE-g-MA/PEO blends, and non-compatibilized PE/PLA blends.

The material properties of the pure materials are shown in Table A.1. Melting temperature, T_m, was measured by dynamic scanning calorimetry (DSC, TA Instruments Q1000). Number average and weight average molecular weight, M_n and M_w, were measured by gel permeation chromatography. Polyethylene (PE) samples were measured using a high temperature GPC (PL-GPC 220 High Temperature GPC/SEC System) at 155 °C using 1,2,4-trichlorobenzene as the eluent and compared to polystyrene standards. Polyethylene oxide (PEO) samples were measured using room temperature GPC (Wyatt Instruments) using 0.1M sodium sulfate in 1% acetic acid aqueous solution as the eluent, and M_n and M_w were measured directly by light scattering (Wyatt HELEOS II) and refractive index (Wyatt Optilab rEX) using a d*n*/d*c* value of 0.1350. Polylactic acide (PLA) samples were measured using a room temperature GPC (SpectraSYSTEM AS 1000, Thermo Separation Products) using tetrahydrofuran as the eluent and compared to polystyrene standards. Density values were provided by the material supplier.

Table A.1. Pure material thermal and molecular weight properties.

	T_m (°C)	M_n (kg/mol)	M_w (kg/mol)	ρ (g/cm^3) @ 23 °C
LDPE	105	11.8	59	0.92
HDPE	120	18	90	0.954
PE-g-MA	125	13.5	79	0.96
20K PEO	63	17.8	18.2	1.2
40K PEO	65	36.8	79.7	1.2
60K PEO	65	58.8	121	1.2
200K PEO	65	216	386	1.2
Linear PLA	165	137	231	1.24
Branched PLA	165	134	331	1.18

A.2.2 Blend Preparation

Blends for interfacial tension analysis were prepared in a recirculating batch microcompounder (DACA Instruments). The mixer was filled to a volume of 5 cm^3 in all cases. PE/PEO and PE-g-MA/PEO blends were prepared at a mixing temperature of 150 °C and a rotor speed of 200 RPM. PE/PLA blends were prepared at a mixing temperature of 180 °C and a rotor speed of 200 RPM. In all cases, PE was used as the major phase with PEO or PLA forming the droplet phase with a mass fraction of 10%. Following melt mixing, the mixer chamber was opened, and all material around the walls and screws was collected and rapidly quenched in liquid nitrogen to freeze the morphology. Material was formed into 1-mm thick, 25-mm diameter disks using a compression mold (Carver, Inc., Wabash, Indiana), at the mixing temperature of the sample.

The blends analyzed are reported in Table A.2**Error! Reference source not found.**, along with the total volume fraction of the droplet phase and the volume average droplet radius, as measured by the SEM microscopy, described below.

Table A.2. Droplet blends prepared for rheological analysis.

Blend name	**Major Phase**	**Minor Phase**	**Droplet volume fraction, ϕ**	**Volume average droplet radius, R_v (μm)**
n-PEO-1	LDPE	20K PEO	0.079	3.12
n-PEO-2	LDPE	40K PEO	0.079	0.76
n-PEO-3	LDPE	60K PEO	0.079	0.44
n-PEO-4	LDPE	200K PEO	0.079	2.03
c-PEO-1	PE-g-MA	20K PEO	0.082	0.19
c-PEO-2	PE-g-MA	40K PEO	0.082	0.075
c-PEO-3	PE-g-MA	60K PEO	0.082	0.50
c-PEO-4	PE-g-MA	200K PEO	0.082	0.97
n-PLA-1	HDPE	Linear PLA	0.079	0.36

n-PLA-2	HDPE	Branched PLA	0.082	0.56
n-PLA-3	LDPE	Linear PLA	0.076	0.66
n-PLA-4	LDPE	Branched PLA	0.080	13.2

A.2.3 SEM Microscopy

Cross-sections of the 25-mm diameter disks were imaged by scanning electron microscopy (SEM, JEOL 6500). Prior to imaging, smooth cross-sections of the blends were prepared by cryo-microtome (Reichert UltraCut S Ultramicrotome) at -140 °C using a diamond knife. Blends were then soaked in a selective solvent for 48 hours to extract the minor phase from the surface of the blend – water was used as the solvent for PEO minor phases, and chloroform was used for PLA minor phases. The sections were dried in a vacuum oven and sputter coated with 50 Å of platinum. Samples were imaged at an accelerating voltage of 5 kV and a working distance of 10 mm.

The images were analyzed to measure the distribution of droplet sizes for each of the blends. A minimum of 4 images were analyzed for each blend. Droplet sizes histrograms were prepared following the method explained in Appendix B, and the volume average droplet radii shown in Table A.2 were calculated from the collected distributions.

A.2.4 Rheological Measurements

The linear viscoelastic rheological properties of the droplet blends and the individual blend components were measured by small amplitude oscillatory shear (SAOS) measurements in an ARES rheometer (TA Instruments). Prior to SAOS measurements, the critical strain of the materials was probed via strain sweeps, to determine the strain at which the materials exhibited non-linear viscoelastic properties. SAOS measurements were then conducted across a frequency range of 100-0.01 s^{-1}, using the auto-strain function in the TA Orchestrator software to increase

the strain with decreasing frequency, using the critical strain as the maximum allowable strain. Since much of the elastic response of the droplets occurred in the lower frequency regime, typically < 0.1 s^{-1}, high precision and accuracy was needed to accurately measure the interfacial tension and interfacial modulus. Measurements were repeated a minimum of three times to ensure repeatability.

A.2.5 Palierne/Jacobs Viscoelastic Droplet Model

The viscoelastic droplet model first proposed by Palierne and expounded upon in work by Jacobs accounts for the complex viscoelastic response of a distribution of viscoelastic droplets within a viscoelastic matrix. The viscoelastic response of the droplet blend can be characterized by the following set of equations:

$$G^*_{blend} = G^*_m \left(\frac{1 + 3\sum_i \frac{\phi_i E_i}{D_i}}{1 - 2\sum_i \frac{\phi_i E_i}{D_i}} \right) \tag{A.2}$$

$$\begin{aligned} E_i = {} & \left(G^*_d - G^*_m\right)\left(19G^*_d + 16G^*_m\right) + 24\beta^*_d \frac{\Gamma}{R_i^2} + 16\beta^*_s \frac{\Gamma + \beta^*_d}{R_i^2} + \\ & 4\frac{\Gamma}{R_i}\left(5G^*_d + 2G^*_m\right) + \frac{\beta^*_d}{R_i}\left(23G^*_d - 16G^*_m\right) + \frac{2\beta^*_s}{R_i}\left(13G^*_d + 8G^*_m\right) \end{aligned} \tag{A.3}$$

$$\begin{aligned} D_i = {} & \left(2G^*_d + 3G^*_m\right)\left(19G^*_d + 16G^*_m\right) + 48\beta^*_d \frac{\Gamma}{R_i^2} + 32\beta^*_s \frac{\Gamma + \beta^*_d}{R_i^2} + \\ & 40\frac{\Gamma}{R_i}\left(G^*_d + G^*_m\right) + \frac{2\beta^*_d}{R_i}\left(23G^*_d + 32G^*_m\right) + \frac{4\beta^*_s}{R_i}\left(13G^*_d + 12G^*_m\right) \end{aligned} \tag{A.4}$$

where G_{blend}^*, G_m*, and G_d* are the complex moduli of the blend, matrix material, and droplet material respectively, ϕ_i is the volume fraction of droplets with radius R_i, Γ is interfacial tension, β^*_s is the interfacial shear modulus, and β^*_d is the dilatation modulus. It should be noted that in the version presented by Jacobs and coworkers, the summations present in Eq. A.2 are replaced

with integral functions so that continuous droplet distributions can be evaluated within the model. This was impractical for the image analysis methods used here, and so the summation as originally presented by Palierne is used instead.

For the current application of the model, the terms Γ, β_s^*, and β_d^* are used as fitting parameters, given known data about the component complex moduli and the droplet size distribution. However, when applied in this manner, the model presents an ambiguity when fitting β_s^*, and β_d^*, due to the similar mathematic structure in which both parameters appear in the model. Given that measurements here are conducted over small oscillations, and therefore changes in the droplet interfacial area which relates to dilational modulus is minimized, and the non-isotropic interfacial tension expected from dilatational effects can also be sufficiently described by an elastic interface [Van Hemelrijck], the present application will resolve the ambiguity by setting β_d^*=0, and fitting only with two parameters, Γ and β_s^*, treating the interfacial phase as completely elastic.

In the original model proposed by Palierne, the interfacial moduli β_s^* and β_d^* are frequency dependent, similar to the bulk elastic modulus of viscoelastic materials. However, in this case where the interface is assumed to be purely elastic (solid-like), the modulus β_s^* can be treated as frequency independent, conceptually similar to *G'* for a solid material.

A.2.6 Van Hemelrijck Viscoelastic Droplet Model

Palierne's viscoelastic droplet model was modified in work by Van Hemelrijck by applying three key assumptions. First is that the droplet distribution can be simplified to a single volume-averaged droplet size R_v. The second assumption and third assumptions are described above: that dilatational effects can be sufficiently described by an interfacial modulus, and that the interface is purely elastic, such that β_d^*=0 and β_s^* is frequency independent. Using these

assumptions and then modifying the original Palierne model to account for *G'* and *G"* independently (as opposed to the combined complex modulus G^*), the elastic modulus of the blend, G'_b, is given by the following equations:

$$G'_b(\omega) = \frac{G'_m(\omega)\left(y^2 + z^2 + \phi(xy + qz) - 6\phi^2\left(x^2 + q^2\right)\right) - 5G''_m(\omega)\phi(qy - xz)}{(y - 2\phi x)^2 + (z - 2\phi q)^2} \tag{A.5}$$

$$\begin{aligned} x = {} & \left[G'_d(\omega) - G'_m(\omega)\right]\left[19G'_d(\omega) + 16G'_m(\omega)\right] \\ & - \left[G''_d(\omega) - G''_m(\omega)\right]\left[19G''_d(\omega) + 16G''_m(\omega)\right] \\ & + 4\frac{\Gamma}{R_v}\left[5G'_d(\omega) + 2G'_m(\omega)\right] + 2\frac{\beta_s^*}{R_v}\left[13G'_d(\omega) + 8G'_m(\omega) + 8\frac{\Gamma}{R_v}\right] \end{aligned} \tag{A.6}$$

$$\begin{aligned} q = {} & \left[G'_d(\omega) - G'_m(\omega)\right]\left[19G''_d(\omega) + 16G''_m(\omega)\right] \\ & + \left[G''_d(\omega) - G''_m(\omega)\right]\left[19G'_d(\omega) + 16G'_m(\omega)\right] \\ & + 4\frac{\Gamma}{R_v}\left[5G''_d(\omega) + 2G''_m(\omega)\right] + 2\frac{\beta_s^*}{R_v}\left[13G''_d(\omega) + 8G''_m(\omega)\right] \end{aligned} \tag{A.7}$$

$$\begin{aligned} y = {} & \left[2G'_d(\omega) + 3G'_m(\omega)\right]\left[19G'_d(\omega) + 16G'_m(\omega)\right] \\ & - \left[2G''_d(\omega) + 3G''_m(\omega)\right]\left[19G''_d(\omega) + 16G''_m(\omega)\right] \\ & + 40\frac{\Gamma}{R_v}\left[G'_d(\omega) + G'_m(\omega)\right] + 4\frac{\beta_s^*}{R_v}\left[13G'_d(\omega) + 12G'_m(\omega) + 8\frac{\Gamma}{R_v}\right] \end{aligned} \tag{A.8}$$

$$\begin{aligned} z = {} & \left[2G''_d(\omega) + 3G''_m(\omega)\right]\left[19G'_d(\omega) + 16G'_m(\omega)\right] \\ & + \left[2G'_d(\omega) + 3G'_m(\omega)\right]\left[19G''_d(\omega) + 16G''_m(\omega)\right] \\ & + 40\frac{\Gamma}{R_v}\left[G''_d(\omega) + G''_m(\omega)\right] + 4\frac{\beta_s^*}{R_v}\left[13G''_d(\omega) + 12G''_m(\omega)\right] \end{aligned} \tag{A.9}$$

where G'_d and G''_d are the storage and loss moduli of the droplets, G'_m and G''_m are the storage and loss moduli of the matrix, R_v is the volume average droplet radius, and ϕ is the volume fraction of droplets within the blend. The same two fitting parameters, Γ and β_s^*, are used.

A.2.7 Gramespacher-Meissner Droplet Model

Another simplified model was also proposed in work by Gramespacher and Meissner

[Gramespacher and Meissner 1992], which also sought to correlate the rheological response of a droplet blend to the rheology of the pure components and the interface between them. Contrary to the Jacobs and Van Hemelrijck models, this model does not include any interfacial moduli – the interfacial term depends only on interfacial tension. However, the model is useful due to the ease of interpretation of the results. The model assumes that the viscoelastic response can be handled by a rule of mixtures for the pure components plus an additional Maxwell mode for the interfacial contribution. This makes interpretation of the results simple, as a relaxation time for the interface can be easily extracted from the equations.

$$G'_{blend} = \phi G'_{droplet} + (1-\phi)G'_{matrix} + \frac{\eta}{\tau_1}\left(1-\frac{\tau_2}{\tau_1}\right)\frac{\omega^2\tau_1^2}{1+\omega^2\tau_1^2} \tag{A.10}$$

$$G''_{blend} = \phi G''_{droplet} + (1-\phi)G''_{matrix} + \frac{\eta}{\tau_1}\left(1-\frac{\tau_2}{\tau_1}\right)\frac{\omega\tau_1}{1+\omega^2\tau_1^2} \tag{A.11}$$

$$\eta = \eta_{matrix}\left[1+\phi\frac{(5k+2)}{2(k+1)}+\phi^2\frac{(5k+2)^2}{8(k+1)^2}\right] \tag{A.12}$$

$$\tau_1 = \tau_0\left[1+\phi\frac{5(19k+16)}{4(k+1)(2k+3)}\right] \tag{A.13}$$

$$\tau_2 = \tau_0\left[1+\phi\frac{3(19k+16)}{4(k+1)(2k+3)}\right] \tag{A.14}$$

$$\tau_0 = \frac{\eta_{matrix}R}{\Gamma}\frac{(19k+16)(2k+3)}{40(k+1)} \tag{A.15}$$

$$k = \frac{\eta_{droplet}}{\eta_{matrix}} \tag{A.16}$$

From these equations, the relaxation time of the Maxwell element that describes the interfacial contribution to the storage and loss moduli is given by the term τ_1.

A.3 Results

A.3.1 LDPE/PEO blends

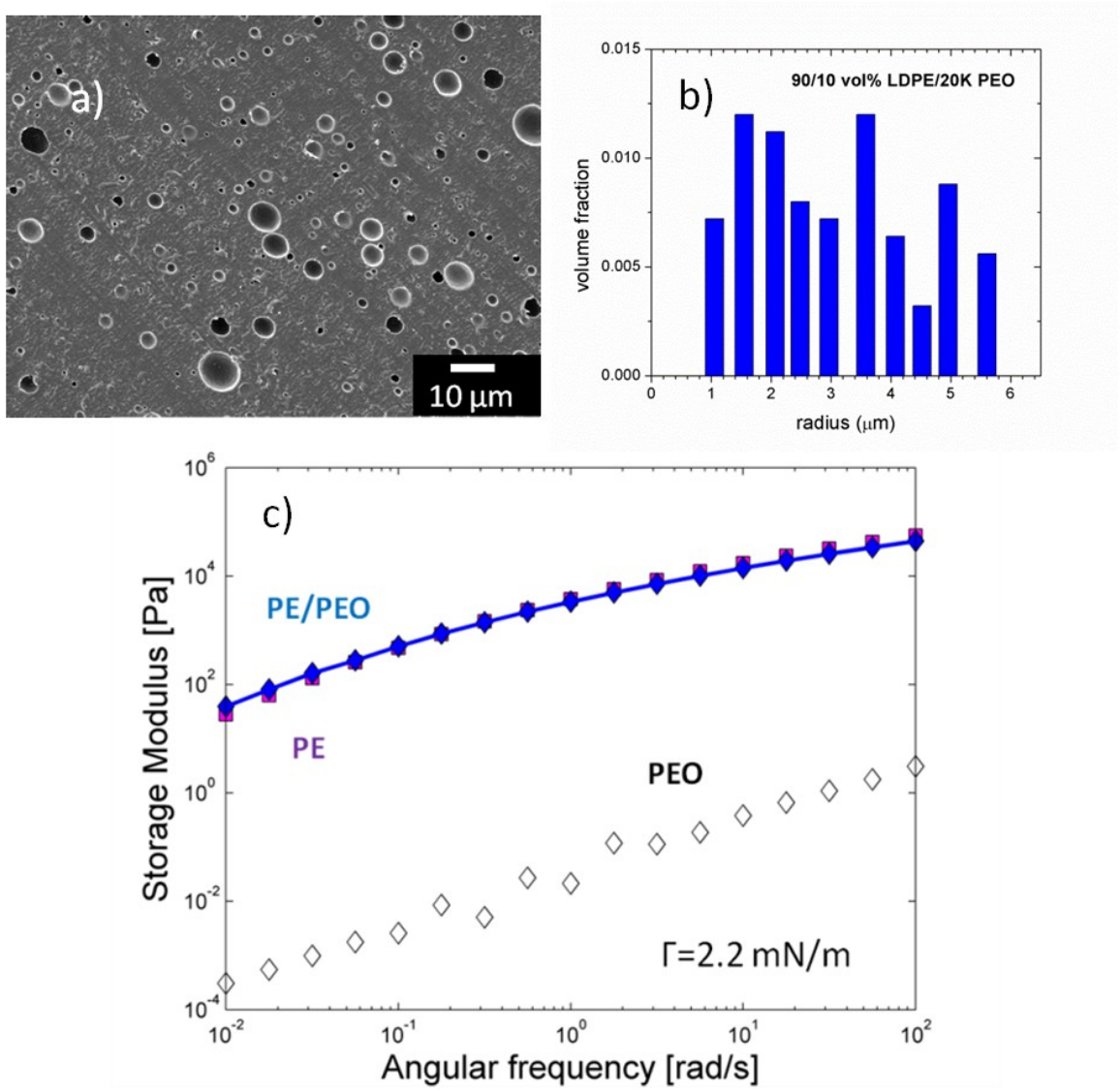

Figure A.1. Palierne model data for LDPE/20K PEO, 90/10 vol%. a) Characteristic SEM image of cross-sectioned blend. b) Droplet size histogram. c) Storage modulus for pure materials and the blend. The line represents the Palierne model fit based on the droplet size distribution, the pure material rheology, and the parameters as listed on the plot.

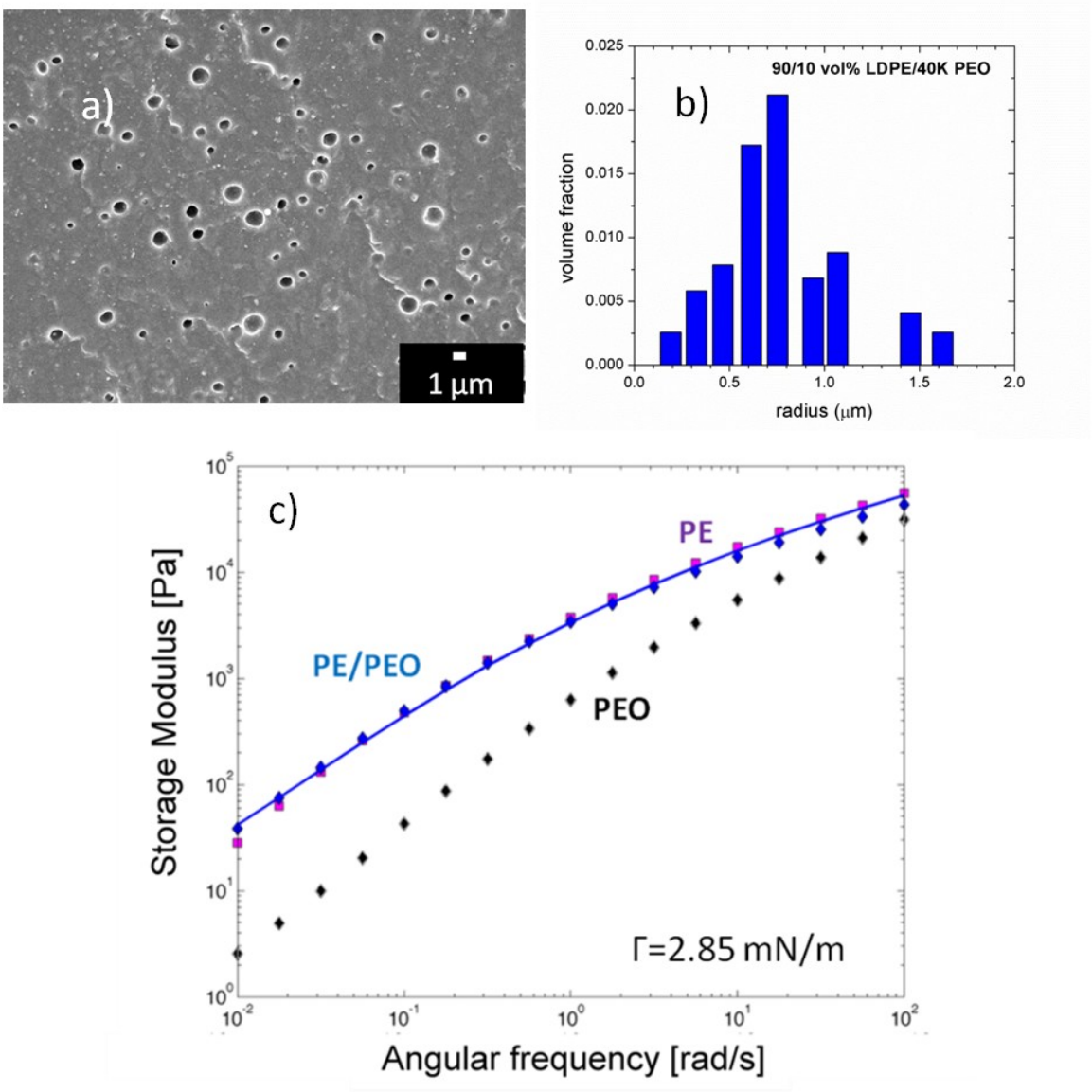

Figure A.2. Palierne model data for LDPE/40K PEO, 90/10 vol%. a) Characteristic SEM image of cross-sectioned blend. b) Droplet size histogram. c) Storage modulus for pure materials and the blend. The line represents the Palierne model fit based on the droplet size distribution, the pure material rheology, and the parameters as listed on the plot.

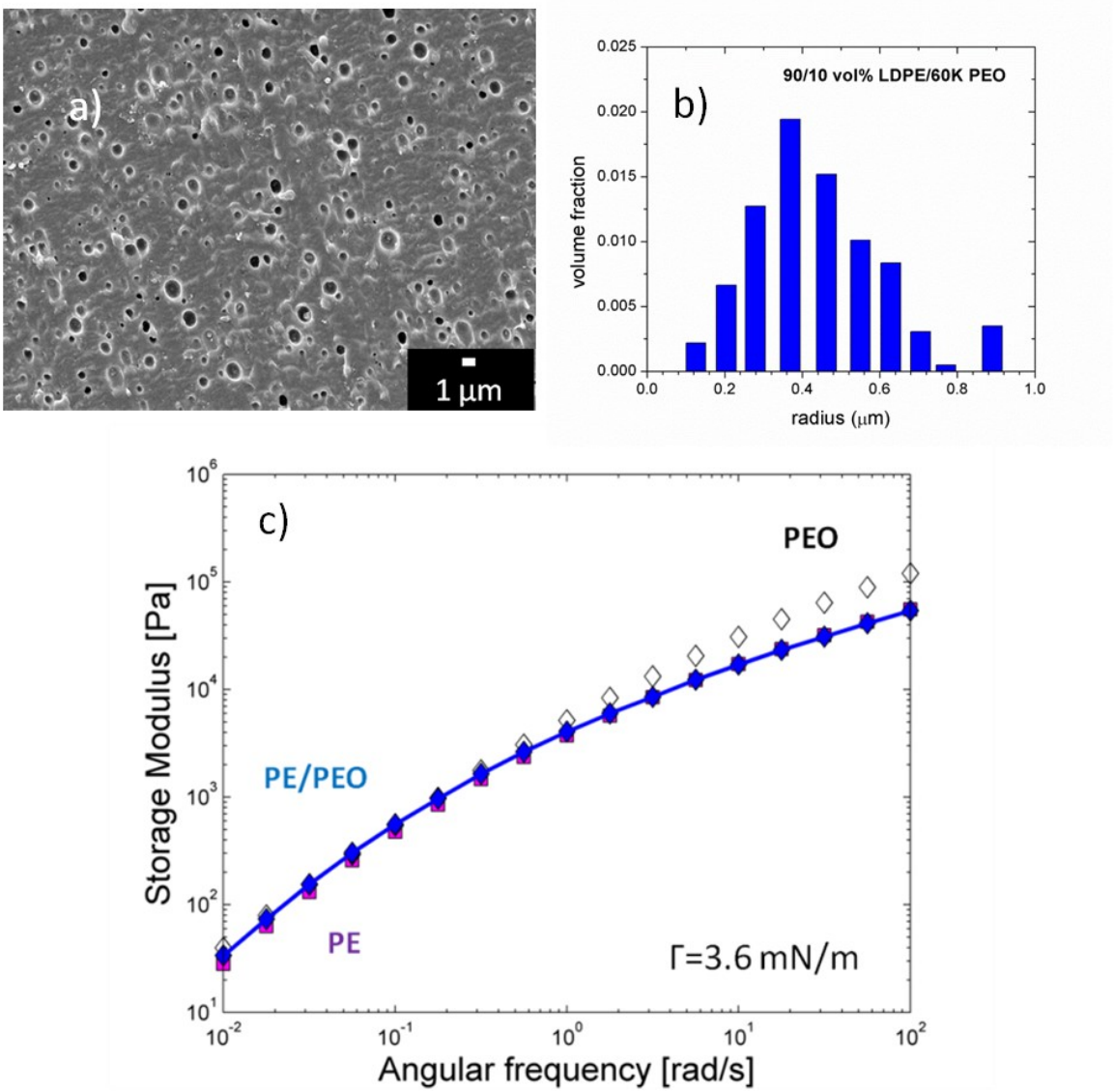

Figure A.3. Palierne model data for LDPE/60K PEO, 90/10 vol%. a) Characteristic SEM image of cross-sectioned blend. b) Droplet size histogram. c) Storage modulus for pure materials and the blend. The line represents the Palierne model fit based on the droplet size distribution, the pure material rheology, and the parameters as listed on the plot.

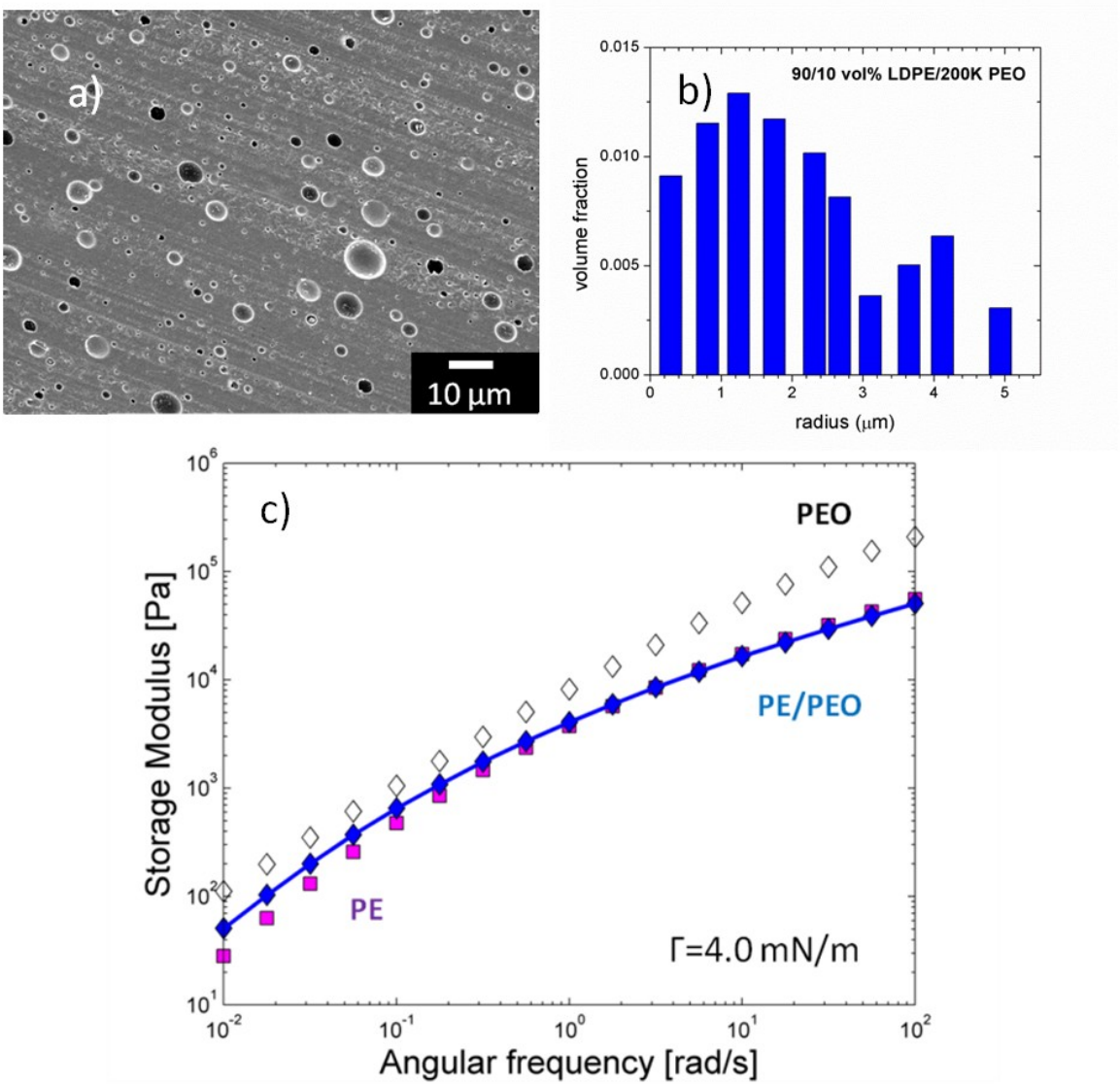

Figure A.4. Palierne model data for LDPE/200K PEO, 90/10 vol%. a) Characteristic SEM image of cross-sectioned blend. b) Droplet size histogram. c) Storage modulus for pure materials and the blend. The line represents the Palierne model fit based on the droplet size distribution, the pure material rheology, and the parameters as listed on the plot.

A.3.2 PE-g-MA/PEO blends

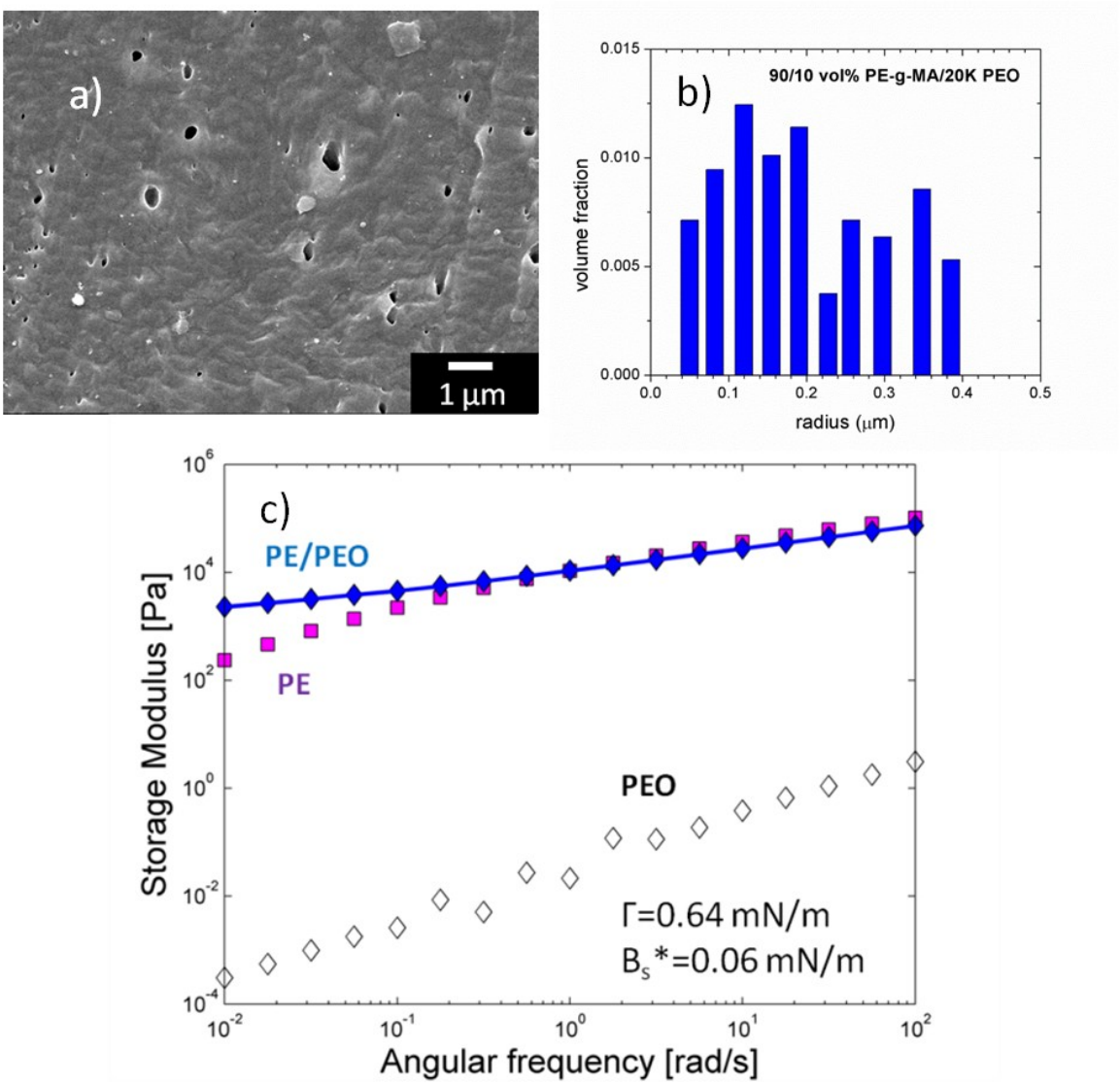

Figure A.5. Palierne model data for PE-g-MA/20K PEO, 90/10 vol%. a) Characteristic SEM image of cross-sectioned blend. b) Droplet size histogram. c) Storage modulus for pure materials and the blend. The line represents the Palierne model fit based on the droplet size distribution, the pure material rheology, and the parameters as listed on the plot.

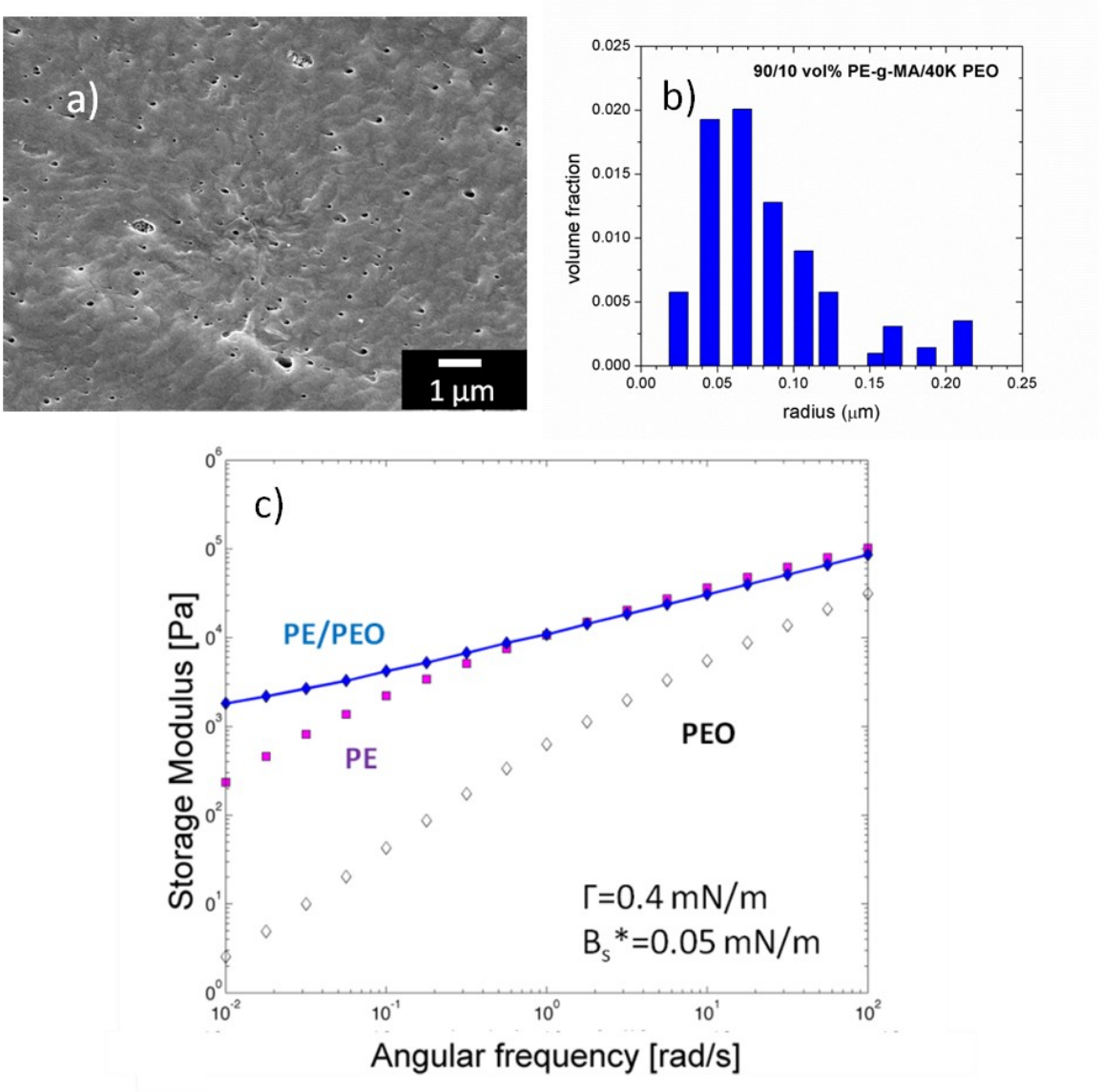

Figure A.6. Palierne model data for PE-g-MA/40K PEO, 90/10 vol%. a) Characteristic SEM image of cross-sectioned blend. b) Droplet size histogram. c) Storage modulus for pure materials and the blend. The line represents the Palierne model fit based on the droplet size distribution, the pure material rheology, and the parameters as listed on the plot.

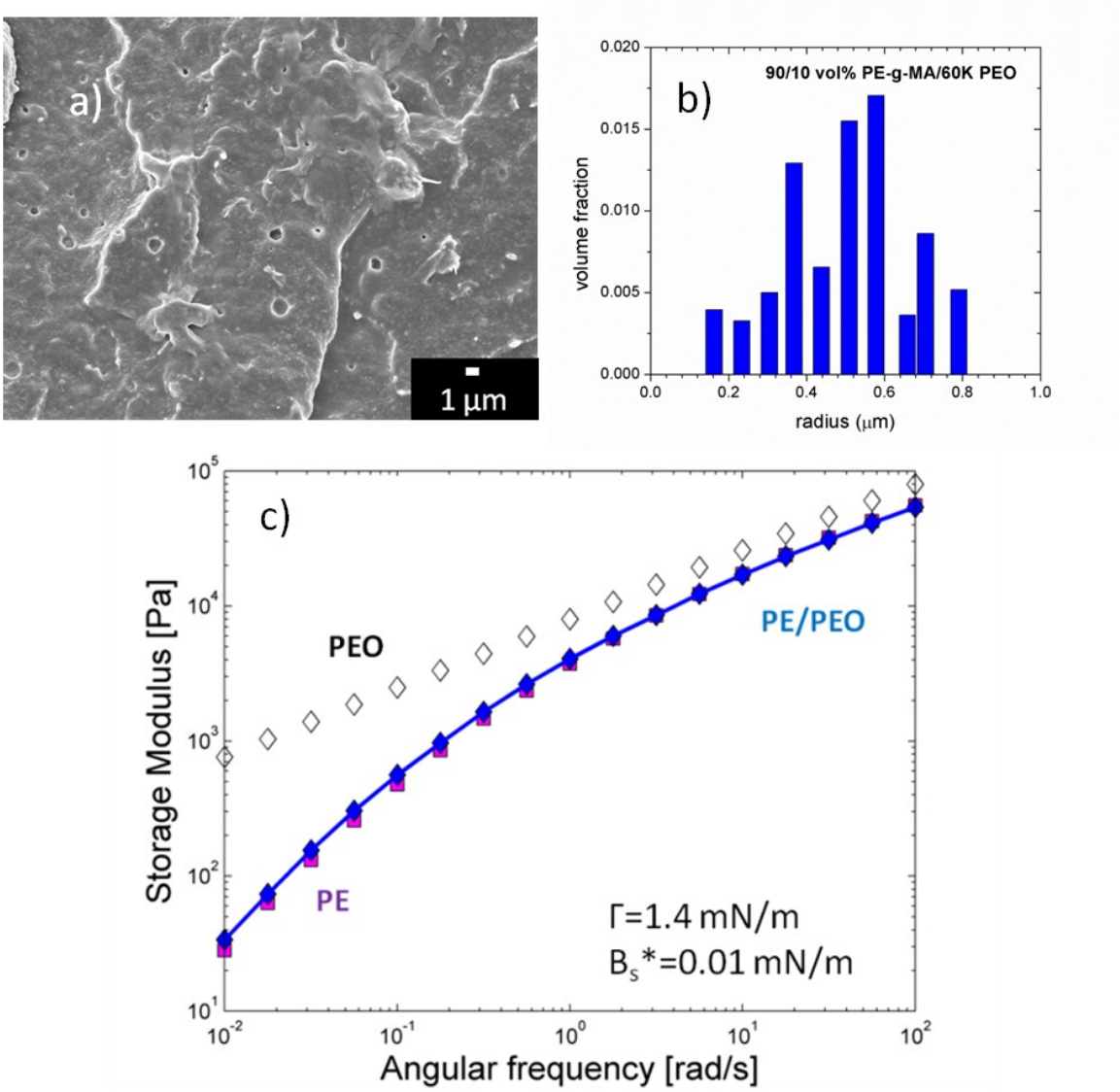

Figure A.7. Palierne model data for PE-g-MA/60K PEO, 90/10 vol%. a) Characteristic SEM image of cross-sectioned blend. b) Droplet size histogram. c) Storage modulus for pure materials and the blend. The line represents the Palierne model fit based on the droplet size distribution, the pure material rheology, and the parameters as listed on the plot.

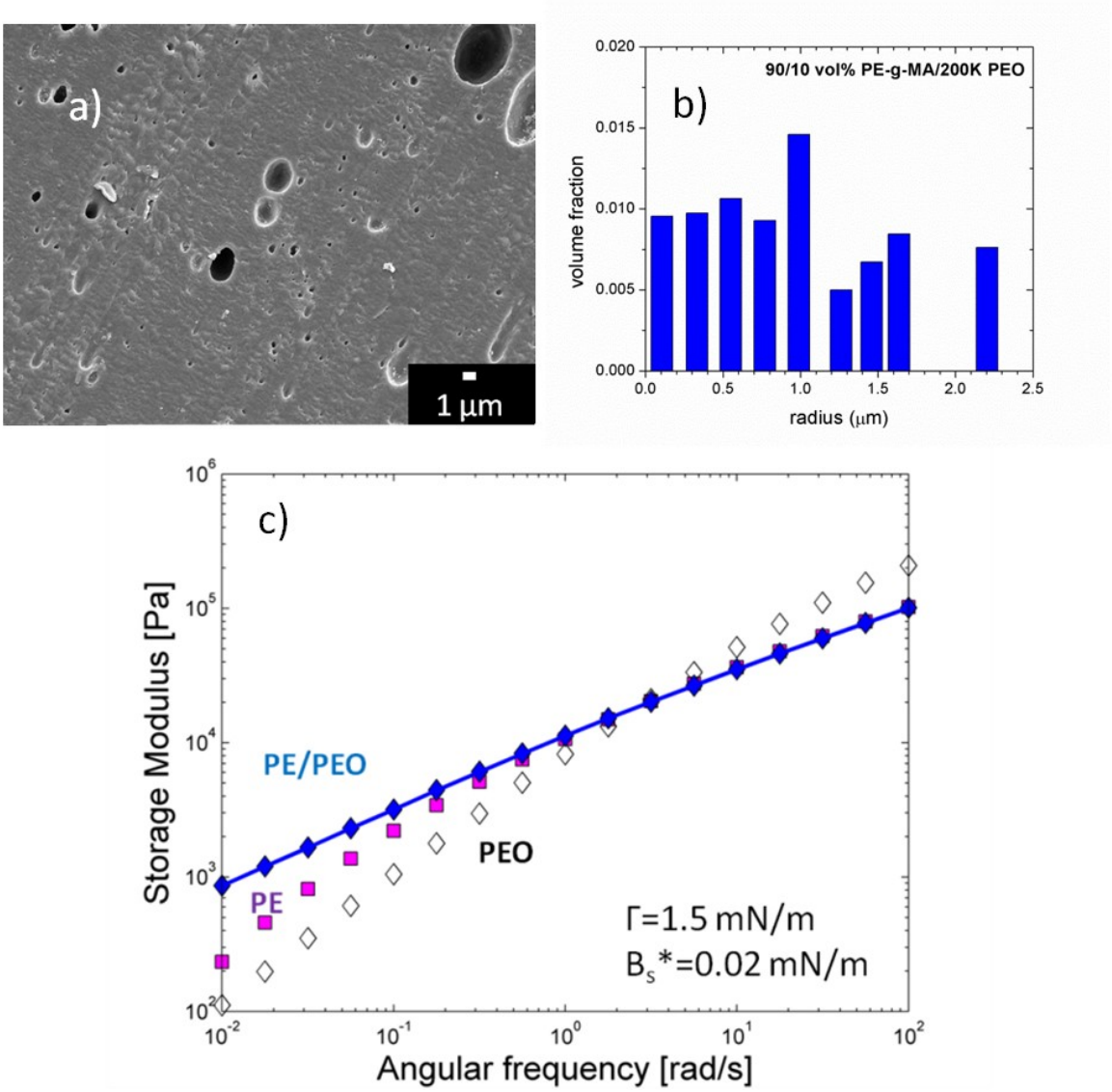

Figure A.8. Palierne model data for PE-g-MA/200K PEO, 90/10 vol%. a) Characteristic SEM image of cross-sectioned blend. b) Droplet size histogram. c) Storage modulus for pure materials and the blend. The line represents the Palierne model fit based on the droplet size distribution, the pure material rheology, and the parameters as listed on the plot.

Appendix B: Comparison of 2D and 3D image analysis methods for polymer blends

B.1 3D Imaging by LSCM

PE/PEO cocontinuous blends are opaque and not fluorescent. In order to image them via LSCM, thin slices were cut from the extrudate. After overnight extraction of PEO in water, slices were dried for 24 hours and then placed on glass microscope slides. 2-Hydroxyethyl(methacrylate) (HEMA) containing 0.01wt% Rhodamine B fluorescent dye, which fluoresces when exposed to a laser with 563 nm wavelength, and 1wt% azobisisobutyronitrile (AIBN) radical initiator was dropped via pipette onto the sections, and was allowed to fill the pores in the PE. The samples were then covered with glass cover slips and heated at 80 °C for 10 minutes to polymerize the HEMA. The refractive index of the polymerized HEMA matched that of the PE, thus fulfilling the requirements of optical transparence and fluorescent phase contrast, with the fluorescent HEMA phase representing the extracted PEO phase. Under these conditions, blends could be imaged to a depth of approximately 100 μm.

An iterative selection tresholding method was developed by Milana Trifkovic in MATLAB and applied to binarize the stacks of 2D images acquired by LSCM. The 3D image was reconstructed using Avizo (v. 6.3, http://www.vsg3d.com/avizo) interactive visualization package. A triangular mesh was generated along the interface of the 3D images using a marching cubes algorithm included in the Avizo software package. Interfacial area was calculated by summing the areas of all the triangles, A_i of the generated mesh. Dividing volume of the sample, V, by the total interfacial area gives a characteristic size of the blend features, a:

$$a = V \Big/ \sum_{i=1}^{N} A_i \tag{B.1}$$

A sample image for analysis is shown above in Figure 3.3.

B.2 Droplet Analysis by SEM Images

The complete MATLAB code is provided here for 2D image analysis of SEM images of droplet blends. This technique works best when the edges of the droplets are traced, as is shown in Figure B.1.

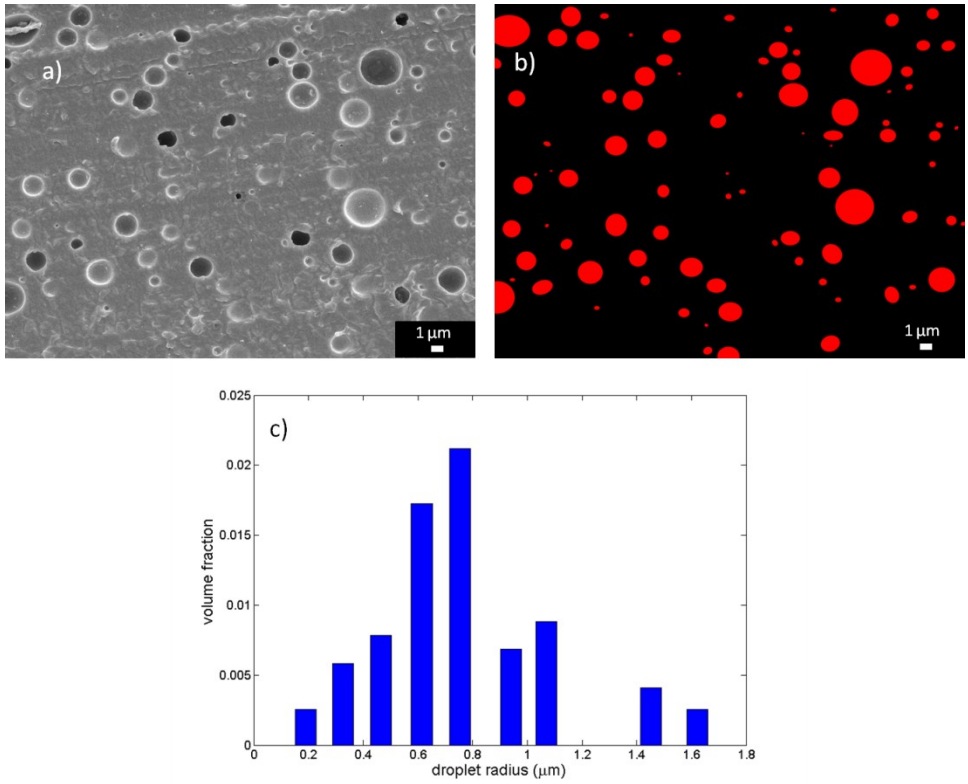

Figure B.1. Example image for droplet tracing to improve the edge detection of the droplet sizing software. a) Raw SEM image. b) Image with traced and filled drops and background, to improve contrast. c) Droplet size histogram the above image, generated by the provided code.

Figure B.2. MATLAB code for 2D droplet size analysis.

```
function [numNodes,edgePicture,numStruc,numPPS,VADsize,NADsize] = fp(filename, thresh1, numGloops, thresh2, outfilename)
%FP (FindPerimeter)  02/15/2011 revision by Aaron Hedegaard
%   (based on 2/22/2001 version, by Matthew Montminy)
%
%[numNodes,edgePicture]=fp(filename,thresh1,numGloops,thresh2,outfilename)
%
%This routine finds the edges in a picture.  It is specially tuned for SEM
%pictures which have shadows and thick boundaries between regions.  The
%input parameters can be used to tune the routine so that double edges can
%be ignored.
```

```
%
%INPUTS:
%  All but filename are optional.
%  filename must be in 'single quotes'.
%    All files must be grayscale images.
%  thresh1 is the sesitivity of the filter used to find edges in the
%    original image.  Making thresh1 smaller will increase the number of
%    edges detected in the first pass, (represented by Figure 2.)
%  numGloops specifies the number of times the gaussian smoothing filter is
%    applied to the result.  This blurs the thresh1 edge image and allows
%    for merging of close edges.  The result of this step is shown in
%    Figure 3.
%  thresh2 is the threshold used to determine what parts of the blurred
%    image will be accepted as edges.  This number must be between 0 and 1.
%  outfilename is the filename of the tif image of the detected edges.
%    This image will be written into the working directory.
%
%OUTPUTS:
%  numNodes, the default return value, is the number of (white) edge pixels
%    found in the result.  This corresponds to the number of white dots in
%    Figure 5.
%  edgePicture, the optional return value, is the array representing the
%    locations of edges in the picture.  All values are 0 or 1; this array
%    is used to create Figure 5 and the output image.

if (nargin <4)
   numGloops=3;
end

if (nargin < 3)
   thresh2 = 0.15;
end

if (nargin < 2)
   thresh1 = 0.08;
end

a=imread(filename, 'tif');

figure(1); colormap(gray);
a=a(1:512, 1:640);
imshow(a);
a=medfilt2(a);

figure(2); colormap(gray);
b=edge(a, 'sobel', thresh1);
imshow(b);

h=fspecial('gaussian');
```

```
c=filter2(h,b);
for i=1:numGloops
   c=filter2(h,c);
end
c=medfilt2(c);

figure(3); colormap(gray);
imshow(c);
c=c>thresh2;

figure(4); colormap(gray);
imshow(c);

c=bwmorph(c,'thin',Inf);

figure(5); colormap(gray);
imshow(c);

disp('Number of edge pixels found: ')
numNodes=sum(sum(c))
edgePicture=c;

if nargin==5
   imwrite(c, outfilename);
end

quatSum = 0;
cubeSum = 0;
linSum = 0;

CC = bwconncomp(c);

disp('Number of structures found: ')
numStruc=CC.NumObjects

numPPSunsort=cellfun(@numel, CC.PixelIdxList)/1;
%% This line above serves to find radius of spherical particles, based on perimeter.
%% Have /1 at the end if you just want the raw perimeter values.
%% This will throw off area calculations, however.

%% Have /4 at the end if analyzing images with X over drops,
%% Have /(2*3.14159) at the end if analyzing circles.

numPPS = sort(numPPSunsort);

for i = 1:numStruc
   quatSum = (numPPS(i))^4+quatSum;
   cubeSum = (numPPS(i))^3+cubeSum;
   linSum = (numPPS(i))+linSum;
end
```

```
nbins = 20;
figure, hist(numPPS, nbins)
title('Histogram of Droplet Radius (in pixels)');


distro = hist(numPPS, nbins);

stepnum = 0;
binvalue = [];
binvolfrac = [];
for i = 1:nbins
   binQuatSum = 0;
   binCubeSum = 0;
   binLinSum = 0;
   distrobin = [];
   binarea = 0;
   for j = 1:distro(i)

      stepnum = stepnum + 1;

      distrobin = [distrobin numPPS(stepnum)];
      binQuatSum = (numPPS(stepnum))^4+binQuatSum;
      binCubeSum = (numPPS(stepnum))^3+binCubeSum;
      binLinSum = (numPPS(stepnum))+binLinSum;
      binarea = binarea + pi*(numPPS(stepnum))^2;

   end

   numavbinrad = binLinSum/distro(i);
   binvalue = [binvalue numavbinrad];
   binvolfrac = [binvolfrac binarea/(512*640)];
end

binvalue = binvalue(isfinite(binvalue));
distro = distro(distro > 0);
binvolfrac = binvolfrac(binvolfrac > 0);

disp('Histogram of droplet Radius (in pixels)')
histy = [binvalue; distro; binvolfrac];
histfinal = histy'

columnsum = sum(histfinal)

disp('Number Average droplet radius: ')
NADsize = linSum/numStruc

disp('Volume Average droplet radius: ')
VADsize = quatSum/cubeSum
end
```

B.3 Cocontinuous Blend Size by 2D and 3D

The MATLAB code provided in Section B.2 could also be used to measure the total interfacial perimeter shown in a two-dimensional micrograph. This value could be used to calculate a characteristic size given by the cross-sectional area divided by interfacial perimeter, which should be related to the characteristic size given by volume per interfacial area calculated using Eq. B.1 for the three-dimensional reconstructions.

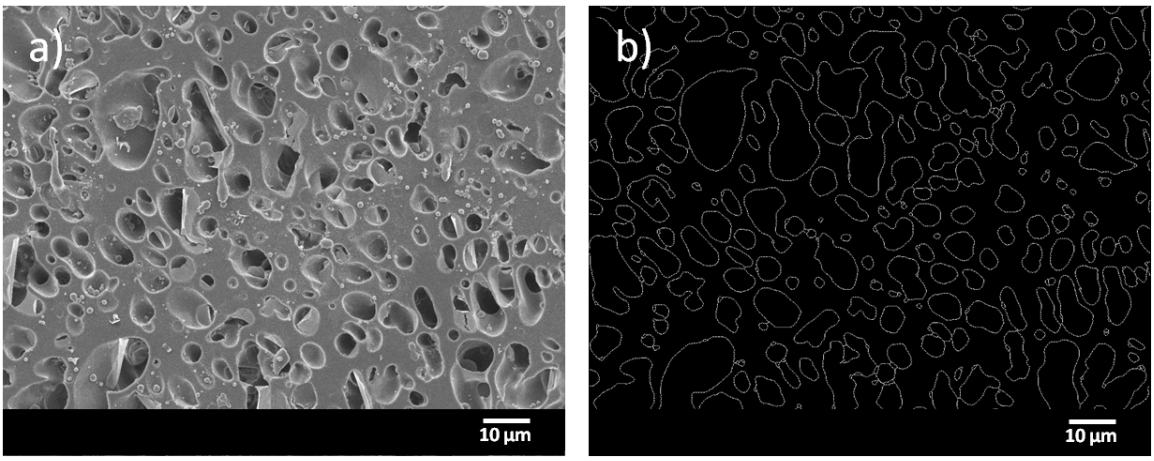

Figure B.3. Tracing of an SEM micrograph to calculate interfacial perimeter per area. a) SEM micrograph of a cocontinuous 45/55 vol% HDPE/Branched PLA blend. b) The results from the MATLAB code after tracing around the blends interface. The cross-sectional area/interfacial perimeter is 3.5 microns.

Before applying the MATLAB code to a two dimensional image, the interface was traced to heighten the contrast to better measure the total perimeter. This was particularly important for SEM micrographs of extracted cocontinuous blends, as the SEM image gave the perception of "depth" in the image, and features below the cross-sectional plane could be seen when looking inside the washed out phase. This resulted in numerous false positives, where the edge detection software would report the existence of an interface within the washed out phase in addition to the edges along the cross-sectional plane. An example of a traced SEM micrograph is shown in Figure B.3. The characteristic size measured by tracing of two-dimensional results compared favorably to similar results for the three-dimensional image processing, as shown in Figure B.4.

However, 3D image processing was preferred in the present work due to improved accuracy since the features were measured in three dimensions as opposed to two, which does not necessarily detect anisotropy. Furthermore, 3D image processing was less time consuming experimentally, as no manual tracing was required for image analysis.

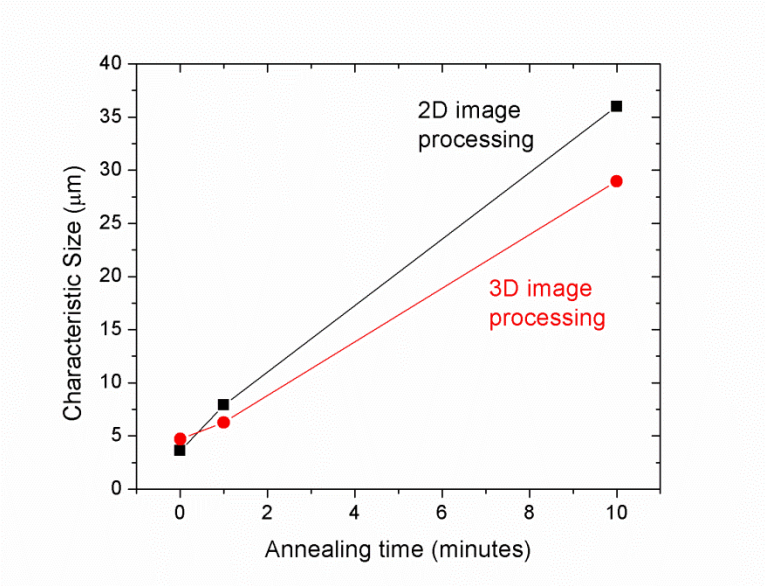

Figure B.4. Comparison of characteristic size, as measured by 2D and 3D images. The samples shown here were cocontinuous 45/55 vol% HDPE/Branched PLA, subjected to up to 10 minutes of annealing at 180 °C.

Appendix C: Fumed Silica and Molecular Weight Dependence of PEO Viscosity

This overview is intended to elucidate the rheological differences observed between commercially available polyethylene oxide (PEO) resins which contain on the order of 2 wt% fumed silica and PEO prepared with no silica.

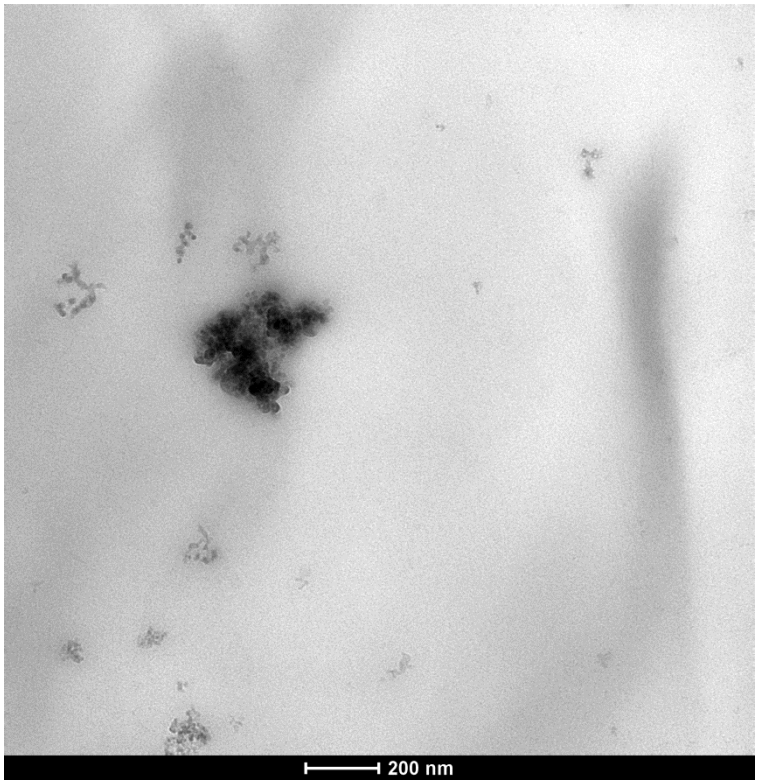

Figure C.1. TEM micrograph of Polyox N10 PEO resin, showing clusters of fumed silica.

The commercial resins that were investigated were trade named Polyox PEO water soluble resins, available from Dow Chemical, specifically the N10, N80, and N3000 grades with a reported weight average molecular weight (M_w) of 100, 200, and 400 kg/mol, respectively. Figure C.1 shows a TEM micrograph taken of Polyox N10, verifying the presence of fumed silica. The silica free resin used for this study was batch #52. The molecular weight of the silica-free PEO was tuned by melt mixing the resin in a conical twin-screw batch mixer (DACA Instruments) for a variable residence time with no antioxidants and no nitrogen purge to cause

molecular weight breakdown. A minimum of 1 minute blending time was needed to densify the as-received silica free PEO powder so that could it be measured on the rheometer.

Molecular weights of the resins were measured by room temperature aqueous GPC (Wyatt Instruments) using 0.1M sodium sulfate in 1% acetic acid aqueous solution as the eluent. Prior to testing, solutions were filtered through 220 nm pore size PVDF membranes in order to remove nanoparticles or any material that failed to dissolve. The number average (M_n) and weight average (M_w) molecular weight were measured directly by light scattering (Wyatt HELEOS II) and refractive index (Wyatt Optilab rEX) using a dn/dc value of 0.1350.

Table C.1 shows the results from the GPC experiments. As expected, a longer residence time in the melt compounder more greatly reduced the molecular weight. All melt-mixed silica free PEO showed slightly higher polydispersity compared to the commercial resins. The commercial resins showed M_w that aligned somewhat closely to the reported values.

Table C.1. Number and weight average molecular weight, as determined by aqueous GPC, and zero-shear melt viscosity as determined by complex viscosity from small amplitude oscillatory shear rheology and fit with a Cross model.

Material	M_n (kg/mol)	M_w (kg/mol)	PDI	η_o (Pa s)
Polyox N3000 (2 ± 0.5 wt% fumed silica, reported M_w ~ 400 kg/mol)	216	386	1.79	60100
Polyox N80 (2 ± 0.5 wt% fumed silica, reported M_w ~ 200 kg/mol)	58.8	121	2.06	30200
Polyox N10 (2 ± 0.5 wt% fumed silica, reported M_w ~ 100 kg/mol)	36.8	79.7	2.17	10500
Silica free PEO #52, 1 minute blended	38.2	107	2.80	13200
Silica free PEO #52, 5 minute blended	26.4	90.9	3.44	7570
Silica free PEO #52, 10 minute blended	25.6	69.5	2.71	5130
Silica free PEO #52, 15 minute blended	7.42	39.0	5.26	2820

Rheological measurements were conducted at 150 °C on an ARES oscillatory shear rheometer (TA Instruments) using 25 mm parallel plates. The rheometer oven was continually

purged with N_2 gas to prevent molecular weight breakdown during the experiment. The critical strain of all the resins was verified by strain sweep experiments to ensure that subsequent frequency sweeps were conducted at strains within the linear viscoelastic regime.

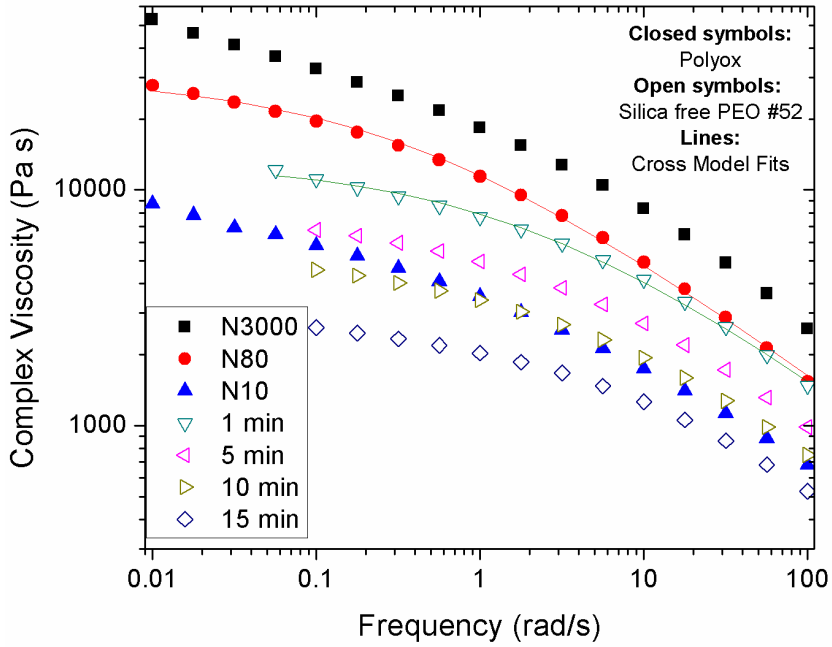

Figure C.2. Complex viscosity as a function of frequency. The closed symbols show the results for the commercial PEO resins, while the open symbols show the silica-free PEO after varying blending times. The lines are shown as examples of the Cross model fitting used to ascertain the zero-shear viscosity.

Figure C.2 shows the complex viscosity results from frequency sweeps of each of the resins at 150 °C. As expected, the viscosity decreases with longer blending time, indicative of the reduced molecular weight. Complex viscosity data for each material was fit with a Cross model:

$$\frac{\eta - \eta_\infty}{\eta_o - \eta_\infty} = \frac{1}{1 + (K\dot{\gamma})^n} \qquad \text{(C.1)}$$

where η_o is zero shear viscosity, η_∞ is infinite shear viscosity (assumed to be zero), n is the power law coefficient, and K is a time constant for the onset of shear thinning.

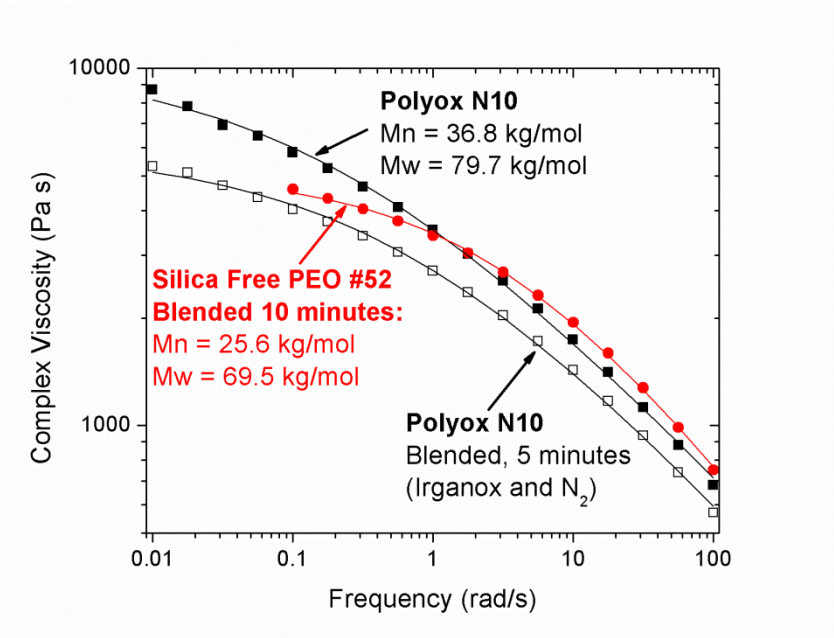

Figure C.3. Complex viscosity for Polyox N10, both as received and following 5 minutes of blending with Irganox antioxidant and nitrogen purge, and the silica-free PEO after 10 minutes of blending. The lines show Cross model fits.

Figure C.3 shows the complex viscosity data (with Cross model fits) for the silica-free PEO blended for 10 minutes and Polyox N10. These two materials showed a nearly matched molecular weight, and so they were used to investigate the role of the fumed silica on the rheological properties of the resins. At frequencies greater than 1 rad/s, complex viscosity of the materials are nearly identical, suggesting that silica has not strongly affected the properties of the resins under higher shear rate flow conditions. However, the silica-free PEO appears to begin to approach a zero-shear viscosity plateau starting at a much higher frequency than the Polyox resins containing the fumed silica. This also results in the Polyox resin showing a zero-shear viscosity double that of the silica-free PEO.

Also of interest is the complex viscosity data of Polyox N10 following 5 minutes of blending in the DACA microcompounder. Blending was conducted under nitrogen purge with 0.2 wt% Irganox 1010 antioxidant added to the material. The commercial PEO shows approximately a two-fold decrease in zero-shear complex viscosity as a result of the blending

procedure, which is related to a decrease in molecular weight. It should be noted that this may correlate more closely to the true viscosity of the PEO during blending experiments, where the process of creating the cocontinuous blends is likely to reduce PEO molecular weight. This is a potential source of error with interfacial tension measurements and coarsening rates as well, as described earlier in Chapter 5.

Figure C.4 shows the zero-shear viscosity for each sample as a function of M_w. The zero-shear viscosity appeared to scale roughly linearly with M_w, an unexpected result considering that reptation theory for polymer melts predicts that $\eta_o \propto M_w^{3.4}$. Commercial resins containing fumed silica did see a slight increase in zero-shear viscosity relative the silica-free resins.

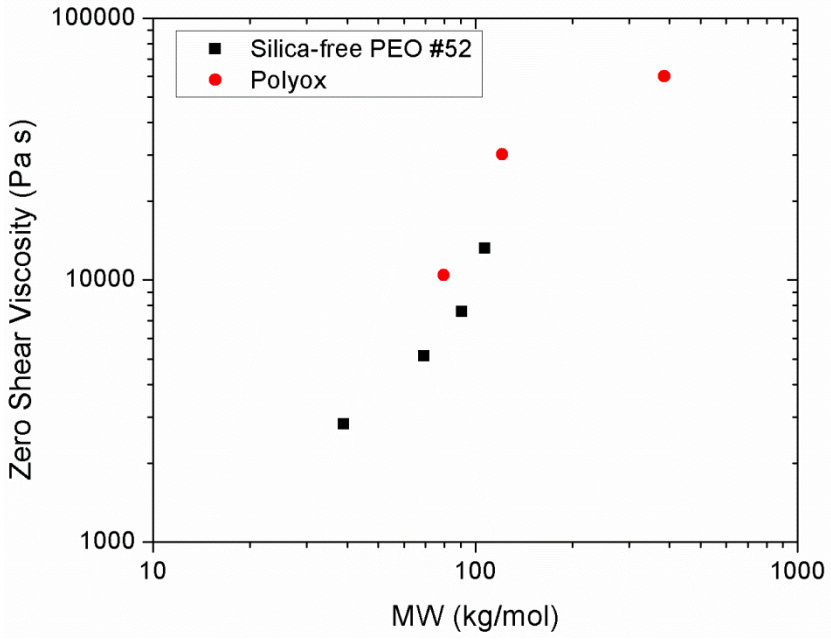

Figure C.4. Zero shear viscosity as a function of weight average molecular weight.

Figure C.5 and Figure C.6 show the storage modulus, *G'*, as a function of frequency for the PEO resins at 150 °C. Particularly in the case of nearly matching molecular weight between Polyox N10 and silica-free PEO blended for 10 minutes (as shown in Figure 6), PEO containing fumed silica shows a stronger elastic response at frequencies below approximately 5 rad/s, while showing little change to *G'* at higher frequencies. At a frequency of 0.1 rad/s, *G'* for Polyox N10

was approximately twice that of the M_w-matched silica-free PEO, analogous to the results observed from the zero-shear viscosity.

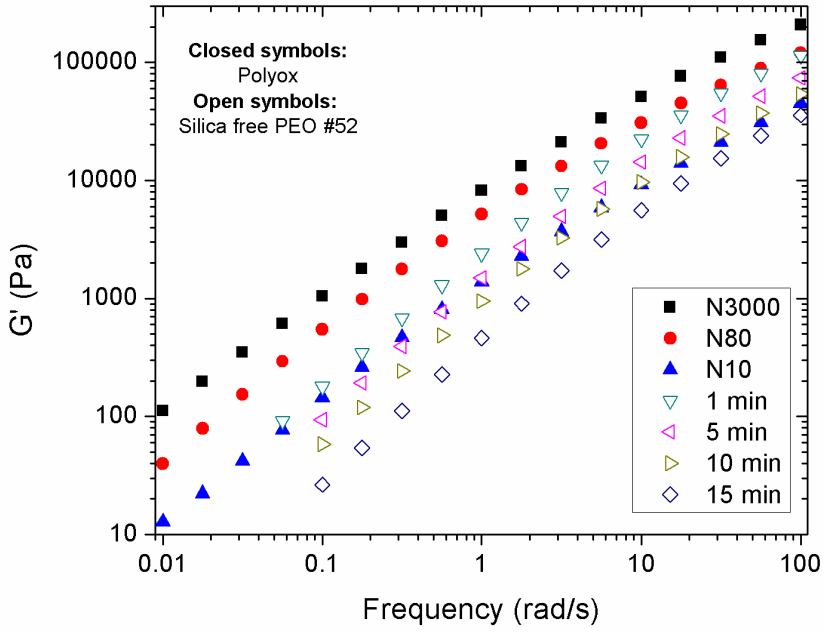

Figure C.5. Storage modulus for PEO resins.

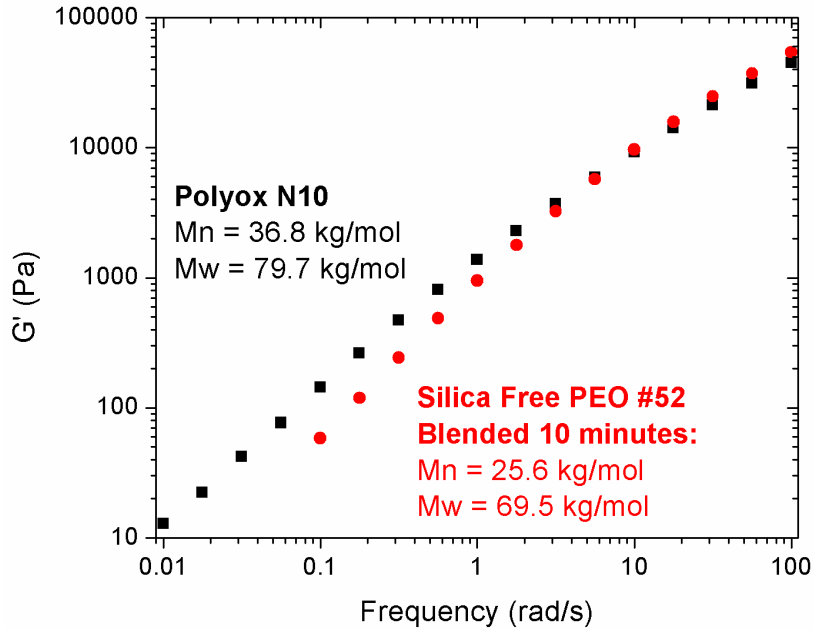

Figure C.6. Direct comparison of storage modulus for Polyox N10 and silica-free PEO blended for 10 minutes.

In summary, we were able to tune the molecular weight of the silica-free PEO resin via

melt processing in a batch microcompounder. PEO resins containing fumed silica showed the strongest changes in rheological response at low frequencies, increasing both η_o and low frequency G' by roughly a factor of 2. Little change was observed in high frequency rheological responses, suggesting that in high shear rate processing flows these materials will behave very similarly. The fumed-silica, however, would aid in post-processing handling – if the resin is still molten but no longer under strong processing flows (such as after exiting an extrusion die), the higher viscosity and elasticity should be able to reduce "stickiness" and prevent running or sagging.

Appendix D: Additional Figures

D.1 High-resolution XPS Scans, for Chapter 2

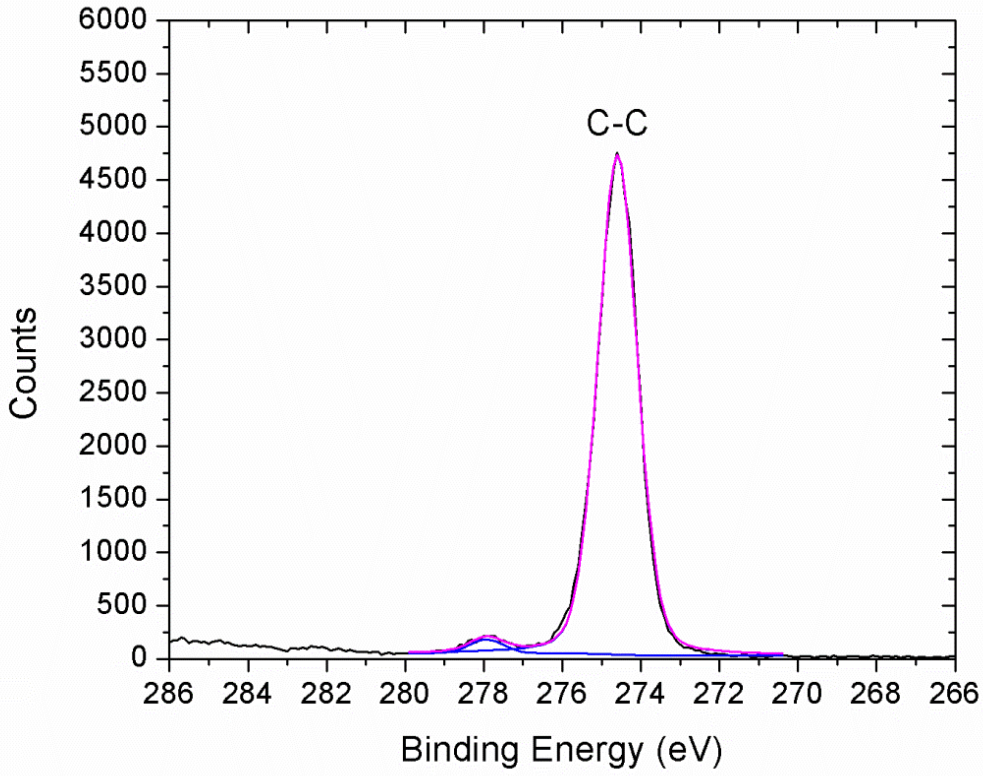

Figure D.1. High-resolution scan of C1s peak for LDPE.

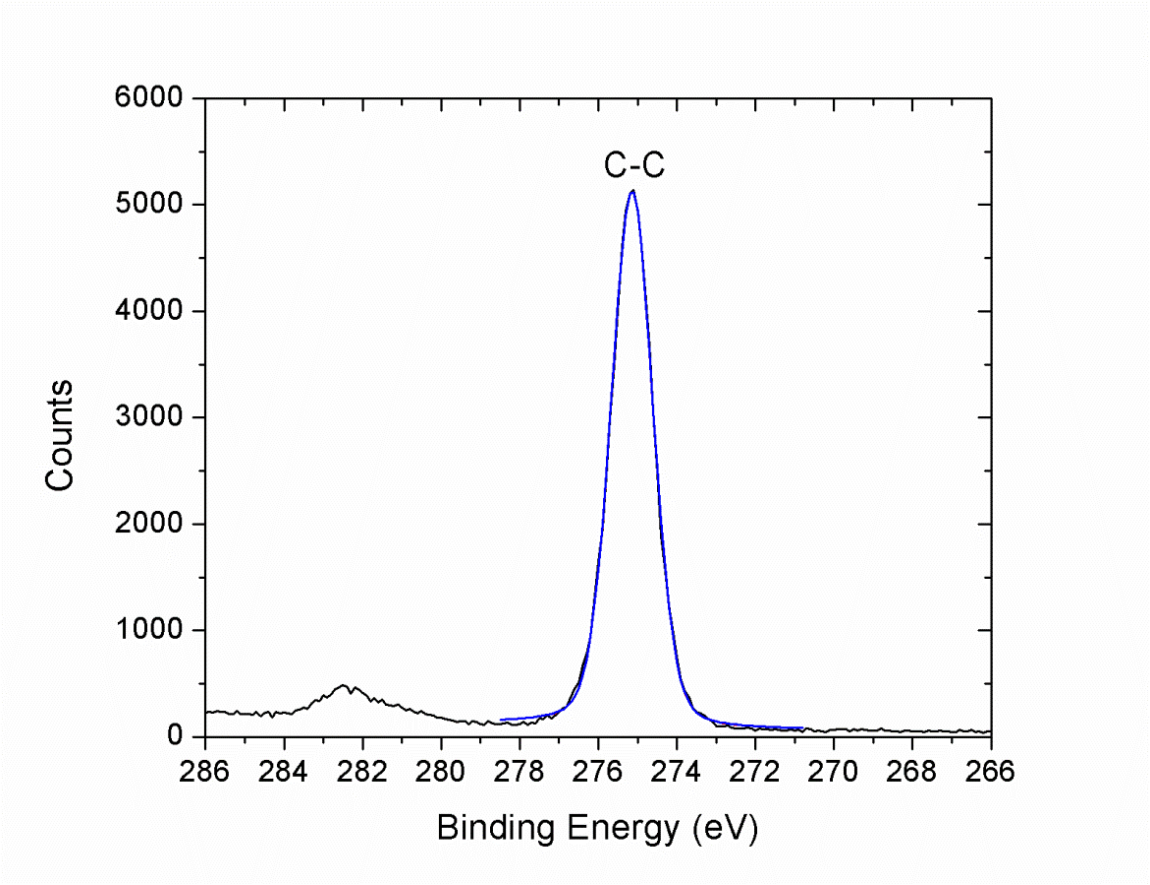

Figure D.2. High-resolution scan of C1s peak for PE-g-MA. PE-g-MA was observed to contribute only to the C-C intensity in the C1s peak, with no contribution to C-O peak intensity.

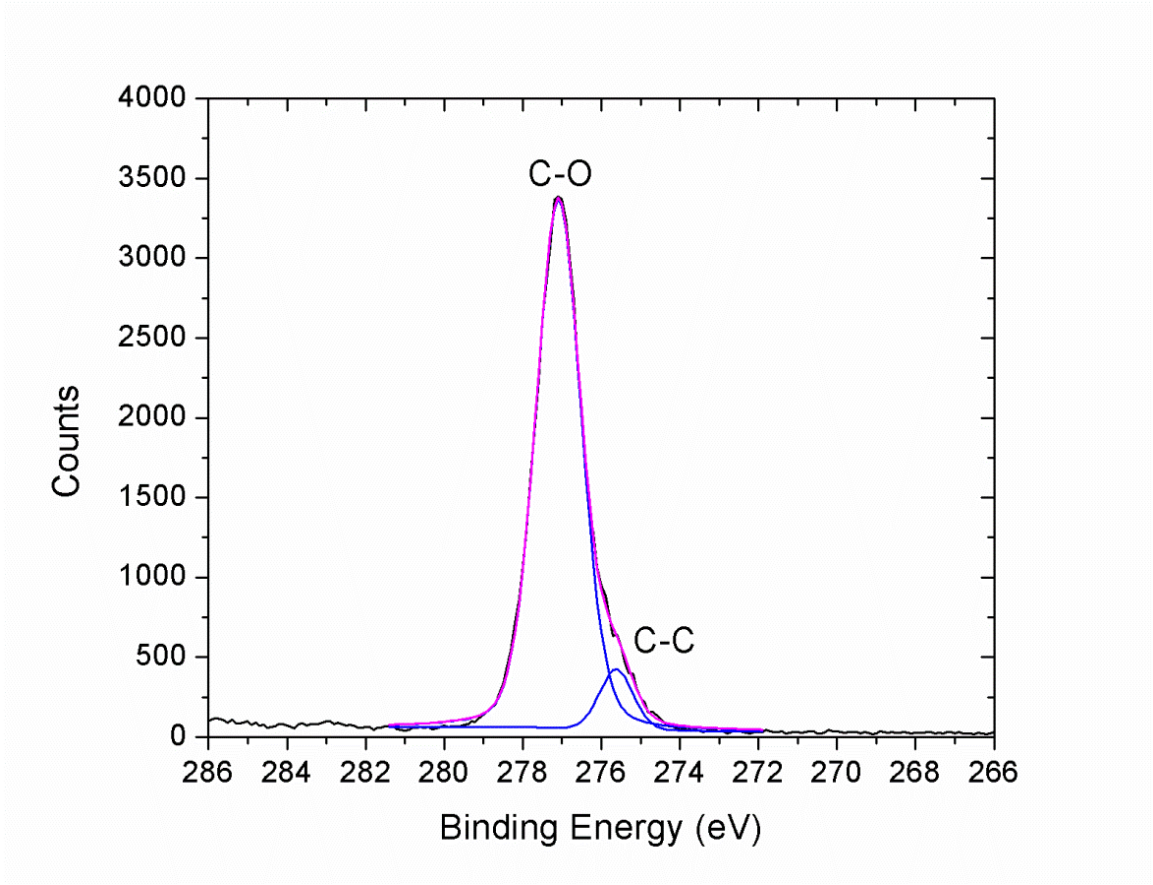

Figure D.3. High-resolution scan of C1s peak for 40K PEO. PEO was observed to contribute only to the C-O intensity in the C1s peak, with only a negligible contribution to C-C peak intensity.

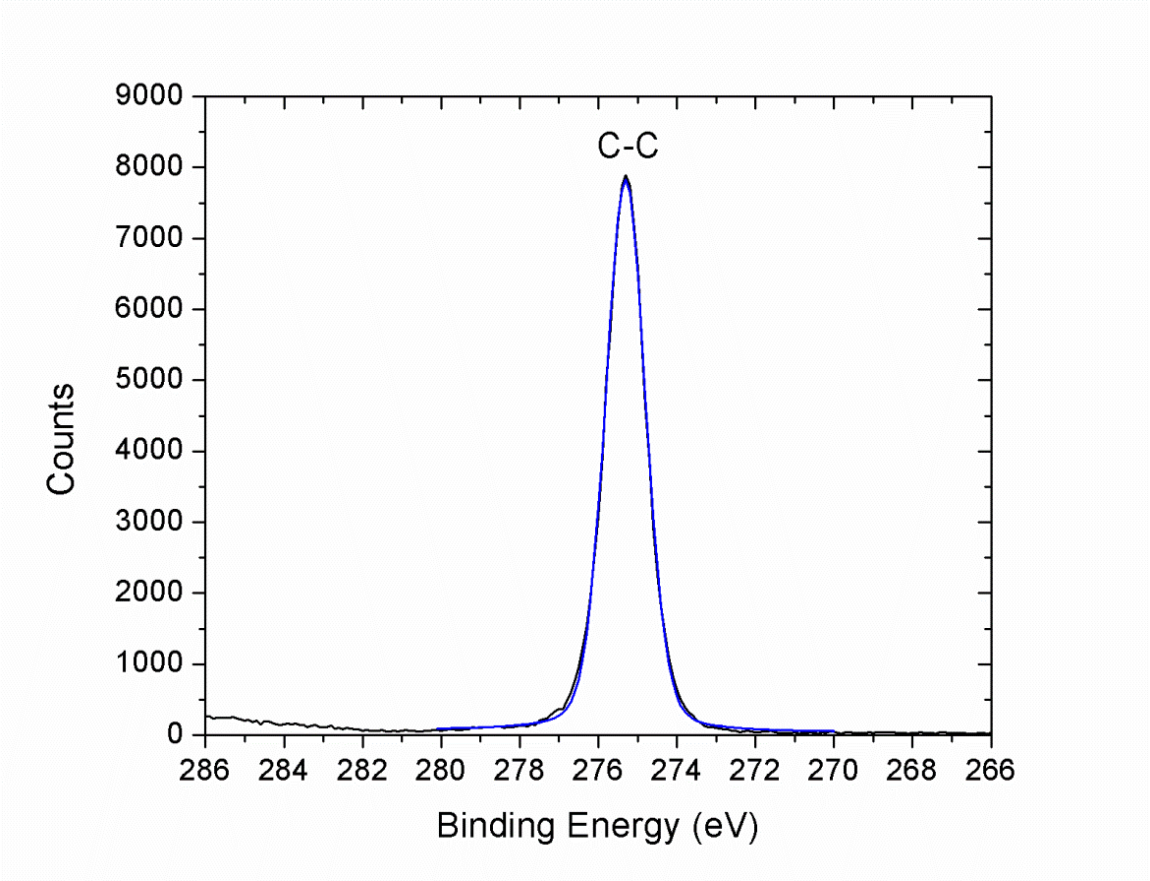

Figure D.4. High-resolution scan of C1s peak for 40K PEO laminated onto non-reactive LDPE for 10 minutes at 150 °C. No reaction was observed, as shown by the absence of the C-O C1s peak.

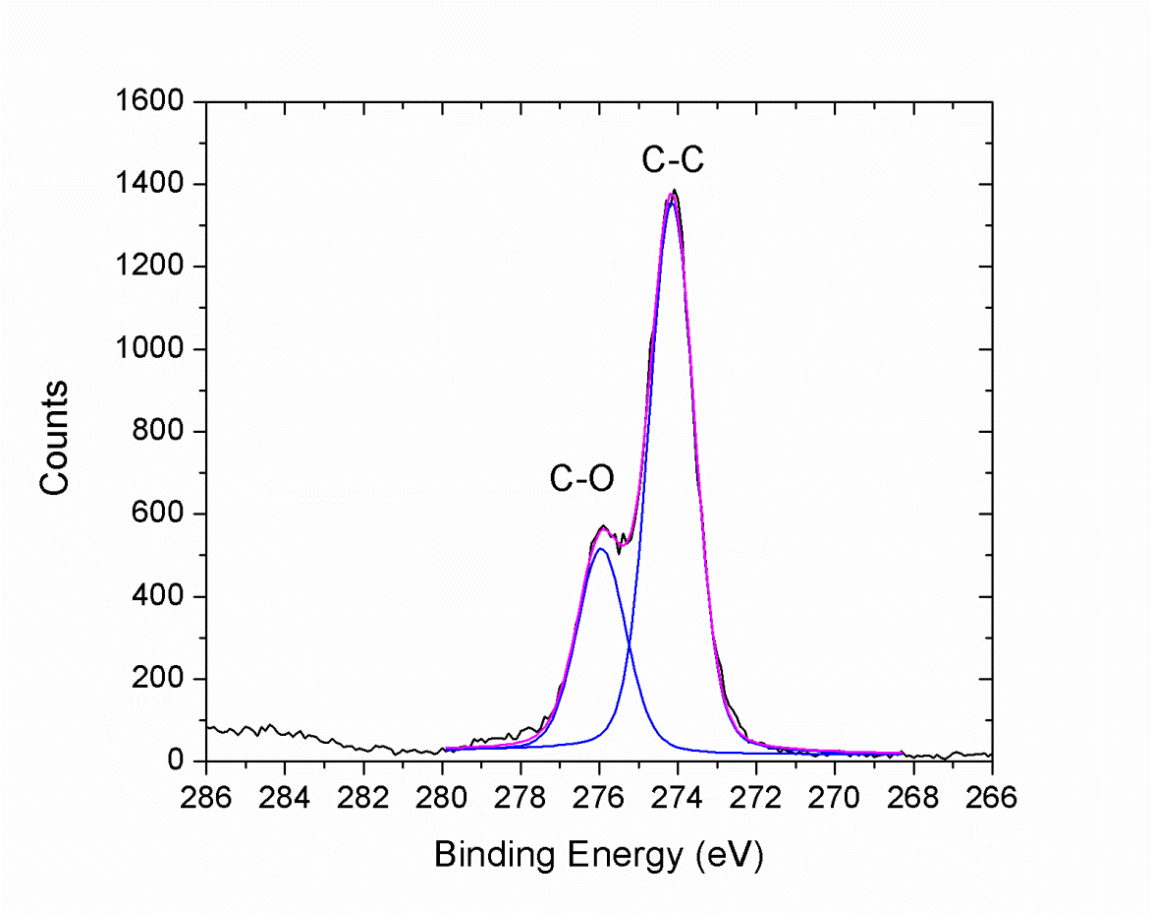

Figure D.5. High-resolution scan of C1s peak for 20K PEO laminated onto PE-g-MA for 10 minutes at 150 °C.

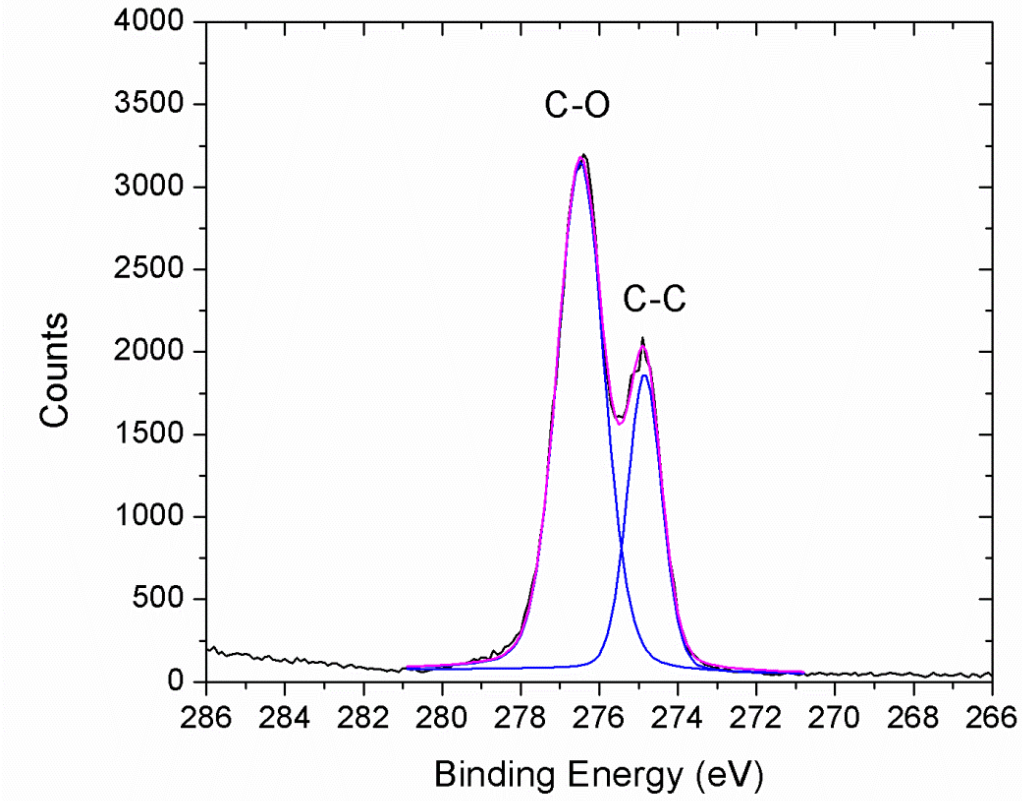

Figure D.6. High-resolution scan of C1s peak for 40K PEO laminated onto PE-g-MA for 10 minutes at 150 °C.

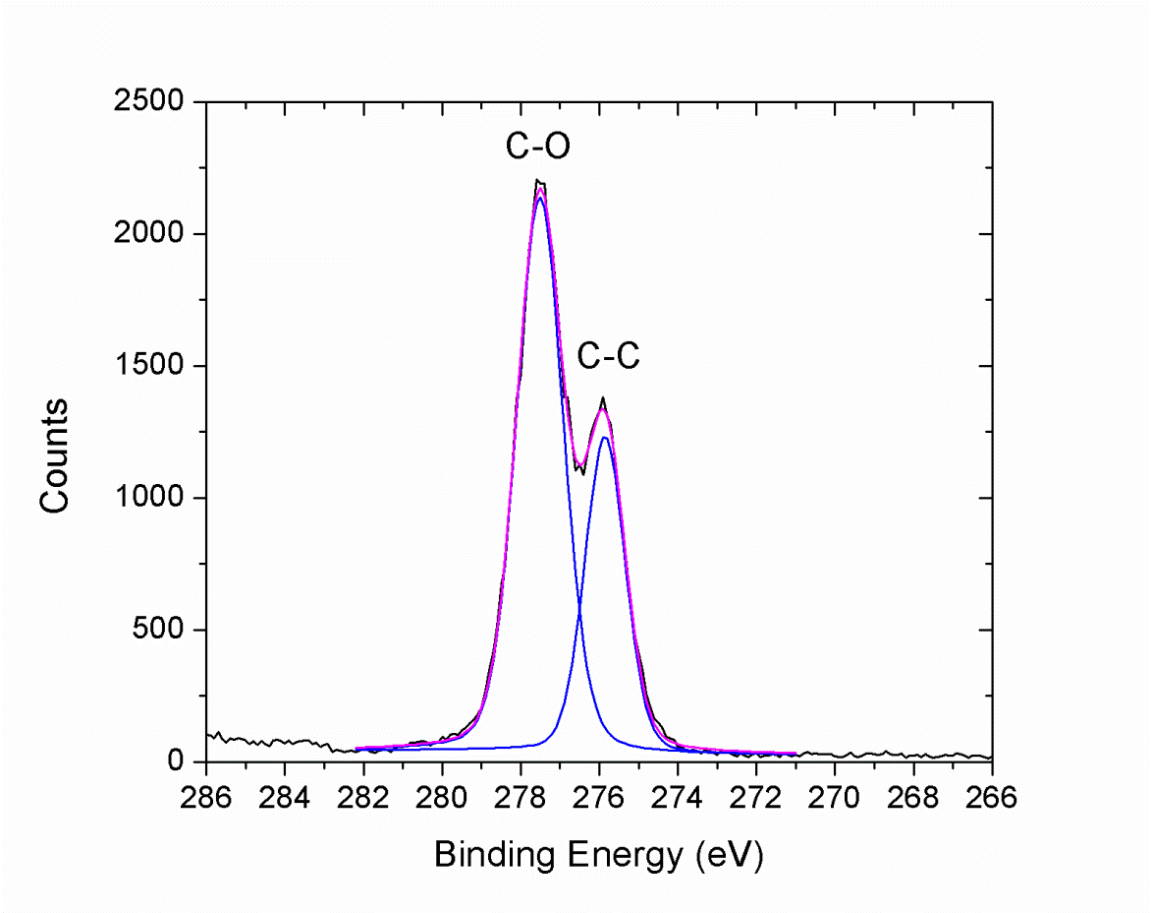

Figure D.7. High-resolution scan of C1s peak for 60K PEO laminated onto PE-g-MA for 10 minutes at 150 °C.

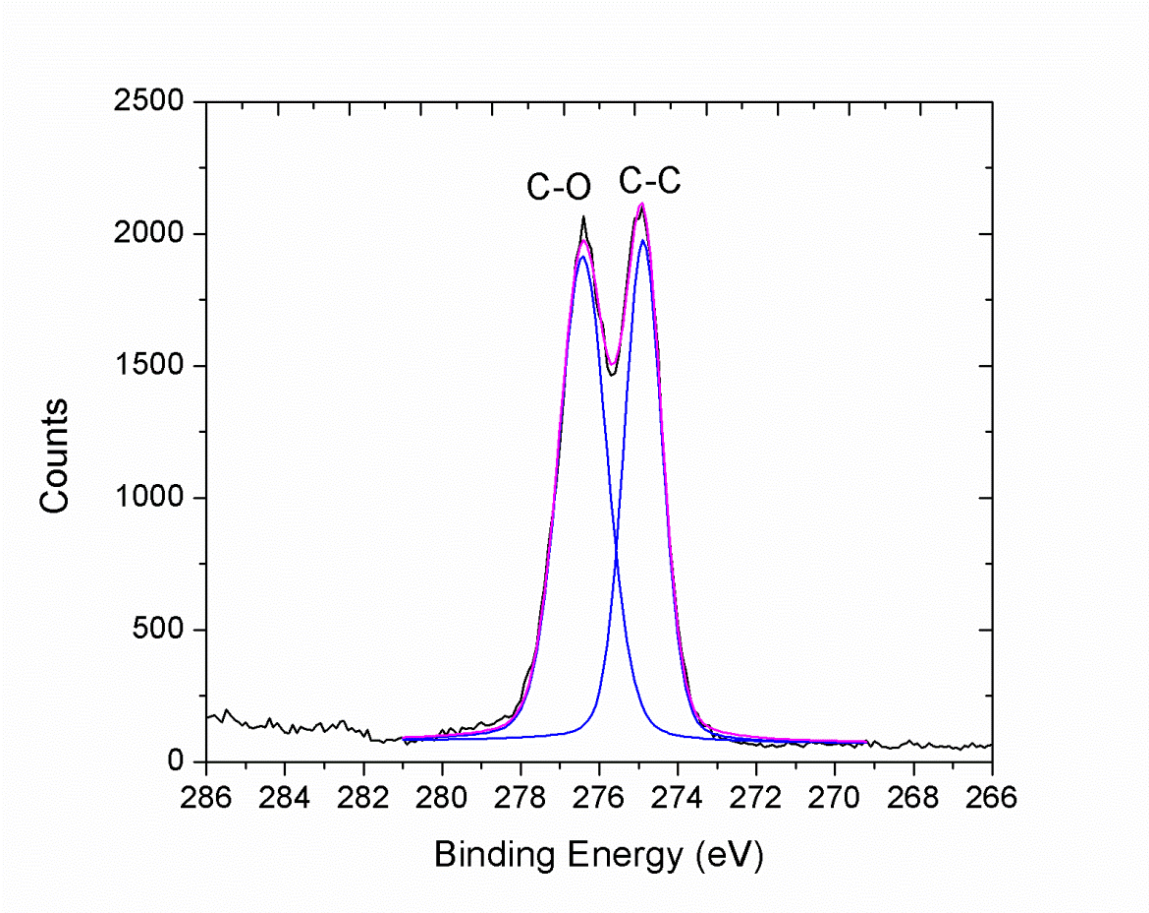

Figure D.8. High-resolution scan of C1s peak for 200K PEO laminated onto PE-g-MA for 10 minutes at 150 °C.

D.2 Non-reactive LDPE/PEO Cocontinuity, for Chapter 4

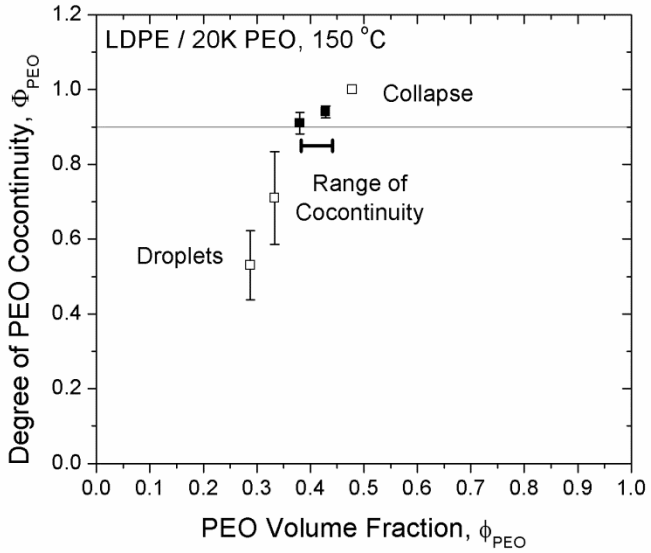

Figure D.9. Degree of cocontinuity (Eq. 4.10) for blends containing LDPE and 20K PEO. Closed symbols indicate compositions of complete cocontinuity, defined as having at least 90% of PEO mass extracted (shown by the horizontal line) while remaining self supporting. Samples with high PEO volume fraction collapsed following extraction.

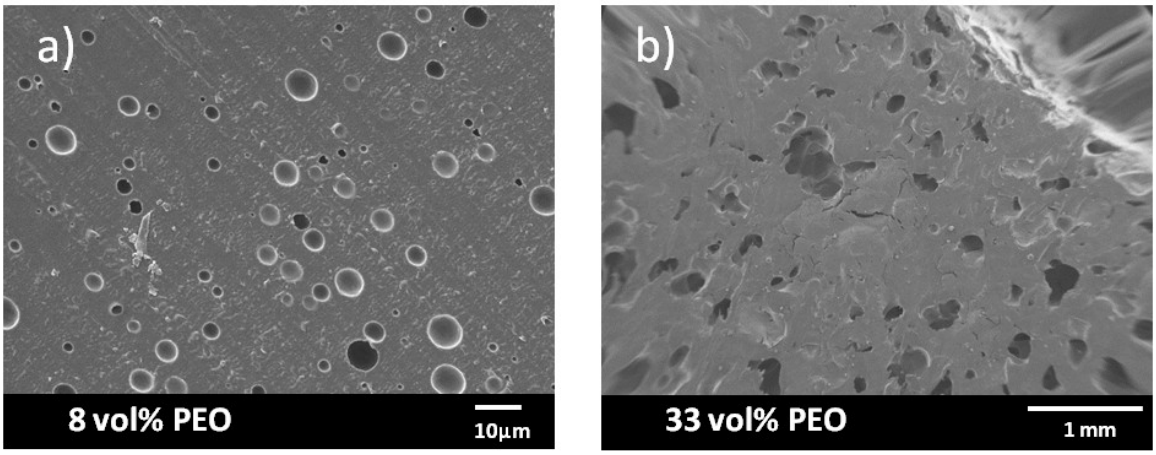

Figure D.10. SEM micrographs of LDPE / 20K PEO blends at different compositions following PEO extraction. The composition and scale bars are indicated individually on each image.

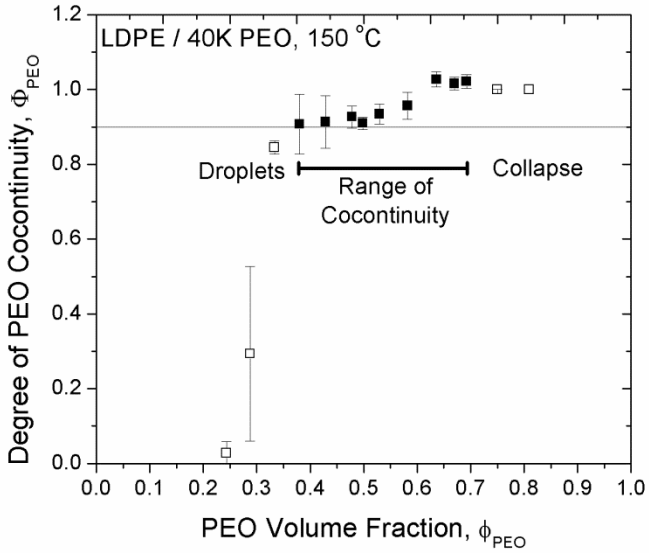

Figure D.11. Degree of cocontinuity (Eq. 4.10) for blends containing LDPE and 40K PEO.

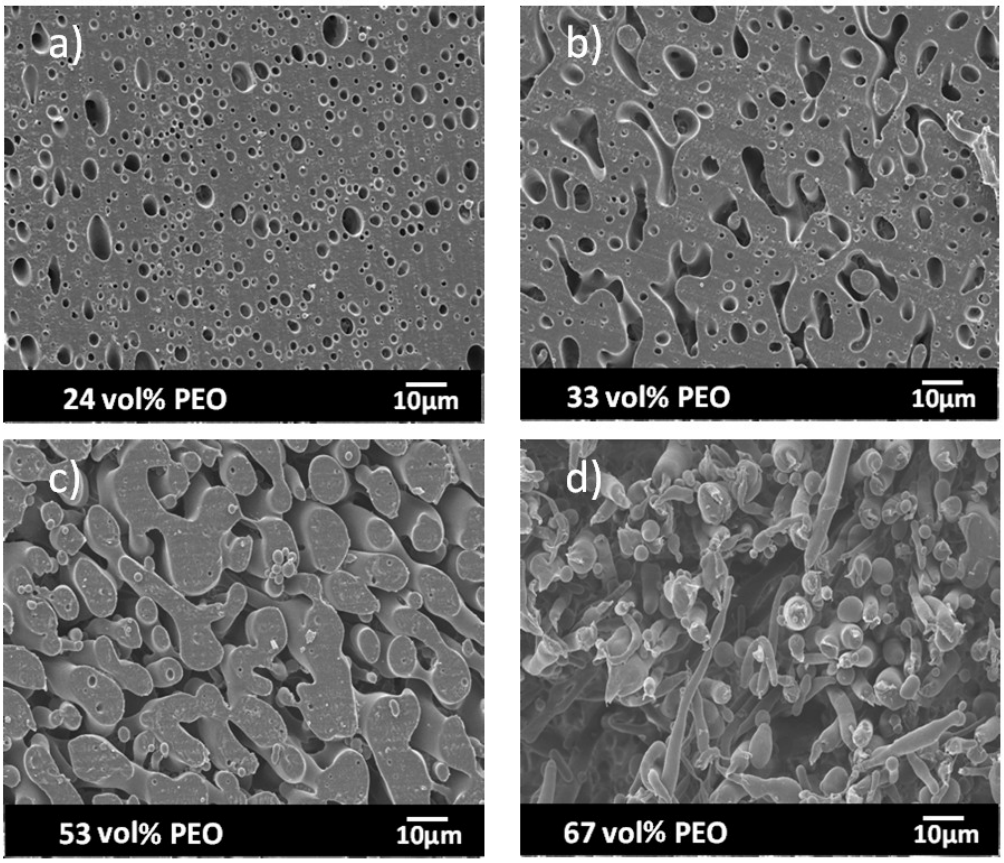

Figure D.12. SEM micrographs of LDPE / 40K PEO blends following PEO extraction.

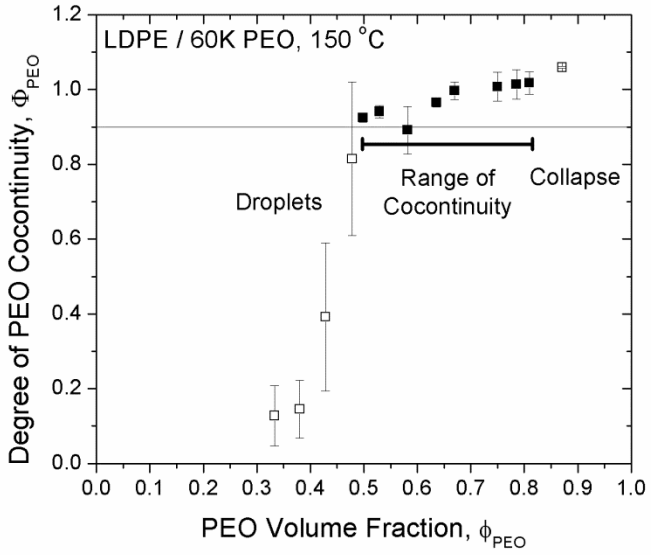

Figure D.13. Degree of cocontinuity (Eq. 4.10) for blends containing LDPE and 60K PEO.

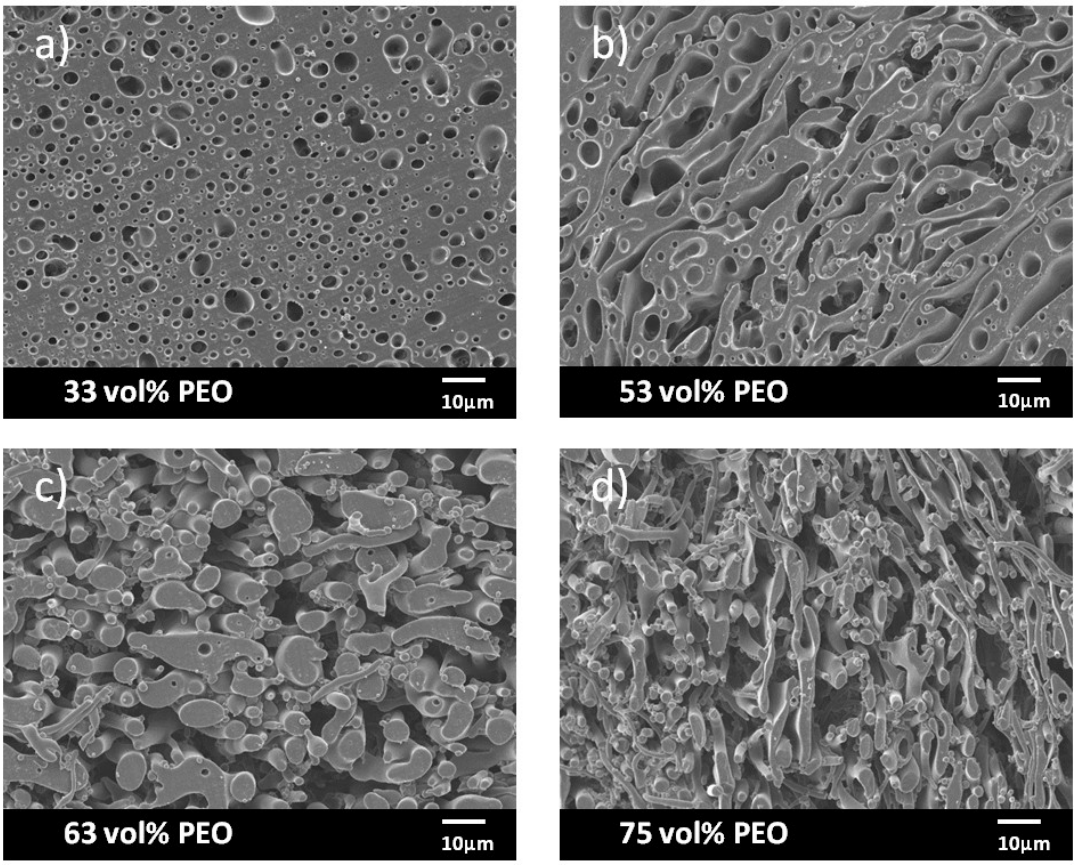

Figure D.14. SEM micrographs of LDPE / 60K PEO blends following PEO extraction.

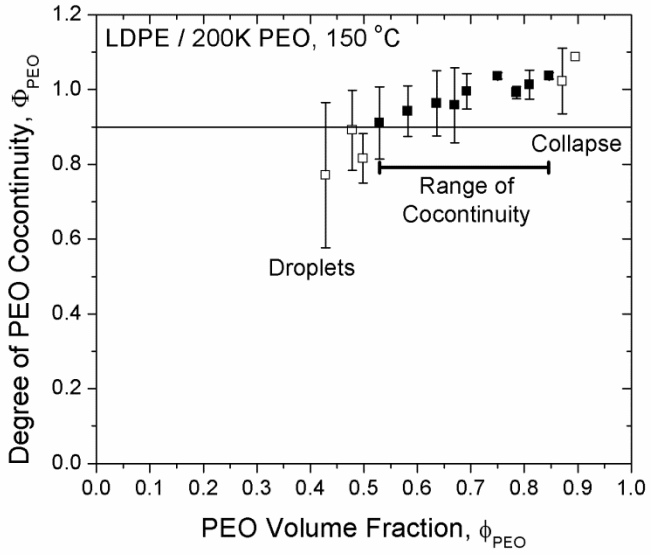

Figure D.15. Degree of cocontinuity (Eq. 4.10) for blends containing LDPE and 200K PEO.

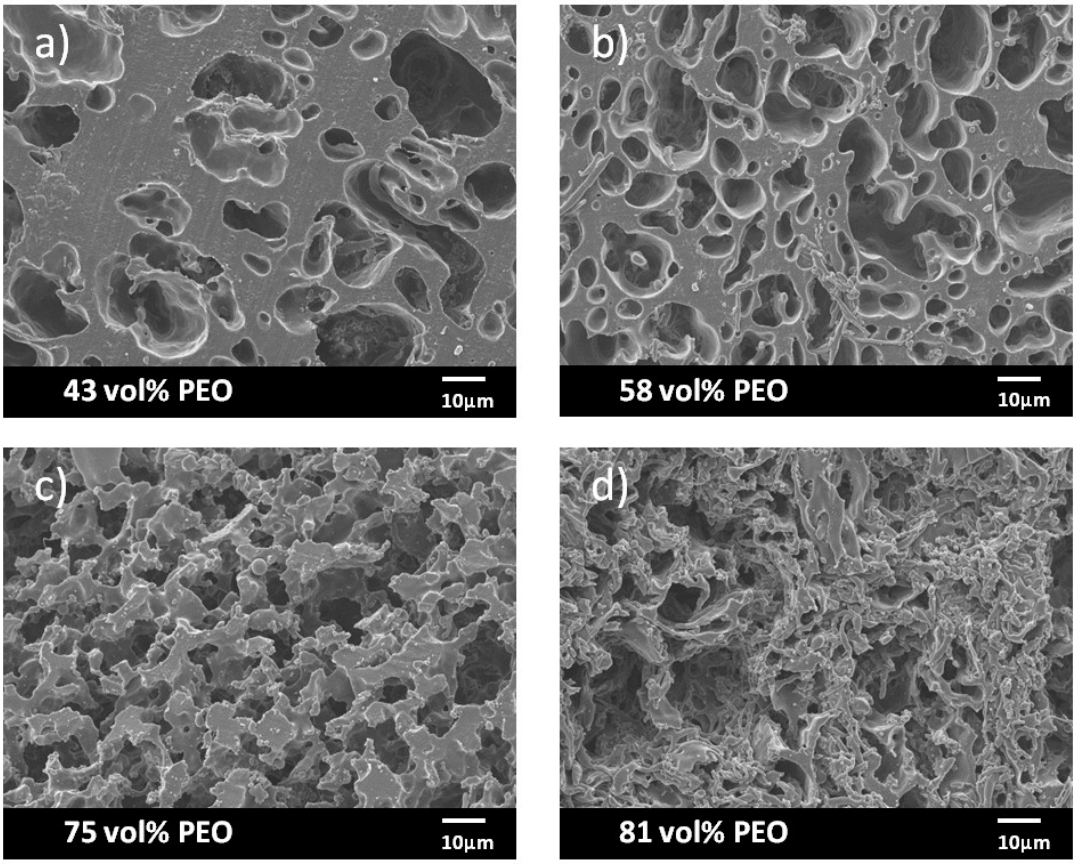

Figure D.16. SEM micrographs of LDPE / 200K PEO blends following PEO extraction.

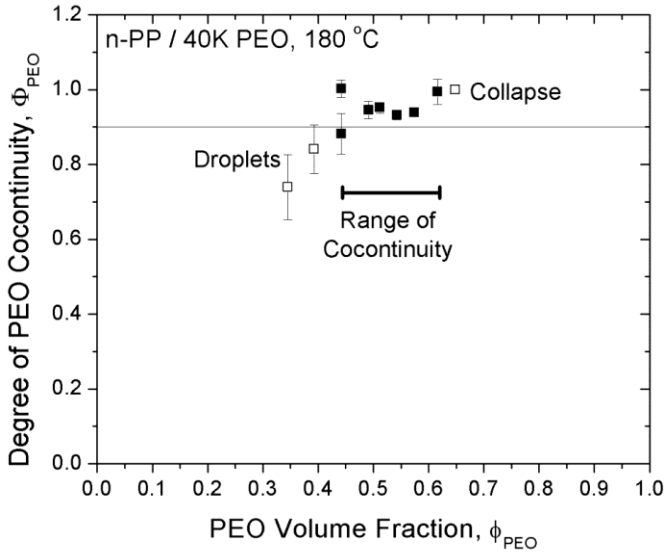

Figure D.17. Degree of cocontinuity (Eq. 4.10) for blends containing n-PP and 40K PEO.

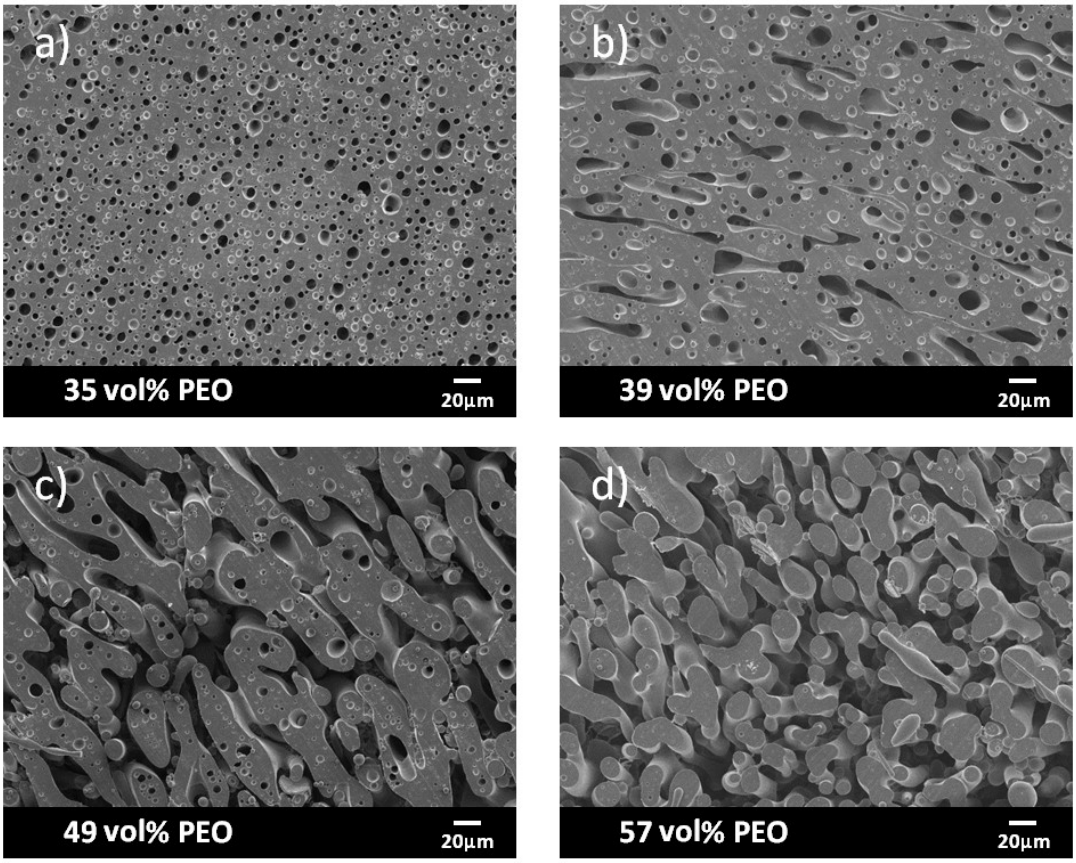

Figure D.18. SEM micrographs of n-PP / 40K PEO blends following PEO extraction.

D.3 Reactive PE-g-MA/PEO Cocontinuity, for Chapter 4

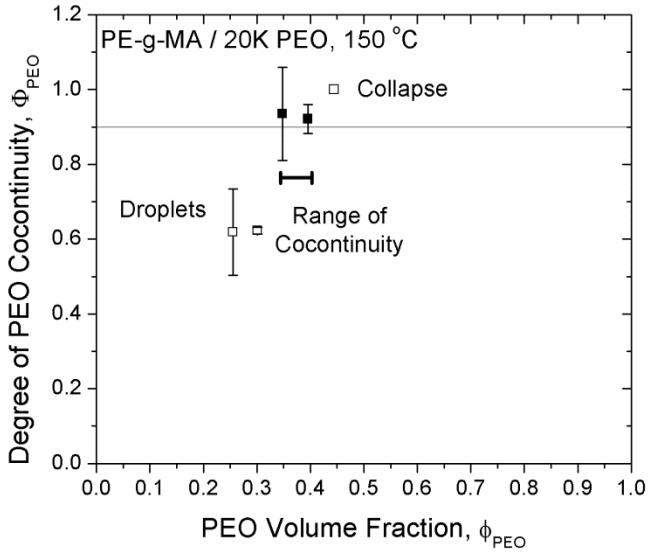

Figure D.19. Degree of cocontinuity (Eq. 4.10) for blends containing PE-g-MA and 20K PEO.

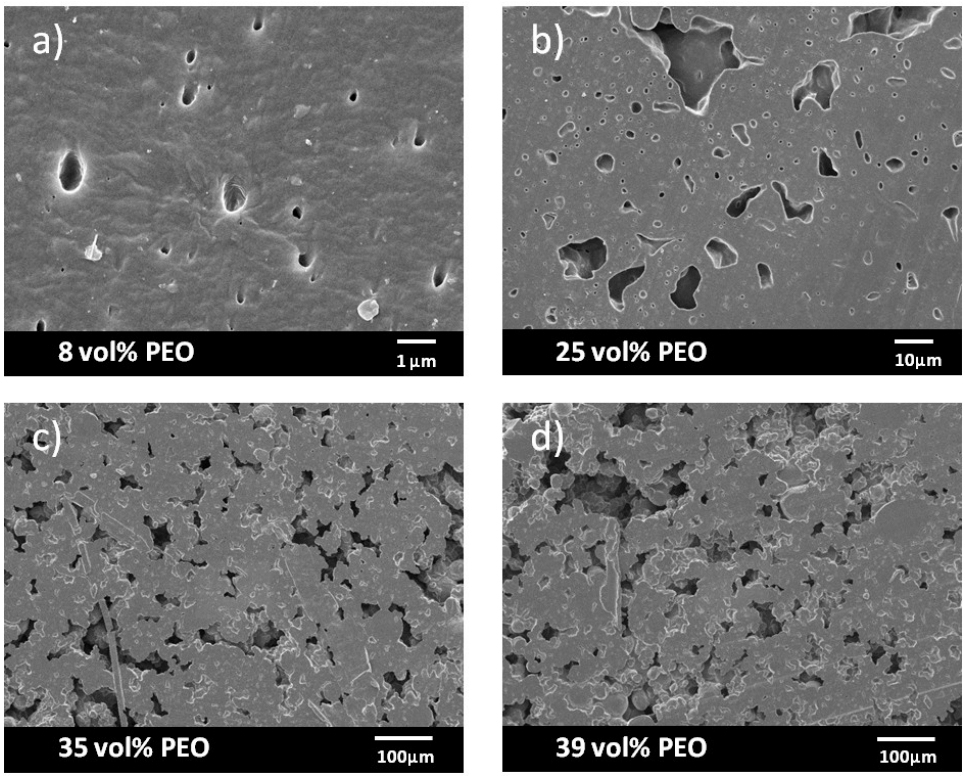

Figure D.20. SEM micrographs of PE-g-MA / 20K PEO blends following PEO extraction.

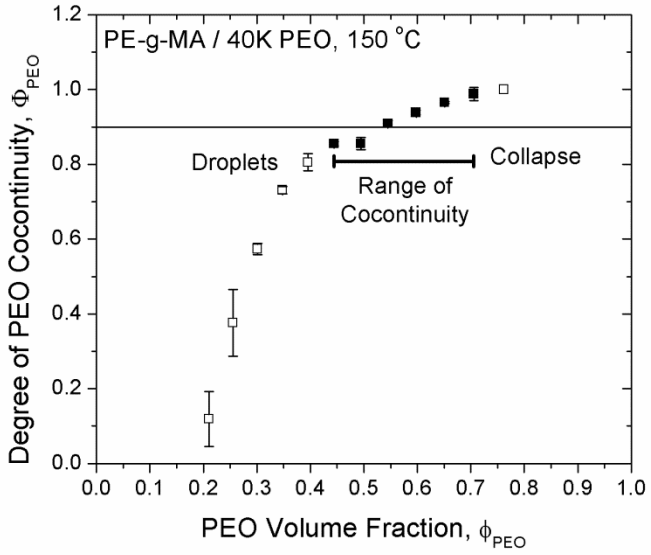

Figure D.21. Degree of cocontinuity (Eq. 4.10) for blends containing PE-g-MA and 40K PEO.

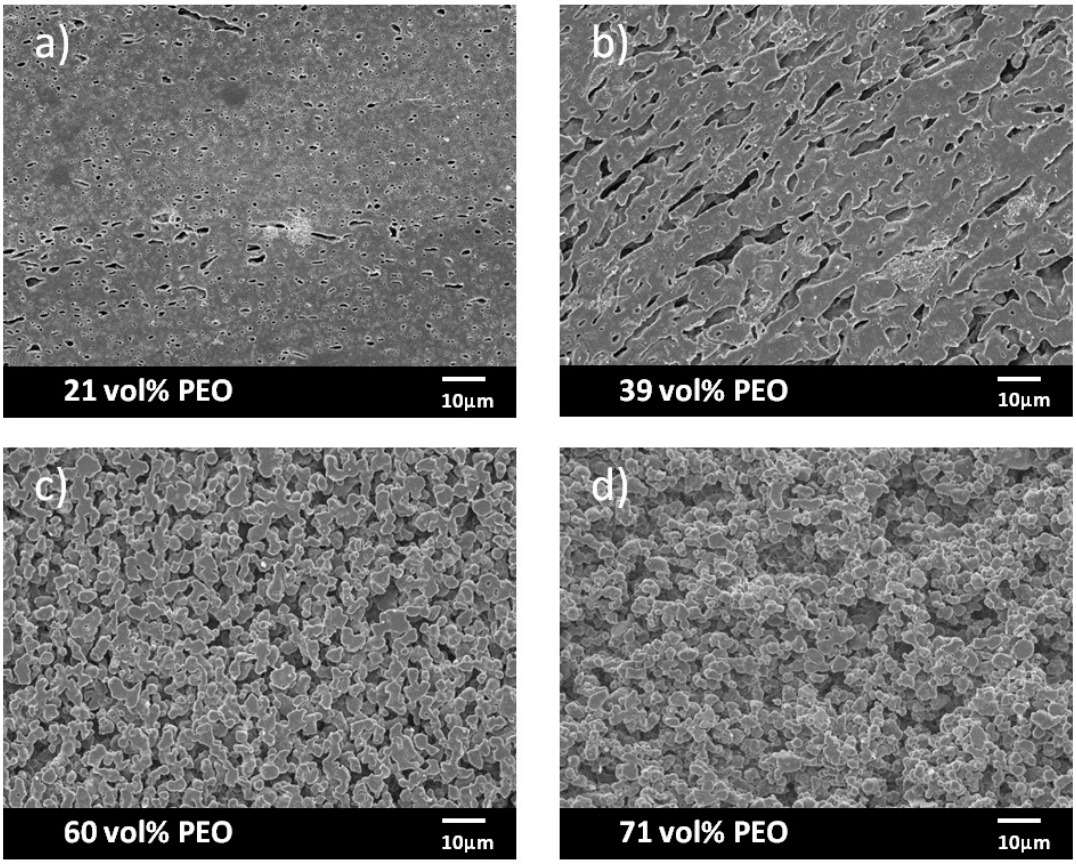

Figure D.22. SEM micrographs of PE-g-MA / 40K PEO blends following PEO extraction.

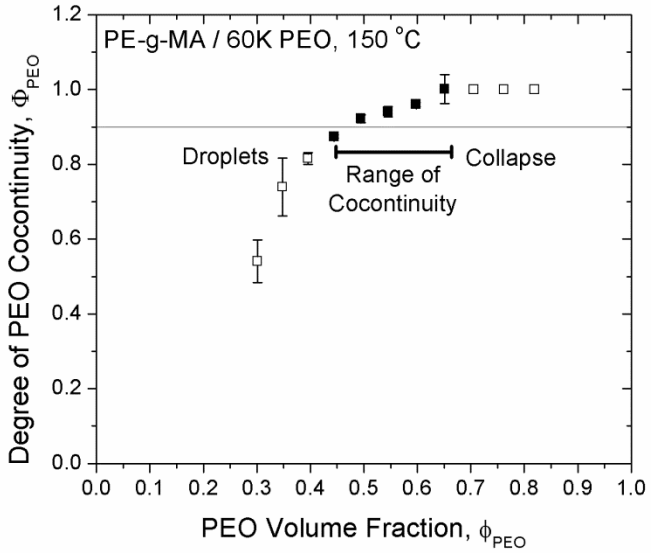

Figure D.23. Degree of cocontinuity (Eq. 4.10) for blends containing PE-g-MA and 60K PEO.

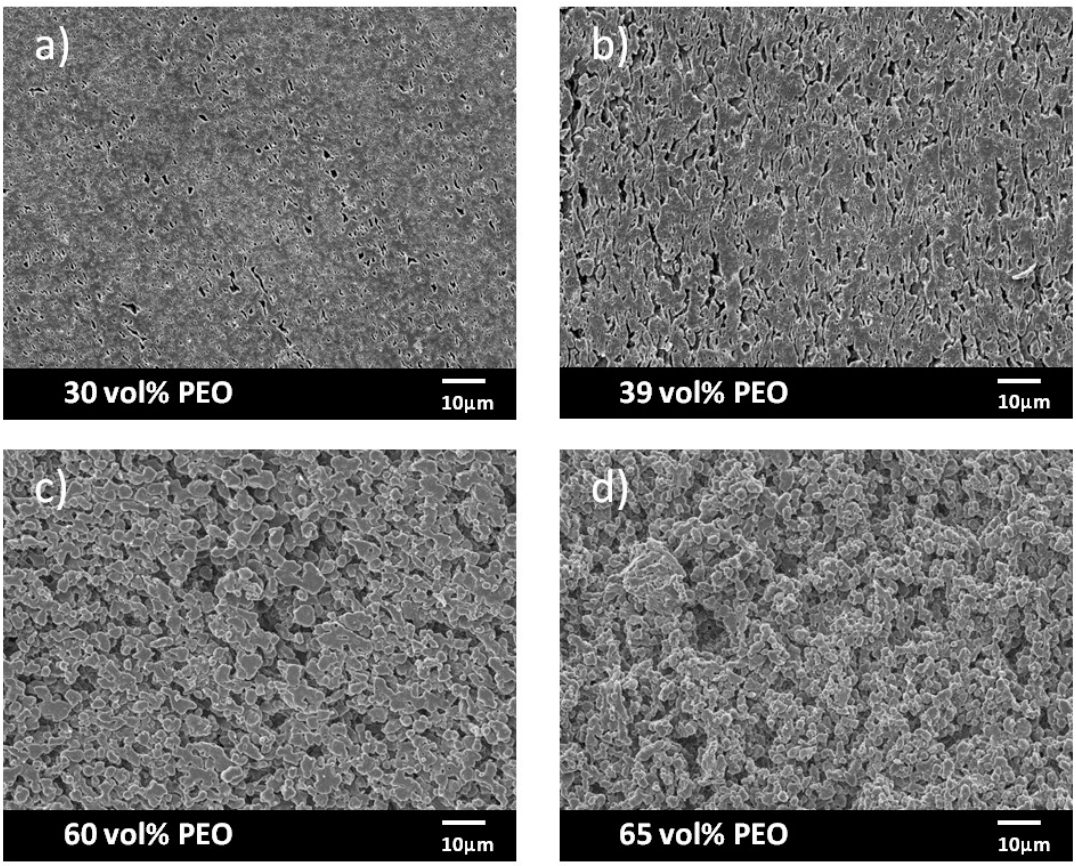

Figure D.24. SEM micrographs of PE-g-MA / 60K PEO blends following PEO extraction.

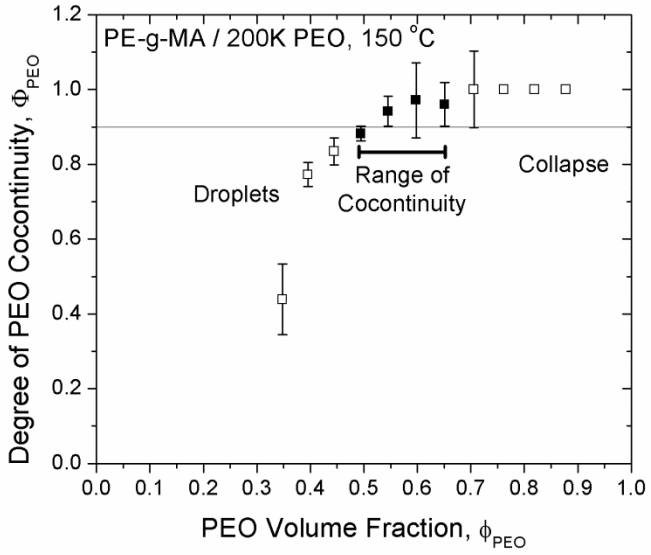

Figure D.25. Degree of cocontinuity (Eq. 4.10) for blends containing PE-g-MA and 200K PEO.

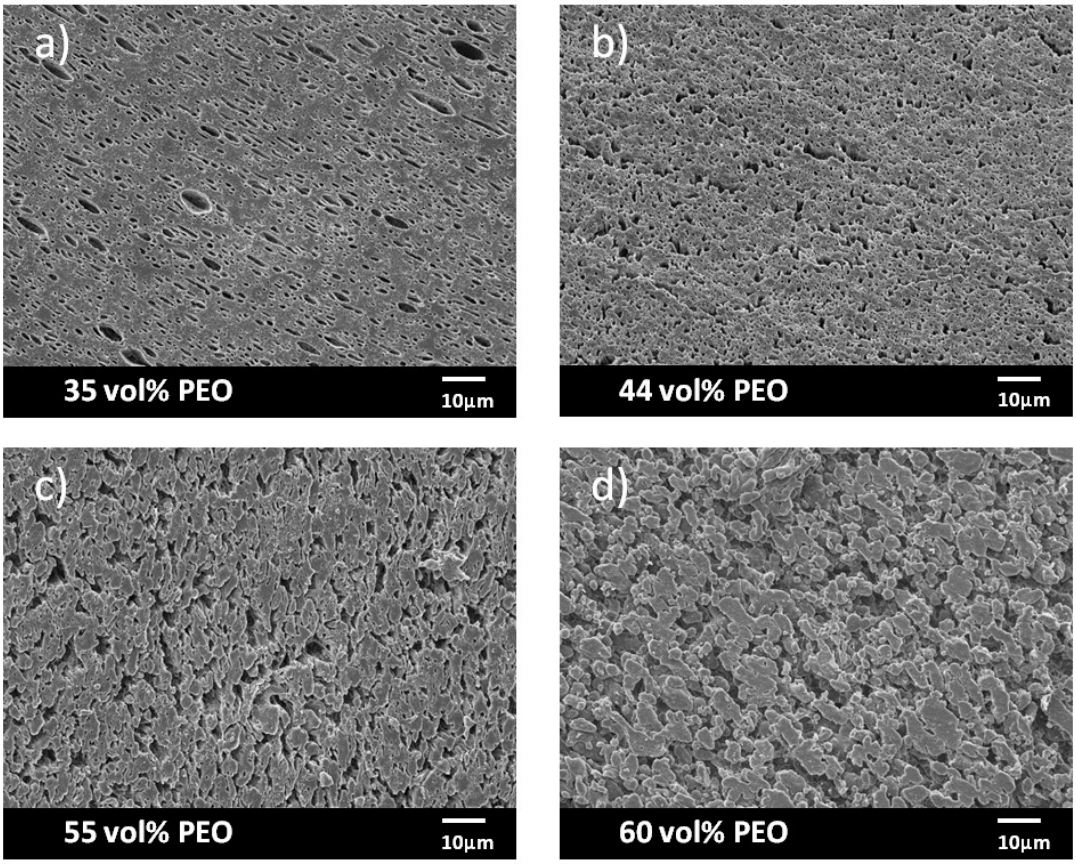

Figure D.26. SEM micrographs of PE-g-MA / 200K PEO blends following PEO extraction.

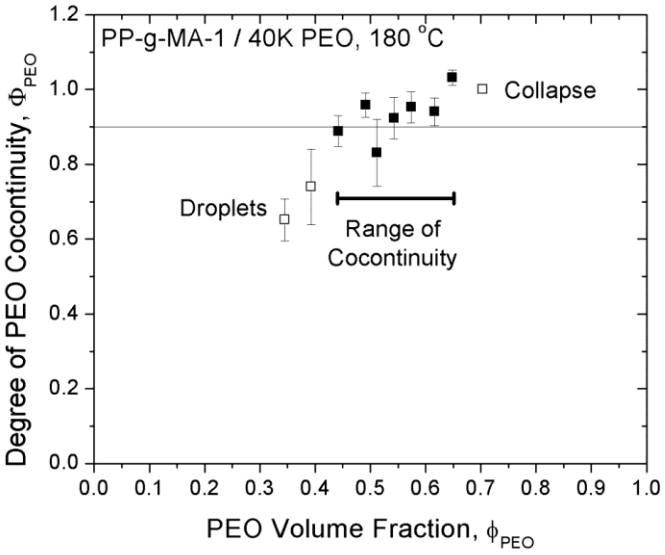

Figure D.27. Degree of cocontinuity (Eq. 4.10) for blends containing PP-g-MA-1 and 40K PEO.

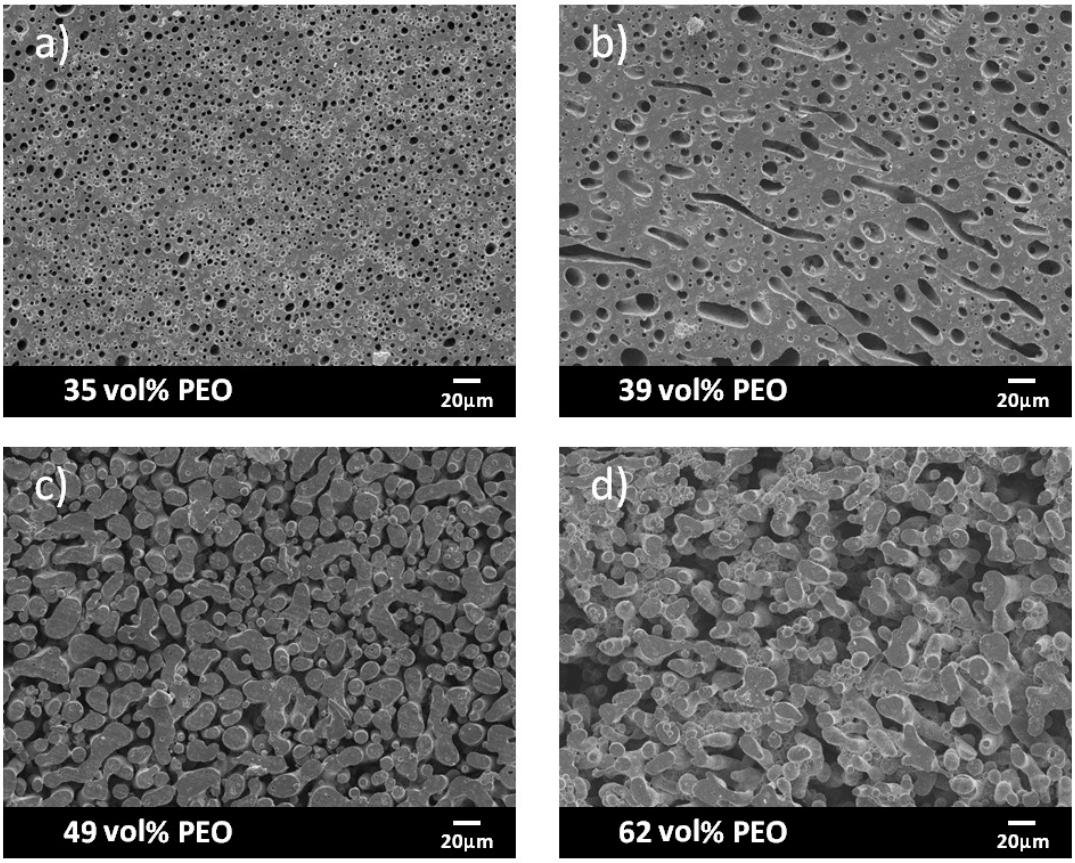

Figure D.28. SEM micrographs of PP-g-MA-1 / 40K PEO blends following PEO extraction.

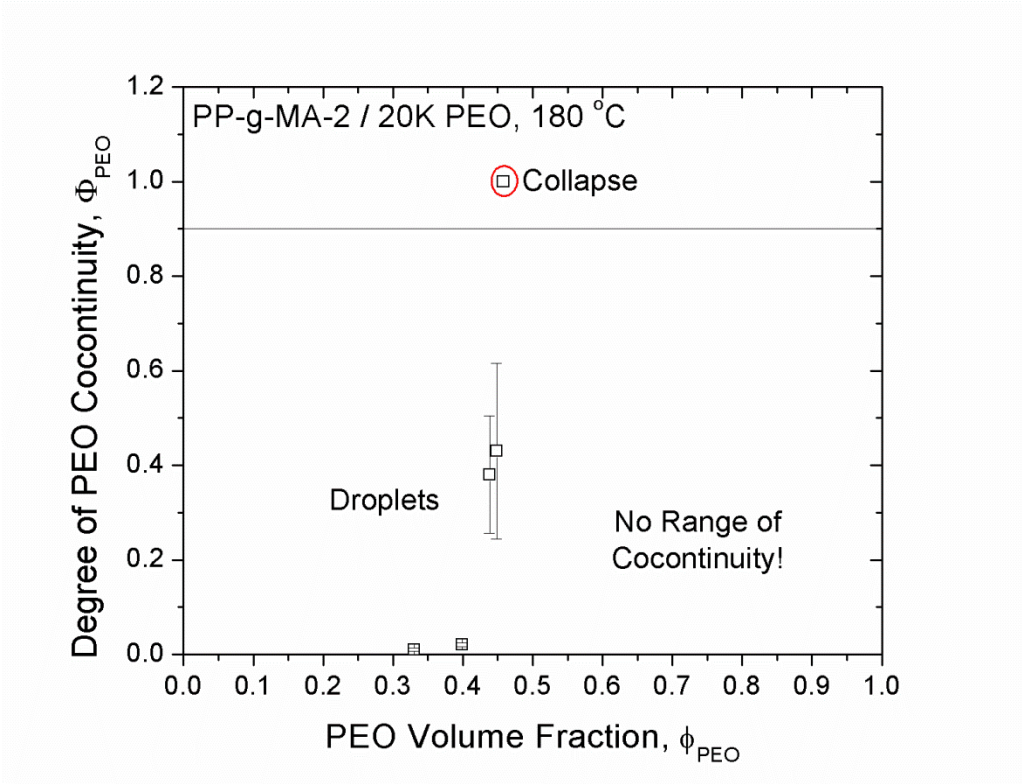

Figure D.29. Degree of cocontinuity (Eq. 4.10) for blends containing PP-g-MA-2 and 20K PEO.

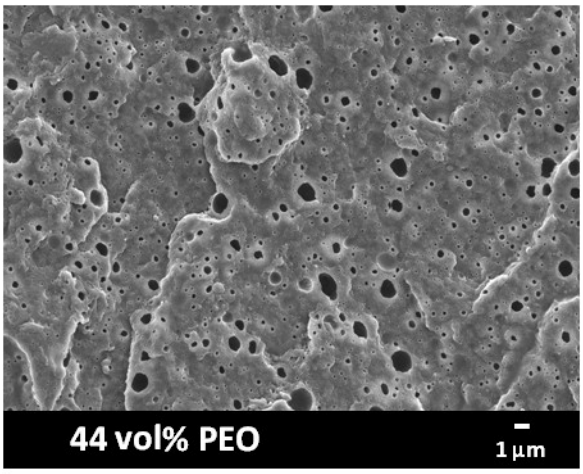

Figure D.30. SEM micrograph of a PP-g-MA-2 / 20K PEO blend following PEO extraction. All other PP-g-MA-2 / 20K PEO blends with higher PEO content collapsed upon PEO extraction.

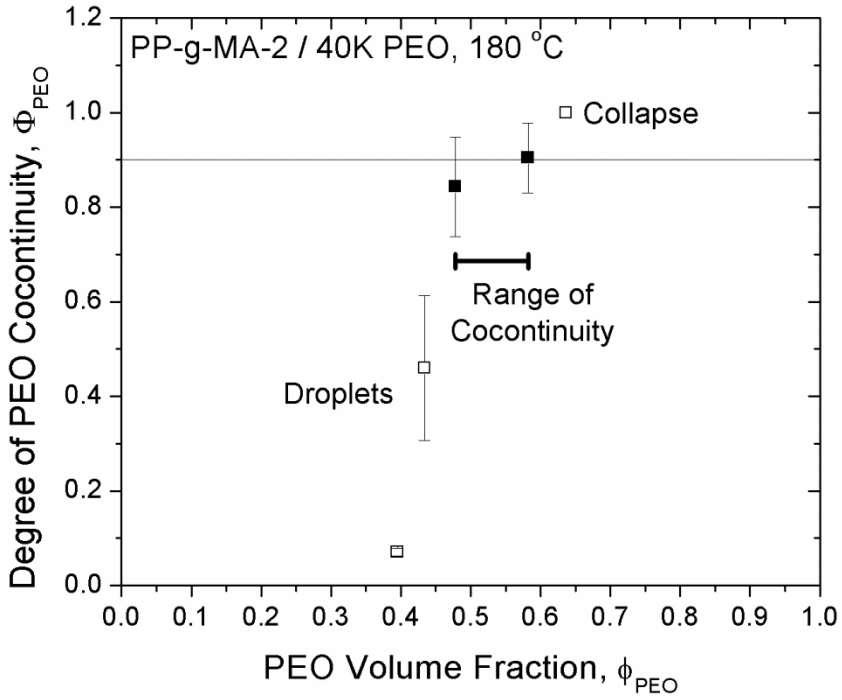

Figure D.31. Degree of cocontinuity (Eq. 4.10) for blends containing PP-g-MA-2 and 40K PEO.

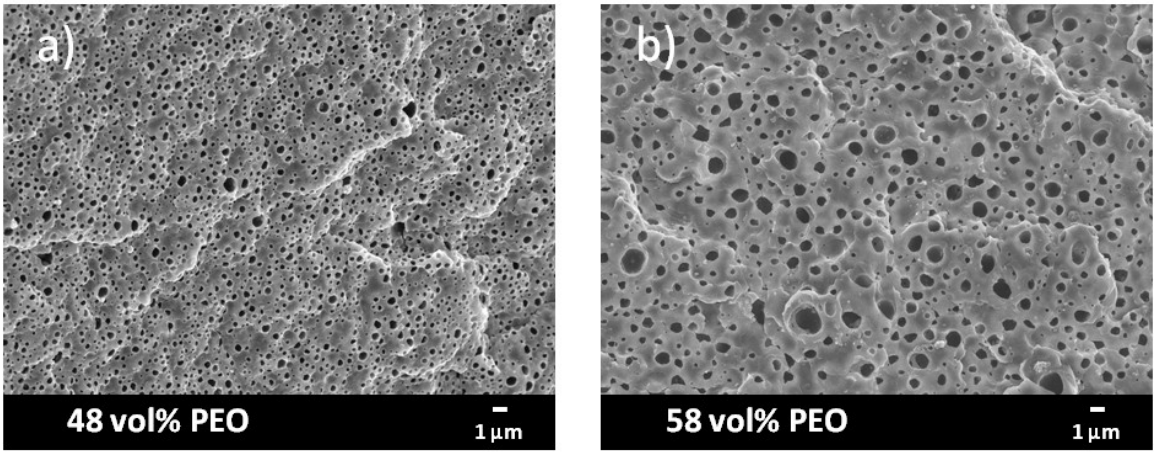

Figure D.32. SEM micrographs of PP-g-MA-2 / 40K PEO blends following PEO extraction.